Title
Controls on planktonic ecosystem structure in Eastern Boundary Upwelling Systems: a modeling perspective

Author
Moscoso, Jordyn Elizabeth

Publication Date
2022

Peer reviewed|Thesis/dissertation

UNIVERSITY OF CALIFORNIA

Los Angeles

Controls on planktonic ecosystem structure in Eastern Boundary Upwelling Systems: a modeling perspective

A dissertation submitted in partial satisfaction
of the requirements for the degree
Doctor of Philosophy in Atmospheric and Oceanic Sciences

by

Jordyn Elizabeth Moscoso

2022

ABSTRACT OF THE DISSERTATION

Controls on planktonic ecosystem structure in
Eastern Boundary Upwelling Systems: a modeling perspective

by

Jordyn Elizabeth Moscoso
Doctor of Philosophy in Atmospheric and Oceanic Sciences
University of California, Los Angeles, 2022
Professor Andrew L. Stewart, Co-Chair
Professor Daniele Bianchi, Co-Chair

Eastern boundary upwelling systems (EBUSs) are among the most ecologically diverse and productive regions in the ocean. EBUSs account for approximately 1% of the global ocean by area, but yields nearly 20% of the global fish catch. Thus, consequences to changes in productivity in EBUSs anticipated under climate change span from regional socioeconomic stability to global food security. Ecological responses to wind-driven upwelling in EBUSs have long been studied, yet questions still remain on the controls of the cross-shore (zonal) ecosystem composition. Previous studies indicate that large plankton contribute to a majority of the biomass near the coast, where upwelling supports high levels of productivity, whereas small plankton account for most of the biomass in offshore regions with low productivity. However, little is known about the variations in zonal ecosystem composition with respect to perturbations in the large-scale physical forcing. In this thesis, I present a new quasi-2D, idealized physical model of EBUSs and a size structured ecosystem model, in which an organism's size is chosen to represent ecological diversity. With this coupled

physical-biogeochemical model, we characterize the zonal ecosystem composition and its responses to perturbations. These results are an important step toward understanding the sensitivities of plankton communities and higher food-web structure in EBUSs.

The dissertation of Jordyn Elizabeth Moscoso is approved.

Naomi Levine

James C. McWilliams

Daniele Bianchi, Committee Co-Chair

Andrew L. Stewart, Committee Co-Chair

University of California, Los Angeles

2022

To Tami, Rick, Erica, and Dylan

TABLE OF CONTENTS

LIST OF FIGURES

LIST OF TABLES

ACKNOWLEDGMENTS

The deepest gratitude for my advisors, Andrew Stewart and Daniele Bianchi, who have guided me over the last six years and helped shape me into a scientist. Both of their enthusiasm, encouragement, and genuine kindness have helped make my time at UCLA incredibly enjoyable.

A huge thank you to my friends who have given me their unwavering love and support while I've been working toward this immense goal: Kaylie Cohanim, Al Fritzmann, Kyra Bergsund, Sadie Rose, David Gonzalez, Michael Andrews, Tom Rasulo, and Paul Mattern. I don't have enough words to tell you how much I appreciate you.

I would also like to acknowledge my friends, mentors, and colleagues, who have made UCLA feel like home: Ken Zhao, Tomas Chor, Matt Grieco, Angie Chen, Dial Hoang, Francis Tourney, Matthew McKinney, Clara Si, Carlyn Schmidgall, Aviv Solodoch, Todd Emmenegger, Katie Tuite, Alli Moreno, Paige Hoel, Cat Banach, Jon Aurnou, Tina Treude, Suzanne Paulson, Marcelo Chamecki, Jacob Bortnik, Kelsey Warren, the Stewart group, the Bianchi group, and many others.

And last but certainly, not least, I'd like to thank the people who have ecouraged me, inspired me, and helped me along my path toward my PhD: Chris Curtis, Laura Lamkin, Adam Neiblum, Natalie Winkler, Lisa Moscoso-Wagner, Ben Tran, Daniel Merkh, Howard Heaton, Margo Heaton, Darren Utterback, and many more.

VITA

2014	B.A. (Pure Mathematics), University of California – Santa Cruz
2014–2016	Graduate Research Assistant III, San Diego State University
2016	M.S. (Applied Mathematics – Dynamical Systems and Chaos Theory), San Diego State University
2020	M.S. (Atmospheric and Oceanic Sciences), University of California – Los Angeles
2016–2022	Graduate Student Researcher, University of California – Los Angeles

CHAPTER 1

Introduction

Eastern boundary upwelling systems (EBUSs), driven by coastal wind-forcing, are among the most productive regions in the ocean, supporting diverse and productive food-webs (Bakun and Parrish, 1982; Chavez and Messié, 2009; Croll et al., 2005). The cold, nutrient-rich water that is brought to the surface via Ekman pumping fuels a productive nearshore ecosystem (Cabre et al., 2013; Chavez and Messié, 2009; Jacox and Edwards, 2011; Messié et al., 2009). Additionally, upwelling supports a surface-intensified geostrophic current which sheds mesoscale eddies, redistributing local productivity (Capet et al., 2008; Colas et al., 2013; Gruber et al., 2011; Renault et al., 2016). This complex interplay between strong physical forcing and ecosystem cycling directly determines food-web structure and drives across-slope gradients in the composition of phytoplankton and zooplankton communities (Worden et al., 2004; Hood et al., 1991; Partensky et al., 1999). Qualitatively, the lower-trophic communities in EBUSs can be described as high biomass from large plankton at the surface nearshore, transitioning to low biomass from small plankton beneath the mixed layer, offshore (Hood et al., 1991; Worden et al., 2004; Zubkov et al., 2000).

Zonal nutrient and plankton distributions in EBUSs have been well studied in both models and observations (Jacox and Edwards, 2012; Renault et al., 2016; Gruber et al., 2011; Traganza et al., 1987). Observational studies have shown that high nutrient concentrations are correlated with *in situ* measurements of intermediate and large size classes, contributing to the plurality of the biomass (Hood et al., 1991; Worden et al., 2004; Zubkov et al., 2000). Furthermore, distributions of phytoplankton and zooplankton sizes in high nutrient

environments skew toward large cell sizes (Hood et al., 1991; Jonasz and Fournier, 1996). In some specific cases, biomass will aggregate among specific modes along the size spectrum (Sheldon et al., 1972); we refer to local maxima in biomass along the phytoplankton and zooplankton size spectra as quantization. This is in contrast to the low offshore surface nutrient concentration where smaller size classes tend to dominate the ecosystem (Collier and Palenik, 2003; Partensky et al., 1999; Sherr et al., 2005). In the subsurface, small plankton also make up a large portion of the total biomass due to a combination of light limitation and subsurface nutrient availability (Worden et al., 2004; Hood et al., 1991). **While this pattern of ecosystem community composition is a common phenomenon across all EBUSs, there remains a substantial gap in understanding of the physical and biogeochemical drivers that control zonal variations in the size distribution of phytoplankton.** Motivated by this gap, our work uses a hierarchy of physical and biogeochemical models to understand the main controls on the zonal transition of plankton in an idealized, meridionally-averaged EBUS.

While there is evidence that along-shore variations in topography and wind-stress can affect upwelling strength and productivity, (Castelao and Luo, 2018; Fiechter et al., 2018), EBUSs exhibit much larger changes over a few hundred kilometers zonally than meridionally (Van Oostende et al., 2018). In models, Fiechter et al. (2018) found that spatial variability in along-shore topography and wind-stress modulates regional productivity. However, the chlorophyll concentration only varies alongshore by a factor of 2 or 3 over the entire California Current system. Additionally, they show that over several hundreds of kilometers, along-shore averages of chlorophyll concentrations are approximately constant over an upwelling season. In observations, Hood et al. (1991) found that the zonal patterns in size distribution of planktonic ecosystems in observations is ubiquitous within the upwelling nutrient fronts, with large cells on the shoreward side of the upwelling front and smaller cells offshore. Thus we conclude that the zonal transitions are more salient and opt to study two-dimensional physical and biogeochemical dynamics.

Other modeling work of EBUSs like the California Current System (CCS) have shown the surface transition between simulated large phytoplankton at high nutrient concentrations, and small phytoplankton at low nutrient concentrations (Franks and Walstad, 1997; Goebel et al., 2010; Van Oostende et al., 2018). Goebel et al. (2010) presents an intermediate complexity model, coupled to ROMS (Shchepetkin and McWilliams, 2005) that shows a zonal transition from large plankton onshore to small plankton onshore. Additionally, Van Oostende et al. (2018) show that a large diatom class was essential to capturing a near-shore surface chlorophyll maximum averaged over an upwelling season in the CCS. **As a result of these surface and subsurface patterns in plankton community composition, we choose size as the primary axis of diversity in our food-web model, due to strong empirical relationships that are found between size and other physiological traits** (Anderson, 2005).

While we focus on size as our axis of diversity, there are other traits that can be used. Some additional proposed ecological characteristics that can be used as axis of diversity are sensitivity of growth to light and temperature, and nutrient acquisition (Follows et al., 2007; Litchman and Klausmeier, 2008). For example, nitrogen utilization abilities can be an indicator of zonal ecosystem composition. Worden et al. (2004) describes the relationship between two phytoplankton genera *Synechococcus* and *Prochlorococcus*, two common groups of picophytoplankton of different size. They note that *Prochlorococcus* can either rely on its small size and fast uptake rates to out-compete other organisms, or on the ability to uptake ammonia. On the other hand, *Synechococcus* competes for nitrate with other phytoplankton, but their abundance depends on reduced grazing pressure as a consequence of the organisms size. While reducing simulated size structured ecosystem models are likely an oversimplification of the food-web, important controls on ecosystem dynamics – general nutrient uptake rates, respiration, nutrient limitation, preferential grazing, and predator-prey interactions – often scale with respect to cell size (Tang, 1995; Litchman et al., 2007). Furthermore, in their review, Follows and Dutkiewicz (2011) note that using cell size as the axis of diversity in an

ecosystem model can reduce the dimensionality of the model's parameter space, allowing for reduced complexity in interpretation.

Bottom-up and top-down controls on the ecosystem are important in determining ecosystem dynamics and community structure (McQueen et al., 1986; Lehman, 1991; Banse, 1994; Verity and Smetacek, 1996; Chenillat et al., 2013). The specific physical processes which control the delivery of nutrients to the euphotic zone, and thus the variations in zonal ecosystem composition, is still not well understood. A large array of physical forcings influence the upwelling strength, source depth, and the resulting nutrient concentration within the euphotic zone (Jacox and Edwards, 2011, 2012). Additionally, the physical scales in EBUSs range from large-scale processes such as the mean wind-driven circulation, to smaller scale processes like diapycnal mixing (Capet et al., 2008; Jacox and Edwards, 2011, 2012; Gruber et al., 2011; Renault et al., 2016).

Specific physical drivers that may have important impacts on zonal ecosystem compositions include eddies, wind-forcing, and nutrient availablity in the source waters of upwelling (Gruber et al., 2011; Jacox and Edwards, 2011, 2012; Renault et al., 2016; Pozo Buil et al., 2021). For example, the shape and strength of the wind profile has important effects on the mean upwelling and primary productivity (Renault et al., 2016) and is expected to intensify with future climate forcing (Rykaczewski and Dunne, 2010). A secondary circulation is controlled by mesoscale eddies formed by baroclinic instability of the coastal geostrophic current (Colas et al., 2013). Eddies work to redistribute newly upwelled nutrients zonally, and subduct nutrients and other tracers beneath the ocean surface (Capet et al., 2008; Gruber et al., 2011), with potential to supply nutrients to the subsurface and in the deep chlorophyll maximum (DCM) (Tréguer et al., 2018; Cullen, 1982a). The source depths of the upwelled water also affect the total nutrient concentration across an EBUS, near the coast (Jacox and Edwards, 2012; Pozo Buil et al., 2021), and in the DCM (Cullen, 1982a).

Through idealized modeling, we are able to quantify and compare the importance of a set of physical forcings that controls the properties of the planktonic ecosystem in a represen-

tative EBUS. We build upon our current understanding of ecosystem structure by exploring a wide physical parameter space using a hierarchy of idealized physical and biogeochemical models, with increasing dimensionality and ecosystem complexity, as outlined in the following chapters. The overarching science questions this research seeks to answer are summarized below:

- What is the minimal configuration for a coupled physical and biogeochemical model to capture the zonal distribution of phytoplankton in an idealized EBUS? (Ch. 2, Ch. 3, and Ch. 4)
- What controls quantization observed in size structured ecosystems? (Ch. 3)
- What are the relevant physical drivers that control the total biomass of primary producers and ecosystem diversity in EBUSs? (Ch. 4)

The rest of this document is organized as follows:

In Chapter 2, we present an idealized, quasi-2D Meridionally Averaged Model of Eastern Boundary Upwelling Systems (MAMEBUS). This project was predominantly focused on developing the idealized physical framework that we will use in Chapter 4. While other 2D models have previously been used to study the zonal response of upwelling in idealized EBUSs (Jacox and Edwards, 2011, 2012), they often lack explicit representation of three dimensional processes that control biology in upwelling systems. These processes include the effects of eddies (Gent and McWilliams, 1990), isopycnal diffusivity (Redi, 1982), surface mixed and bottom boundary layer mixing (Ferrari et al., 2008), and diapyncal mixing (Large et al., 1994). Furthermore, MAMEBUS allows for the effect of meridional pressure gradients which allow for interior upwelilng (Lentz and Chapman, 2004), and the effect of meridional advection that transports nutrients and other tracers into and out of the computational domain (Hood et al., 1991; Sherr et al., 2005). We present MAMEBUS as a tool to test and tune ecosystem models and other physical and biogeochemical parameterizations (e.g.

mesoscale/submesoscale eddy parameterizations, surface mixed- and bottom boundary-layer parameterizations), and validate it with *in situ* data from CalCOFI (McClatchie, 2016). A major benefit to using 2D models over more comprehensive 3D models is that 2D models are less computationally expensive and can be used to understand a larger parameter space. Furthermore, we are able to impose a wide variety of physical perturbations independently of one another.

In Chapter 3, we present a minimum complexity size-structured NPZD model, referred to as size structured ecosystem model (SSEM) throughout this proposal. This Chapter is predominantly focused on understanding what controls quantization of biomass along the planktonic size spectrum. Previous studies have shown that time integrated solutions of size structured ecosystem models are quantized and do not adhere to log-normal distributions (Banas, 2011; Sauterey et al., 2017). *In situ* studies have also found that this quantization of biomass occurs in productive ocean regions (Hood et al., 1991; Jonasz and Fournier, 1996; Worden et al., 2004). We show that biomass tends to aggregate as peaks along the phtyoplankton and zooplankton size spectrum. Furthermore, we find that the characteristics of this quantization are controlled by the width of the grazing profile, and that the biomass peaks are robust under variations in external nutrient forcing. These finding are confirmed in one vertical dimension in the presence of light- and temperature-limitation and surface mixed layer diffusion. We take advantage of this behavior to reduce the computational expenses of SSEMs. We are able to reduce the ecosystem complexity to a few size classes, chosen to coincide with the centers of mass of the biomass peaks, without losing significant accuracy in zero- and one-dimensions.

In Chapter 4, we combine the models developed in Chapters 2 and 3. Taking advantage of the computational efficiency of MAMEBUS, we implement the high-resolution SSEM described in Chapter 3, with 50 phytoplankton and zooplankton size classes. At this resolution in size space, we are able to capture quantization of biomass similar to that found in 0- and 1-D (Moscoso et al., 2022). We identify three regions of the model that show ecological

responses to changes in the physical and biological parameter space: the continental shelf, the surface chlorophyll maximum (SCM), and the deep chlorophyll maximum (DCM). We conduct experiments over a subset of the physical parameter space representative of the California Current System (CCS). These parameters include the shape and the strength of the wind, the eddy advection and stirring, and the offshore distribution of nitrate, which is assumed to be set by processes occuring in the interior of the Pacific Ocean. We identify trends in various metrics of ecological diversity, including the average size of plankton in the model, and the Shannon diversity index. With this study, we are able to characterize the zonal ecological response in EBUSs to changes in a representative parameter space.

CHAPTER 2

A Meridionally Averaged Model of Eastern Boundary Upwelling Systems

This section contains the manuscript, Moscoso et al. (2021) without any changes.

2.1 Abstract

Eastern Boundary Upwelling Systems (EBUSs) are physically and biologically active regions of the ocean with substantial impacts on ocean biogeochemistry, ecology, and global fish catch. Previous studies have used models of varying complexity to study EBUS dynamics, ranging from minimal two-dimensional (2D) models to comprehensive regional and global models. An advantage of 2D models is that they are more computationally efficient and easier to interpret than comprehensive regional models, but their key drawback is the lack of explicit representations of important three-dimensional processes that control biology in upwelling systems. These processes include eddy quenching of nutrients and meridional transport of nutrients and heat. The authors present a Meridionally Averaged Model of Eastern Boundary Upwelling Systems (MAMEBUS) that aims at combining the benefits of 2D and 3D approaches to modeling EBUSs by parameterizing the key 3D processes in a 2D framework. MAMEBUS couples the primitive equations for the physical state of the ocean with a nutrient-phytoplankton-zooplankton-detritus model of the ecosystem, solved in terrain following coordinates. This article defines the equations that describe the tracer, momentum, and biological evolution, along with physical parameterizations of eddy advec-

tion, isopycal mixing, and boundary layer mixing. It describes the details of the numerical schemes and their implementation in the model code, and provides a reference solution validated against observations from the California Current. The goal of MAMEBUS is to facilitate future studies to efficiently explore the wide space of physical and biogeochemical parameters that control the zonal variations in EBUSs.

2.2 Introduction

Eastern Boundary Upwelling Systems (EBUSs) are among of the most biologically productive regions in the ocean, supporting diverse ecosystems, and contributing to a significant portion of the global fish catch (Bakun and Parrish, 1982). The characteristic wind-driven upwelling dominant in EBUSs is forced by an equatorward meridional wind stress that decreases toward the shore, driving a zonal Ekman transport offshore. The resulting Ekman pumping brings cold, nutrient-rich water to the surface, fueling primary productivity (Jacox and Edwards, 2012; Chavez and Messié, 2009; Rykaczewski and Dunne, 2010).

The upwelling-favorable winds also drive baroclinic, equatorward geostrophic current, which sheds mesoscale eddies (Colas et al., 2013). Together with offshore Ekman transport, mesoscale eddies redistribute nutrients zonally and subduct nutrients and other tracers into the ocean subsurface (Capet et al., 2008; Gruber et al., 2011; Renault et al., 2016). The resulting cross-shore gradient of nutrients at the surface supports a zonal variation in the abundance of phytoplankton, with high biomass and chlorophyll nearshore, and low offshore (Chavez and Messié, 2009). The size structure of phytoplankton is similarly affected, with larger cells with higher nutrient demand onshore, and smaller cells offshore (Cabre et al., 2013).

While these qualitative patterns of productivity are common to upwelling systems, previous studies have shown that productivity varies substantially between EBUSs, but the causes of these inter-EBUS variations are not well understood. Possible physical drivers of

these inter-EBUS variations include the shape and strength of the wind stress curl, which set the upwelling strength and source depth (Bakun and Nelson, 1991; Jacox and Edwards, 2012). This in turn controls the energy transferred to the baroclinic eddy field, modulating surface nutrient availability via the "eddy quenching" mechanism (Gruber et al., 2011; Renault et al., 2016). Additionally, inter-EBUS variations may have biogeochemical origins, for example due differing subsurface oxygen inventories (Chavez and Messié, 2009).

Our understanding of these drivers is hindered in part by the observational limitations, and in part by the computational expense of regional models that can resolve the processes mentioned above. A range of models of varying complexity have been used to study EBUSs, from minimal two-dimensional (2D) models (Jacox and Edwards, 2012; Jacox et al., 2014) to comprehensive regional models (Shchepetkin and McWilliams, 2005; Chenillat et al., 2018). While 2D models require fewer computational resources than comprehensive regional model studies, and thus allow a more comprehensive exploration of the relevant parameter space, they lack the explicit representation of important physical processes that affect biology in upwelling systems (i.e. eddy-quenching and meridional transport of nutrients).

Here, we aim to close the current gap in understanding by developing an idealized, quasi-2D model of the physics and biogeochemistry of EBUSs. The model includes parameterizations of the key three-dimensional processes, while retaining the computational efficiency of a 2D model. The model is cast in a residual-mean framework (Plumb and Ferrari, 2005a) in terrain following coordinates (Song and Haidvogel, 1994), and is referred to as the Meridionally Averaged Model of Eastern Boundary Upwelling Systems (MAMEBUS). A schematic of all the important processes in MAMEBUS is shown in Figure 2.1.

The rest of the paper is organized as follows. In Section 2, we describe the equations and physical parameterizations implemented in MAMEBUS, including general formulation of tracer advection and diffusion, the time-dependent turbulent thermal wind approximation of the momentum equations (T3W), eddy and boundary layer parameterizations, and our ecosystem formulation. In Section 3, we detail the algorithms and discretizations, including

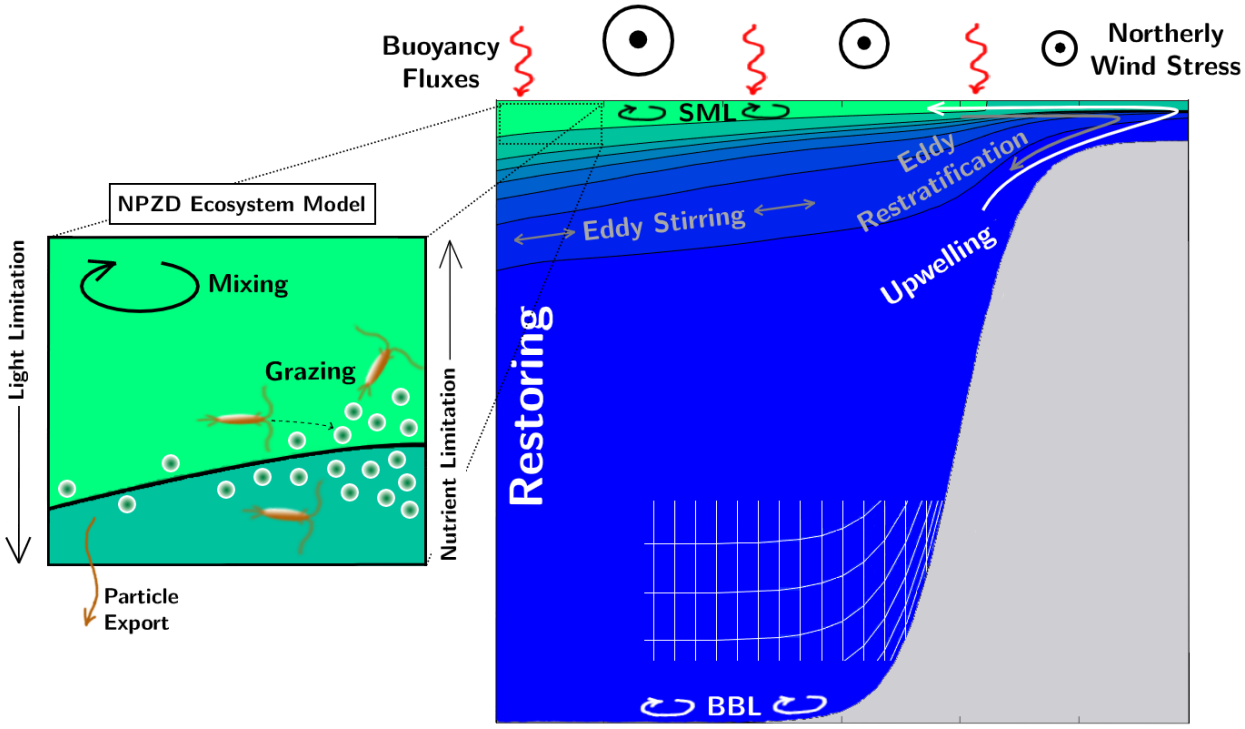

Figure 2.1: A schematic of the essential components of the Meridionally Averaged Model of Eastern Bounday Upwelling Systems (MAMEBUS). This schematic highlights some components that the user is able to control including the offshore restoring conditions, the eddy mixing along isopycnals, the wind forcing, the surface mixed layer and bottom boundary layer parameterizations and grid spacing.

mesh specification, vertical coordinate transformation, and time integration. In Section 4, we describe the implementation of MAMEBUS including the various options available to the user, parameter choices, initialization, and output. In Section 5, we describe reference solutions for MAMEBUS, discussing model sensitivities to changes in bathymetry, wind forcing, and surface heat fluxes. Finally, in Section 6 we discuss further model development and future work.

2.3 MAMEBUS Framework

MAMEBUS is comprised of a series of components that are necessary to capture physical-biogeochemical dynamics in EBUSs: (1) explicit momentum conservation in form of geostrophic, hydrostatic, and Ekman balances implemented as part of the T3W formulation; (2) eddies and their effect on material transport; (3) surface and bottom boundary layers; (4) nutrient and plankton cycles in form of a size-structured "NPZD"-type model (Banas, 2011).

With the exception of the velocity field, all tracers in MAMEBUS evolve according to the following conservation equation:

$$\frac{\partial \bar{c}}{\partial t} = \left.\frac{\partial \bar{c}}{\partial t}\right|_{\text{phys}} + \left.\frac{\partial \bar{c}}{\partial t}\right|_{\text{bio}} + \left.\frac{\partial \bar{c}}{\partial t}\right|_{\text{nct}}, \tag{2.1}$$

where the bar indicates a meridional average. The key physical tracer that follows Equation (2.1) is temperature, θ, which serves as the thermodynamic variable in our model. We choose temperature as our thermodynamic variable because of its important effects on biogeochemistry (Sarmiento and Gruber, 2006). The biogeochemical tracers that are affected by the biogeochemical evolution term, $\partial_t \bar{c}\big|_{\text{bio}}$, are a limiting nutrient N (here expressed in nitrogen units, akin to nitrate); a phytoplankton tracer, P; a zooplankton tracer, Z; and a detrital pool, D. The non-conservative terms, $\partial_t \bar{c}\big|_{\text{nct}}$, represent physical sources and sinks of tracers, including surface fluxes, restoring at the offshore boundary, and optional restoring throughout the domain.

2.3.1 Tracer evolution

We first formulate an evolution equation for the meridionally-averaged concentration of an arbitrary tracer c. We assume that c evolves according to a combination of advection by the three-dimensional ocean flow and diffusion by microscale mixing processes,

$$\left.\frac{\partial c}{\partial t}\right|_{\text{phys}} = \underbrace{-\nabla_3 \cdot (\mathbf{u}_3 c)}_{\text{advection}} + \underbrace{\nabla_3 \cdot (\kappa_{\text{dia}} \nabla_3 c)}_{\text{mixing}}, \tag{2.2}$$

Here $\mathbf{u}_3$ is the three-dimensional velocity vector, ∇_3 is the three-dimensional gradient operator, and κ_{dia} the microscale diffusivity. In (2.2) we have assumed that the velocity field is nondivergent, *i.e.* $\nabla_3 \cdot \mathbf{u}_3 = 0$. We further assume that $\mathbf{u}_3$ and c have already been averaged over a short timescale to exclude fluctuations associated with microscale eddies, whose effects are parameterized via the microscale mixing term (*e.g.* Aiki and Richards, 2008). We further simplifiy (2.2) by assuming that horizontal tracer gradients are small compared with vertical gradients, *i.e.* $\partial_z c \gg \partial_x c, \partial_y c$, as is typical for oceanic scales of evolution (*e.g.* Vallis, 2017). This implies that the microscale mixing acts primarily in the vertical, *i.e.*,

$$\left.\frac{\partial c}{\partial t}\right|_{\text{phys}} \approx -\nabla_3 \cdot (\mathbf{u}_3 c) + \frac{\partial}{\partial z}\left(\kappa_{\text{dia}} \frac{\partial c}{\partial z}\right). \tag{2.3}$$

We now reduce the dimensionality of (2.3) by taking a meridional average, which we denote via an overbar,

$$\bar{\bullet} = \frac{1}{L_y}\int_0^{L_y} \bullet \, \mathrm{d}y. \tag{2.4}$$

Here L_y is the meridional length of the region of interest and y is the meridional coordinate. Though we refer to this average as "meridional" throughout the text, for the purpose of comparison with EBUSs in nature this average might be thought of instead as an alongcoast average, or as an average following isobaths, under the assumption that the additional metric terms introduced by such coordinate transformations are negligible. We next perform a Reynolds decomposition of the velocity and tracer fields,

$$\mathbf{u} = \bar{\mathbf{u}} + \mathbf{u}', \tag{2.5a}$$

$$c = \bar{c} + c', \tag{2.5b}$$

where primes $'$ denote perturbations from the meridional average. Taking a meridional average of (2.3) then yields

$$\left.\frac{\partial \bar{c}}{\partial t}\right|_{\text{phys}} = \underbrace{-\nabla \cdot (\bar{\mathbf{u}}\,\bar{c})}_{\text{mean advection}} \underbrace{-\nabla \cdot (\bar{\mathbf{u}'c'})}_{\text{eddy flux}} \underbrace{-\frac{1}{L_y}\left[vc\right]_0^{L_y}}_{\text{meridional advection}} + \underbrace{\frac{\partial}{\partial z}\left(\bar{\kappa_{\text{dia}}}\frac{\partial c}{\partial z}\right)}_{\text{mixing}}. \tag{2.6}$$

Here we have used (2.5a)–(2.5b) and the property that perturbations vanish under the average, *i.e.* $\bar{\mathbf{u}}' = \bar{c}' = 0$. We further define $\nabla \equiv \partial_x \hat{\mathbf{x}} + \partial_z \hat{\mathbf{z}}$ as the zonal/vertical gradient operator, and $\mathbf{u} = u\hat{\mathbf{x}} + w\hat{\mathbf{z}}$ as the zonal/vertical velocity vector. The square bracket indicates the difference between vc at the northern and southern boundaries of the domain of integration, *i.e.*

$$\Big[vc\Big]_0^{L_y} = vc\Big|_{y=L_y} - vc\Big|_{y=0}. \tag{2.7}$$

In its current form, Equation (2.6) cannot be solved prognostically for $\bar{c}$ because it includes correlations between perturbation quantities, *i.e.* the eddy tracer flux $\overline{\mathbf{u}'c'}$. Assuming that these perturbations are associated with mesoscale eddies, we parameterize the eddy tracer flux following Gent and McWilliams (1990) and Redi (1982). Specifically, we decompose the eddy tracer flux into advection of the mean tracer $\bar{c}$ by "eddy-induced velocity" $\mathbf{u}^\star$ and diffusion of $\bar{c}$ along the mean buoyancy surfaces (see Burke et al., 2015),

$$\nabla \cdot (\overline{\mathbf{u}'c'}) = \nabla \cdot (\mathbf{u}^\star \bar{c}) - \nabla \cdot \left(\kappa_{\text{iso}} \nabla_\parallel \bar{c}\right). \tag{2.8}$$

Here $\nabla_\parallel$ denotes the gradient along mean buoyancy surfaces (see §2.3.2. A more detailed derivation of (2.8) is given in Appendix 2.9. We additionally simplify the meridional tracer advection term by assuming that $\partial \overline{v'}/\partial y \approx 0$, *i.e.* that the meridional tracer flux convergence is dominated by meridional tracer gradients, and that correlations between κ_{dia} and c are negligible, *i.e.* that the meridionally averaged vertical diffusive tracer flux serves to diffuse $\bar{c}$ downgradient. With these simplifications, the full equation for the physical evolution of tracers is given by,

$$\left.\frac{\partial \bar{c}}{\partial t}\right|_{\text{phys}} = \underbrace{-\nabla \cdot (\bar{\mathbf{u}}\bar{c})}_{\text{mean advection}} \underbrace{-\frac{\bar{v}}{L_y}\Big[c\Big]_0^{L_y}}_{\text{meridional advection}} \underbrace{-\nabla \cdot (\mathbf{u}^\star \bar{c})}_{\text{eddy advection}} \underbrace{-\nabla \cdot \left(\kappa_{\text{iso}} \nabla_\parallel \bar{c}\right)}_{\text{eddy stirring}} + \underbrace{\partial_z \left(\kappa_{\text{dia}} \partial_z \bar{c}\right)}_{\text{mixing}}. \tag{2.9}$$

The terms on the right-hand side of (2.9) are discussed further in the following sections: in Section 2.3.2 we discuss the evolution of the mean velocity $\bar{\mathbf{u}}$ via the momentum equations, and in Section 2.3.3 we discuss the sub-gridscale parameterizations, *i.e.* eddy advection, eddy stirring and mixing.

2.3.2 Momentum evolution equations

To evolve a meridionally-averaged tracer $\bar{c}$ using (2.9), the meridionally-averaged velocity field $\bar{\mathbf{u}}_3$ is required. This velocity field is evolved in MAMEBUS by solving a simplified form of the hydrostatic Boussinesq momentum and continuity equations with a linear equation of state (Vallis, 2017),

$$\frac{\partial u}{\partial t} = -\mathbf{u}_3 \cdot \nabla_3 u + fv - \frac{\partial \phi}{\partial x} + \frac{\partial}{\partial z}\left(\kappa_{\text{dia}} \frac{\partial u}{\partial z}\right), \tag{2.10a}$$

$$\frac{\partial v}{\partial t} = -\mathbf{u}_3 \cdot \nabla_3 v - fu - \frac{\partial \phi}{\partial y} + \frac{\partial}{\partial z}\left(\kappa_{\text{dia}} \frac{\partial v}{\partial z}\right), \tag{2.10b}$$

$$\frac{\partial \phi}{\partial z} = b, \tag{2.10c}$$

$$\nabla_3 \cdot \mathbf{u}_3 = 0, \tag{2.10d}$$

$$b = g\alpha\theta. \tag{2.10e}$$

Here, $\phi = p/\rho_0$ is the dynamic pressure, where ρ_0 is an arbitrary reference density, b is the buoyancy, θ is the potential temperature, α is the thermal expansion coefficient (assumed constant), g is the gravitational constant and f is the Coriolis parameter. Note that we have assumed that momentum is mixed by microscale turbulence following the same diffusivity κ_{dia} as tracers (see Section 2.3.1), *i.e.* that the turbulent Prandtl number (*e.g.* Kays, 1994) is exactly equal to one.

As in Section 2.3.1, we now meridionally average (2.10a)–(2.10e) to obtain evolution equations for $\bar{u}$ and $\bar{v}$, and thus implicitly also for $\bar{w}$. This yields the following set of

averaged equations:

$$\frac{\partial \bar{u}}{\partial t} = f\bar{v} - \frac{\partial \bar{\phi}}{\partial x} + \frac{\partial}{\partial z}\left(\kappa_{\text{dia}}\frac{\partial \bar{u}}{\partial z}\right), \tag{2.11a}$$

$$\frac{\partial \bar{v}}{\partial t} = -f\bar{u} - \frac{1}{L_y}\left[\phi\right]_0^{L_y} + \frac{\partial}{\partial z}\left(\kappa_{\text{dia}}\frac{\partial \bar{v}}{\partial z}\right), \tag{2.11b}$$

$$\nabla \cdot \bar{u} = 0, \tag{2.11c}$$

$$\frac{\partial \bar{\phi}}{\partial z} = \mathbf{u}, \tag{2.11d}$$

$$\bar{b} = g\alpha\bar{\theta}. \tag{2.11e}$$

Here, we have made the frictional-geostrophic approximation (*e.g.* Edwards et al., 1998), assuming that the Rossby number of the flow is small (*e.g.* Vallis, 2017) and thus that momentum advection (second terms from the left in (2.10a)–(2.10b)) is negligible compared to other terms in the momentum equation. This assumption may indeed have some limitations in upwelling regions with steep topography and strong stratification. Lentz and Chapman (2004) show that in the cross-shelf momentum flux divergence balances the wind-stress and supports an on shore return flow, which can impact nitrate concentrations on the shelf (Jacox and Edwards, 2011).

On the other hand, we have retained the time-evolution terms (leftmost terms in (2.10a)–(2.10b)) to allow forward evolution of the horizontal velocity fields; if these terms were neglected then these terms would need to be computed diagnostically at each time step. The resulting system is almost identical to the time-dependent turbulent thermal wind (T3W) equations (Dauhajre and McWilliams, 2018), a time-varying extension of the turbulent thermal wind balance (Gula et al., 2014), which was developed to explain the circulation of submesoscale fronts. The meridional pressure gradient in (2.11a) is imposed, rather than solved for prognostically, and is assumed to be set by the larger-scale subtropical gyre circulation encompassing the EBUS, which expicitly differs from the work done in Dauhajre and McWilliams (2018) which focuses on more rapid time varying evolution on smaller scales. Together with the tracer advection equation for potential temperature (*i.e.* (2.9) with $c = \theta$),

(2.11a)–(2.11e) comprise a closed set of equations for the physical evolution of MAMEBUS.

In (2.11c) we have invoked the earlier assumption that $\partial\bar{v}/\partial y \approx 0$ (see Section 2.3.1), such that the averaged velocity field is nondivergent in the x/z plane. This implies that the zonal/vertical velocity field can be related to a mean streamfunction $\bar{\psi}$ via

$$\bar{u} = -\frac{\partial\bar{\psi}}{\partial z}, \qquad \bar{w} = \frac{\partial\bar{\psi}}{\partial x}. \tag{2.12}$$

These relationships allow us to calculate $\bar{\psi}$, and thus $\bar{w}$, from $\bar{u}$, subject to the boundary conditions

$$\bar{\psi} = 0 \quad \text{at} \quad z = 0, z = \bar{\eta}_b(x). \tag{2.13}$$

Here $z = \bar{\eta}_b(x)$ is the mean sea floor elevation.

Additional boundary conditions are required to solve (2.11a)–(2.11e) prognostically. Specifically, we require that the vertical turbulent stress in (2.11a)–(2.11b) matches the wind stress applied at the sea surface and the drag stress at the sea floor, with the latter formulated via a linear drag law. Formally, these boundary conditions are

$$\kappa_{\text{dia}}\frac{\partial\bar{u}}{\partial z} = 0, \qquad \kappa_{\text{dia}}\frac{\partial\bar{v}}{\partial z} = \frac{\bar{\tau}^y}{\rho_0} \qquad \text{at } z = 0, \tag{2.14a}$$

$$\kappa_{\text{dia}}\frac{\partial\bar{u}}{\partial z} = r\bar{u}, \qquad \kappa_{\text{dia}}\frac{\partial\bar{v}}{\partial z} = r\bar{v} \qquad \text{at } z = \bar{\eta}_b(x). \tag{2.14b}$$

Here r is a linear drag coefficient and $\bar{\tau}^y$ is the meridional wind-stress.

2.3.3 Physical parameterizations

In this section we describe the parameterization of unresolved microscale mixing in the tracer evolution Equation (2.9) and the horizontal momentum Equations (2.11a)–(2.11b), and of mesoscale eddy advection and stirring in (2.9). This amounts to parameterizing the diapycnal diffusivity κ_{dia}, the isopycnal diffusivity κ_{iso}, and the eddy velocity $\mathbf{u}^\star$.

2.3.3.1 Diapycnal mixing

We formulate the diapycnal mixing coefficient $\kappa_{\rm dia}$ as a sum of four distinct contributing processes: surface mixed layer turbulence ($\kappa_{\rm sml}$), bottom boundary layer turbulence ($\kappa_{\rm bbl}$), turbulence due to convective overturns within the water column ($\kappa_{\rm conv}$), and background mixing due to internal wave breaking ($\kappa_{\rm bg}$). Formally, we write

$$\kappa_{\rm dia}(x,z,t) = \kappa_{\rm sml}(x,z) + \kappa_{\rm bbl}(x,z) + \kappa_{\rm conv}(x,z,t) + \kappa_{\rm bg}(x,z). \tag{2.15}$$

The terms on the right-hand side of (2.15) are discussed in turn in the following paragraphs.

The diapycnal diffusivity in the surface mixed layer, $\kappa_{\rm sml}$, is prescribed to have the same structure as that used in the K-profile parameterization (KPP) of Large et al. (1994). However, for simplicity, the mixed layer depth $H_{\rm sml}(x)$ and maximum magnitude $\kappa_{\rm sml}(x)$ are prescribed functions, rather than depending on the local surface forcing. The vertical profile of $\kappa_{\rm dia}$ in the surface mixed layer, *i.e.* $-H_{\rm sml} < z < 0$, is given by

$$\kappa_{\rm sml}(x,z) = \kappa^0_{\rm sml} G_{\rm KPP}(\sigma_{\rm sml}), \tag{2.16}$$

where the dimensionless surface mixed layer vertical coordinate $\sigma_{\rm sml} = -z/H_{\rm sml}$ is defined such that $0 \le \sigma_{\rm sml} \le 1$ within the mixed layer. The structure function $G_{\rm KPP}(\sigma_{\rm sml})$ is given by,

$$G_{\rm KPP}(\sigma) = \begin{cases} \dfrac{27}{4}\sigma_{\rm sml}(1-\sigma_{\rm sml})^2, & 0 \le \sigma_{\rm sml} \le 1, \\ 0, & \sigma_{\rm sml} \ge 1, \end{cases} \tag{2.17}$$

following Large et al. (1994) and Troen and Mahrt (1986). The scaling factor $27/4$ ensures that $G_{\rm KPP}(\sigma_{\rm sml})$ has a maximum of 1 for $0 < \sigma_{\rm sml} < 1$.

The diapycnal diffusivity in the bottom boundary layer, $\kappa_{\rm bbl}$, is prescibed in the same way as $\kappa_{\rm sml}$, but over the depth range $\bar{\eta}_b < z < \bar{\eta}_b + H_{\rm bbl}(x)$. Thus, analogous to (2.16), we prescribe

$$\kappa_{\rm bbl}(x,z) = \kappa^0_{\rm bbl} G_{\rm KPP}(\sigma_{\rm bbl}), \tag{2.18}$$

where the dimensionless bottom boundary layer vertical coordinate is defined as $\sigma_{\text{bbl}} = (z - \bar{\eta}_b)/H_{\text{bbl}}$.

At any point in space and time at which the water column is statically unstable, *i.e.* when $N^2 < 0$, we increase the value of κ_{dia} is increased locally to parameterize the effect of density-driven convection. That is, we prescribe κ_{conv} following

$$\kappa_{\text{conv}} = \begin{cases} \kappa^0_{\text{conv}}, & N^2 < 0, \\ 0, & N^2 \geq 0. \end{cases} \tag{2.19}$$

Finally, the background diapycnal mixing, $\kappa_{\text{bg}}(x, z)$, is simply prescribed as a constant background diffusivity. There are other that can be used (e.g. St. Laurent et al. (2002)), but we opt for simplicity in the first version of this model.

2.3.3.2 Eddy advection and isopycnal mixing

We now discuss the formulation of the eddy advection and isopycnal mixing terms in (2.9). As discussed in Section 2.3.1, we follow the assumptions and formalism of the Gent and McWilliams (1990) and Redi (1982) parameterizations, which are commonly used in ocean models that do not explicitly resolve mesoscale eddies (*e.g.* Gent, 2011). These parameterizations assume that eddy-induced fluxes of buoyancy and tracer diffusion are directed along isopycnal slopes, and so must be augmented in the ocean's surface mixed layer (SML) and bottom boundary layer (BBL). Here the isopycnal slopes become very steep and isopycnals incrop at the sea surface and floor (Tréguier et al., 1997). MAMEBUS therefore uses a modified form of the Ferrari et al. (2008) boundary layer parameterization, in which eddy buoyancy and tracer fluxes are rotated through the SML and BBL in order to enforce vanishing eddy-induced mass and tracer fluxes through the boundaries. Here we summarize salient properties of this scheme, and in Appendix 2.11 we highlight differences between our scheme and that of Ferrari et al. (2008).

The eddy-induced velocity $\mathbf{u}^\star = (u^\star, w^\star)$, introduced in (2.8), is nondivergent by con-

struction (see Appendix 2.9) and so we write it as

$$u^\star = -\frac{\partial \psi^\star}{\partial z}, \qquad w^\star = \frac{\partial \psi^\star}{\partial x}, \tag{2.20}$$

where $\psi^\star$ is the "eddy streamfunction". This advecting streamfunction is assumed to be the same for all tracers, which is accurate in the limit of small-amplitude fluctuations of the velocity and tracer fields (Plumb, 1979), and takes the form

$$\psi^\star = \kappa_{\rm gm} S_{\rm gm}. \tag{2.21}$$

Here $\kappa_{\rm gm}$ is the Gent–McWilliams diffusivity and the $S_{\rm gm}$ is the is the Gent–McWilliams slope. The latter is conventionally set equal to the mean isopycnal slope (Gent and McWilliams, 1990),

$$S_{\rm int} = -\partial_x \bar{b} / \partial_z \bar{b}. \tag{2.22}$$

However we allow $S_{\rm gm}$ to diverge from $S_{\rm int}$ in the SML and BBL, in part to ensure that the no-flux surface and bottom boundary conditions are satisfied (Ferrari et al., 2008)

$$\psi^\star = 0 \qquad \text{at} \qquad z = 0, \ z = \bar{\eta}_b(x). \tag{2.23}$$

Specifically, we prescribe

$$S_{\rm gm} = \begin{cases} S_{\rm sml}, & -H_{\rm sml}(x) < z < 0, \\ S_{\rm int}, & \bar{\eta}_b(x) + H_{\rm bbl}(x) < z < -H_{\rm sml}(x), \\ S_{\rm bbl}, & \bar{\eta}_b(x) < z < \bar{\eta}_b(x) + H_{\rm bbl}(x), \end{cases} \tag{2.24}$$

The formulation of the modified slopes $S_{\rm sml}$ and $S_{\rm bbl}$ are discussed below in Sections 2.3.3.2 and 2.3.3.2.

The isopycnal mixing operator serves to mix tracers down their mean gradients, in a direction that is parallel to mean isopycnal surfaces in the ocean interior, following Redi (1982). This may be written component-wise as

$$\nabla \cdot \left(\kappa_{\rm iso} \nabla_\parallel \bar{c} \right) = \frac{\partial}{\partial x} \left(\kappa_{\rm iso} \frac{\partial \bar{c}}{\partial x} + \kappa_{\rm iso} S_{\rm iso} \frac{\partial \bar{c}}{\partial z} \right) + \frac{\partial}{\partial z} \left(\kappa_{\rm iso} S_{\rm iso} \frac{\partial \bar{c}}{\partial x} + \kappa_{\rm iso} S_{\rm iso}^2 \frac{\partial \bar{c}}{\partial z} \right), \tag{2.25}$$

where $S_{\rm iso}$ denotes the slope of the surface along which the tracer is to be mixed and is assumed to be small ($S_{\rm iso} \ll 1$). Similar to $S_{\rm gm}$, this slope is conventionally set equal to the mean isopycnal slope $S_{\rm int}$, but we apply modifications to the formulation of $S_{\rm iso}$ in the SML and BBL to ensure that there is zero eddy-induced tracer flux through the domain boundaries, *i.e.*

$$\kappa_{\rm iso} \nabla_\parallel \bar{c} \cdot \hat{\mathbf{n}} = 0 \qquad \text{at} \qquad z = 0,\ z = \bar{\eta}_b(x), \tag{2.26}$$

where $\hat{\mathbf{n}}$ is a unit vector oriented perpendicular to the sea surface or sea floor. Specifically, we prescribe

$$S_{\rm iso} = \begin{cases} S_{\rm sml}, & -H_{\rm sml}(x) < z < 0, \\ S_{\rm int}, & \bar{\eta}_b(x) + H_{\rm bbl}(x) < z < -H_{\rm sml}, \\ \widetilde{S}_{\rm bbl}, & \bar{\eta}_b(x) < z < \bar{\eta}_b(x) + H_{\rm bbl}(x). \end{cases} \tag{2.27}$$

Thus $S_{\rm gm}$ and $S_{\rm iso}$ are identical everywhere above the BBL. The need for a distinction within the BBL is explained below in Sections 2.3.3.2 and 2.3.3.2.

Surface Mixed Layer We now discuss the formulation of $S_{\rm sml}$, the effective isopycnal slope in the surface mixed layer. Following Ferrari et al. (2008), we construct $S_{\rm sml}$ in a way that avoids singularities due to the vanishingly small vertical buoyancy gradients, and thus near-infinite isopycnal slopes, that occur in the mixed layer. This is achieved by using the vertical buoyancy gradient at the base of the mixed layer to define the effective slope as

$$S_{\rm sml} = -G_{\rm sml}(\sigma_{\rm sml}) \frac{\partial_x \bar{b}}{\partial_z \bar{b}|_{z=-H_{\rm sml}}}, \tag{2.28}$$

where $\sigma_{\rm sml} = -z/H_{\rm sml}$ is a dimensionless vertical coordinate for the SML, as in Section 2.3.3.1. The corresponding eddy streamfunction (2.21) is identical to that of Ferrari et al. (2008),

$$\psi^\star = -\kappa_{\rm gm} G_{\rm sml}(\sigma_{\rm sml}) \frac{\partial_x \bar{b}}{\partial_z \bar{b}|_{z=-H_{\rm sml}}}, \qquad z \geq -H_{\rm sml}. \tag{2.29}$$

The structure function $G_{\rm sml}(z)$ is required to enforce continuity of the vertical tracer fluxes and flux divergences at the surface and at the base of the mixed layer. For example,

(2.23) requires that $G_{\rm sml}$ vanish at the surface:

$$G_{\rm sml}(0) = 0. \tag{2.30}$$

We further require that the eddy streamfunction and eddy residual tracer fluxes be continuous at the base of the SML, *i.e.* that $S_{\rm sml} = S_{\rm int}$, which requires that

$$G_{\rm sml}(1) = 1. \tag{2.31}$$

Finally, we require continuity of the divergence of the eddy tracer flux in order to avoid producing singularities at the SML base. The zonal and vertical components of the eddy tracer flux are

$$\overline{u'c'} = \kappa_{\rm gm} S_{\rm gm} \frac{\partial \bar{c}}{\partial z} - \kappa_{\rm iso} \left(\frac{\partial \bar{c}}{\partial x} + S_{\rm iso} \frac{\partial \bar{c}}{\partial z} \right), \tag{2.32a}$$

$$\overline{w'c'} = -\kappa_{\rm gm} S_{\rm gm} \frac{\partial \bar{c}}{\partial x} - \kappa_{\rm iso} S_{\rm iso} \left(\frac{\partial \bar{c}}{\partial x} + S_{\rm iso} \frac{\partial \bar{c}}{\partial z} \right). \tag{2.32b}$$

It may be shown that continuity of $\nabla \cdot \overline{\mathbf{u}'c'}$ across $z = -H_{\rm sml}$ is guaranteed if

$$\left. \frac{\partial S_{\rm sml}}{\partial z} \right|_{z=-H_{\rm sml}^+} = \left. \frac{\partial S_{\rm int}}{\partial z} \right|_{z=-H_{\rm sml}^-} \implies G'_{\rm sml}(1) = \frac{H_{\rm sml}}{\lambda_{\rm sml}} \tag{2.33}$$

where $\lambda_{\rm sml} = \partial_{zz}\bar{b} / \partial_z \bar{b}|_{z=-H_{\rm sml}}$ is a vertical lengthscale for eddy motions at the base of the mixed layer.

The simplest form for $G_{\rm sml}(z)$ that satisfies conditions (2.30), (2.31) and (2.33) is a quadratic function of depth,

$$G_{\rm sml}(\sigma_{\rm sml}) = -\left(1 - \frac{H_{\rm sml}}{\lambda_{\rm sml}}\right) \sigma_{\rm sml}^2 + \left(2 - \frac{H_{\rm sml}}{\lambda_{\rm sml}}\right) \sigma_{\rm sml}. \tag{2.34}$$

Equation (2.34) is currently implemented in MAMEBUS. A more sophisticated form of $G_{\rm sml}$ that arguably has stronger physical motivation is given by Ferrari et al. (2008). They split the SML into a true mixed layer, in which $G_{\rm sml}$ varies linearly (and so the eddy velocity is approximately uniform), overlying a transition layer, in which $G_{\rm sml}(\sigma_{\rm sml})$ varies quadratically.

Bottom boundary layer The scheme described above for the SML relies on the fact that the ocean surface is approximately flat, which allows the same effective slopes $S_{\rm sml}$ to be used for $S_{\rm gm}$ and $S_{\rm iso}$. The sloping sea floor requires separate BBL slopes, $S_{\rm bbl}$ and $\widetilde{S}_{\rm bbl}$, and structure functions, $G_{\rm bbl}$ and $\widetilde{G}_{\rm bbl}$ to satisfy the required conditions of no volume nor tracer flux through the boundary, *i.e.* (2.23) and (2.26).

Analogous to the SML, we define the effective slope $S_{\rm bbl}$ as

$$S_{\rm bbl} = -G_{\rm bbl}(\sigma_{\rm bbl}) \frac{\partial_x \bar{b}}{\partial_z \bar{b}|_{z=\eta_b+H_{\rm bbl}}}, \tag{2.35}$$

where $\sigma_{\rm bbl} = (z-\eta_b(x))/H_{\rm bbl}(x)$ is the BBL vertical coordinate, as in Section 2.3.3.1. The eddy streamfunction in the BBL is therefore

$$\psi^\star = -\kappa_{\rm gm} G_{\rm bbl}(\sigma_{\rm bbl}) \frac{\partial_x \bar{b}}{\partial_z \bar{b}|_{z=\eta_b+H_{\rm bbl}}}, \qquad z \le \eta_b + H_{\rm bbl}. \tag{2.36}$$

To satisfy the condition of zero volume flux through the sea floor, (2.23), the effective slope must vanish at $z=\eta_b(x)$, which requires

$$G_{\rm bbl}(0) = 0. \tag{2.37}$$

To ensure continuity of the eddy streamfunction at the top of the BBL, we require that $S_{\rm bbl}$ approach $S_{\rm int}$, *i.e.*

$$G_{\rm bbl}(1) = 1. \tag{2.38}$$

Finally, to ensure continuity of the eddy bolus velocity, we require that the gradient of $S_{\rm gm}$ be continuous at $z=\eta_b+H_{\rm bbl}$. This imposes a constraint analogous to (2.33) on $G_{\rm bbl}$,

$$G'_{\rm bbl}(1) = -\frac{H_{\rm bbl}}{\lambda_{\rm bbl}}, \tag{2.39}$$

where $\lambda_{\rm bbl} = \bar{b}_{zz}/\bar{b}_z\big|_{z=\bar{\eta}_b+H_{\rm bbl}}$ is a vertical lengthscale for eddies at the top of the BBL. To satisfy (2.37)–(2.39), we select a quadratic form for the structure function $G_{\rm bbl}(\sigma_{\rm bbl})$,

$$G_{\rm bbl}(\sigma_{\rm bbl}) = -\left(1+\frac{H_{\rm bbl}}{\lambda_{\rm bbl}}\right)\sigma_{\rm bbl}^2 + \left(2+\frac{H_{\rm bbl}}{\lambda_{\rm bbl}}\right)\sigma_{\rm bbl}. \tag{2.40}$$

However, the effective slope S_{bbl} can no longer be used to define S_{iso} in the BBL: (2.26) requires that the effective slope be aligned with the bottom slope at the sea floor, $S_b = \partial_x \bar{\eta}_b$ at $z = \bar{\eta}_b$. We must therefore employ a modified effective slope $\widetilde{S}_{\text{bbl}}$ in the isopycnal mixing operator, as expressed in Equation (2.27). We define $\widetilde{S}_{\text{bbl}}$ as

$$\widetilde{S}_{\text{bbl}} = S_{\text{bbl}} + \left(1 - \widetilde{G}_{\text{bbl}}(z)\right) S_b, \tag{2.41}$$

where $\widetilde{G}_{\text{bbl}}(\sigma_{\text{bbl}})$ is a modified structure function that also vanishes at the ocean bed,

$$\widetilde{G}_{\text{bbl}}(0) = 0. \tag{2.42}$$

Continuity of the eddy tracer fluxes at the top of the BBL requires that

$$\widetilde{G}_{\text{bbl}}(1) = 1. \tag{2.43}$$

Finally, continuity of the eddy flux divergence is enforced by

$$\left.\frac{\partial \widetilde{G}_{\text{bbl}}}{\partial z}\right|_{z=\bar{\eta}_b + H_{\text{bbl}}} = 0. \tag{2.44}$$

To satisfy (2.42)–(2.44), we select a quadratic form for the structure function $\widetilde{G}_{\text{bbl}}(\sigma_{\text{bbl}})$,

$$\widetilde{G}_{\text{bbl}}(\sigma_{\text{bbl}}) = \sigma_{\text{bbl}}(2 - \sigma_{\text{bbl}}). \tag{2.45}$$

2.3.4 Biogeochemical model formulation

The current biogeochemical model implemented in MAMEBUS is an NPZD (nutrient, phytoplankton, zooplankton, and detritus) model. This NPZD model is modeled after the size-structured AstroCAT (Banas, 2011) and Darwin models (Ward et al., 2012). For the purpose of this paper, we reduced the size structured ecosystem model to a single phytoplankton and zooplankton size classes, while preserving the option to run multiple size classes in future versions of the model. We also includes a detritus variable, which allows for sinking and export of organic matter away from the euphotic zone, and redistribution of nutrients in the water column.

The biogeochemical equations in MAMEBUS are formulated similarly to previous NPZD models, but cast in terms of the meridionally-averaged nutrient, phytoplankton, zooplankton and detrirus concentrations. We neglect additional terms that would be introduced by first formulating the equations and then taking the meridional average, *e.g.* covariances of the type $\bar{P'Z'}$. This assumption is partially predicated on the idea that zonal gradients in biogeochemical tracers (e.g. nutrients and chlorophyll) are much stronger than meridional gradients, as supported by observations and models (Fiechter et al., 2018). For example, Venegas et al. (2008) show that average chlorophyll concentrations during the upwelling season vary approximately two-fold in the Northern California Current System, whereas observations from CalCOFI (Figure 2.7) show variations by an order of magnitude between nearshore and offshore stations. Alongshore gradients in chlorophyll are observed along the coast, where they are driven by wind and topographic variations; however they are generally much smaller than the gradient between the coast and the offshore region (Fiechter et al., 2018). We recognize that this is a simplification of the true variability in EBUSs, but we consider it appropriate on average over the entire upwelling system, in particular within the idealized MAMEBUS framework, and plan to reassess it in future work.

We drop the bar notation indicating a meridional average for this section, with the understanding that all variables denote meridionally-averaged quantities. In the following, we include size dependent uptake and grazing, along with variable sinking speeds for detritus, to retain essential size-dependent biogeochemical interactions and export fluxes. This will facilitate a future introduction of multiple size classes in the model. All variables and coefficients are given in Table 3.1. We note that all of the parameter values and equations described below measure time in days, whereas more generally MAMEBUS measures time in seconds; appropriate conversions are made in the model code to ensure dimensional consistency. The

main conservation equations for biogeochemical tracers are:

$$\left.\frac{\partial N}{\partial t}\right|_{\text{bio}} = -\mathcal{U}(N, I, T, P) + \mathcal{R}(D), \tag{2.46a}$$

$$\left.\frac{\partial P}{\partial t}\right|_{\text{bio}} = \mathcal{U}(N, I, T, P) - \mathcal{G}(P, Z) - \mathcal{M}(P), \tag{2.46b}$$

$$\left.\frac{\partial Z}{\partial t}\right|_{\text{bio}} = \lambda\mathcal{G}(P, Z) - \mathcal{M}(Z), \tag{2.46c}$$

$$\left.\frac{\partial D}{\partial t}\right|_{\text{bio}} = \mathcal{M}(P) + \mathcal{M}(Z) + (1-\lambda)\mathcal{G}(P, Z) - \frac{\partial}{\partial z} w_{\text{sink}} D - \mathcal{R}(D), \tag{2.46d}$$

where T (^{o}C) is the model temperature, I (W/m^2) is the local irradiance profile, N (mmol N/m^3) is nitrate concentration, P (mmol N/m^3) is phytoplankton concentration, Z (mmol N/m^3) is zooplankton concentration, and D (mmol N/m^3) is the detritus concentration. The terms on the right-hand sides of (2.46a)–(2.46d) are explained in the following subsections.

2.3.4.1 Nutrient uptake

Common controls on phytoplankton population are bottom-up limitation (i.e. nutrient control), and top-down grazing by zooplankton (Sarmiento and Gruber, 2006). We formulate bottom-up controls using typical choices for light- and temperature-dependent terms, and Michaelis-Menten uptake (Sarmiento and Gruber, 2006). The functional form of uptake is given by:

$$\mathcal{U}(N, I, T, P) = \varphi(I)\varphi(T)U^{\max}\frac{N}{N + k_N}P, \tag{2.47}$$

where $\varphi(I)$ and $\varphi(T)$ are light and temperature limiting functions, respectively. The light attenuation is modeled by integrating the Beer-Lambert Law, following Moore et al. (2001),

$$\frac{\partial I(z)}{\partial z} = -k_{\text{par}} I(z), \quad \text{where} \quad I_0 = I(z=0) = Q_{sw} I_p, \tag{2.48a}$$

$$k_{\text{par}} = k_w + P \cdot k_c, \tag{2.48b}$$

Table 2.1: Parameters and values used in the ecosystem model implemented in MAMEBUS. Coefficients without explicit references are chosen by the user.

ccll

Parameter	Value	Description and Units	Reference
I_p	0.45	Fraction of light available for photosynthesis (PAR)	Moore et al. (2001)
k_c	0.01	Absorption coefficient for photosynthesis (mmol N m)$^{-1}$	Moore et al. (2001)
k_p	3	Half saturation coefficient for phytoplankton grazing mmol N m^{-3}	Banas (2011)
k_w	0.04	Absorption coefficent for water (m^{-1})	Moore et al. (2001)
$\Delta\ell$	0.25	Width of grazing profile ($\log_{10}\mu$m)	Banas (2011)
ℓ_p	5	Length (ESD) of phytoplankton cell (μm)	
ℓ_z	10	Length (ESD) of zooplankton cell (μm)	
λ	0.33	Biomass assimilation efficiency	
Q_{sw}	340	Surface irradiance (Wm^{-2})	Moore et al. (2001)
r_T	0.05	Temperature dependence of nutrient uptake (^{o}C^{-1})	Ward et al. (2012)
r_{remin}	0.04	Remineralization rate (d^{-1}	Ward et al. (2012)
T_0	10	Reference temperature (^{o}C)	
μ_p	0.02	Phytoplankton mortality as a fraction of growth rate	Banas (2011)
w_{sink}	10	Sinking speed of detritus (md^{-1})	

Table 2.2: Allometric parameters and values used in the ecosystem model implemented in MAMEBUS.

cccll

Parameter	Value	Units	Description	Reference
a_u	2.6	1/d	Uptake rate	Tang (1995)
b_u	-0.45		Scaling parameter for uptake	Tang (1995)
a_g	26	1/d	Grazing rate	Hansen et al. (1994)
b_g	-0.4		Scaling parameter for grazing	Hansen et al. (1994)
a_o	0.65	μm	Optimal predator-prey length scale	Hansen et al. (1994)
b_o	0.56		Scaling parameter for optimal predator-prey interaction	Hansen et al. (1994)

and the light-dependent uptake function is modeled following Sarmiento and Gruber (2006),

$$\varphi(I) = \frac{I(z)}{\sqrt{I_0^2 + I(z)^2}}. \tag{2.49}$$

The temperature component of the uptake function is,

$$\varphi\left(T\right) = e^{-r_T(T-T_0)}. \tag{2.50}$$

The maximum uptake rate is an allometric relationship defined as,

$$U^{\max} = a_u \left(\frac{\ell_p}{\ell_0}\right)^{b_u}, \tag{2.51}$$

where ℓ_p is the user-determined phytoplankton size expressed as equivalent spherical diameter (ESD), and $\ell_0 = 1\mu$m is a normalized length scale, with all allometrically defined variable listed in Table 2.2. While there are other options for the bases of these allometric relationships outlined in this section, (eg. cell volume), we make the decision to use ESD as a measure of cell size. Finally, the half saturation coefficient is $k_N = 0.1$ mmol N/m^3.

2.3.4.2 Grazing

Top-down processes are represented by zooplankton grazing on phytoplankton. Andersen et al. (2016) noted that there is an optimal length scale for active predation and grazing, as a strategic trade-off for optimal biomass assimilation. We make the assumption that the biomass assimilation of phytoplankton by zooplankton also follows Michaelis-Menten dynamics, then the functional form of grazing is given by

$$\mathcal{G}(P, Z) = G^{\max} \frac{\vartheta P}{k_P + \vartheta P} Z, \tag{2.52}$$

where the maximum grazing rate is defined by an allometric relationship defined as,

$$G^{\max} = a_g \left(\frac{\ell_z}{\ell_0} \right)^{b_g}. \tag{2.53}$$

where d^{-1} represents a "per day" quantity. We define a Gaussian distribution about an optimal grazing length-scale following Banas (2011),

$$\vartheta = \exp\left(-\frac{\log_{10}(\ell_p) - \log_{10}(\ell_{\mathrm{opt}})}{\Delta\ell} \right), \tag{2.54}$$

where $\Delta\ell$ sets the width of the optimal grazing profile, and defines a band of grazing about the optimal prey size, ℓ_{opt}. By allowing for a variable band of grazing, we are able to control the assimilation efficiency of phytoplankton by zooplankton through direct preferential grazing. Accordingly, we model the optimal prey size based on a preferential grazing profile centered about an optimal predator-prey length scale,

$$\ell_{\mathrm{opt}} = a_o \left(\frac{\ell_z}{\ell_0} \right)^{b_o}. \tag{2.55}$$

2.3.4.3 Mortality

Mortality closure terms often set important internal dynamics in ecosystem models (Poulin and Franks, 2010b). While linear mortality terms are generally used for phytoplankton, zooplankton mortality is often modeled via a quadratic term to avoid unrealistic oscillations

and stabilize the solution (Poulin and Franks, 2010b). The quadratic mortality term may be rationalized as a representation of mixotrophic grazing, zooplankton self-grazing and higher order grazing in NPZD models (Raick et al., 2006). Therefore, we model phytoplankton mortality as,

$$\mathcal{M}(P) = \mu_p U^{\max} P, \tag{2.56}$$

and zooplankton mortality as,

$$\mathcal{M}(Z) = \mu_z Z^2. \tag{2.57}$$

2.3.4.4 Remineralization and particle sinking

Sinking particles are an essential component of the vertical transport of nutrients from the surface to the deep ocean (Sarmiento and Gruber, 2006). Once particles sink past the euphotic zone, they are remineralized and returned to the subsurface nutrient pool. In this model, we represent remineralization processes via a linear rate, *i.e.*:

$$\mathcal{R}(D) = r_{\text{remin}} D. \tag{2.58}$$

where r_{remin} is the specific remineralization rate.

Particles sink at a constant average speed in the water column, following Equation (2.46d). At the bottom boundary we impose zero sinking flux, *i.e.* $w_{\text{sink}} = 0$ at $z = \bar{\eta}_b(x)$. Thus any nutrients that sink to the sea floor as detritus must remineralize there. This allows for redistribution of nutrients by mixing within the bottom boundary layer, diffusion into the interior, and transport via upwelling onto the shelf.

2.3.5 Non-conservative terms

In this section we describe the treatment of all non-conservative terms in the tracer evolution equation. MAMEBUS allows arbitrary restoring of all tracers, which may be used, for example, to impose offshore boundary conditions or to impose restoring at the sea surface.

Fixed fluxes of all tracers may also be imposed through the surface. More precisely, we formulate the non-conservative tracer tendency as

$$\left.\frac{\partial \bar{c}}{\partial t}\right|_{\text{nct}} = \left.\frac{\partial \bar{c}}{\partial t}\right|_{\text{restore}} + \left.\frac{\partial \bar{c}}{\partial t}\right|_{\text{flux}}. \tag{2.59}$$

The restoring and surface flux components of this tendency are discussed separately below.

2.3.5.1 Restoring

The restoring of a tracer is represented as an exponential decay to a prescribed, spatially-varying tracer field, $\bar{c}_r(x, z)$, with time scale $t_r(x, z)$. The tracer restoring is then formulated as

$$\left.\frac{\partial \bar{c}}{\partial t}\right|_{\text{restore}} = -\frac{\bar{c} - \bar{c}_r}{t_r}. \tag{2.60}$$

2.3.5.2 Tracer fluxes

Surface fluxes are represented as a tendency in the tracer concentration in the surface grid-boxes. For an arbitrary tracer c, we formulate the surface flux term as follows:

$$\left.\frac{\partial \bar{c}}{\partial t}\right|_{\text{flux}} = \frac{\partial F^c_{\text{flux}}}{\partial z}, \qquad F_{\text{flux}} = \begin{cases} F^c_{\text{flux},0}, & z = 0, \\ 0, & z < 0. \end{cases} \tag{2.61}$$

Here $F^c_{\text{flux},0}$ is the downward flux of c (units of $[c]$m/s) at the surface. For the case of buoyancy, the surface flux is imposed as a surface energy flux, Q_s (W/m^2), with

$$F^b_{\text{flux},0} = \frac{g\alpha Q_s}{\rho_0 C_p}, \tag{2.62}$$

where $C_p = 4000$J/°C kg is the specific heat capacity.

2.4 MAMEBUSv1.0 Algorithm

In this section we discuss the numerical solution of the model equations presented in Section 2.3. This entails a recasting of the equations in terrain-following, or "sigma" coordinates

(*e.g.* Song and Haidvogel, 1994; Shchepetkin and McWilliams, 2003), followed by the spatial discretization of the equations and algorithms for numerical time stepping.

2.4.1 Formulation in terrain-following coordinates

We solve the model equations presented in Section 2.3 in a coordinate system that "stretches" in the vertical to follow the shape of the sea floor. Such a coordinate system avoids "steps" in the sea floor that arise, for example, when using geopotential vertical coordinates, and allows fine vertical resolution of the bottom boundary layer (*e.g.* Song and Haidvogel, 1994; Shchepetkin and McWilliams, 2003). Formally, we make a coordinate transformation $(x, z) \rightarrow (x, \sigma)$, where σ is a dimensionless vertical coordinate and is defined such that $\sigma = 0$ at $z = 0$ and $\sigma = -1$ at $z = \overline{\eta}_b(x)$. This transformation requires a relationship between z and σ via a transformation function

$$z = \zeta(x, \sigma). \tag{2.63}$$

For example, a "pure" sigma coordinate corresponds to the choice

$$\zeta(x, \sigma) = -\sigma \overline{h}_b(x), \tag{2.64}$$

where $\overline{h}_b(x) = -\overline{\eta}_b(x)$ is the merionally-averaged water column thickness. However, this is not necessarily the most practical choice for numerical applications, in which it is useful to focus the vertical resolution over certain depth ranges (especially those close to the top and bottom boundaries of the ocean). MAMEBUS currently implements the UCLA-ROMS (Shchepetkin and McWilliams, 2005) transformation function,

$$\zeta(x, \sigma) = h_b(x) \left[\frac{h_c \sigma + h_b(x) C(\sigma)}{h_c + h_b(x)} \right]. \tag{2.65}$$

Here $C(\sigma)$ is the stretching function, defined as

$$C(\sigma) = \begin{cases} \dfrac{\exp\left(\theta_b \tilde{C}(\sigma)\right) - 1}{1 - \exp(-\theta_b)}, & \theta_b > 0, \\ \tilde{C}(\sigma), & \theta_b \leq 0, \end{cases} \tag{2.66}$$

where

$$\tilde{C}(\sigma) = \begin{cases} \dfrac{1-\cosh(\theta_s\sigma)}{\cosh(\theta_s)-1}, & \theta_s > 0, \\ -\sigma^2, & \theta_s \leq 0. \end{cases} \tag{2.67}$$

Here C and $\tilde{C}$ are the bottom and surface components of the stretching function, respectively. The parameters $\theta_s \in [0, 10]$ and $\theta_b \in [0, 4]$ are surface and bottom stretching parameters; larger values cause the near-surface and near-bottom portions of the domain to occupy larger fraction of σ-space. The parameter h_c defines a surface layer thickness, in which the coordinate system is approximately aligned with geopotentials, provided that $h_b \gg h_c$.

We now write the physical tracer evolution Equation (2.9) in σ-coordinates. For a given function $f = f(x, z(x, \sigma))$, we can write derivatives with respect to x and σ as

$$\left.\frac{\partial f}{\partial x}\right|_\sigma = \left.\frac{\partial f}{\partial x}\right|_z + \left.\frac{\partial \zeta}{\partial x}\frac{\partial f}{\partial z}\right|_x, \tag{2.68a}$$

$$\left.\frac{\partial f}{\partial \sigma}\right|_x = \left.\frac{\partial \zeta}{\partial \sigma}\frac{\partial f}{\partial z}\right|_x. \tag{2.68b}$$

Using these identities, we may write the divergence of an arbitrary vector $\mathbf{F}$, with components $F^{(x)}$ and $F^{(z)}$ in the $\hat{\mathbf{x}}$ and $\hat{\mathbf{z}}$ directions, respectively, as

$$\nabla \cdot \mathbf{F} = \left.\frac{\partial}{\partial x}\right|_z F^{(x)} + \left.\frac{\partial}{\partial z}\right|_x F^{(z)} = \zeta_\sigma^{-1}\left.\frac{\partial}{\partial x}\right|_\sigma \left(\zeta_\sigma F^{(x)}\right) + \zeta_\sigma^{-1}\left.\frac{\partial}{\partial \sigma}\right|_x \left(F^{(z)} - \zeta_x F^{(x)}\right). \tag{2.69}$$

Equation (2.69), combined with the definition of the mean streamfunction (2.12), allows us to write the mean advection term in (2.9) as

$$\nabla \cdot (\overline{\mathbf{u}}\overline{c}) = \nabla \cdot \left(-\overline{c}\left.\frac{\partial \overline{\psi}}{\partial z}\right|_x, \overline{c}\left.\frac{\partial \overline{\psi}}{\partial x}\right|_z\right) = \zeta_\sigma^{-1}\left.\frac{\partial}{\partial x}\right|_\sigma \left(-\overline{c}\left.\frac{\partial \overline{\psi}}{\partial \sigma}\right|_x\right) + \zeta_\sigma^{-1}\left.\frac{\partial}{\partial \sigma}\right|_x \left(\overline{c}\left.\frac{\partial \overline{\psi}}{\partial x}\right|_\sigma\right). \tag{2.70}$$

An analogous expression may be obtained for the eddy advection term, $\nabla \cdot (\mathbf{u}^\star \overline{c})$, in (2.9), using the definition (2.21) of the eddy streamfunction.

Next, we apply (2.69) to the isopycnal mixing operator, defined by (2.25), in Equation

(2.9) to obtain

$$\nabla \cdot \left(\kappa_{\rm iso} \nabla_{\|} \overline{c}\right) = \zeta_\sigma^{-1} \left. \frac{\partial}{\partial x} \right|_\sigma \left[\zeta_\sigma \kappa_{\rm iso} \left(\left. \frac{\partial \overline{c}}{\partial x} \right|_\sigma + (S_{\rm iso} - S_\sigma) \zeta_\sigma^{-1} \left. \frac{\partial \overline{c}}{\partial \sigma} \right|_x \right) \right] + \zeta_\sigma^{-1} \left. \frac{\partial}{\partial \sigma} \right|_x \left[\kappa_{\rm iso} (S_{\rm iso} - S_\sigma) \left(\left. \frac{\partial \overline{c}}{\partial x} \right|_\sigma + (S_{\rm iso} - S_\sigma) \zeta_\sigma^{-1} \left. \frac{\partial \overline{c}}{\partial \sigma} \right|_x \right) \right], \quad (2.71)$$

where $S_\sigma = \zeta_x$ is the slope of surfaces of constant σ in x/z space, *i.e.* the slope of the σ-coordinate grid lines. Thus the isopycnal mixing operator is essentially just modified by subtracting S_σ from $S_{\rm iso}$ to obtain the mixing slope *relative to the slope of the σ-coordinate grid*. Over most of the water column $S_{\rm iso}$ is equal to the isopycnal slope $S_{\rm int}$, given by

$$S_{\rm int} = -\frac{\left. \frac{\partial \overline{b}}{\partial x} \right|_z}{\left. \frac{\partial \overline{b}}{\partial z} \right|_x} = -\frac{\left. \frac{\partial \overline{b}}{\partial x} \right|_\sigma - S_\sigma \left. \frac{\partial \overline{b}}{\partial z} \right|_x}{\left. \frac{\partial \overline{b}}{\partial z} \right|_x} = -\frac{\left. \frac{\partial \overline{b}}{\partial x} \right|_\sigma}{\zeta_\sigma^{-1} \left. \frac{\partial \overline{b}}{\partial \sigma} \right|_x} + S_\sigma. \quad (2.72)$$

Thus, the quantity $S_{\rm int} - S_\sigma$ can actually be computed more directly than the true isopycnal slope, as

$$S_{\rm int} - S_\sigma = -\frac{\left. \frac{\partial \overline{b}}{\partial x} \right|_\sigma}{\zeta_\sigma^{-1} \left. \frac{\partial \overline{b}}{\partial \sigma} \right|_x}. \quad (2.73)$$

Finally, the σ-coordinate transformation of the vertical (quasi-diapycnal) mixing operator is

$$\left. \frac{\partial}{\partial z} \right|_x \left(\kappa_{\rm dia} \left. \frac{\partial \overline{c}}{\partial z} \right|_x \right) = \zeta_\sigma^{-1} \left. \frac{\partial}{\partial \sigma} \right|_x \left(\kappa_{\rm dia} \zeta_\sigma^{-1} \left. \frac{\partial \overline{c}}{\partial \sigma} \right|_x \right). \quad (2.74)$$

To summarize, we write (2.9) in σ coordinates as

$$\left. \frac{\partial \overline{c}}{\partial t} \right|_{\rm phys} = G_{\rm adv} + G_{\rm iso} + G_{\rm dia} + G_{\rm lat}, \quad (2.75)$$

where the tendency terms are

$$G_{\text{adv}} = -\zeta_\sigma^{-1} \left.\frac{\partial}{\partial x}\right|_\sigma \left[\zeta_\sigma \left(-\overline{c}\,\zeta_\sigma^{-1} \left.\frac{\partial \psi^\dagger}{\partial \sigma}\right|_x\right)\right] - \zeta_\sigma^{-1} \left.\frac{\partial}{\partial \sigma}\right|_x \left(\overline{c}\, \left.\frac{\partial \psi^\dagger}{\partial x}\right|_\sigma\right), \tag{2.76a}$$

$$\begin{aligned} G_{\text{iso}} = {} & \zeta_\sigma^{-1} \left.\frac{\partial}{\partial x}\right|_\sigma \left[\zeta_\sigma \kappa_{\text{iso}} \left(\left.\frac{\partial \overline{c}}{\partial x}\right|_\sigma + (S_{\text{iso}} - S_\sigma)\zeta_\sigma^{-1} \left.\frac{\partial \overline{c}}{\partial \sigma}\right|_x\right)\right], \\ & + \zeta_\sigma^{-1} \left.\frac{\partial}{\partial \sigma}\right|_x \left[\kappa_{\text{iso}}(S_{\text{iso}} - S_\sigma) \left(\left.\frac{\partial \overline{c}}{\partial x}\right|_\sigma + (S_{\text{iso}} - S_\sigma)\zeta_\sigma^{-1} \left.\frac{\partial \overline{c}}{\partial \sigma}\right|_x\right)\right], \end{aligned} \tag{2.76b}$$

$$G_{\text{dia}} = \zeta_\sigma^{-1} \left.\frac{\partial}{\partial \sigma}\right|_x \left(\kappa_{\text{dia}} \zeta_\sigma^{-1} \left.\frac{\partial \overline{c}}{\partial \sigma}\right|_x\right) \tag{2.76c}$$

$$G_{\text{lat}} = -\frac{\overline{v}}{L_y} \Big[c\Big]_0^{L_y}. \tag{2.76d}$$

Here we define

$$\psi^\dagger = \overline{\psi} + \psi^\star \tag{2.77}$$

as the total advective or "residual" streamfunction (Plumb and Ferrari, 2005b), and we have added factors of ζ_σ in (2.76a) so that the fluxes can be directly identified with the zonal velocity, $u^\dagger = -\zeta_\sigma^{-1}\partial\psi^\dagger/\partial\sigma|_x$, and the dia-$\sigma$ velocity, $\varpi^\dagger = \partial\psi^\dagger/\partial x|_\sigma$. Note also that every derivative with respect to σ is multiplied by ζ_σ^{-1}, and that their product $\zeta_\sigma^{-1}\partial_\sigma$ is equivalent to a derivative with respect to z. This allows us to simplify the numerical discretization by avoiding explicit references to σ coordinates, and computing these derivatives via finite differencing in z coordinates.

2.4.2 Spatial discretization of the tracer evolution equation

We solve (2.9) using the slope-limited finite-volume scheme of Kurganov and Tadmor (2000) for systems of conservation laws. We divide the domain into a grid of N_x by N_ζ cells, with uniform side lengths Δ_x and Δ_ζ in x/ζ space, as shown in Fig. 2.2. We store the cell-averaged value of $\overline{c}$ at the center of the $(j,k)^{\text{th}}$ grid cell, which we denote as $\overline{c}_{j,k}(t)$. The mean, eddy and residual streamfunctions are most naturally defined at the cell corners, as this allows a

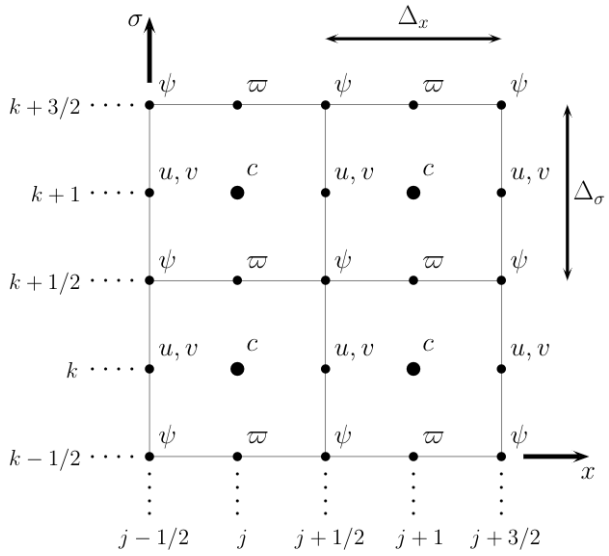

Figure 2.2: Illustration of the numerical grid used to compute solutions to the model equations.

straightforward calculation of the residual velocities at the cell edges,

$$u^\dagger_{j+1/2,k} = -\frac{\psi^\dagger_{j+1/2,k+1/2} - \psi^\dagger_{j+1/2,k-1/2}}{(\Delta_z)_{j+1/2,k}}, \tag{2.78a}$$

$$\varpi^\dagger_{j,k+1/2} = \frac{\psi^\dagger_{j+1/2,k+1/2} - \psi^\dagger_{j-1/2,k+1/2}}{\Delta_x}. \tag{2.78b}$$

Here we use Δ_z as a shorthand for the spatially-varying vertical grid spacing, defined as a centered difference between adjacent grid points. The vertical grid spacing is defined for all cell centers, corners and faces,

$$(\Delta_z)_{j,k} = z_{j,k+1/2} - z_{j,k-1/2}, \tag{2.78c}$$

$$(\Delta_z)_{j+1/2,k} = z_{j+1/2,k+1/2} - z_{j+1/2,k-1/2}, \tag{2.78d}$$

$$(\Delta_z)_{j,k+1/2} = z_{j,k+1} - z_{j,k}, \tag{2.78e}$$

$$(\Delta_z)_{j+1/2,k+1/2} = z_{j+1/2,k+1} - z_{j+1/2,k}, \tag{2.78f}$$

where $z_{j+1/2,k+1/2}$ denotes the physical elevation of each gridpoint. Note again that ϖ is the velocity normal to the upper and lower faces of the grid cell, and so differs slightly from the

true vertical velocity w.

To compute the advective tendency, G_{adv}, the Kurganov and Tadmor (2000) scheme requires a linear interpolation of $\overline{c}$ over each grid cell. The linear slopes in the x and ζ directions around $\overline{c}_{j,k}(t)$ are calculated via slope-limited finite differences between $\overline{c}_{j,k}(t)$ and its adjacent gridpoints,

$$(\partial_x \overline{c})_{j,k} = \text{minmod}\left(\theta\frac{\overline{c}_{j+1,k}-\overline{c}_{j,k}}{\Delta_x}, \frac{\overline{c}_{j+1,k}-\overline{c}_{j-1,k}}{2\Delta_x}, \theta\frac{\overline{c}_{j,k}-\overline{c}_{j-1,k}}{\Delta_x}\right), \tag{2.79}$$

$$(\partial_z \overline{c})_{j,k} = \text{minmod}\left(\theta\frac{\overline{c}_{j,k+1}-\overline{c}_{j,k}}{(\Delta_z)_{j,k+1/2}}, \frac{\overline{c}_{j,k+1}-\overline{c}_{j,k-1}}{z_{j,k+1}-z_{j,k-1}}, \theta\frac{\overline{c}_{j,k}-\overline{c}_{j,k-1}}{(\Delta_z)_{j,k-1/2}}\right), \tag{2.80}$$

with parameter $1 < \sigma < 2$. The minmod function evaluates to zero if its arguments have differing signs, and otherwise evaluates to its argument with smallest modulus. The cell center estimates of the derivatives are then used to construct two different estimates of $\overline{c}$ at each cell faces via

$$\overline{c}^{(-)}_{j+1/2,k} = \overline{c}_{j,k} + \tfrac{1}{2}\Delta_x(\partial_x\overline{c})_{j,k}, \tag{2.81a}$$

$$\overline{c}^{(+)}_{j+1/2,k} = \overline{c}_{j+1,k} - \tfrac{1}{2}\Delta_x(\partial_x\overline{c})_{j+1,k}, \tag{2.81b}$$

$$\overline{c}^{(-)}_{j,k+1/2} = \overline{c}_{j,k} + (z_{j,k+1/2}-z_{j,k})(\partial_z\overline{c})_{j,k}, \tag{2.81c}$$

$$\overline{c}^{(+)}_{j,k+1/2} = \overline{c}_{j,k} - (z_{j,k+1}-z_{j,k+1/2})(\partial_z\overline{c})_{j,k+1/2}. \tag{2.81d}$$

Finally, advective fluxes are determined at the cell faces using an estimate of the maximum propagation speed in the system, which in our case is simply the residual velocity, and thus the fluxes reduce to an upwind approximation

$$F^{(u)}_{j+1/2,k} = \frac{1}{2}(\Delta_z)_{j+1/2,k}\left[u^{\dagger}_{j+1/2,k}\left(\overline{c}^{(+)}_{j+1/2,k}+\overline{c}^{(-)}_{j+1/2,k}\right) - |u^{\dagger}_{j+1/2,k}|\left(\overline{c}^{(+)}_{j+1/2,k}-\overline{c}^{(-)}_{j+1/2,k}\right)\right], \tag{2.82a}$$

$$F^{(\varpi)}_{j,k+1/2} = \frac{1}{2}\left[\varpi^{\dagger}_{j,k+1/2}\left(\overline{c}^{(+)}_{j,k+1/2}+\overline{c}^{(-)}_{j,k+1/2}\right) - |\varpi^{\dagger}_{j,k+1/2}|\left(\overline{c}^{(+)}_{j,k+1/2}-\overline{c}^{(-)}_{j,k+1/2}\right)\right]. \tag{2.82b}$$

For this version of the model, the formulation of the Kurganov and Tadmor (2000) scheme considers only the maximum propagation speed of the momentum, $\mathbf{u}$, and excludes the

internal gravity wave speed which is supported with the momentum calculation in Section 2.3.2. As a result, this would alter the overall advective fluxes, however, we omit this in the current version of the model and note that the full formulation can be implemented here, but we choose to leave this calculation to be updated in a future version of the model. The advective tendency in (x, z) space is then computed via straightforward finite-differencing of these fluxes,

$$(G_{\text{adv}})_{j,k} = -\frac{F^{(u)}_{j+1/2,k} - F^{(u)}_{j-1/2,k}}{\Delta_x (\Delta_z)_{j,k}} - \frac{F^{(\varpi)}_{j,k+1/2} - F^{(\varpi)}_{j,k-1/2}}{(\Delta_z)_{j,k}} - \frac{F^{v}_{j,k}}{L_y}. \tag{2.83}$$

The advective discretization (2.83) requires the residual streamfunction to be known on all grid cell corners, which allows the numerical fluxes to be computed at the cell edges. The mean streamfunction $\overline{\psi}$ is computed from the mean velocity field via (2.12),

$$\overline{\psi}_{j+1/2,k+1/2} = -\sum_{m=0}^{k} \overline{u}_{j+1/2,k} (\Delta_z)_{j+1/2,k}. \tag{2.84}$$

The eddy streamfunction (2.21) depends on the "true" slope (2.72) of the local $\overline{b}$ contours, which we discretize as

$$(S_{\text{int}})_{j+1/2,k+1/2} = -\frac{(\partial_x \overline{b}|_z)_{j+1/2,k+1/2}}{(\partial_z \overline{b}|_x)_{j+1/2,k+1/2}}. \tag{2.85}$$

The calculation of the derivatives with respect to x and z is described in Section 2.4.5. We then construct $\psi^\star$ on cell corners as

$$\psi^\star_{j+1/2,k+1/2} = (\kappa_{\text{gm}})_{j+1/2,k+1/2} (S_{\text{int}})_{j+1/2,k+1/2}. \tag{2.86}$$

The tracer tendency due to isopycnal diffusion, G_{iso}, is discretized following the formulation of Kurganov and Tadmor (2000) for parabolic operators.

$$H^{(x)}_{j+1/2,k} = (\Delta_z)_{j+1/2,k} (\kappa_{\text{iso}})_{j+1/2,k} \left[\frac{\overline{c}_{j+1,k} - \overline{c}_{j,k}}{\Delta_x} + (S_{\text{iso}} - S_\sigma)_{j+1/2,k} \frac{(\partial_z \overline{c})_{j,k} + (\partial_z \overline{c})_{j+1,k}}{2} \right], \tag{2.87a}$$

$$H^{(\sigma)}_{j,k+1/2} = (\kappa_{\text{iso}})_{j,k+1/2} (S_{\text{iso}} - S_\sigma)_{j,k+1/2} \left[\frac{(\partial_x \overline{c})_{j,k} + (\partial_x \overline{c})_{j,k+1}}{2} + (S_{\text{iso}} - S_\sigma)_{j,k+1/2} \frac{\overline{c}_{j,k+1} - \overline{c}_{j,k}}{(\Delta z)_{j,k+1/2}} \right], \tag{2.87b}$$

where $(\partial_z \overline{c})_{j,k}$, $(\partial_z \overline{c})_{j+1,k}$, $(\partial_x \overline{c})_{j,k}$, and $(\partial_x \overline{c})_{j,k+1}$ are computed via (2.81a)–(2.81d). In the interior, the isopycnal diffusion slope $S_{\text{iso}} = S_{\text{int}}$ and is calculated on cell corners via (2.85) and interpolated to cell faces via

$$(S_{\text{iso}})_{j+1/2,k} = \frac{1}{2}\left((S_{\text{iso}})_{j+1/2,k+1/2} + (S_{\text{iso}})_{j+1/2,k-1/2}\right), \tag{2.88a}$$

$$(S_{\text{iso}})_{j,k+1/2} = \frac{1}{2}\left((S_{\text{iso}})_{j+1/2,k+1/2} + (S_{\text{iso}})_{j-1/2,k+1/2}\right). \tag{2.88b}$$

The diffusive tendency is then computed via straightforward finite-differencing of the H fluxes,

$$(G_{\text{iso}})_{j,k} = -\frac{H^{(x)}_{j+1/2,k} - H^{(x)}_{j-1/2,k}}{\Delta_x (\Delta_z)_{j,k}} - \frac{H^{(\sigma)}_{j,k+1/2} - H^{(\sigma)}_{j,k-1/2}}{(\Delta_z)_{j,k}} \tag{2.89}$$

The tracer tendency due to diapycnal mixing, G_{dia}, is computed implicitly. During each time step, all other physical and biogeochemical tendencies are computed and used to advance $\overline{c}_{j,k}$ forward one time step Δ_t, *i.e.*

$$\overline{c}^{\star}_{j,k} = \overline{c}^{n}_{j,k} + \mathcal{F}[\overline{c}^{n}]. \tag{2.90}$$

Here n denotes the time step number, and $\overline{c}^{\star}$ denotes an estimate of $\overline{c}$ at $t + \Delta_t$ (see Section 2.4.3 for details of the time stepping schemes). The updated tracer concentration is then further modified via the addition of a "correction" due to diapycnal diffusion. At each longitude, or for each j, we solve

$$\frac{\overline{c}^{n+1}_{j,k} - \overline{c}^{\star}_{j,k}}{\Delta_t} = \frac{1}{z_{j,k+1/2} - z_{j,k-1/2}}\left[(\kappa_{\text{dia}})_{j,k+1/2}\frac{\overline{c}^{n+1}_{j,k+1} - \overline{c}^{n+1}_{j,k}}{z_{j,k+1} - z_{j,k}} - (\kappa_{\text{dia}})_{j,k-1/2}\frac{\overline{c}^{n+1}_{j,k} - \overline{c}^{n+1}_{j,k-1}}{z_{j,k} - z_{j,k-1}}\right]. \tag{2.91}$$

Equation (2.91) defines a tridiagonal matrix system of algebraic equations for the unknowns $\{\overline{c}^{n+1}_{j,k} | k = 1 \ldots N_z\}$, which is inverted using the Thomas algorithm.

Finally, the meridional advection is discretized via a straightforward upwind advection scheme,

$$(G_{\text{lat}})_{j,k} = \frac{v^{(c)}_{j,k}}{L_y}\left(c_{j,k} - c^{u}_{j,k}\right), \qquad v^{(c)}_{j,k} = \frac{1}{2}\left(v^{\dagger}_{j+1/2,k} + v^{\dagger}_{j-1/2,k}\right) \tag{2.92}$$

where $v^{(c)}$ denotes the meridional velocity on tracer points and c^u denotes the upstream tracer concentration, defined as

$$c^u_{j.k} = \begin{cases} c^N_{j,k}, & v < 0, \\ c^S_{j,k}, & v > 0. \end{cases} \tag{2.93}$$

Here c^N and c^S are the tracer concentrations at the northern and southern ends of the domain, respectively. In all of the steps listed above, conditions of zero residual streamfunction and zero normal tracer flux are applied at the domain boundaries. These conditions are imposed by simply setting $\psi^\dagger$ to zero on all boundary points, and by setting the numerical fluxes (F, H, etc.) to zero on the boundary cell faces.

2.4.3 Temporal discretization

MAMEBUS evolves the model equations forward in time using Adams-Bashforth methods (*e.g.* Durran, 1991) modified to allow for adaptive time step sizes. In this section, we outline the derivation of these methods, and formally show the derivation in Appendix 2.10. We implement the adaptive time-step AB-methods because this family of methods are numerically stable with our scheme for the momentum equations (see Section 2.3.2). We then describe the constraints on the time-step imposed by the Courant–Fredrichs–Lewy (CFL) condition.

2.4.3.1 Adaptive-time step Adams-Bashforth methods

Our time integration scheme uses a family of time-step variable Adams-Bashforth integrative methods. This specific formulation of the AB methods allows for the model time step to be adjusted dynamically following the CFL conditions described in Section 2.4.3.2. Consider a tracer quantity c that evolves according to

$$\frac{\partial c}{\partial t} = f(t, c(t)). \tag{2.94}$$

Here the function f conceptually represents the entire model state, including the physical, biogeochemical, and non-conservative tendencies. We make a note here that the diffusive component of the time-integration step is calculated implicitly and not included in the ABIII integration step (see Equation (2.91)). We implement the third order Adams-Bashforth or ABIII method in this version of the model as the default option for time integration.
ABIII:

$$c(t_{n+1}) = c(t_n) + \frac{1}{6}\left(f^{n-2}\frac{\Delta t_{n+1}^2(2\Delta t_{n+1} + 3\Delta t_n)}{\Delta t_{n-1}(\Delta t_n + \Delta t_{n-1})} - f^{n-1}\frac{\Delta t_{n+1}^2(2\Delta t_{n+1} + 3\Delta t_n + 3\Delta t_{n-1})}{\Delta t_{n-1}\Delta t_n} + f^n\frac{\Delta t_{n+1}(2\Delta t_{n+1}^2 + 6\Delta t_{n+1}\Delta t_n + 3\Delta t_{n+1}\Delta t_{n-1} + 6\Delta t_n^2 + 6\Delta t_n\Delta t_{n-1})}{(\Delta t_n + \Delta t_{n-1})\Delta t_n}\right). \tag{2.95}$$

The first two time-steps require the lower order methods. We implement a forward Euler for the first time step and a second-order AB scheme (defined below) for the second time step, ABII:

$$c(t_{n+1}) = c(t_n) + \frac{\Delta t_{n+1}}{2\Delta t_n}\left(2f(t_n, c(t_n))\Delta t_n + f(t_n, c(t_n))\Delta t_{n+1} - f(t_{n-1}, c(t_{n-1}))\Delta t_{n+1}\right). \tag{2.96}$$

Here the notation Δt_n indicates the n^{th} time step. Derivations for the adaptive time-stepping ABII and ABIII methods are given in Appendix 2.10.

2.4.3.2 CFL conditions

MAMEBUS selects each model time step adaptively to ensure that time stepping is numerically stable. The time step is chosen to ensure that the CFL conditions for each of MAMEBUS's various advective and diffusive operators, described in preceding subsections, are satisfied.

The time step for advection of tracers is limited by the time scale associated with advective propagation across the width of a grid box (Δ_x or Δ_z). These constraints can

approximately be expressed as

$$\Delta t < \frac{\Delta_x}{|\overline{u}| + u_{\text{igw}}}, \tag{2.97a}$$

$$\Delta t < \frac{\Delta_z}{|\overline{w}|}, \tag{2.97b}$$

(Durran, 2010). Here u_{igw} is the maximum horizontal propagation speed of internal gravity waves (Chelton et al., 1998),

$$c_{\text{igw}} = \frac{1}{\pi} \int N \, \mathrm{d}z. \tag{2.98}$$

Particulate sinking in the NPZD model is also calculated explicitly and constrains the time step via a similar CFL criterion

$$\Delta t < \frac{(\Delta_z)}{|w_{\text{sink}}|} \tag{2.99}$$

where w_{sink} is the sinking speed of the particles.

We apply additional constraints on the time step to ensure that diffusive operators are stable. The standard numerical stability criterion for a Laplacian diffusion operator is (Griffies, 2018)

$$\Delta t < \frac{1}{2} \frac{\Delta_s^2}{\kappa}, \tag{2.100}$$

where κ is a diffusion coefficient and Δ_s is the spatial grid spacing. In the horizontal ($\Delta_s = \Delta_x$, the diffusion coefficients that determine the diffusive timestep are the eddy diffusion and isopycnal diffusion coefficients, when $\kappa = \kappa_{\text{gm}}$ and $\kappa = \kappa_{\text{iso}}$ respectively. [a] In the vertical ($\Delta_s = \Delta_z$), the diffusive time step is determined by the diapycnal diffusivity, $\kappa = \kappa_{\text{dia}}$, and by the vertical component of the eddy and isopycnal diffusion operators, $\kappa = \kappa_{\text{gm}} S_{\text{int}}^2$ and $\kappa = \kappa_{\text{iso}} S_{\text{int}}^2$ respectively (see *e.g.* Ferrari et al., 2008).

[a] Note that although κ_{iso} appears only in an advective operator in (2.83), this operator can be written as the divergence of a diffusion tensor (Griffies, 2018), and experience with MAMEBUS suggests that the more restrictive, diffusive formulation more accurately constrains the model time step.

2.4.4 Discrete momentum equations and barotropic pressure correction

In this section, we describe the discretization of the momentum equations presented in Section 2.3.2, specifically in Equations (2.11a), (2.11b), and (2.11c). To facilitate our discretization, we split the pressure ϕ, into barotropic and baroclinic components,

$$\phi = \underbrace{\Pi}_{\text{barotropic}} + \underbrace{\frac{g}{\rho_0}\int_z^0 \rho \, \mathrm{dz}}_{\text{baroclinic}}. \tag{2.101}$$

The barotropic and baroclinic components correspond to the pressure at the surface and the hydrostatic pressure variation with depth, respectively.

The numerical time-integration is calculated in a series of steps which include an explicit calculation of the non-diffusive time-step, an implicit calculation of the vertical diffusion, and a barotropic corrector step in order to ensure that the flow is non-divergent. The calculation of the explicit time-step is outlined in Section 2.4.3 and Appendix 2.10. In order to be numerically consistent with the calculation of the streamfunction, the mean horizontal velocities $\overline{u}$ and $\overline{v}$ are stored on the western face of each grid cell. In Figure 2.2, these are labeled as the u points. The time-step calculation is shown below, noting that the explicit components of the time-step, $\mathcal{E}\{\cdot\}$ are calculated following the ABIII methods outlined in Section 2.4.3, and the implicit diffusion $\mathcal{I}\{\cdot\}$ is calculated following Equation (2.91).

Given the mean momentum at time step n, $\overline{\mathbf{u}}^n$, we first perform the explicit component of the time-step to construct an estimate of $\overline{\mathbf{u}}^{n+1}$, denoted as $\overline{\mathbf{u}}^\star$,

$$\overline{\mathbf{u}}^\star = \overline{\mathbf{u}}^n + \mathcal{E}\left\{ -f\hat{z} \times \mathbf{u}^n - \frac{\partial \Pi}{\partial y}\hat{y} - \frac{g}{\rho_0}\nabla \int_z \rho^n \, \mathrm{d}z \right\}. \tag{2.102}$$

Note that the zonal barotropic pressure gradient, $\partial_x \Pi \hat{\mathbf{y}}$, is excluded from this equation; this will be revisited in the final component of the time-step. The discretization of the horizontal pressure gradient terms in (2.102) described in Section 2.4.5.

We next compute the tendency due to vertical viscosity following equation (2.91), which we denote via the operator $\mathcal{I}$. We thereby construct a second estimate of the velocity at

time step $n+1$, denoted as $\overline{\mathbf{u}}^{\star\star}$,

$$\overline{\mathbf{u}}^{\star\star} = \mathcal{I}\{\overline{\mathbf{u}}^{\star}\}. \tag{2.103}$$

Finally, we apply a tendency due to the zonal barotropic pressure gradient, ensuring that mass is conserved in each vertical fluid column (Dauhajre and McWilliams, 2018),

$$\int_z \overline{u}^{n+1} \, \mathrm{d}z = \int_z \overline{u}^{n} \, \mathrm{d}z = 0, \tag{2.104}$$

as required by (2.11c). We formulate the barotropic pressure correction as

$$\overline{u}^{n+1} = \overline{u}^{\star\star} - \Delta t \frac{\partial \Pi}{\partial x} \tag{2.105}$$

Substituting Equation (2.105) into (2.104), we obtain

$$\Delta t \frac{\partial \Pi}{\partial x} \hat{x} = \frac{1}{|\eta_b(x)|} \int_z \overline{u}^{\star\star} \, \mathrm{d}z. \tag{2.106}$$

This implies that the tendency in the mean zonal velocity due to the barotropic zonal pressure gradient must serve to bring the depth-integrated zonal velocity to zero, *i.e.*

$$\overline{u}^{n+1} = \overline{u}^{\star\star} - \frac{1}{|\eta_b(x)|} \int_z \overline{\mathbf{u}}^{\star\star} \, \mathrm{d}z. \tag{2.107}$$

The calculation of the vertical integral of $\overline{\mathbf{u}}^{\star\star}$ is computed in the model using a Kahan sum (Kahan, 1965).

2.4.5 Horizontal pressure- and buoyancy-gradient calculations

Pressure gradient calculations in sigma coordinates have been long known to produce discretization errors from the misalignment of geopotential and sigma coordinate surfaces and rely on large cancellations in the vertical gradient near steep slopes (Arakawa and Suarez, 1983; Haney, 1991; Mellor et al., 1994, 1998). We follow Shchepetkin and McWilliams (2003) to calculate the horizontal pressure gradient force and reduce the errors in horizontal gradient calculations, which otherwise produce large spurious along-slope currents in MAMEBUS (not shown). This algorithm has been extensively tested via its implementation in ROMS

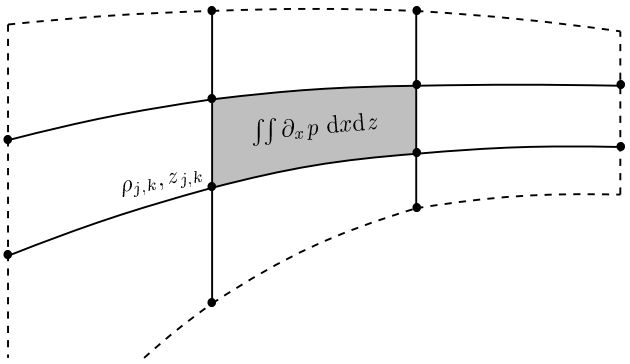

Figure 2.3: Stencil for the isopycnal slope and pressure gradient scheme given by Shchepetkin and McWilliams (2003). The points indicate the buoyancy (density) points. The solid lines are the reconstructed coordinate lines used in the horizontal calculation, and the shaded area shows the area integral of the horizontal buoyancy gradient.

(Shchepetkin and McWilliams, 2003, 2005), so we omit our own tests of the pressure gradient calculation scheme in this study. For numerical consistency, we also calculate horizontal buoyancy gradients, required to evaluate the isopycnal slope (see §2.4.2), using the same algorithm.

2.4.5.1 Zonal Pressure Gradients

In this section, we outline the implementation of the baroclinic zonal pressure gradient calculation used in MAMEBUS following Shchepetkin and McWilliams (2003). The ultimate goal of the algorithm is to calculate the following baroclinic pressure gradient at a cell center (*c.f.* (2.102)),

$$-\frac{\partial\overline{\phi}}{\partial x}\bigg|_z^{\text{baroclinic}} = -\frac{1}{A}\frac{g}{\rho_0}\left(\iint_A \frac{\partial\rho}{\partial x}\bigg|_z \mathrm{d}x\mathrm{d}z\right), \tag{2.108}$$

where ρ, like the linear case, is the density anomaly, ρ_0 is a reference density, and A is the area between four adjacent buoyancy grid points (shaded area in Figure 2.3. Shchepetkin and McWilliams (2003) calculate the second term by implementing a Lagrange polynomial reconstruction of the z and ρ fields. By Green's theorem, we write the integrated horizontal

density gradient as

$$\iint_A \left.\frac{\partial \rho}{\partial x}\right|_z \mathrm{d}x\mathrm{d}z = \oint \rho \mathbf{dz}. \tag{2.109}$$

The two algorithms differ on the treatment of the vertical integration of pressure. The *Density Jacobian Algorithm* first interpolates the density field onto the sigma grid and calculates the values of ρ and z along the solid lines in Figure 2.3, then integrates to obtain the pressure. The *Sigma Coordinate Primitive Form Algorithm* first integrates the pressure and calculates the gradients using a vertical correction term. We opt for the second algorithm which results in an equation for the horizontal gradient which closely resembles a Equation (2.68a). Furthermore, this algorithm tends to be more stable in our model. The algorithm is calculated as follows:

First, we calculate all elementary differences in ρ and z

$$(\Delta_x)\rho_{j+1/2,k} = \rho_{j+1,k} - \rho_{j,k}, \tag{2.110a}$$

$$(\Delta_z)\rho_{j,k+1/2} = \rho_{j,k+1} - \rho_{j,k}, \tag{2.110b}$$

$$(\Delta_x)z_{j+1/2,k} = z_{j+1,k} - z_{j,k}, \tag{2.110c}$$

$$(\Delta_z)z_{j,k+1/2} = z_{j,k+1} - z_{j,k}, \tag{2.110d}$$

where $z_{j,k}$ is the depth value at the cell centers, where the density tracer is located. Note that the edges of Figure 2.3 correspond to the cell centers in MAMEBUS, this requires some extrapolation at the boundaries so that the elementary differences are fully calculated throughout the domain. For all variables, we assume that the elementary differences at the boundary are zero.

We then calculate the hyperbolic differences of all variables. This step calculates an estimate of the derivatives following a cubic spline formalism outlined in more detail in Shchepetkin and McWilliams (2003). The derivatives are then given by,

$$h_x\rho_{j,k} = \frac{2(\Delta_x)\rho_{j+1/2,k}(\Delta_x)\rho_{j-1/2,k}}{(\Delta_x)\rho_{j+1/2,k} + (\Delta_x)\rho_{j-1/2,k}}, \tag{2.111a}$$

$$h_x z_{j,k} = \frac{2(\Delta_x)z_{j+1/2,k}(\Delta_x)z_{j-1/2,k}}{(\Delta_x)z_{j+1/2,k} + (\Delta_x)z_{j-1/2,k}}. \tag{2.111b}$$

The vertical hyperbolic differences for ρ and z are calculated similarly using Equations (2.110b) and (2.110d). Again, the hyperbolic differences on the boundaries are not defined using Equations (2.111a) and (2.111b), so we extrapolate the hyperbolic averages of density. For example, at the western edge of the domain we define

$$h_x\rho_{N,k} = \frac{3}{2}\left((\Delta_x)\rho_{N-1/2,k} - (\Delta_x)\rho_{N-3/2,k}\right) - \frac{1}{2}\left(h_x\rho_{N-1,k}\right) \tag{2.112}$$

Analogous extrapolation schemes are applied at all domain boundaries.

We the calculate the pressure field using the hydrostatic relationship. This is done via a vertical integration of the density reconstructed along the vertical lines in Figure 2.3. The pressure field is calculated from the surface down. The pressure is calculated in the surface grid cells as

$$\phi_{j,N} = \frac{g}{\rho_0}\left(\rho_{j,N} + \frac{1}{2}\left(\zeta_j - z_{j,N}\right)\frac{\rho_{j,N} - \rho_{j,N-1}}{z_{j,N} - z_{j,N-1}}\right)\left(\zeta_j - z_{j,N}\right), \tag{2.113}$$

where $\zeta_j = 0$ from the rigid lid assumption in MAMEBUS. Then the pressure is calculated at successively deeper grid levels as,

$$\begin{aligned}\phi_{j,k} = \phi_{j,k+1} + \frac{g}{\rho_0}\Bigg(&\frac{\rho_{j,k+1} + \rho_{j,k}}{2}\left(z_{j,k+1} - z_{j,k}\right) \\ &- \frac{1}{10}\Bigg\{\left(h_z\rho_{j,k+1} - h_z\rho_{j,k}\right)\left[z_{j,k+1} - z_{j,k} - \frac{h_z z_{j,k+1} + h_z z_{j,k}}{12}\right] \\ &-\left(h_z z_{j,k+1} - h_z z_{j,k}\right)\left[\rho_{j,k+1} - \rho_{j,k} - \frac{h_z\rho_{j,k+1} + h_z\rho_{j,k}}{12}\right]\Bigg\}\Bigg).\end{aligned} \tag{2.114}$$

We then correct for the iso-σ pressure gradient introduced by the slope of the sigma coordinate grid, analogous to the continuous expression in Equation (2.68a). This step calculates the product of ρ and the local slope of the σ-coordinate, and corrects for the interpolation errors from the coordinate transformation. Following the notation used in

Shchepetkin and McWilliams (2003),

$$FC_{j+1/2,k} = \frac{\rho_{j+1,k} + \rho_{j,k}}{2}(z_{j+1,k} - z_{j,k}) - \frac{1}{10}\left\{(h_x\rho_{j+1,k} - h_x\rho_{j,k})\left[z_{j+1,k} - z_{j,k} - \frac{h_x z_{j+1,} + h_x z_{j,k}}{12}\right] -(h_x z_{j+1,k} - h_x z_{j,k})\left[\rho_{j+1,k} - \rho_{j,k} - \frac{h_x\rho_{j+1,k} + h_x\rho_{j,k}}{12}\right]\right\}. \quad (2.115)$$

Finally, we use Equations (2.114) and (2.115) to calculate the pressure gradients.

$$\left(\frac{\partial\phi}{\partial x}\bigg|_z\right)_{j+1/2,k} = \frac{1}{\Delta x}\left(\phi_{j+1,k} - \phi_{j,k} + \frac{g}{\rho_0}\cdot FC_{j+1/2,k}\right). \quad (2.116)$$

2.4.5.2 Buoyancy gradients

The buoyancy gradient is calculated similarly to the pressure gradient. However, because we do not vertically integrate the buoyancy term, we opt to use the *Density Jacobian Algorithm* described in Shchepetkin and McWilliams (2003). The pressure gradient algorithm described above integrates the pressure and then corrects for the pressure gradient in sigma coordinates. The density gradient algorithm described below calculates the line integral about the area enclosed by the ϕ-points where the buoyancy gradient is located (see Figure 2.3). Therefore, we use the following form to calculate the buoyancy gradient,

$$\iint_A \frac{\partial b}{\partial x}\mathrm{d}x\mathrm{d}z = \oint b\mathrm{d}\mathbf{z} = FX_{j+1,k+1/2} + FC_{j+1/2,k} - FX_{j,k+1/2} - FC_{j+1/2,k+1}, \quad (2.117)$$

where $FX_{j,k+1/2}$ are the value of the integral (Equation (2.117)) along the vertical sides, and $FC_{j+1/2,k}$ is the value of the integral along the horizontal sides. This calculation follows a similar procedure as the pressure gradient.

First, we calculate the elementary differences, and the hyperbolic averages in b and z, given by Equations (2.110a) through (2.111b). Then calculate the value of the integral along

the upper and lower sides of the domain following,

$$FC_{j+1/2,k} = \frac{b_{j+1,k}+b_{j,k}}{2}(z_{j+1,k}-z_{j,k}) - \frac{1}{10}\left\{(h_x b_{j+1,k}-h_x b_{j,k})\left[z_{j+1,k}-z_{j,k}-\frac{h_x z_{j+1,}+h_x z_{j,k}}{12}\right] -(h_x z_{j+1,k}-h_x z_{j,k})\left[b_{j+1,k}-b_{j,k}-\frac{h_x b_{j+1,k}+h_x b_{j,k}}{12}\right]\right\}. \quad (2.118)$$

Note that this formulation is the same as Equation (2.115), but with buoyancy instead of pressure. Then we calculate the value of the line integral along the vertical components of the cell,

$$FX_{j,k+1/2} = \frac{b_{j,k+1}+b_{j,k}}{2}(z_{j,k+1}-z_{j,k}) - \frac{1}{10}\left\{(h_z b_{j,k+1}-h_z b_{j,k})\left[z_{j,k+1}-z_{j,k}-\frac{h_z z_{j,k+1}+h_z z_{j,k}}{12}\right] -(h_z z_{j,k+1}-h_z z_{j,k})\left[b_{j,k+1}-b_{j,k}-\frac{h_z b_{j,k+1}+h_z b_{j,k}}{12}\right]\right\}. \quad (2.119)$$

Shchepetkin and McWilliams (2003) write Equation 2.68a as,

$$\left.\frac{\partial b}{\partial x}\right|_z = \mathcal{J}(b,z) = \left.\frac{\partial b}{\partial x}\right|_\sigma \frac{\partial z}{\partial \sigma} - \frac{\partial b}{\partial \sigma}\left.\frac{\partial z}{\partial x}\right|_\sigma, \quad (2.120)$$

This allows us to numerically integrate the buoyancy gradient in the cell as,

$$\oint b \mathrm{d}\mathbf{z} = \left(A\frac{\partial b}{\partial x}\right)_{j+1/2,k+1/2} = FX_{j+1,k+1/2} + FC_{j+1/2,k} - FX_{j,k+1/2} - FC_{j+1/2,k+1} \quad (2.121)$$

where, A, again is the area of the cell. At the surface, the boundary condition is given that $FC_{j+1/2,N+1} \equiv 0$.

Finally, in order to calculate the horizontal buoyancy gradient, we divide by the area. Since, the area of each cell is defined by the cell-centered, ϕ-points, we implement Gauss' Area Formula,

$$A_{j+1/2,k+1/2} = \frac{1}{2}\left|x_{j,k+1}z_{j,k} + x_{j,k}z_{j+1,k} + x_{j+1,k}z_{j+1,k+1} + x_{j+1,k+1}z_{j,k+1} - x_{j,k}z_{j,k+1} - x_{j+1,k}z_{j,k} - x_{j+1,k+1}z_{j+1,k} - x_{j,k+1}z_{j+1,k+1}\right| \quad (2.122)$$

2.4.5.3 Meridional Pressure Gradients

The alongshore pressure gradient in Equation (2.11b), denoted by $\left[\phi\right]_0^{L_y}/L_y$, and is determined by along-shore gradients in the surface pressure and buoyancy/density that are imposed as model input parameters. We integrate the profiles of pressure following the hydrostatic relationship. We define ρ^N and ρ^S as the densities at the northern and southern ends of the domain, and $\Pi^y = \Pi^{N,S}$ as the surface pressures at northern and southern ends of the domain. Then the pressure is given by,

$$\begin{aligned}\frac{1}{L_y}\left[\phi\right]_0^{L_y} &= \frac{\partial \Pi}{\partial y} - \frac{g}{\rho_0}\int_z^0 \frac{\partial \rho}{\partial y}\,\mathrm{d}z, \\ &= \frac{\Pi^N - \Pi^S}{\rho_0 L_y} + \frac{g}{\rho_0}\int_z^0 \frac{\rho^N - \rho^S}{L_y}\,\mathrm{d}z. \end{aligned} \tag{2.123}$$

Here the along shore variations in sea surface pressure and density are both model inputs. We discretize the meridional pressure gradient as,

$$\frac{1}{L_y}\left[\phi\right]_0^{L_y}\Bigg|_{j,k} = \frac{1}{L_y}\left[\left(\Pi^N_{j,N} - \Pi^S_{j,N}\right) + \frac{g}{\rho_0}\sum_{k=k'}^{N-1}\left(\frac{\rho^N_{j,k'+1} + \rho^N_{j,k'}}{2} - \frac{\rho^S_{j,k'+1} + \rho^S_{j,k'}}{2}\right)\left(z_{j,k'+1} - z_{j,k'}\right)\right]. \tag{2.124}$$

Though MAMEBUS allows meridional pressure gradients to be imposed, we have excluded them from our reference solutions in the interest of simplicity. However, previous studies have highlighted the importance of meridional pressure gradients in supporting interior cross-slope transport, and in driving poleward undercurrents Connolly et al. (2014). We plan to address the effects of meridional pressure gradients on EBUS ecosystem dynamics in future scientific studies using MAMEBUS.

2.5 Implementation Details

In this section, we outline the details for implementation in MAMEBUS. The model code is written in the C programming language. The model expects various user inputs that include initial conditions, along with user-defined model calculation details in Table 2.4 that

include, but are not limited to, the momentum calculation scheme and the time-stepping scheme. The MAMEBUS distribution includes sample Matlab codes that package these user inputs.

The software needed to run this model include:

1. MATLAB (2016) or later
2. A C compiler (eg. GCC)

Our provided setup also includes example scripts for running the model on a cluster, however, this model can be easily run locally on a laptop or desktop on any operating system so long as the necessary software is installed. Table 2.6 shows run times for the model on both the cluster and a 2015 Macintosh Laptop.

MAMEBUS has three active physical variables: the zonal and meridional momenta, and the temperature (buoyancy). The current implementation of the biogeochemical model has four active variables: nitrate (N), phytoplankton (P), zooplankton (Z), and detritus (D). A variable number of additional passive tracers may also be included.

2.5.1 Expected user-inputs, and options available

MAMEBUS expects a list of parameters given in Table 2.3, that control the physical components of the model, the model run details, and the grid setup. Other identifiers included in this model are given in Table 2.4 which determine which internal schemes the model uses for each specific run. Furthermore, MAMEBUS expects a set of input parameters from physical tracers, forcing, diffusivity, and restoring, along with initial profiles of biogeochemical tracers that are listed in Table 2.5.

For the solutions shown in Section 2.6, the following intial conditions are detailed in Section 2.6.1.

Table 2.3: Input parameters expected by the MAMEBUS model code. All parameters listed in this table are chosen by the user. The sample values listed in this table are those used in the reference experiments described in Section 2.6.

Description	Value	Units
Number of horizontal grid points	64	
Number of vertical grid points	64	
Computational domain width	400	km
Computational domain height	3000	m
Depth of the shelf	50	m
Location of the continental slope in the domain from the eastern boundary	50	km
Topographic slope	9.8e-3	
Depth of surface mixed layer	40	m
Depth of bottom boundary layer	40	m
Drag coefficient in the bottom boundary layer	1e−3	m/s
Reference density	1000	kg/m^3
Coriolis parameter	1e−4	1/s
Surface grid stretching parameter	9	
Bottom grid stretching parameter	4	
Depth below the surface over over which the vertical coordinate the coordinate is approximately aligned with geopotentials	300	m
The fraction of the maximum time-step taken for each Δt to ensure the CFL condition is met	0.75	
The end time for integration	30	years
Output frequency of model data	1	day

Table 2.4: MAMEBUS numerical scheme options and descriptors.

Parameter	Identifier	Value	Scheme description
modelType	BGC_NONE	0	Physics only, no biogeochemistry
	BGC_NPZD	1	Nutrient-Phytoplankton Zooplankton-Detritus (NPZD) Model described in Section 2.3.4
timeSteppingScheme	TIMESTEPPING_AB1	0	First-order Adams Bashforth variable timestepping
	TIMESTEPPING_AB2	1	Second-order Adams Bashforth variable timestepping
	TIMESTEPPING_AB3	2	Third-order Adams Bashforth variable timestepping

2.5.2 Model run details

The main function of the mamebus.c file has five major components and steps:

1. Calculate the time tendency of each tracer. The time step is calculated using the tderiv function detailed in Figure 2.4. The explicit tendencies are calculated following Section 2.3.

2. Add implicit vertical diffusion and remineralization, Equation (2.91).

3. Apply zonal barotropic pressure gradient correction if the momentumScheme is MOMENTUM_TTW (Section 2.4.4)

4. Enforce zero tendency where relaxation time is zero (Section 2.3.5.1).

5. Write model state (Section 2.5.3).

Table 2.5: A table outlining the initial profiles that MAMEBUS expects during initializaiton. To visualize the grid locations, see Figure 2.2. Each initial profile is included in all modelTypes unless otherwise stated. Note that Nx is the number of zonal domain points and Nz is the number of vertical domain points given in Table 2.3.

Initial Profile	Parameter	Grid Location	Size	Descriptions
Zonal Momentum	$u(x,z)$	u-points	Nx+1 $\times$ Nz	All modelTypes
Meridional Momentum	$v(x,z)$	v-points	Nx+1 $\times$ Nz	All modelTypes
Temperature	T	ϕ-points	Nx $\times$ Nz	All modelTypes
Nitrate	N	ϕ-points	Nx $\times$ Nz	NPZD Model
Phytoplankton	P	ϕ-points	Nx $\times$ Nz	NPZD model
Zooplankton	Z	ϕ-points	Nx $\times$ Nz	NPZD model
Detritus	D	ϕ-points	Nx $\times$ Nz	NPZD model
Buoyancy Diffusivity	κ_{gm}	ψ-points	Nx+1 $\times$ Nz+1	See Equation (2.131)
Isopycnal Diffusivity	κ_{iso}	ψ-points	Nx+1 $\times$ Nz+1	See Section 2.6.2
Topography	$h_b(x)$	w, ψ-points	Nx+1 $\times$ 1	See Equation (2.126)
Wind Stress	$\tau(x,t)$	ψ-points	Nx+1 $\times$ 1	See Equation (2.125)

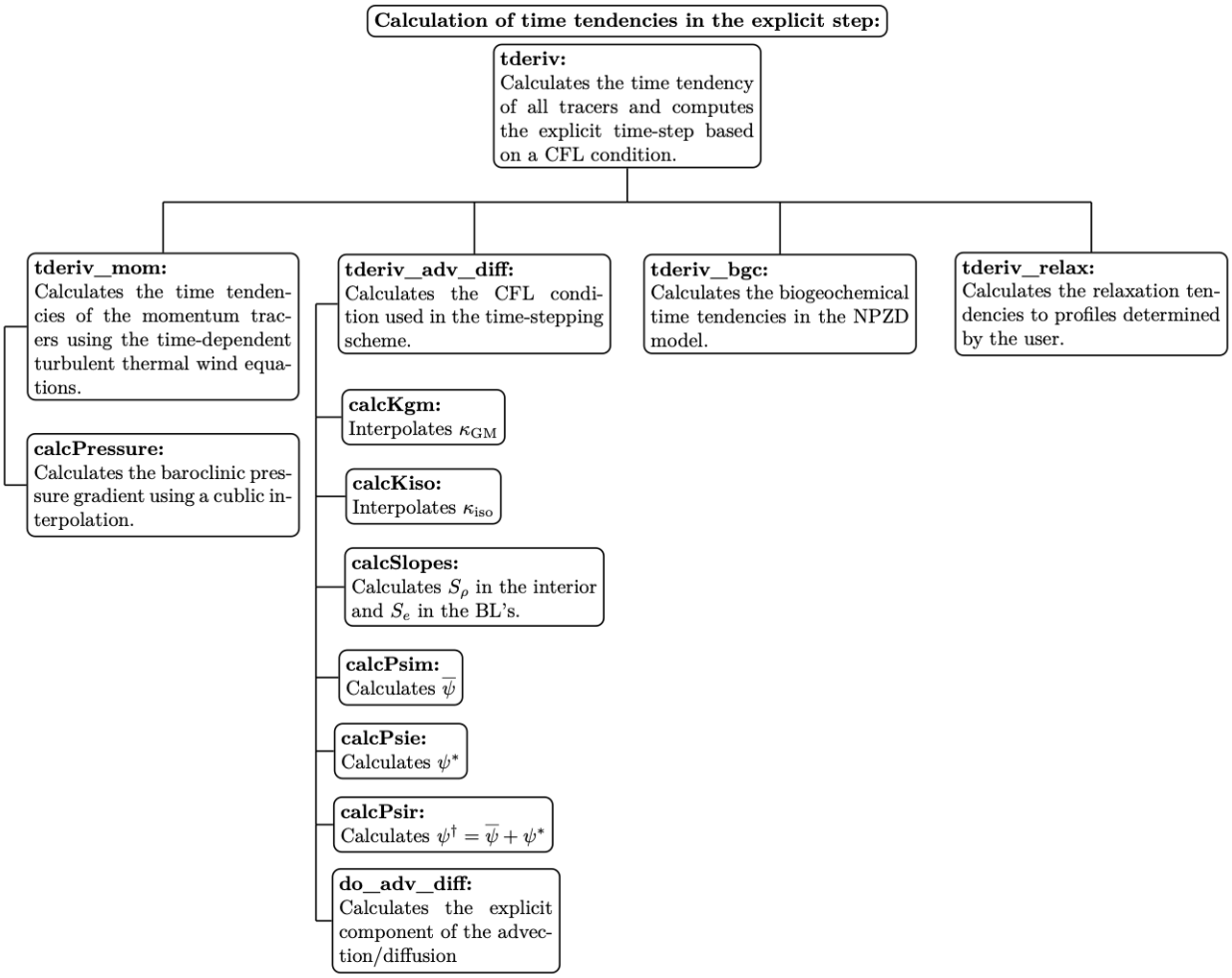

Figure 2.4: The call tree from the main function of mamebus.c

2.5.3 Model data

All of the model input and output are saved in binary files. Depending on the "monitorFreq" or the frequency of output, the model will interpolate the between timesteps, if necessary, calculate the correct model state, and write the data to file. The following list contains all files that are written to file during the time integration step. For each model, there is an option to include an arbitrary number of passive tracers, however these are the standard list of tracers that are included in the indicated modelTypes.

- Residual Streamfunction, $\psi^\dagger$, (all modelTypes)
- Mean Streamfunction, $\overline{\psi}$, (all modelTypes)
- Eddy Streamfunciton, $\psi^\star$, (all modelTypes)
- Temperature field, (all modelTypes)
- Nitrate, (NPZD model)
- Phytoplankton (NPZD model)
- Zooplankton (NPZD model)
- Detritus (NPZD model)

2.6 Reference Solution and Model Validation

In this section we present reference solutions for MAMEBUS. Below we discuss the choice of parameters, the non-conservative forcing, and profiles of restoring. We focus predominantly on the output of a single run, and plan in the future to run parameter sweeps to better understand the response of the ecosystem dynamics to the physical forcing.

2.6.1 Model geometry, initial conditions, and forcing

The model is configured to represent an idealized California Current System (CCS). While the model can be formulated to represent a general EBUS, we use the California Current System as a test case because this allows comparison of our results with measurements from California Cooperative Oceanic Fisheries Investigations (McClatchie, 2016). Note that we exclude salinity as a physical tracer; while it may be important in determining the structure of the California undercurrent (Connolly et al., 2014), we find that the main features of stratification can be well described by temperature.

A list of input fields that MAMEBUS expects is given in Table 2.5, with a subset illustrated in Figure 2.5. The solutions shown in Section 2.6 use the following choices for these input fields. The wind stress profile is given by

$$\tau(x) = \tau_0 \tanh\left(\lambda_\tau \frac{L_x - x}{L_x}\right), \tag{2.125}$$

where L_x is the width of the computational profile given in Table 2.3, and $\lambda_\tau = 4$ is a tuning parameter that controls the horizontal width of the wind stress drop off, or wind stress curl. We tune the offshore maximum to approximate values reported by Castelao and Luo (2018). While this is the example of wind-stress forcing we choose to use to validate our model, any form of wind-stress forcing can be defined by the user.

The topography for the reference solutions is ,

$$\eta_b(x) = H - \frac{1}{2}(H - H_s)\tanh\left(\frac{x - x_t}{L_t}\right), \tag{2.126}$$

where H is depth of the computational domain, H_s is the slope depth, x_t is the location of the continential slope in the computational domain, and L_t is the width of the continental slope given from the topographic slope parameter. All parameters are given in Table 2.3. The topography is tuned to represent an idealized profile of bathymetry ETOPO5 (NOAA, 1988) taken from the geographic coordinates given from Line 80 in the CalCOFI data (McClatchie, 2016).

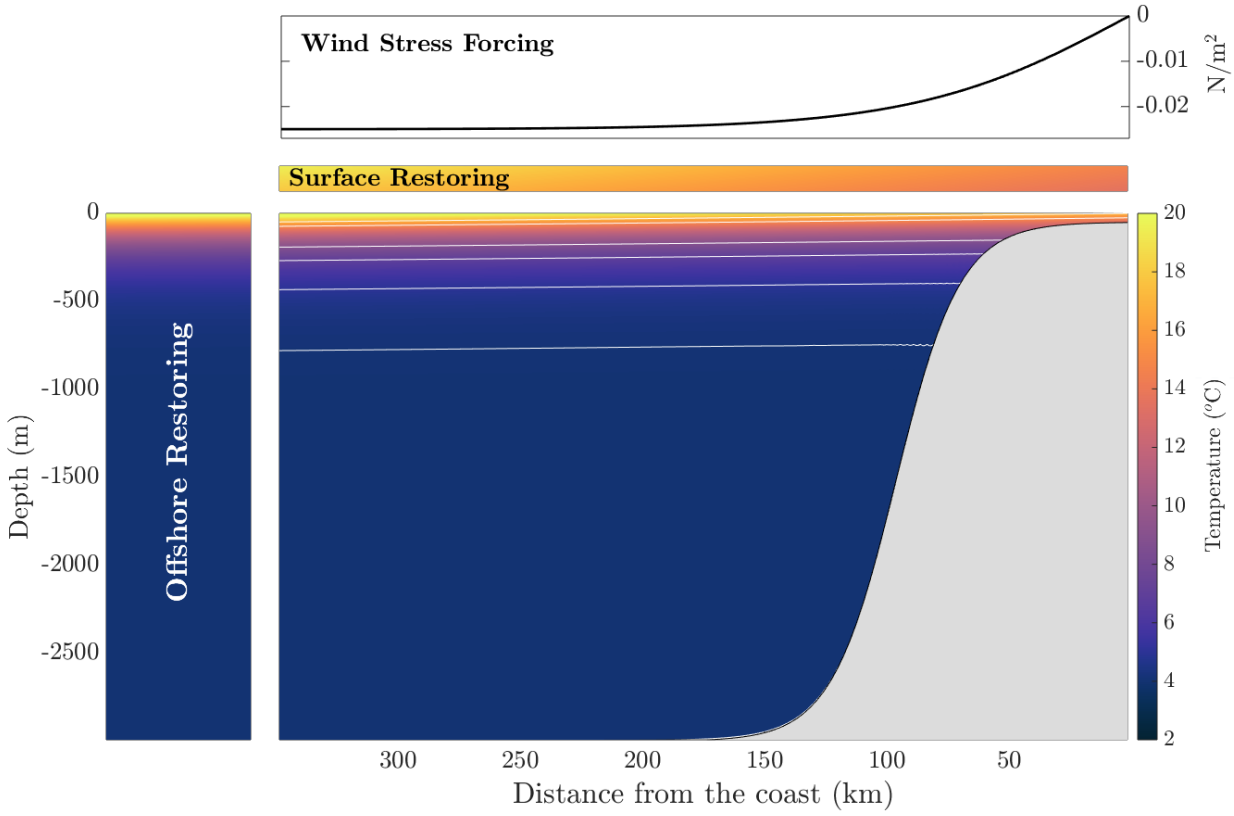

Figure 2.5: Initial temperature profile with a profile of offshore restoring which is modeled as a sponge layer on the western side of the boundary, and at the surface, there is a surface restoring to an atmospheric profile, idealized to a profile of temperature from the California Cooperative Oceanic Fisheries Investigations (CalCOFI). The northward wind stress is shown at the top of the figure. The white lines in the temperature field are a few lines of constant initial temperature.

The initial conditions for the tracers in the model are the intial temperature profile, including timescales and inputs for restoring, and initial conditions for the NPZD model, which are tuned to give an approximate concentration of 30 mmol/m^3 in the deep ocean. The biogeochemical tracers are not restored in this set of reference solutions. The initial profile of temperature is shown in Figure 2.5 and given by,

$$T_{\text{init}}(x,z) = T_{\min} + (T_{\max} - T_{\min}) \frac{\exp\left(\frac{z}{H^\star}+1\right) - \exp\left(-\frac{H}{H^\star}+1\right)}{\exp(1) - \exp\left(-\frac{H}{H^\star}+1\right)}, \tag{2.127}$$

where the minimum and maximum temperatures in the domain are $T_{\min} = 4^o$C, $T_{\max} = T^s_{\max} - (T^s_{\max} - T^s_{\min})x/L_x$. The maximum and minimum surface temperatures are $T^s_{\max} = 22^o$C and $T^s_{\min} = 18^o$C, respectively. $H^\star$ is a decay scale for the temperature from the surface. This profile is tuned so that the temperature profile on the western side of the domain approximately matches the profile of temperature from CalCOFI (McClatchie, 2016) in Figure 2.7. We initialize the temperature field with a small tilt in the iso-surfaces to speed up the spin-up process. This same initial condition is used as the reference for temperature restoring. The timescale for restoring is given by

$$R_T^{\text{west}}(x,z) = \left(\frac{1}{R_T^{\max}} \frac{L_r - x}{L_r}\right)^{-1}, \qquad x < L_r \tag{2.128}$$

where $L_r = 50$km is the width of the sponge layer on the western side of the domain, and $R_T^{\max} = 30$ days is the fastest relaxation timescale for temperature. In the surface grid boxes, the restoring timescale is given by,

$$R_T^{\text{surf}}(x) = 1 \text{ day} , \tag{2.129}$$

which is consistent with the formulation of Haney (1971) for surface grid box thicknesses of approximately 1 m. The restoring at the surface grid box is set to the initial profile of temperature given in Equation 2.127.

The initial conditions for NPZD tracers a a constant concentration of nitrate, $N_{\max} = 30$ mmol/m^3, phytoplankton $P_{\max} = 0.02$ mmol/m^3, zooplankton, $Z_{\max} = 0.01$ mmol/m^3, and an initial profile of detritus of zero. This choice allows for the internal ecosystem dynamics to

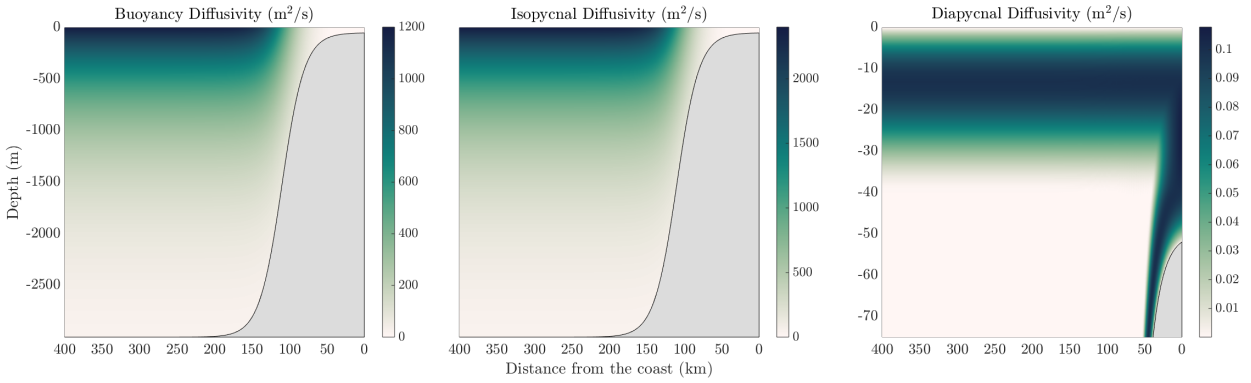

Figure 2.6: Inputs of buoyancy diffusivity (left), isopycnal diffusivity (center), and diapycnal diffusivity (right) used in the reference solution to MAMEBUS shown in Section 2.6. Note that the isopyncal and diapycnal diffusivities are shown over the entire domain, and the diapycnal diffusivities are shown over the upper 75m of the domain to highlight the boundary layer mixing and the mixing in the eastern side of the domain on the shelf where the boundary layers merge.

control the biogeochemical solutions. Finally, the cell sizes we choose for the phytoplankton cell is, $\ell_p = 1\mu$m. The zooplankton cell is optimized to give the optimal predator-prey length scale between the phytoplankton and zooplankton interactions, ie,

$$\ell_z = \exp\left(\frac{1}{0.56}\log\left(\frac{\ell_p}{0.65}\right)\right). \tag{2.130}$$

2.6.2 Isopycnal, buoyancy, and diapycnal mixing

The unresolved mesoscale and microscale mixing in the tracer evolution Equation (2.9) are detailed in Sections 2.3.3.1 and 2.3.3.2, respectively. The diapycnal diffusivities are independent of wind-stress, and are determined by user-input mixed layer depth and maximum magnitudes. The isopycnal and buoyancy diffusivities are time-invariant fields whose spatial structure is prescribed by the user.

In our model reference configuration, the eddy and buoyancy diffusivities are functions of the baroclinic radius of deformation – the preferential length scale at which baroclinic

instability occurs, and closest to the fastest growing mode in the Eady model (Eady, 1949). In MAMEBUS, these diffusivities also exponentially decreases with depth. There are choices for more sophisticated parameterzations of eddy transfer acros continential slopes (Wang and Stewart, 2018, 2020), but in this current version of the model, we opt for a simpler description. For example, the buoyancy diffusivity coefficient is defined as:

$$\kappa_{\text{gm}} = \frac{\kappa^0_{\text{gm}} R_d}{H_{\text{max}}} \exp\left(\lambda \frac{z}{\eta_b}\right), \tag{2.131}$$

where $\lambda < 1$ is a tuning coefficient that allows for adjustment of the depth of the exponential profile of diffusivity, H_{max} is the maximum depth of the topography offshore, and η_b is the depth of the topography. For all solutions shown in this section $\lambda = 0.25$ Note that for this formulation, we assume that $z < 0$. The maximum buoyancy diffusivity is $\kappa^0_{\text{gm}} = 1200$ m^2/s. Furthermore, $\kappa_{\text{iso}} = 2\kappa_{\text{gm}}$, following Smith and Marshall (2009) and Abernathey and Marshall (2013). The isopycnal and buoyancy diffusivity profiles are shown in the left and center panels of Figure 2.6, respectively.

The diapycnal diffusivities shown in the right panel of Figure 2.6, with structure function described in Equation (3.22), are set so that the maximum diffusivity in the mixed layers are given by, $\kappa^0_{\text{sml}} = \kappa^0_{\text{bbl}} = 0.1$ m^2/s, otherwise the ambient diffusivity in the interior is given by, $\kappa_{\text{bg}} = $ 1e-5 m^2/s. In the case where the mixed layers join at the eastern edge of the domain, the profiles of diffusivity are simply added.

2.6.3 Model validation

We run the reference solutions of MAMEBUS for 25 model years, with initial conditions and physical forcing described in Section 2.6.1. We validate the model against observations of temperature, nitrate, and chlorophyll-a concentration in the euphotic zone, based on observations from the CalCOFI program (McClatchie, 2016). For this comparison, we interpolate a typical CalCOFI section (Line 80) to a sigma coordinate grid with realistic topography from the ETOPO database (NOAA, 1988). We chose to validate our model with a single

transect of from CalCOFI instead of several transects along the same line because averaging over time smooths over the deep chlorophyll maximum.

Furthermore, we prescribed a continental shelf that is deeper than in nature in order to reduce the model's computation time. Further shallowing the continental shelf is possible, but the CFL constraint imposed by the finer vertical resolution on the shelf extends the computation time.

While the continental slope is tuned to have a similar slope as observations in Central California near the shelf break, the mixed layers in this model run are set to a constant depth zonally and overlap on the shelf. This choice has been made for simplicity, and could be refined via zonally-varying mixed layer depths to improve agreement with specific EBUSs. The well mixed area on the shelf is an analogue to the inner shelf, albeit somewhat deeper than those found in nature (Lentz and Fewings, 2012). In our model comparison, we neglect the inner shelf region in the model and compare the solutions and starting approximately 50km from the coast.

The model temperature is generally in good agreement with observations for the upper ocean, reproducing sloping isotherms towards the coast, and realistic surface values. We observe a cold bias near the coast, which could be a result of the constant wind-stress curl forcing over the domain, inducing upwelling that is too strong in the model. A cold bias observed in the surface just outside the shelf, and a warm bias offshore, are likely caused by the prescription of a constant mixed layer depth, which may be too deep in the model for this particular section and time of the year.

As shown by the middle row of Figure 2.7 model nitrate agrees reasonably well with observations in the upper layers, although biases remain, in particular in deeper layers. This may be caused by several factors, including biases in the cross-shore and vertical circulation, and in the cycling of inorganic nutrients and organic matter. For example, remineralization processes are simplified in the model, which does not include dissolved organic matter, and represents export by a single particle size class with a constant sinking speed that was not

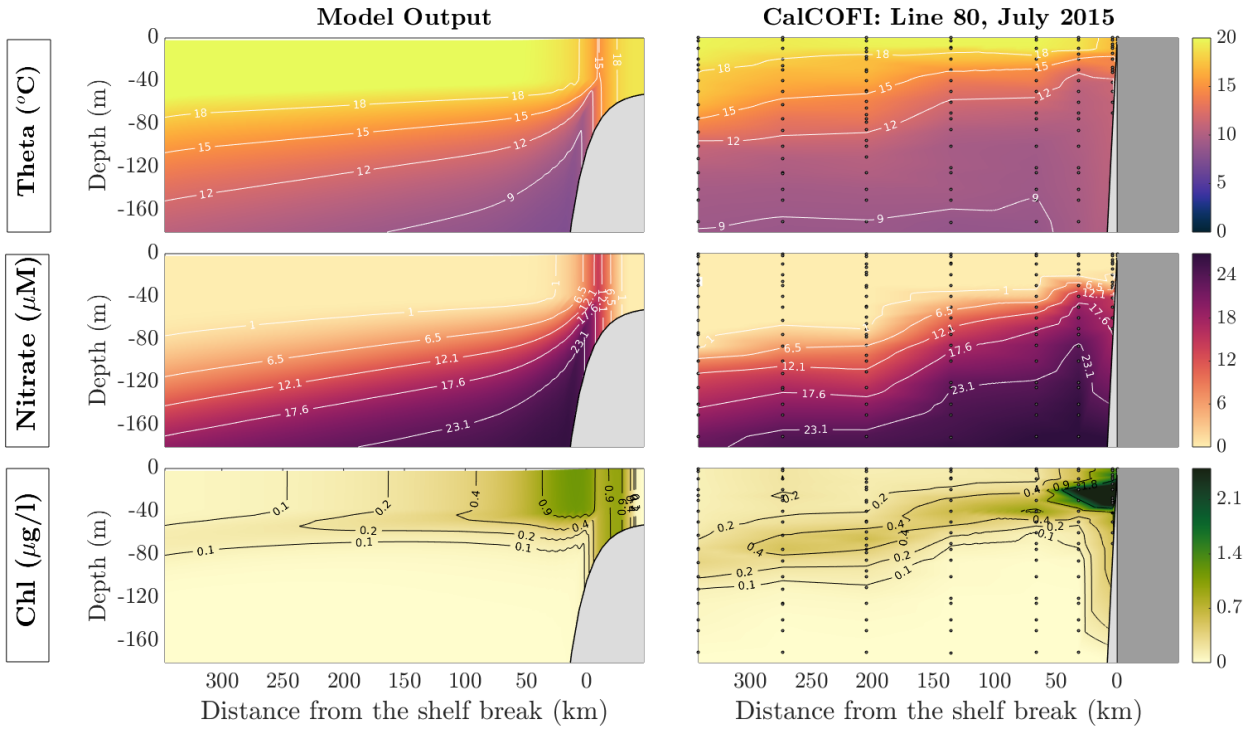

Figure 2.7: Model validation against *in situ* California Cooperative Oceanic Fisheries Investigations (CalCOFI) data taken along Line 80 (Point Conception) during July of 2015. The column on the left shows output from the model under constant wind forcing and is averaged over the last five model years. The column on the right are values taken from CalCOFI and interpolated onto a sigma coordinate grid to allow for direct comparison. The dots on the figures are locations where the data is sampled. This figure shows the comparison between potential temperature, θ (top), nitrate (middle), and chlorophyll concentration (bottom).

explicitly tuned to match nutrients.

The bottom row of Figure 2.7 shows that the model captures the main features of the observed chlorophyll distribution (here calculated based on a fixed chlorophyll to phytoplankton nitrogen ratio of 4:5 mg, chl/m^3:mmol N/m^3 following Furuya (1990)). High surface concentrations are reproduced near the shelf, with values decreasing further offshore. A deep chlorophyll maximum develops in the lower euphotic zone, at depths between 40 and 80 m, progressively deepening from the coastal to the oligotrophic region offshore. while these patterns are fairly realistic, we note that the very high chlorophyll concentrations observed near the shelf are missing from the model. This underestimate may be caused by the oversimplification of the ecosystem structure in the NPZD model, which only includes a single phytoplankton group, while multiple groups are likely required for a more correct representation of enhanced coastal phytoplankton biomass (Van Oostende et al., 2018). Furthermore, aspects of these differences could be caused by the idealized nature of the 2-D circulation simulated by the physical model.

In order to compare physical solutions, we also include solutions which show the residual streamfunction, including the mean and eddy components in Figure 2.8. The mean streamfunction is calculated via the momentum equations given in Section 2.3.2, whereas the eddy streamfunction is described in Section 2.3.3. The positive values indicate clockwise circulation, which, in this case, is indicative of eddy restratification opposing the mean upwelling branch (Colas et al., 2013). The negative values indicate counterclockwise circulation. Figure 2.8 shows that residual upwelling of waters onto the continental shelf via the bottom boundary layer, as interior transport onto the shelf is compensated by eddies. In the deep ocean ($> 500\,$m there is a relatively strong residual overturning circulation that is likely associated with bottom intensification of the diapycnal mixing coefficient (McDougall and Ferrari, 2017, *e.g.*).

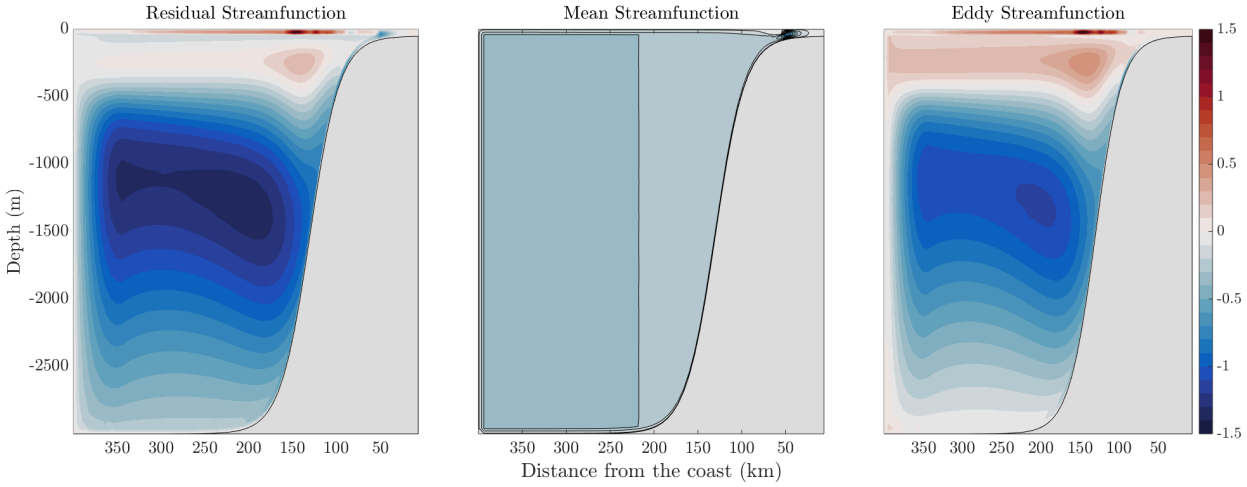

Figure 2.8: Streamfunctions calculated by MAMEBUS. This figure shows the residual streamfunction (left), $\psi^\dagger = \overline{\psi} + \psi^\star$, the mean streamfunction (center) as calculated in Section 2.3.2, and the eddy streamfunction (right) as described in Section 2.3.3. Note that positive values indicate clockwise circulation, whereas negative values indicate counter-clockwise circulation.

2.6.4 Resolution parameter sweep

In this section, we describe the changes in solutions due to model resolution. We chose four different resolutions, and explored the results. Figure 9 shows the solutions of MAMEBUS after 30 model years. Each panel in Figure 2.9 shows the model state in the euphotic zone, averaged over the final 10 years of integration . All resolutions have the same setup and forcing as described in Sections 2.5 and 2.6. The top row shows the potential temperature (θ), the middle row shows the nitrate concentration, and the bottom row shows the phytoplankton concentration. The model grid resolution increases from left to right, with the coarsest simulation run on a grid of 32 points horizontally and vertically, and the highest-resolution simulation run on a grid of 128 points horizontally and vertically.

Increasing the resolution leads to an overall shoaling of nutrients toward the surface. The largest overall change in near-slope nutrient concentration occurs when the resolution

Resolution (Horizontal and Vertical Levels)	Cluster (Single Core)	Laptop
32x32	32 min	22 min
64x64	499 min	401 min
96x96	3295 min (55 hours)	–
128x128	13000 min (9 days)	–

Table 2.6: A table outlining model run times of varying resolution between a computational cluster comprised of Intel Xeon E5-2650 v3 CPUs, and a 2015 Mac Laptop running macOS Catalina (version 10.15.7) for 20 model years, for both computing systems, the model is run on a single core. The highest resolution simulation (128x128 horizontal and vertical levels) was conducted on the cluster only due to computational constraints on a laptop.

doubles from 32 to 64 horizontal points and vertical levels. Increasing the resolution beyond a 64x64 grid does not substantially change the horizontal distribution of phytoplankton . As referenced in Table 2.6, doubling the resolution increases the model run time by a multiple of approximately 20. Thus while the model can practically be run at higher resolution, our tests show that intermediate resolution (64 horizontal and vertical levels) is sufficient to produce a favorable comparison with in situ data, without substantially increasing the computation time.

2.7 Discussion and Future Work

In this paper, we described the formulation, implementation, and main features of MAME-BUS, an idealized, meridionally-averaged model of eastern boundary upwelling systems. The solutions are determined by a general evolution equations for materially conserved tracers (Section 2.3) and the fluid momentum equations under the time-dependent turbulent thermal wind (T3W) approximation (Dauhajre and McWilliams, 2018). It includes parameterizations of mesoscale eddy transfer and surface and bottom boundary layer mixing (Section 2.3.3),

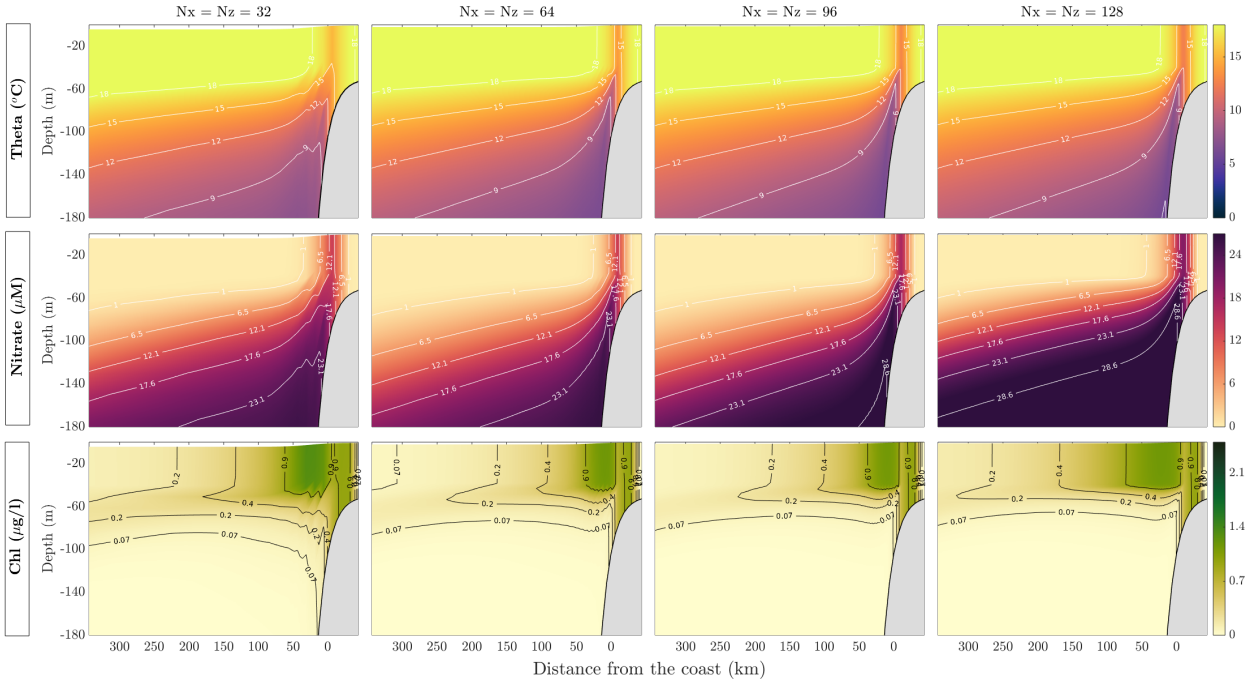

Figure 2.9: This figure shows the model output of temperature, nitrate, and chloroplyll with varying resolution. The model was run for 30 years, and solutions shown are averaged over the final 10 years of the model run.

and a simple ecosystem formulation (Section 2.3.4). We further detailed the algorithms and discretizations implemented in the model (Section 2.4), and discussed reference model inputs and solutions (Section 2.5). Finally we performed a preliminary validation based on observations from the California Current system, and we discussed the sensitivity of the model to horizontal and vertical resolution (Section 2.6).

MAMEBUS represents a simple, physically-consistent tool in which to test and tune a variety of physical parameterizations and ecosystem model formulations. The ultimate goals of this research include exploration of physical-biogeochemical interactions in EBUS, mechanistic understanding of the factors that control cross-shore gradients in biogeochemical and ecological properties, and investigation of the processes that drive differences between distinct EBUS.

Because of the 2D framework, we acknowledge shortcomings to the model formulation, including physical aspects like intensification of upwelling around topographic features, for example resulting from variations in the wind-stress curl (Castelao and Luo, 2018) or fine-scale ocean dynamics. Furthermore, while we parameterize the effect of mesoscale eddies on circulation, we do not account for submesoscale eddies on the shelf, which could play an important role in tracer transport (Dauhajre and McWilliams, 2018). We also do not explicitly represent breaking internal waves and tides on the shelf, which may play an important role in dissipating energy and mixing tracers when the water column is shallow (Lamb, 2014).

In future studies, we plan to use MAMEBUS to explore the effect of physical drivers such as wind stress, bathymetry, stratification, and eddies, in controlling the zonal distribution of phytoplankton and food web processes, as informed by a size-structured ecosystem model. Furthermore, we plan to expand upon the physical framework in this paper by expanding eddy parameterizations to include the effect of submesoscale eddies on the shelf, where the mesoscale eddy activity is inhibited. An aspect of MAMEBUS that requires further investigation is the effect of meridional pressure gradients, which we neglected in our reference solutions in Section 2.6. In reality, the presence of along-shore pressure gradients may support

interior across-shore transport away from the surface and bottom boundary layers, with the potential to reshape the coastal ecosystem.

With its limited computational cost, MAMEBUS can be used to investigate a wide parameter space in EBUSs, and determine their sensitivity to a range of perturbations in major physical forcings, from changes in wind-stress to increasing buoyancy forcing associated with climate change (Rykaczewski and Dunne, 2010; Sarmiento et al., 1998). Furthermore, by allowing coupling to a variety of biogeochemical and ecosystem models, MAMEBUS can be used to inform comprehensive regional models (Shchepetkin and McWilliams, 2005), for which computational costs preclude exhaustive sensitivity studies.

2.8 Appendices from Chapter 2: Moscoso et al. (2021)

2.9 Decomposing mesoscale eddy advective/diffusive fluxes

In this Appendix we discuss the partitioning of the mesoscale eddy tracer flux into components due to advection and isopycnal diffusion, used in Section 2.3.1 to derive MAMEBUS's central tracer evolution equation, (2.9). We show that the eddy tracer flux, $\overline{\mathbf{u}'c'}$, can be arbitrarily decomposed into components directed along mean buoyancy surfaces and along mean tracer surfaces. These components will later be associated with eddy advection and isopycnal stirring, respectively.

The effect of mesoscale eddies on the averaged tracer concentrations is given by the convergence of the eddy tracer flux (2.8),

$$\left.\frac{\partial \overline{c}}{\partial t}\right|_{\text{eddies}} = -\nabla \cdot \left(\overline{\mathbf{u}'c'}\right), \tag{2.132}$$

and appears on the right-hand side of (2.6). Being quasi-adiabatic flows, mesoscale eddies serve to stir material tracers along isopycnal surfaces; this corresponds to an eddy tracer flux directed along buoyancy surfaces (Redi, 1982). Eddies also induce a "bolus" advective transfer of tracers, a generalized "Stokes drift" that corresponds to an eddy tracer flux

directed along mean tracer iso-surfaces (Gent and McWilliams, 1990). Both of these effects are routinely parameterized in general circulation models (Griffies, 1998, 2018). To partition the eddy tracer flux between isopycnal stirring and bolus advection, we therefore pose a decomposition of $\overline{\mathbf{u}'c'}$ into components directed along mean isopycnals and along mean tracer surfaces, respectively,

$$\overline{\mathbf{u}'c'} = \alpha_c \hat{\boldsymbol{\tau}}_c + \alpha_b \hat{\boldsymbol{\tau}}_b. \tag{2.133}$$

Here $\hat{\boldsymbol{\tau}}_c$ and $\hat{\boldsymbol{\tau}}_b$ are unit vectors that point along mean $\overline{c}$ surfaces and along mean $\overline{b}$ surfaces, respectively:

$$\hat{\boldsymbol{\tau}}_c = \hat{\mathbf{y}} \times \frac{\nabla \overline{c}}{\|\nabla \overline{c}\|}, \qquad \hat{\boldsymbol{\tau}}_b = \hat{\mathbf{y}} \times \frac{\nabla \overline{b}}{\|\nabla \overline{b}\|}. \tag{2.134}$$

Note that the x-components of $\hat{\boldsymbol{\tau}}_b$ and $\hat{\boldsymbol{\tau}}_c$ are positive provided that $\overline{b}$ and $\overline{c}$ increase monotonically upward. By taking the vector cross products $\hat{\boldsymbol{\tau}}_c \times$ (2.133) and $\hat{\boldsymbol{\tau}}_b \times$ (2.133), we can solve for the vector lengths α_c and α_b,

$$\alpha_c = \frac{\overline{\mathbf{u}'c'} \times \hat{\boldsymbol{\tau}}_b}{\hat{\boldsymbol{\tau}}_c \times \hat{\boldsymbol{\tau}}_b}, \qquad \alpha_b = \frac{\overline{\mathbf{u}'c'} \times \hat{\boldsymbol{\tau}}_c}{\hat{\boldsymbol{\tau}}_b \times \hat{\boldsymbol{\tau}}_c}. \tag{2.135}$$

Then, using Equations (2.133)–(2.135), we write Equation (2.132) as

$$\left.\frac{\partial \overline{c}}{\partial t}\right|_{\text{eddies}} = -\left(\nabla \times \frac{\alpha_c}{\|\nabla \overline{c}\|}\hat{\mathbf{y}}\right) \cdot \nabla \overline{c} - \nabla \cdot \left(\frac{\alpha_b}{(\nabla \overline{c} \cdot \hat{\boldsymbol{\tau}}_b)} (\nabla \overline{c} \cdot \hat{\boldsymbol{\tau}}_b) \hat{\boldsymbol{\tau}}_b\right). \tag{2.136}$$

The first term on the right-hand side of (2.136) takes the form of an advection operator, in which we can identify the eddy streamfunction

$$\psi^\star = \frac{\alpha_c}{\|\nabla \overline{c}\|} = \frac{\overline{\mathbf{u}'c'} \cdot \nabla b}{\nabla \overline{c} \times \nabla b}. \tag{2.137}$$

Note that this definition is ill-defined in the limit $\nabla \overline{c} \times \nabla b \to 0$; in this limit $\hat{\boldsymbol{\tau}}_b$ and $\hat{\boldsymbol{\tau}}_c$ are parallel, the eddy tracer flux is purely advective, and the streamfunction becomes

$$\psi^\star = \frac{\overline{\mathbf{u}'c'} \times \nabla \overline{c}}{\|\nabla \overline{c}\|^2}. \tag{2.138}$$

The second term on the right-hand side of (2.136) has been written in the form of the divergence of a flux along mean buoyancy surfaces, with the isopycnal gradient operator (see

Section 2.3.1) appearing explicitly as

$$\nabla_{\|} \equiv (\nabla \overline{c} \cdot \hat{\boldsymbol{\tau}}_b)\hat{\boldsymbol{\tau}}_b. \tag{2.139}$$

We can then identify the isopycnal diffusivity κ_{iso} as

$$\kappa_{\text{iso}} = -\frac{\alpha_b}{(\nabla \overline{c} \cdot \hat{\boldsymbol{\tau}}_b)} = -(\overline{\mathbf{u}'c'} \cdot \nabla \overline{c}) \frac{\left\|\nabla \overline{b}\right\|^2}{\left\|\nabla \overline{b} \times \nabla \overline{c}\right\|^2} = -\frac{\overline{\mathbf{u}'c'} \cdot \nabla \overline{c}}{\left\|\nabla \overline{c}\right\|^2 \cos^2 \theta}, \tag{2.140}$$

where θ is the angle between the vectors $\nabla \overline{b}$ and $\nabla \overline{c}$.

While the above derivation is general, for application in MAMEBUS we must make assumptions about the eddy tracer fluxes. Specifically, we assume: (i) that approximately identical eddy streamfunctions $\psi^\star$ advect each different model tracer, and (ii) that the isopycnal diffusivity is positive (*i.e.* that eddy tracer fluxes are always directed down the mean tracer gradients), and (iii) that the isopycnal diffusivity is approximately equal for different model tracers. These assumptions are satisfied in the limit of small-amplitude fluctuations $\mathbf{u}'$ and c' (Plumb, 1979; Plumb and Ferrari, 2005b).

2.10 Derivation of time variable Adams-Bashforth methods

For a given tracer defined with an associated time tendency equation of the form,

$$\frac{\partial c}{\partial t} = f(t, c(t)). \tag{2.141}$$

We integrate Equation (2.141) in time from $[t_{n+2}, t_{n+1}]$,

$$\int_{t_{n+1}}^{t_{n+2}} \frac{\partial c}{\partial t} d\tau = \int_{t_{n+1}}^{t_{n+2}} f(\tau, c(\tau)) d\tau. \tag{2.142}$$

By the fundamental theorem of calculus,

$$c(t_{n+2}) - c(t_{n+1}) = \int_{t_{n+1}}^{t_{n+2}} f(\tau, c(\tau)) d\tau. \tag{2.143}$$

We interpolate the right hand side using a Lagrange polynomial of the form:

$$p(\tau) = \frac{\tau - t_{n+1}}{t_n - t_{n+1}} f(t_n, c(t_n)) + \frac{\tau - t_n}{t_{n+1} - t_n} f(t_{n+1}, c(t_{n+1})). \tag{2.144}$$

Then using 2.144 and substituting it into 2.143, we have,

$$\begin{aligned}\int_{t_{n+1}}^{t_{n+2}} f(\tau, c(\tau))d\tau &= \int_{t_{n+1}}^{t_{n+2}} p(\tau)d\tau \\ &= \int_{t_{n+1}}^{t_{n+2}} \left(\frac{\tau - t_{n+1}}{t_n - t_{n+1}} f(t_n, c(t_n)) + \frac{\tau - t_n}{t_{n+1} - t_n} f(t_{n+1}, c(t_{n+1})) \right) d\tau \\ &= \frac{1}{2} \left[\frac{(\tau - t_{n+1})^2}{t_n - t_{n+1}} f(t_n, c(t_n)) + \frac{(\tau - t_n)^2}{t_{n+1} - t_n} f(t_{n+1}, c(t_{n+1})) \right]_{t_{n+1}}^{t_{n+2}}.\end{aligned}$$

Defining $\Delta t_{n+1} = t_{n+1} - t_n$, we obtain

$$\begin{aligned}\int_{t_{n+1}}^{t_{n+2}} f(\tau, c(\tau))d\tau = \frac{\Delta t_{n+2}}{2\Delta t_{n+1}} &(2f(t_{n+1}, c(t_{n+1}))\Delta t_{n+1} \\ &+ f(t_{n+1}, c(t_{n+1}))\Delta t_{n+2} - f(t_n, c(t_n))\Delta t_{n+2}) .\end{aligned} \tag{2.145}$$

Substituting Equation (2.143) into Equation (2.145) yields the full ABII time stepping scheme, given by Equation (2.96).

For higher order AB methods, we consider a s-th order Lagrange polynomial of the form,

$$p(\tau) = \sum_{m=0}^{s-1} p_m(\tau) f(t_{n+m}, c(t_{n+m})) \tag{2.146}$$

$$p_m(\tau) = \prod_{\substack{l=0 \\ l \neq m}}^{s-1} \frac{\tau - t_{n+l}}{t_{n+m} - t_{n+l}} \tag{2.147}$$

where setting $s = 3$ as the number of known points in the interpolating polynomial results in the ABIII method. Then, $s - 1$ is the degree of the polynomial. The general form of higher order AB methods is,

$$c(t_{n+s}) - c(t_{n+s-1}) = \int_{t+s-1}^{t+s} \sum_{m=0}^{s-1} p_m(\tau) f(t_{n+m}, c(t_{n+m}))d\tau. \tag{2.148}$$

The algebra to solve for the full discrete form of the ABIII method follows the derivation of the ABII method above. The solution to the integration in Equation (2.148) is given by Equation (2.95).

2.11 Comparison of boundary layer parameterizations with Ferrari et al. (2008)

Our representation of eddy advection and isopycnal stirring in the surface mixed layer (SML) and bottom boundary layer (BBL) is adapted from Ferrari et al. (2008), and is described in Section 2.3.3.2. We now directly compare our SML/BBL scheme against that of Ferrari et al. (2008) to highlight the key differences.

As discussed in Section 2.3.3.2 our SML scheme leads to the same eddy streamfunction as that of Ferrari et al. (2008), given by (2.29). In contrast, the residual eddy tracer flux in the SML differs as follows

$$(\kappa_{\rm iso}\nabla_{\|}\overline{c})_{\rm FMCD} = \kappa_{\rm iso}\left(\overline{c}_x + S_{\rm sml}\overline{c}_z\right)\hat{\mathbf{x}} + \kappa_{\rm iso}\left(S_{\rm sml}\overline{c}_x + S_{\rm sml}S_{\rm int}\overline{c}_z\right)\hat{\mathbf{z}}, \tag{2.149a}$$

$$\kappa_{\rm iso}\nabla_{\|}\overline{c} = \kappa_{\rm iso}\left(\overline{c}_x + S_{\rm sml}\overline{c}_z\right)\hat{\mathbf{x}} + \kappa_{\rm iso}\left(S_{\rm sml}\overline{c}_x + S_{\rm sml}^2\overline{c}_z\right)\hat{\mathbf{z}}, \tag{2.149b}$$

where "FMCD" denotes the formulation of Ferrari et al. (2008). Thus our Equation (2.149b) differs from Equation (2.149a) only by the replacement $S_{\rm int}$ by $S_{\rm sml}$ in the vertical eddy residual tracer flux. A drawback of using $S_{\rm int}$ is that typically the vertical buoyancy gradient is very small in the SML, so the form (2.149a) may not be numerically stable. Ferrari et al. (2008) propose a modification of the vertical component of the tracer residual eddy flux to avoid dividing by small vertical buoyancy gradients in the mixed layer,

$$(\kappa_{\rm iso}\nabla_{\|}\overline{c})_{\rm FMCD}\cdot\hat{\mathbf{z}} = -\kappa_{\rm iso}\hat{G}(z)\left(-\frac{\overline{b}_x\overline{b}_z}{\overline{b}_z|^2_{z=-H_{\rm sml}}}\overline{c}_x + \frac{\overline{b}_x^2}{\overline{b}_z|^2_{z=-H_{\rm sml}}}\overline{c}_z\right)\hat{\mathbf{z}}, \tag{2.150}$$

However, this alternative breaks the symmetry of the diffusion tensor, and requires the introduction of an additional vertical structure function, $\hat{G}(z)$. Our formulation, Equation (2.151b)m retains the symmetry of the stress tensor and preserves continuity of the vertical flux and its derivative at $z = -H_{\rm sml}$ with the same structure function $G_{\rm sml}(z)$ (see Section 2.3.3.2). It is also simpler to implement, as both the streamfunction (2.29) and the residual eddy flux (2.149b) can be written succinctly in terms of the effective slope (2.28).

Another difference between our formulation and that of Ferrari et al. (2008) arises in the eddy stirring of buoyancy in the SML,

$$(\kappa_{\rm iso}\nabla_\parallel \overline{b})_{\rm FMCD} = \kappa_{\rm iso}\left(\overline{b}_x + S_{\rm sml}\overline{b}_z\right)\hat{\mathbf{x}}, \tag{2.151a}$$

$$\kappa_{\rm iso}\nabla_\parallel \overline{b} = \kappa_{\rm iso}\left(\overline{b}_x + S_{\rm sml}\overline{b}_z\right)\hat{\mathbf{x}} + \kappa_{\rm iso}\left(S_{\rm sml}\overline{b}_x + S^2_{\rm sml}\overline{b}_z\right)\hat{\mathbf{z}}. \tag{2.151b}$$

The Ferrari et al. (2008) residual eddy buoyancy flux has no vertical component, whereas ours does. This impacts the rate of available potential energy release in the SML by modifying the total vertical eddy buoyancy flux,

$$\overline{w'b'}_{\rm FMCD} = \kappa_{\rm gm}G_{\rm sml}(z)\frac{\overline{b}_x^2}{\overline{b}_z|_{z=-H_{\rm sml}}}, \tag{2.152a}$$

$$\overline{w'b'} = \kappa_{\rm gm}G_{\rm sml}(z)\frac{\overline{b}_x^2}{\overline{b}_z|_{z=-H_{\rm sml}}} + \kappa_{\rm iso}G_{\rm sml}(z)\frac{\overline{b}_x^2}{\overline{b}_z|_{z=-H_{\rm sml}}}\left(1 - G_{\rm sml}(z)\frac{\overline{b}_z}{\overline{b}_z|_{z=-H_{\rm sml}}}\right), \tag{2.152b}$$

The key difference here is that our version (2.152b) typically releases more potential energy, and is not strictly positive definite; if $\overline{b}_z \gg \overline{b}_z|_{z=-H_{\rm sml}}$ then in principle $\overline{w'b'}$ may be negative. This corresponds to creation of potential energy, whereas previous studies suggest that potential energy should be consistently released in the SML (Colas et al., 2013). However, by construction, the vertical derivative of this term is zero at $Z = -H_{\rm sml}$, and in any practical case $\overline{b}_z$ will be smaller than $\overline{b}_z|_{z=-H_{\rm sml}}$ throughout the boundary layer. This suggests that if the vertical eddy lengthscale λ is positive $\overline{b}_z z < 0$ then our scheme releases potential energy everywhere. Note also that the GM component of the vertical eddy buoyancy flux always releases potential energy.

Finally, we compare the horizontal component of the eddy buoyancy flux in the SML,

$$\overline{u'b'}_{\rm FMCD} = -\kappa_{\rm gm}\overline{b}_x, \tag{2.153a}$$

$$\overline{u'b'} = -\kappa_{\rm iso}\overline{b}_x + (\kappa_{\rm gm} - \kappa_{\rm iso})S_{\rm sml}\overline{b}_z. \tag{2.153b}$$

Whereas the Ferrari et al. (2008) scheme preserves strict lateral downgradient diffusion, this is only true in our scheme if $\kappa_{\rm gm} = \kappa_{\rm iso}$.

Further to this comparison with the formulation of Ferrari et al. (2008), we note that the fluxes discussed above differ substantially in the BBL over sloping topography. For example, the vertical buoyancy flux becomes

$$\overline{w'b'} = \kappa_{\rm gm} G_{\rm bbl}(z) \frac{\overline{b}_x^2}{\overline{b}_z|_{z=\overline{\eta}_b+H_{\rm bbl}}} - \kappa_{\rm iso} \widetilde{S}_e \overline{b}_z (\widetilde{S}_e - S_{\rm int}) \tag{2.154}$$

Thus in general the eddy buoyancy flux will act to create potential energy ($\overline{w'b'} < 0$) unless the isopycnal slope $S_{\rm int}$ is of the same sign as the bottom slope and larger in magnitude. In order to avoid this, it would be necessary to set $\kappa_{\rm iso} = 0$ throughout the BBL. This is a separate consideration from the orientation of the residual flux vector, which must certainly lie parallel to the topography if the diffusivity is nonzero.

CHAPTER 3

Controls and Characteristics of Biomass Quantization in Size-Structured Planktonic Ecosystem Models

This section contains the manuscript, Moscoso et al. (2022) without any changes.

3.1 Abstract

Strong relationships between size and other traits have long motivated studies of the size structure and dynamics of planktonic food webs. Size structured ecosystem models (SSEMs) are often used to represent the behavior of these ecosystems, with organism size as a first order approximation of the axis of biological diversity. Previous studies using SSEMs have reported the emergence of localized "peaks" in the size spectrum, a phenomenon that will be referred to in this study as "quantization". However, SSEMs that are used routinely in Earth System Models (ESMs), they tend to be too coarsely discretized to resolve quantization. Observational studies of plankton biomass have also shown qualitatively similar patterns, with localized peaks along the size spectrum. The conditions under which quantization emerges and the ecosystem parameters that control the locations of the biomass "peaks" along the size spectrum have not been systematically explored. This study serves to simultaneously advance our understanding of the constraints on quantization in size-structured ecosystems, and to suggest an approach to discretizing SSEMs that leverages emergent quantization to select a greatly reduced number of size classes. A size-structured model of the pelagic food web, similar to those implemented in global models, is used to investigate the sensitivity of

biomass peaks to predator-prey interactions, and nutrient forcing. This study shows that the location of biomass peaks along the size spectrum is strongly controlled by the the size selectivity of predation, and the location of biomass peaks along the size spectrum is less sensitive to variations in nutrient supply, external ecosystem forcing, and vertical hetereogeneity. Taking advantage of a robust localization of biomass peaks, the dynamics of a continuous planktonic size spectrum to be represented using a few selected size classes, corresponding to locations of the peaks along the size spectrum. These findings offer an insight on how to approach discretization of size structured ecosystem model in Earth system models.

3.2 Introduction

Phytoplankton form the base of the marine food-web, and understanding their community structure can aid in predicting the composition and productivity of higher trophic levels and top predators (Stock et al., 2017). Community composition depends on complex interactions between the physical environment, resource availability, competition, and predation, which in turn determine patterns of productivity (Hutchinson, 1961; Hillebrand and Azovsky, 2001; Righetti et al., 2019; Mousing et al., 2016; Steele and Henderson, 1992; Vallina et al., 2014).

Numerical and theoretical models have long been used as a tool to understand plankton behavior and interactions in the context of physical drivers, ecology, and food-web dynamics (Armstrong and McGehee, 1980; Follows and Dutkiewicz, 2011; Adjou et al., 2012; Ward et al., 2014; Lévy et al., 2014). However, models often lack levels of diversity found in oceanic plankton communities (Loeuille and Loreau, 2005). Instead of explicitly capturing large-scale biodiversity, specific ecological and functional traits are often chosen to represent planktonic diversity in models (Follows and Dutkiewicz, 2011). Size has long been used to model planktonic diversity (**?**Poulin and Franks, 2010a; Banas, 2011; Ward et al., 2012; Sauterey et al., 2017) because of strong empirical relationships between size and other physiological and ecological traits (Andersen et al., 2016; Litchman et al., 2007). More broadly, size

mechanistically controls a variety of ecological processes, from resource uptake strategies, to predator-prey interactions across trophic levels (Andersen et al., 2016).

The distribution of dominant phytoplankton sizes is, broadly speaking, a function of resource availability and predation, i.e., bottom-up and top-down processes (McQueen et al., 1986; Lehman, 1991; Banse, 1994; Verity and Smetacek, 1996; Chenillat et al., 2013). In oligotrophic environments, small cells are responsible for most of the total phytoplankton biomass (Chisholm, 1992; Partensky et al., 1999; Worden et al., 2004). In contrast, in productive regions, characterized by high chlorophyll and nutrient concentrations, large cells are responsible for a substantial fraction of phytoplankton blooms and biomass variability (Chavez, 1989; Chisholm, 1992; Cavender-Bares et al., 2001; Venrick, 2002). Ecosystems that are dominated by low levels of surface nutrients and small phytoplankton size are characterized by fast nutrient cycling near the surface (Fowler et al., 2020; Partensky et al., 1999). This is a consequence of rapid uptake rates and strong grazing pressures (Tang, 1995). In contrast, ecosystems with high levels of surface nutrients and large phytoplankton size are characterized by weak recycling at the surface and significant export of sinking organic matter, supporting the oceanic carbon pump (Tréguer et al., 2018; Boyd et al., 2019). Large phytoplankton require more macro-nutrients and are usually characterized by larger half saturation constants, and hence slower uptake rates, compared to smaller organisms. However, they benefit from lower grazing pressure as a consequence of their size (Tang, 1995; Hansen et al., 1994), especially during bloom conditions (Behrenfeld and Boss, 2014). Zooplankton follow patterns of food uptake and limitation as a function of size that are similar to phytoplankton (Hansen et al., 1994). Small zooplankton tend to quickly graze small phytoplankton, whereas large zooplankton grazing rates are often outpaced by large phytoplankton, allowing for the prevalence of large phytoplankton species in nutrient-rich regions (Fuchs and Franks, 2010; Ingrid et al., 1996; Leibold, 1996). This phenomenon favors growth of intermediate and large phytoplankton, even with slower uptake rates relative to their smaller counterparts (Terseleer et al., 2014).

Previous observational studies of ecosystem dynamics have shown that phytoplankton size and total biomass follow a power-law size spectrum with small phytoplankton contributing to a large percentage of the biomass (Partensky et al., 1999; Franks, 2002; Zhou and Huntley, 1997). Sheldon et al. (1972) extended this spectrum to suggest a universal power-law relationship for ocean food-webs between the size of an organism and its standing biomass stock. However, simple power-law relationships have been shown to break down in regions with high nutrient concentrations (e.g., coastal margins) (Hood et al., 1991; Huete-Ortega et al., 2014; Jonasz and Fournier, 1996; Schartau et al., 2010; Worden et al., 2004; Zubkov et al., 2000), which show intermediate peaks in biomass along the size spectrum that tend to aggregate around specific phytoplankton sizes (Cavender-Bares et al., 2001; Karp-Boss et al., 2007; Giometto et al., 2013). We refer to this phenomenon as "quantization" of the phytoplankton size spectrum.

Quantization in plankton size spectra has been previously captured and reported in numerical models (Banas, 2011; Sauterey et al., 2017). Trait-based models like size structured ecosystem models (SSEMs) allow for increased understanding of planktonic dynamics in the context of resource competition (**?**Follows and Dutkiewicz, 2011). The choice to model dynamics with respect to size can lead to quantization in biomass (Loeuille and Loreau, 2005), and has been shown to be affected by the functional formulation of grazing (Banas, 2011). Specifically, Banas (2011) note that varying the width of the "window" of phytoplankton sizes that can be grazed by a given zooplankton size class changes the number of quantized "peaks" that emerge in the resulting biomass size spectra. A smaller grazing window, corresponding to more specialized zooplankton grazing, allows the coexistence of a larger number of size peaks in the phytoplankton and zooplankton size spectrum. Furthermore, in ecosystem models where each zooplankton size class grazes only a single phytoplankton size class, i.e. when grazing is extremely selective, quantization does not occur (e.g. Franks (2002)). Size structured ecosystem models of higher complexity, such as that presented by Ward et al. (2012), show that while small phytoplankton are always globally present, in

agreement with observations, larger phytoplankton are generally found in regions with high nutrient concentrations, such as near continental margins. However, this model does not show size quantization, likely because of the relatively coarse resolution of phytoplankton size spectra. Thus, it remains unclear to what extent quantization is a robust feature of size-structured ecosystems, and what factors determine its emergence and characteristics under typical oceanic conditions.

In this study, we investigate size quantization in a minimal complexity size-structured nutrient, phytoplankton, zooplankton, detritus (NPZD) model, similar to models used in previous work (Banas, 2011; Ward et al., 2012). We run a series of experiments to understand how the model parameters control quantization and the location of the biomass peaks along the size spectrum in both zero- and one-dimensional (0D and 1D) environments. We identify a few salient parameters that have been shown previously to be important in capturing ecosystem dynamics, these include the nutrient supply (Sarmiento and Gruber, 2006), the grazing profile and preference (Banas, 2011; Chenillat et al., 2021), and size resolution as a proxy of diversity, (Henson et al., 2021). As a consequence of robust quantization in the solutions presented in the following sections, we are able to propose a reduction in order in size space, and suggest that planktonic ecosystems can be effectively modeled using a small number of representative size classes, providing additional theoretical support for a widespread practice in ecosystem modeling.

The rest of the paper is organized as follows: In Section 2, we describe the size structured ecosystem model. In Section 3, we investigate the impacts of top-down and bottom-up controls on planktonic size spectra through a series of experiments that explore the ecosystem response to change in grazing strategies and nutrient supply, respectively. In Section 4, we show that quantization is robust in 1D, and that relationships between top-down and bottom-up control found in 0D generalize to 1D solutions. In Section 5, we take advantage of robust quantization in 0D and 1D and demonstrate a method in which SSEMs can be reduced to a few carefully chosen size classes that represent the planktonic ecosystem when a large

number of phytoplantkon size classes are not feasible to use (eg. in high resolution regional models or ESMs). Finally, in Section 6 we discuss the results and conclude the paper.

3.3 Size-Structured Ecosystem Model

3.3.1 Model Rationale

We use a size structured ecosystem model based on those developed by Banas (2011) and Ward et al. (2012), and representative of commonly used size-structured models (Armstrong, 1994; Poulin and Franks, 2010a; Follows et al., 2007; Dutkiewicz et al., 2012). Size is the primary axis of diversity, reflecting robust allometric relationship between an organisms size and resource encounter strategies (e.g. nutrient acquisition and grazing) (Follows et al., 2007; Litchman et al., 2007; Tang, 1995; Eppley et al., 1969; Hansen et al., 1994; Klausmeier et al., 2020). Using individual size as the axis of diversity can further reduce the dimensionality of the model's parameter space (Follows and Dutkiewicz, 2011). While plankton diversity has been thought to be sustained by niche selection and trait adaption (Hutchinson, 1961; Sommer, 1989), modeled planktonic ecosystems have been shown to collapse to a few representative groups as a consequence of competition, (Sauterey et al., 2017; Banas, 2011; Loeuille and Loreau, 2005) even with models that simulate many species (Merico et al., 2014; Bruggeman and Kooijman, 2007; Follows et al., 2007). Therefore, we use a single functional axis of diversity in size as the basis for our ecosystem model. Aspects of the model such as nutrient uptake, grazing, and mortality are a combination of elements from models presented by Banas (2011) and Ward et al. (2012) and discussed in more detail below. Trait (i.e., size) diffusion is formulated following Sauterey et al. (2017).

While we cast ecosystem dynamics in terms of size, many ecosystem models often include a representation of functional diversity (e.g. Moore et al., 2001; Quere et al., 2005), which groups species and taxa with similar nutrient uptake requirements or strategies to form a single functional group — e.g., cells that require silicon are modeled as the functional diatom

group. Thus, each functional group provides a unique control on a biogeochemical pathway. While models based on functional groups have had success in predicting patterns of plankton distribution and productivity on a global scale (Gregg and Casey, 2007), they often require increased complexity relative to trait-based approaches (Follows and Dutkiewicz, 2011). Another challenge with this modeling approach is choosing the appropriate representation of functional groups to resolve the diversity in an ecosystem (Hood et al., 2006; Quere et al., 2005). Finally, functional groups are increasingly represented along a spectrum of different sizes (Ward et al., 2012; Dutkiewicz et al., 2020). Therefore, as a result of both reduced model parameter space and complexity, and a simplicity in representing ecosystem dynamics with allometric relationships, we focus on size alone as our primary axis of variability, with a single nutrient group and two size spectra of phytoplankton and zooplankton.

In the model, allometric relationships control phytoplankton nutrient uptake and limitation, zooplankton grazing rates, and size preference in predator-prey interactions (see equations 3.6a-3.6b and 3.10a-3.10b). This formulation is informed by studies that show that smaller phytoplankton have faster nutrient assimilation rates and are less nutrient limited as a consequence of their small surface area to volume ratio (Eppley et al., 1969; Tang, 1995). On the other hand, large phytoplankton are more nutrient limited and have slower uptake rates. Additionally, smaller zooplankton have faster grazing rates compared to larger zooplankton (Hansen et al., 1994). We omit size dependence on zooplankton half-saturation rates in this model, however previous work by Edwards et al. (2012) has shown that half saturation rates with respect to size exhibit allometric behavior. This choice in our design is to minimize the number of allometrically defined variables and dependencies, as this other size structured ecosystem models include the same assumption.

Grazing dynamics is modeled after broad patterns of predator-prey size interactions. Here, we assume that small zooplankton graze prey of approximately the same size, while larger zooplankton prefer prey smaller than their own size (Hansen et al., 1994). While this is not the case for all zooplankton, and often depends on specific grazing strategies (Kiørboe,

2011), this functional form of grazing is commonly adopted in models (Moore et al., 2001; Poulin and Franks, 2010a; Banas, 2011; Ward et al., 2012) with well documented grazing rates and preferential prey size (Hansen et al., 1994). Other representations of grazing includes the so-called "kill-the-winner" formulation, in which switching between optimal prey groups occurs, depending on prey abundance (Vallina et al., 2014). However, this formulation is dependent on many parameters that need be finely tuned. For the sake of simplicity, we model in this study a process referred to as "agnostic feeding" (Gentleman et al., 2003), which assumes that grazing pressures are constant between prey classes and, in this formulation, distributed only as a function of size.

Finally, while zooplankton and phytoplankton are separated into various sizes classes, detritus is collated as a single particulate group. While this simplification limits the use of the model to investigate the effect of plankton size structure on particle export and remineralization (Dunne et al., 2005; Richardson and Jackson, 2007), the detritus group could be easily expanded to incorporate variable size classes controlled by allometric relationships. However, uncertainty remains on the robustness of such relationships; for example, Iversen and Lampitt (2020) question the usefulness of particle size as an indicator of sinking speed, while other studies support it (Cael et al., 2021). Because the focus of this paper is plankton dynamics and size quantization, we opt to combine all detritus into a single sinking group (in 1D) for simplicity.

In the following, we outline each component of the model. Dependence on size is implicit, with the exception of size diffusion, and all functions in the model are written with respect to N, P, Z, and D. A schematic of the model is shown in Fig. 3.1; model parameters are summarized in Table 3.1.

3.3.2 Evolution Equations

The following mass conservation equations express the time tendencies for a single nutrient akin to nitrate (N), phytoplankton (P), zooplankton (Z), and detritus (D), all expressed in

units of nutrient (i.e., nitrogen) concentration (mmol m^{-3}). The number of phytoplankton size classes is n_p, and the number of zooplankton size classes is n_z. This model allows for an arbitrary number of zooplankton and phytoplankton sizes. The indexing variables for phytoplankton and zooplankton size classes are i and j respectively. Each evolution equation includes a component of physical forcing. In 0D, the physical forcing is a constant nutrient supply in the N equation. In 1D, nutrients are restored to an idealized profile, and all biogeochemical tracers are mixed by vertical diffusion.

The nutrient concentration N evolves in response to uptake by phytoplankton, remineralization, physical forcing:

$$\frac{\partial N}{\partial t} = \underbrace{\Gamma(N)}_{\text{Physical Forcing}} - \underbrace{\sum_{i}^{n_p} \mathcal{U}\left(N, P_i\right)}_{\text{Uptake by phytoplankton}} + \underbrace{\mathcal{R}(D).}_{\text{Remineralization}} \tag{3.1}$$

In 0D, physical nutrient supply takes a constant value (Section **??**), while in 1D it is calculated via a restoring term (Section 3.3.8). In 1D, uptake of nutrients has additional functional dependencies on temperature and light.

The phytoplankton concentration evolves in response to nutrient uptake, grazing by zooplankton, linear mortality, and size diffusion:

$$\begin{aligned}\frac{\partial P_i}{\partial t} = & \underbrace{\Gamma(P)}_{\text{Physical Forcing}} + \underbrace{\sum_{i}^{n_p} \mathcal{U}\left(N, P\right)}_{\text{Uptake by phytoplankton}} - \underbrace{\sum_{j}^{n_z} G\left(Z_j, P_i\right)}_{\text{Grazing by zooplankton}} \\ & - \underbrace{\mathcal{M}_p\left(P_i\right)}_{\text{Mortality}} + \underbrace{\varphi \frac{\partial^2}{\partial \left(\log_{10} \ell_i\right)^2} P_i}_{\text{Size diffusion}},\end{aligned} \tag{3.2}$$

where the length of the i-th phytoplankton size is denoted as ℓ_i. Size diffusion in this model allows for small amounts of trait mutation and variability between phytoplankton and zooplankton along the size spectra (Sauterey et al., 2017), with the diffusion coefficient denoted as φ. Size diffusion is calculated in log-space, and described in Section 3.3.7. This addition to the SSEM captures the ability of plankton to adjust their size as a mechanism for niche selection (Merico et al., 2014).

The zooplankton concentration evolves in response to grazing of phytoplankton, heterotrophic grazing, a quadratic mortality term, and size diffusion:

$$\frac{\partial Z_j}{\partial t} = \underbrace{\Gamma(Z)}_{\text{Physical Forcing}} + \underbrace{\lambda \sum_i^{n_p} G\left(Z_j, P_i\right)}_{\text{Total uptake of phytoplankon}} - \underbrace{\sum_{j'}^{n_z} S\left(Z_{j'}, Z_j\right)}_{\text{Heterotrophic grazing loss}} + \underbrace{\lambda_s \sum_{j''}^{n_z} S\left(Z_j, Z_{j''}\right)}_{\text{Heterotrophic grazing uptake}} - \underbrace{\mathcal{M}_z\left(Z_j\right)}_{\text{Mortality}} + \underbrace{\varphi \frac{\partial^2}{\partial \left(\log_{10} \ell_j\right)^2} Z_j}_{\text{Size diffusion}}. \tag{3.3}$$

The size of the j-th zooplankton size class is defined as ℓ_j. Both the grazing and self grazing profiles are presented as a functional dependence on the predator and prey, listed respectively in the function. For example, $G(Z, P)$ translates to the grazing of the predator zooplankton on the prey phytoplankton, and $S(Z_{j'}, Z_j)$ corresponds to the grazing of predator zooplankton, $Z_{j'}$ on the j-th zooplankton size class, Z_j.

Finally the detrital concentration evolves in response to egestion or "messy grazing", phyto- and zooplankton mortality, remineralization, and sinking and removal:

$$\frac{\partial D}{\partial t} = \underbrace{\Gamma(D)}_{\text{Physical Forcing}} + \underbrace{(1-\lambda) \sum_i^{n_p} \sum_j^{n_z} G\left(Z_j, P_i\right)}_{\text{Egestion from grazing phytoplankton}} + \underbrace{(1-\lambda_s) \sum_j^{n_z} \sum_{j'}^{n_z} S\left(Z_{j'}, Z_j\right)}_{\text{Egestion from heterotrophic grazing}} + \underbrace{\sum_i^{n_p} \mathcal{M}_p\left(P_i\right)}_{\text{Phytoplankton mortality}} + \underbrace{\sum_j^{n_z} \mathcal{M}_z\left(Z_j\right)}_{\text{Zooplankton mortality}} - \underbrace{\mathcal{R}(D)}_{\text{Remineralization}} - \underbrace{\frac{\partial}{\partial z}\left(w_{\text{sink}} D\right)}_{\text{Particle sinking}}. \tag{3.4}$$

Note that the particle sinking term is calculated as an approximate sinking term in 0D and an explicit sinking term in 1D. The detritus equation serves to close the ecosystem model; in the absence of sources and sinks (nutrient forcing and removal via sinking), the size-structured NPZD model conserves total nutrient.

3.3.3 Nutrient uptake

Uptake is calculated using standard Michaelis-Menten dynamics that allows for a saturating response at high nutrient concentration (Franks, 2002), with additional functional dependence on local irradiance and temperature in 1D (Banas, 2011; Ward et al., 2012). This uptake is formulated as

$$\mathcal{U}(N, P_i) = U_i^{\max} \cdot \mathcal{I}(z, P) \cdot \mathcal{T}(z) \frac{N}{N + k_N^i} P_i, \tag{3.5}$$

where the light and temperature dependence functions are denoted as $\mathcal{I}(z, P)$ and $\mathcal{T}(z)$, respectively. In 0D both functions are set to constants, i.e., $\mathcal{I} = \mathcal{T} = 1$. In 1D, they are defined following equations 3.26a and 3.26b. The maximum uptake rate and half-saturation coefficient are allometric, following Banas (2011):

$$U_i^{\max} = a_u \left(\frac{\ell_i}{\ell_0} \right)^{b_u}, \tag{3.6a}$$

$$k_N^i = a_k \left(\frac{\ell_i}{\ell_0} \right)^{b_k}. \tag{3.6b}$$

All allometric parameters are given in Table 3.1. In this formulation, small phytoplankton benefit from fast uptake rates, and are less nutrient limited. Large phytoplankton, on the other hand, have slower rates of nutrient assimilation and are more nutrient limited (Tang, 1995; Banas, 2011; Ward et al., 2012).

3.3.4 Grazing

The grazing pressure is calculated as a function of predator and prey abundance, with an optimal predator-prey length scale, and a grazing preference represented by the width of a grazing profile. Banas (2011) and Ward et al. (2012) note that formulating the grazing profile in this way assumes that the encounter rate between predator and prey decreases outside of an optimal window, meaning that small prey are hard to detect by large predators. On the other hand, very large prey are less efficient forms of nutrient ingestion. This is

commonly represented by a log-normal distribution, $\vartheta_{j,i}$, about an allometrically defined optimal predator-prey length scale, ℓ^{opt}, with a grazing profile width of $\Delta\ell$.

In this formulation, we assume that zooplankton heterotrophically graze on any plankton (phytoplankton or zooplankton) of a specific size with equal preference. Equations 3.7 and 3.8 model grazing as interactions between a predator zooplankton, Z_j, phytoplankton prey P_i and zooplankton prey $Z_{j'}$. Grazing is formulated using Michaelis-Menten dynamics (Franks, 2002; Banas, 2011; Ward et al., 2012) and depends on the total stock of prey plankton B_j, and half saturation coefficient k_p. Prey refuge is defined by equations 3.12a–3.12b, which reduces grazing when the stock of prey becomes scarce.

The general form for grazing interactions between phytoplankton and zooplankton is

$$G(Z_j, P_i) = G_j^{\max} \frac{\vartheta_{j,i} P_i}{k_P + B_j} \cdot \mathcal{F}(P_i) \cdot Z_j, \tag{3.7}$$

where the j-th zooplankton class grazes the i-th phytoplankton size class. The component of heterotrophic grazing is defined as

$$S(Z_j, Z_{j'}) = G_j^{\max} \frac{\vartheta_{j,j'} Z_j}{k_P + B_j} \cdot \mathcal{F}(Z_{j'}) \cdot Z_j, \tag{3.8}$$

where the j-th zooplankton class grazes the j'-th zooplankton size class. The total biomass available for grazing by the j-th predator is defined as

$$B_j = \sum_i^{n_p} \vartheta_{j,i} P_i + \sum_{j'}^{n_z} \vartheta_{j,j'} Z_{j'}. \tag{3.9}$$

Following Banas (2011) and Ward et al. (2012), the maximum uptake rate of phytoplankton by zooplankton along with the optimal predator-prey length scale are allometrically defined by,

$$G_j^{\max} = a_g \left(\frac{\ell_j}{\ell_0} \right)^{b_g}, \tag{3.10a}$$

$$\ell_j^{\text{opt}} = a_l \left(\frac{\ell_j}{\ell_0} \right)^{b_l}. \tag{3.10b}$$

These relationships prescribe that small zooplankton graze prey more efficiently than large zooplankton (Hansen et al., 1994). Predator-prey size interactions also vary with respect to predator size: small zooplankton tend to graze prey around the same body length as their own, whereas large zooplankton tend to graze prey that are much smaller than their own size Hansen et al. (1994). In this formulation, the maximum zooplankton size is set by the largest size class present in the phytoplankton spectra.

The grazing preference of each zooplankton size class, on each prey size class is defined by a $n_p \times n_z$ matrix, represented by,

$$\vartheta_{j,i} = \exp\left[-\left(\frac{\log_{10}(\ell_i) - \log_{10}(\ell_j^{\text{opt}})}{\Delta\ell}\right)^2\right]. \tag{3.11}$$

The total amount of biomass available to each zooplankton size class is represented by the sum in the denominator in Equation 3.7, with the total available biomass for each phytoplankton size class represented in the numerator. Finally, the functions $\mathcal{F}(P_i)$ and $\mathcal{F}(Z_j)$ limit the grazing pressure when the total phytoplankton and zooplankton prey biomass is small, respectively, i.e.,

$$\mathcal{F}(P_i) = 1 - \exp\left(-\sum_j \vartheta_{j,i} P_i\right), \tag{3.12a}$$

$$\mathcal{F}(Z_{j'}) = 1 - \exp\left(-\sum_j \vartheta_{j,j'} Z_{j'}\right). \tag{3.12b}$$

These zooplankton and phytoplankton prey refuge functions, $F(\bullet)$ are defined separately to simulate preference in grazing when one population of prey becomes particularly dominant (**?**).

3.3.5 Mortality

The mortality terms in the ecosystem are formulated linearly for phytoplankton and quadratically for zooplankton. Phytoplankton mortality is almost always modeled as a linear process in NPZD models and SSEMs (Franks, 2002; Poulin and Franks, 2010a; Banas, 2011; Ward

et al., 2012), whereas zooplankton mortality varies between models (Record et al., 2014). A quadratic mortality reflects the assumption that mortality processes not explicitly represented by the model, e.g. disease or grazing by predators outside the modeled size spectrum, are proportional to the total zooplankton stock, $\sum_j Z_j$. Murray and Parslow (1999) and Franks (2002) describe the response of a NPZ model with quadratic mortality and show that, at steady state, phytoplankton biomass increased until nutrient uptake or zooplankton grazing became saturated at the highest loads. By using a quadratic mortality in this model, we are able to simulate the effect of higher trophic level grazing on zooplankton, and allows for the nutrient uptake to become saturated in this model, which in turn allows for large phytoplankton size classes to be represented. The phytoplankton mortality is given by,

$$\mathcal{M}_p(P_i) = \mu_p U_i^{\max} P_i, \tag{3.13}$$

and

$$\mathcal{M}_z(Z_j) = \zeta Z_j \sum_{j'} Z_{j'}. \tag{3.14}$$

Here ζ is diagnosed by Banas (2011) to be,

$$\zeta = \frac{\overline{G^2_{\max}}\lambda}{4\overline{U_{\max}}\, k_p}. \tag{3.15}$$

where overbars denote averages over the uptake and grazing rates for all size classes of phytoplankton and zooplankton, respectively. To diagnose the value of ζ, we use a high resolution grid and calculate the uptake and grazing rates, finding that $\zeta = 1.7$ 1/(mmol N d), and fix this value for all runs in both the SSEM and the ROEM (Sec. 3.6).

3.3.6 Nutrient remineralization, forcing and sinking

Remineralization is formulated following Dutkiewicz et al. (2009, 2012), Banas (2011), and Ward et al. (2012), as a linear function:

$$\mathcal{R}(D) = r_{\mathrm{n}} D. \tag{3.16}$$

This represents bacterial processes by which particulate organic material is remineralized back into inorganic form.

Sinking of particles is the dominant process via which organic material is exported from the surface to depth (McCave, 1975). This serves to reduce near-surface remineralization and increase sub-surface nutrient concentration (Ducklow et al., 2001). In our model, we represent detritus as an aggregate group that sinks at a constant rate (Iversen and Lampitt, 2020). To simulate sinking particles in 0D, we assume a sinking speed, w_{sink}, and a mixed-layer depth, H_{sml}, and approximate the tendency due to sinking and removal as,

$$\frac{\partial}{\partial z}\left(w_{\text{sink}} D\right)\Big|_0 = -\frac{w_{\text{sink}}}{H_{\text{sml}}} D. \tag{3.17}$$

The physical forcing in 0D is constant, and set to

$$\Gamma(N) = 2\text{mmol N/m}^3/d. \tag{3.18}$$

In 1D, the physical terms ($\Gamma(\bullet)$) are a combination of nutrient restoring and diffusion. The one-dimensional extension is described in Section 3.3.8.

3.3.7 Size Diffusion

Adaptations/mutations in the phytoplankton and zooplankton populations are represented as a trait diffusion process, based on the assumption that the phenotypic effect of mutations is small, random, and continuous in size space (Sauterey et al., 2017). Diffusion is calculated in log-size space so that diffusion is not skewed toward smaller sizes along the size spectra:

$$\varphi \frac{\partial^2}{\partial\left(\log_{10}\ell_i^2\right)} P_i = \varphi\left[\frac{1}{\Delta_{i-1/2}^2} P_{i-1} - \left(\frac{1}{\Delta_{i+1/2}\Delta_{i-1/2}} + \frac{1}{\Delta_{i-1/2}^2}\right) P_i + \frac{1}{\Delta_{i+1/2}\Delta_{i-1/2}} P_{i+1}\right], \tag{3.19a}$$

$$\Delta_{i-1/2} = \log_{10}(\ell_i) - \log_{10}(\ell_{i-1}), \tag{3.19b}$$

$$\Delta_{i+1/2} = \log_{10}(\ell_{i+1}) - \log_{10}(\ell_i). \tag{3.19c}$$

Table 3.1: Parameters and values of the size structured ecosystem model. All parameters without specific references are configuration-dependent and can change between experiments.

Parameter	Value	Units	Description	Reference
α	0.45		Percentage of light available for photosynthesis	Moore et al. (2001)
a_g	25	1/d	Coefficient of allometric grazing rate	Hansen et al. (1994)
a_k	0.1	μMN	Coefficient of allometric nutrient limitation	Eppley et al. (1969)
a_l	0.5	μm	Coefficient of optimal predator-prey length scale	Hansen et al. (1994)
a_u	2.6	1/d	Coefficient of allometric nutrient uptake	Tang (1995)
b_g	-0.4		Exponent of allometric grazing rate	Hansen et al. (1994)
b_k	1		Exponent of allometric nutrient limitation	Eppley et al. (1969)
b_l	0.65		Exponent of optimal predator-prey length scale	Hansen et al. (1994)
b_u	-0.45		Exponent of allometric nutrient uptake	Tang (1995)
H_{sml}	50	m	Mixed-layer depth	-
k_c	0.04	m	Absorption coefficient for photosynthesis	Moore et al. (2001)
k_w	0.03	m	Absorption coefficent for water	Moore et al. (2001)
φ	$[0, 3.7 \times 10^{-7})$	$\log 10(\mu m)^2$/d	Size diffusion coefficient	Sauterey et al. (2017)
P^{init}	0.1	mmol N/m^3	Initial concentration of phytoplankton	-
Q_{sw}	340	W/m^2	Surface irradiance	Moore et al. (2001)
r	0.05		Temperature dependence	Ward et al. (2012)
r_{n}	0.04	1/d	Remineralization rate	Ward et al. (2012)
T_0	10	^{o}C	Reference temperature	-
μ_p	0.02		Phytoplankton mortality (fraction of growth rate)	Banas (2011)
w_{sink}	10	m/d	Detritus sinking speed	-
Z^{init}	0.01	mmol N/m^3	Initial concentration of zoplankton	-

Here φ is given in Table 3.1, and ℓ_i is the size of the phytoplankton cell. The coefficient of diffusion is taken from Sauterey et al. (2017). Sauterey et al. (2017) determined that the total number of biomass peaks in the spectra is inversely correlated with the diffusion coefficient. In our model, we allow for weak size diffusion that supports the same number of species as solutions without size diffusion, while still allowing for weak trait evolution. The purpose of this choice is to limit the sharpness of the peaks and allow for small deviations about the optimal plankton size. Without size diffusion, biomass peaks are increasingly sharp, and their width is eventually determined by the numerical resolution in size space.

The solutions at higher diffusivities given in Table 3.1 allow for wider peaks at steady state, but do not significantly affect the overall center of mass or total biomass.

3.3.8 Extension to 1D

We conduct most of the analysis in 0D (Section 3.4). However, in Section 3.5 we extend our analysis to 1D, to investigate the role of spatial heterogeneity. Here, we describe the model extension to 1D.

3.3.8.1 Restoring and Diffusion

Vertical dynamics have a first order impact on the distribution of phtyoplankton within the euphotic zone as a consequence of mixing within the surface mixed layer and light- and temperature-limitation (Ryabov et al., 2010; Klausmeier and Litchman, 2001; Beckmann and Hense, 2007; Venrick, 1993). Within the surface layer, phytoplankton are vertically mixed and exposed to a variety of light conditions as a consequence of light attenuation (Sverdrup, 1953; Huisman et al., 1999; Obata et al., 1996; Mahadevan et al., 2012). If the mixed layer is sufficiently shallow, high concentration of chlorophyll are found in deep chlorophyll maxima as a result of the balance between light limitation and nutrient availability (Partensky et al., 1999; Cullen, 1982a). Thus, in the presence of spatial variations in light and nutrient variability, these "bottom-up" influences on the ecosystem may be expected to affect the vertical distribution of different phytoplankton size classes.

Our 1-D model is an idealized, z-coordinate model with vertical mixing and nutrient-restoring in lieu of vertical advection. The timescale of restoring and profile of nutrients are tuned to approximate values chosen in the nutrient forcing experiments conducted in Section 3.4.3. The vertical diffusivity in the surface mixed layer is prescribed to have the same structure as used in the κ-profile parameterization (KPP) of Large et al. (1994). However, we simplify the formulation by fixing the mixed layer depth, H_{sml} and maximum magnitude,

Parameter	Value	Units	Description
H_{exp}	150	m	Decay scale for surface temperature
H_{rd}	15	m	Minimum depth of non-zero restoring for nutrients
H_{sml}	25	m	Imposed depth of mixed layer
κ_{bg}	10^{-4}	m^2/s	Background vertical diffusivity
κ^0_{sml}	10^{-1}	m^2/s	Maximum surface mixed layer vertical diffusivity
N_{max}	25	mmol N/m^3	Maximum nutrient concentration at depth
N_H	80	m	Decay scale for nutrients
T_0	10	$^\circ$ C	Reference temperature for nutrient uptake
T_{max}	22	$^\circ$ C	Maximum temperature at the surface
T_{max}	4	$^\circ$ C	Minimum temperature in the water column

Table 3.2: Physical parameters used to run the size structured ecosystem model in 1D.

κ_{sml}, rather than computing these quantities from the surface forcing. Given a background diffusivity of $\kappa_{\text{bg}}(z)$, the vertical profile of the vertical mixing coefficient is

$$\kappa_{\text{dia}}(z) = \kappa_{\text{sml}}(z) + \kappa_{\text{bg}}(z). \tag{3.20}$$

Note that we do not include a bottom boundary layer in this formulation, under the assumption that the euphotic zone is shallower than the depth of the water column above the bottom boundary layer. The profile of κ_{dia} in the surface mixed layer, ie. $-H_{\text{sml}} < z < 0$, is given by,

$$\kappa_{\text{sml}}(z) = \kappa^0_{\text{sml}} G_{\text{KPP}}\left(\sigma_{\text{sml}}\right), \tag{3.21}$$

where the dimensionless surface mixed layer coordinate, $\sigma_{\text{sml}} = -z/H_{\text{sml}}$, is defined such that $\sigma_{\text{sml}} \in [0, 1]$ within the mixed layer, and all parameters are given in Table 3.2. The structure function is given by,

$$G_{\text{KPP}}(\sigma) = \begin{cases} \dfrac{27}{4}\sigma_{\text{sml}}(1-\sigma_{\text{sml}})^2, & 0 \le \sigma_{\text{sml}} \le 1, \\ 0, & \sigma_{\text{sml}} \ge 1. \end{cases} \tag{3.22}$$

The scaling factor of 27/4 ensures that the structure function has a maximum factor of 1 over the mixed layer. The tendency due to diffusion is calculated using an implicit diffusion scheme.

The nutrient forcing in the physical model is the restoring of nutrients to an idealized profile, in lieu of advection, and vertical mixing, which allows us to resolve a surface mixed layer. The profile of restoring is given by,

$$N_{\mathrm{R}}(z) = N_{\mathrm{surf}} - (N_{\mathrm{max}} - N_{\mathrm{surf}}) \tanh\left(\frac{z + H_{\mathrm{rd}}}{N_H}\right), \tag{3.23}$$

where N_{surf} is the surface nitrate concentration, N_{max} is the maximum nitrate concentration at depth, N_H is the thickness of the nutricline, and H_{rd} is the depth at which the nutrient concentration begins to monotonically increase.

All runs are initialized using the same initial conditions, noting that the "init" subscript refers only to the initial profile:

$$N_{\mathrm{init}}(z) = N_{\mathrm{R}}(z), \tag{3.24a}$$

$$P_{\mathrm{init}}(\ell_{i_p}, z) = P^{\mathrm{init}}, \tag{3.24b}$$

$$Z_{\mathrm{init}}(\ell_{i_z}, z) = Z^{\mathrm{init}}, \tag{3.24c}$$

$$D_{\mathrm{init}}(z) = 0. \tag{3.24d}$$

Here $N_{\mathrm{R}}(z)$ is defined in equation 3.23, and the profiles of P, and Z are set to constant values P^0 and Z^0 for all sizes and depths, respectively (Table 3.1).

3.3.8.2 Temperature and Light Dependence

In a 1D framework, we additionally include dependence of nutrient uptake on temperature and light (see Equation 3.5). We use an idealized profile of coastal temperature motivated by measurements from California Cooperative Oceanic Fisheries Investigations (McClatchie, 2016), formulated following Moscoso et al. (2021),

$$T(z) = T_{\mathrm{min}} + (T_{\mathrm{max}} - T_{\mathrm{min}}) \exp\left(\frac{z}{H_{\mathrm{exp}}}\right), \tag{3.25}$$

where all parameters are given in Table 3.2.

The profile of irradiance is calculated via the Beer-Lambert Law with coefficients following Moore et al. (2001). The profile of photosynthetically available light is integrated vertically at each time step to calculate the light attenuation by phytoplankton and zooplankton,

$$\frac{\partial I(z)}{\partial z} = -k_{\text{par}} I(z), \quad \text{where} \quad I_0 = I(z=0) = \alpha Q_{sw}, \tag{3.26a}$$

$$k_{\text{par}} = k_w + k_c \left(\sum_i P_i + \sum_j Z_j \right). \tag{3.26b}$$

The light-dependent uptake function represents a saturating response at high levels of irradiation (Franks, 2002):

$$\mathcal{I}(z, P) = \frac{I(z)}{\sqrt{I_0^2 + I(z)^2}}, \tag{3.27}$$

and the temperature component of the uptake function is formulated using a typical exponential equation (Franks, 2002; Ward et al., 2012),

$$\mathcal{A}(z) = e^{-r(T_0 - T(z))}. \tag{3.28}$$

with respect to a reference temperature T_0.

3.4 Emergent Quantization

In this section, we characterize top-down and bottom-up controls on quantization in SSEMs using a set of experiments that independently control nutrient forcing and grazing with a finely-resolved size grid. Other SSEMs models have shown quantized behavior around a few intermediate size classes when a predator-prey grazing width is present (Banas, 2011; Sauterey et al., 2017) in 0D. However, what controls the location and robustness of the peaks in biomass is not well understood. Here, we perform experiments varying the size-space resolution, the nutrient forcing, and the width of the predator-prey interaction window.

We integrate the model under constant forcing for 100 years, which is longer than typical timescales of nutrient supply variability that are found in nature (Whitney et al., 1998;

Messié et al., 2009). In all experiments, except those presented in Section 3.4.2, we resolve 200 phytoplankton and zooplankton size classes. For simplicity, we focus on the steady-state behavior achieved at very long timescales, and discuss the potential consequences of temporal variations in nutrient supply in Section 3.7. For example, we see that abrupt changes in the size structure, such as bifurcations, may even occur after several decades at constant forcing (see Fig. 3.2).

3.4.1 Evolution to quantization in a reference experiment

All experiments run in this study use a relatively weak, constant nutrient forcing, with a long timescale that allows for the internal dynamics of the ecosystem to evolve without additional perturbations. While steady state solutions can help inform ecosystem behavior, plankton are often impacted by ocean circulation on a variety of timescales from hours to months and longer (Deser and Timlin, 1997; Rodriguez et al., 2001; Lévy et al., 2001; Lévy, 2003). Therefore, understanding the spin-up behavior of our model from constant conditions can help understand solutions in more realistic physical setting.

We show an example of a time series during model spin-up in Fig. 3.2. Quantization in this and other model solutions occurs after a relatively short time scale ($\mathcal{O}$(days)) for the smallest phytoplankton and zooplankton, likely as a result of fast uptake rates and rapid grazing, which quickly balance bottom-up and top-down controls. Large phytoplankton on the other hand, have slower grazing rates, but weaker grazing pressures. This likely controls the location of the peaks (see Section 3.4.4) by optimizing predator-prey interactions and competition. We explore this behavior in more detail in Section 3.4.4. Quantization in phytoplankton biomass occurs on longer timescales than quantization in zooplankton biomass. This is likely a consequence of competitive exclusion, where large amplitude variations promote rapid exclusion of some zooplankton size classes (Barton et al., 2010). We note the presence of internal ecosystem variability in phytoplankton over the first 18 months, which forces small oscillations around the stable zooplankton size classes, while the phytoplankton

spectra reaches stability. During this interval of time, the biomass peaks sharpen. In the longer-term, we see sharpening of biomass peaks to aggregate around a few specific size classes, a process that occurs over decades.

3.4.2 Sensitivity to resolution in size-space

Previous studies have found that ecological models with coarse resolution do not adequately capture phytoplankton diversity or quantization (eg. Ward et al. (2012) and Henson et al. (2021)), whereas models with a finely-resolved trait grid are able to capture diversity (eg. Banas (2011)). The purpose of this experiment is to demonstrate the number of size classes required both to achieve quantization in biomass, and ensure that the ecosystem solution is well resolved and accurate in the total concentrations of phytoplankton and zooplankton. We quantify the sensitivity to resolution by running a parameter sweep between resolving 5 and 200 size classes. A motivation for this experiment is to ensure that our model fully resolves steady state behavior and reaches convergence with respect to size-grid resolution. For all experiments, the minimum and maximum size of the phytoplankton are fixed, and the total biomass with respect to the resolution is shown in Fig. 3.3. Note that in the model, it is not necessary for the number of size classes to be the same between phytoplankton and zooplankton, but we opt for this configuration for simplicity. For our analysis, we calculate the concentration-weighted average size for the kth peak as

$$\ell_k^{\text{peak}} = \frac{1}{P_k^{\text{tot}}} \sum_{i=i_{\min,k}}^{i_{\max,k}} P_i \ell_i, \tag{3.29a}$$

$$P_k^{\text{tot}} = \sum_{i=i_{\min,k}}^{i_{\max,k}} P_i. \tag{3.29b}$$

Here the boundaries (in size space) for integration over the kth peak, defined by the indices $i_{\min,k}$ and $i_{\max,k}$, are defined by the locations of local biomass minima along the size spectrum. The locations of the zooplankton peaks in size space are defined analogously to Equations 3.29a–3.29b.

At the coarsest resolution, $n_p = n_z = 5$, the biomass along the phytoplankton and zooplankton size spectra is not quantized. As the resolution in size-space increases, quantization emerges. Phytoplankton and zooplankton biomass exhibits quantized behavior at 10 size classes, but these solutions are not fully resolved. Here, we consider solutions to be fully resolved when the biomass in each peak becomes insensitive to further refinements of the size grid. In this case, we assume convergence when variations in the total biomass between peaks varies by less than 5 percent with increasing resolution. By this metric, quantization in phytoplankton biomass is fully resolved with approximately 85 size classes, whereas quantization in zooplankton occurs at 130 size classes. However, this may be slightly conservative. Despite some oscillations in the zooplankton size classes, the behavior is nearly stabilized at 50 size classes. Regardless, we use a high resolution for the remainder of the sensitivity experiments – 200 phytoplankton and zooplankton size classes to ensure that solutions are fully resolved.

Model changes with finer grid size indicate that zooplankton are more sensitive than phytoplankton to size resolution. With 10 size classes, the maximum number of biomass peaks (4) for this configuration emerges. The total biomass in each peak is approximately the same, with the largest size class contributing to most of the phytoplankton biomass. Zooplankton biomass, however, changes substantially as a function of grid resolution after the emergence of quantization. Specifically, at low resolution, the smallest size class has the highest concentration of biomass, whereas at high resolution, the second size class has the highest concentration of biomass. An explanation for this is that grazing favors intermediate zooplankton size classes, because the smallest zooplankton experiences the most predation pressure.

3.4.3 Sensitivity of quantization to external forcing

Nutrient supply ultimately determines the total biomass and dominant size of phytoplankton in both models and observations (Worden et al., 2004; McQueen et al., 1986; Chenillat

et al., 2013; Verity and Smetacek, 1996; Chavez, 1989; Armstrong, 1994). At high nutrient concentrations, a large fraction of the phytoplankton biomass is concentrated within intermediate and large phytoplankton (Chisholm, 1992; Cavender-Bares et al., 2001; Venrick, 2002). At low nutrient concentrations, most of the phytoplankton biomass is concentrated within small size classes. We conduct two sets of experiments to investigate the response of the model to different nutrient forcing strengths. The first set shows responses to direct changes in nutrient supply rate. The second set restores phytoplankton and zooplankton to a constant small concentration at two different timescales to examine the robustness of quantization in the presence of external sources and sinks. This experiment is designed to mimic reduction of total biomass over different timescales, and may be conceptualized as representing horizontal variability or dilution.

Fig. 3.4 shows the ecosystem response to a variation in nutrient forcing spanning the range between 0.1 and 3 mmol N/m^3/d. The higher end of this nutrient forcing is likely unrealistically large over the long timescales of the experiments. However, Hales et al. (2005) found similarly large nutrient supply averaged over the depth of the mixed layer during an upwelling event. The lower end of this parameter space represents oligotrophic waters (Johnson et al., 2010). At the lowest levels of nutrient forcing ($F \leq 0.1$ mmol N/m^3/d) there is only one biomass peak, consistent with typical oligotrophic, open-ocean conditions (Partensky et al., 1999). At the highest nutrient forcing, the intermediate and large biomass peaks increase in overall biomass, and the largest biomass peak drifts toward larger sizes.

Zooplankton respond indirectly to variations in nutrient forcing, via its impact on the phytoplankton biomass, and similarly exhibit bifurcations in the biomass peaks as the nutrient forcing is increased. At high nutrient forcing, there is an additional bifurcation in the zooplankton distribution at an intermediate size class. This is likely a result of the biomass loading of the largest and second largest phytoplankton size classes, which allows for another large zooplankton class to persist. Additionally, the largest size peak in zooplankton increases along to optimize the spacing between other zooplankton classes and grazing on

the largest phytoplankton peak.

A robust feature of this experiment is that the approximate location of the phytoplankton peaks, and, to some extent, the zooplankton peaks as well, is nearly constant away from bifurcation points. This indicates that while the bottom-up control determines the overall abundance of phytoplankton and the dominant size class (Partensky et al., 1999; Worden et al., 2004; Venrick, 1982; Armstrong, 1994), the top-down control may be more important in determining the locations of the biomass peaks along the size spectra (Cavender-Bares et al., 2001; Chisholm, 1992; Venrick, 2002). We explore this behavior in Section 3.4.4.

We next examine the robustness of quantization by performing experiments in which we restore the phytoplankton and zooplankton concentrations to small values. We restore using three different timescales: 6 months, 1 year, and 5 years. These timescales are representative of different behavior during spin-up (see Fig. 3.2).

We set the restoring to be $P_{\text{restoring}} = P^{\text{init}}$ so that all size classes are restored toward a profile without size-quantization in biomass. We similarly force the zooplankton concentration to the initial concentration Z_{init} using the same restoring timescales. The restoring is calculated as an linear damping with respect to the restoring timescale T_{r}.

At the fastest restoring timescale, there is still some residual quantization, similar to the dynamics that occur in early spin-up times. At fast restoring timescales, the smallest size class is the most robust as a consequence of fast uptake rates (Tang, 1995; Partensky et al., 1999). On longer restoring timescales, the largest phytoplankton size classes contain a substantial fraction of the phytoplankton biomass (see Figure 3.5. This implies that while quantization and the approximate center of mass for each peak is established at shorter timescales, sharperning of the peaks occurs on very long timescales.

The zooplankton exhibits a similar response to the imposed restoring. However, the largest size classes in both the fast and slow restoring experiments are significantly broader than in the steady state solution with no restoring. Because the biomass in the fast restoring

case is located over a wider range of size classes, the largest zooplankton size class can graze a broader range of sizes with less phytoplankton limitation. Thus, with these experiments, we conclude that the concentration-weighted size of the largest phytoplankton mode – and thus zooplankton via grazing – is dependent on the bottom-up nutrient forcing (see Fig. 3.4). To better understand what controls the location of the quantized solutions, we test various grazing profiles and prey-selectivities.

3.4.4 Grazing profile width

Here, we vary the predator-prey selectivity window $\Delta\ell$ in equation 3.11 to understand the behavior of the ecosystem with narrowed and broadened selectivity, *i.e.* with smaller $\Delta\ell$ and larger $\Delta\ell$ respectively. With increased grazing selectivity, the size window in predator-prey interactions decreases, limiting the overall amount of total phytoplankton available to a single zooplankton class. With reduced selectivity, a single zooplankton size class is able to graze a wider variety of phytoplankton sizes. Fig. 3.6 shows a bifurcation diagram varying the predator-prey interaction window. We define the distance between biomass peaks as the distance (in size space) between the concentration-weighted sizes, *i.e.* the difference, $l_{k+1}^{\text{peak}} - l_k^{\text{peak}}$, between adjacent biomass peaks.

Bifurcations in size space reflects trade-offs between bottom-up nutrient availability and top-down grazing pressures, by which phytoplankton optimize their total biomass with respect to size — a driver for quantization. For example, small phytoplankton are less nutrient limited, but have the highest grazing pressure (Tang, 1995). A trade-off in this case would tend to shift biomass toward faster uptake rates and less nutrient limitation over the heavy grazing pressure. Alternatively, large phytoplankton are more nutrient limited but have less overall grazing pressure. A trade-off for large phytoplankton is to tend toward reduced grazing pressure under higher resource competition (Hansen et al., 1994).

With broader prey-selectivity windows, there are fewer biomass peaks along the phytoplankton and zooplankton size spectrum. As the grazing window shrinks, and zooplankton

become more selective, a series of pitchfork bifurcations occur, which give rise to more biomass peaks along the size spectrum, filling niches generated by reduced grazing pressure (Loeuille and Loreau, 2005). At smaller grazing profile widths, more biomass peaks are found along the size spectrum, and in the limit where $\Delta\ell \to 0$, the biomass is no longer quantized. We found that there still exits quantization at very small values of $\Delta\ell \sim 0.01$, assuming that the size grid is adequately resolved.

The distance between biomass peaks has an approximately linear relationship with the grazing window when plot in log-log space (Fig 3.6, bottom), i.e. the relationship can be approximated by a power-law. However, as a consequence of bifurcations, the linear relationship is less accurate near bifurcation points.

In these experiments the phytoplankton biomass peak with the largest organism size is strongly sensitive to the grazing window width. The zooplankton biomass peak with the largest concentration-weighted size, however, has nearly the same size at all grazing profile widths, varying non-monotonically by a multiple of approximately 1.8 over the range of grazing windows considered here. We can explain this behavior as result of trade-offs between grazing pressure, nutrient limitation, and uptake rates (McQueen et al., 1986). On one hand, more biomass peaks along the size spectrum are able to coexist with a narrower grazing window. On the other hand, with increased phytoplankton biomass peaks there is more resource competition between various size classes, benefiting smaller phytoplankton cells and reducing the size of the largest phytoplankton.

To better understand the relationship between the grazing profile width and the locations (in size space) of the biomass peaks, we consider the grazing pressure of zooplankton on phytoplankton in our reference experiments ($\Delta\ell = 0.1, 0.2, 0.3$). We define a peak-integrated grazing pressure, $G^{\text{tot}}_{i,k}$ as the phytoplankton-biomass normalized grazing rate for each inte-

grated zooplankton size class, Z_k^{tot}, e.g.

$$G_{i,k}^{\text{tot}} = \frac{1}{P_i} \sum_{j=j_{\min,k}}^{j=j_{\max,k}} G(Z_j, P_i). \tag{3.30}$$

This metric quantifies the total rate of grazing of the ith phytoplankton due to the kth zooplankton biomass peak. Without the normalization to a rate (*i.e.* units of s^{-1}), this metric would be dominated by the locations of the phytoplankton biomass peaks.

In Fig. 3.7 we plot the total grazing pressure along the phytoplankton size spectrum. The maxima in grazing pressure do not coincide with peaks in phytoplankton biomass; rather, the phytoplankton biomass peaks fall instead in the "shadow zones" of the grazing profile, emerging as a balance between grazing pressure and uptake rates, which dynamically co-vary. Due to the non-linearity and large number of phytoplankton and zooplankton size classes, predicting the exact location of the biomass peaks with the full system is challenging. However, Fig. 3.7 lends insight into the relationship between grazing profile width and the spacing between biomass peaks (Fig. 3.6): widening the grazing profile widens the space between"shadow zones" in which the phytoplankton biomass peaks fall.

We note that zooplankton self-grazing (not shown) does not have as much as an effect on the location of the biomass peaks in the zooplankton size spectra. Instead, it redistributes the total biomass from small zooplankton to large phytoplankton, as the self-grazing strength increases.

3.5 Persistent quantization in 1D

We now use our 1D model setup (Section 3.3.8) to examine quantization in a vertically heterogeneous environment that, while idealized, provides a first order representation of environmental gradients found in the ocean. The solutions shown in Fig. 3.8 are forced with three different nutrient supply strengths, $N_{\text{surf}} = 0$ (top row), 1 (center row), and 2

mmol N/m^3/d (bottom row), corresponding respectively to oligotrophic, intermediate, and eutrophic conditions.

In the 1D framework, quantization persists in the presence of vertical diffusion, variable nutrient supply, and variable light- and temperature- limitation (Fig. 3.8). As a result of low nutrient concentration, the smallest phytoplankton class contains all of the biomass at the surface, whereas at depth, larger phytoplankton contribute to the high biomass concentration. Zooplankton solutions (not shown) are similarly quantized. At depth, the largest phytoplankton outcompete smaller phytoplankton. At high nutrient forcing throughout the mixed layer, intermediate and large phytoplankton are responsible for most of the biomass and outcompete smaller phytoplankton at depth. We note that between the two solutions in 0D and 1D, the phytoplankton biomass is approximately distributed in the same size classes.

Surprisingly, we find no vertical variations of phytoplankton size even with vertical variations in nutrient supply (see Fig. 3.4). This suggest that a vertically heterogeneous environment is still able to support homogeneous quantization. A possible explanation is the presence of vertical mixing of the dominant size classes, which in turn out-compete other groups. This finding is consistent with 0D studies (Banas, 2011) that show that size quantization is robust to seasonal variations in nutrient supply.

We now repeat the experiments discussed shown in Section 3.4.4, varying the grazing selectivity window $\Delta\ell$ in the 1D framework. Once each solution has reached steady state, we integrate the biomass vertically through the water column and then compute the concentration-weighted, vertically-integrated biomass peak locations in size space using Equations 3.29a–3.29b. Since the size of the largest phytoplankton peak is dependent on the total nutrient forcing (Section 3.4.3), we use the largest surface nutrient forcing (see bottom row in Fig. 3.8) to ensure that the largest phytoplankton size class is represented.

We find qualitatively similar behavior between the 0D and 1D parameter sweeps, with a series of pitchfork bifurcations in the plankton biomass as the width of the grazing profile decreases. Due to the similarities, we do not include an additional bifurcation diagram.

The spacing between peaks retains a nearly linear relationship away from regions containing bifurcations (see Fig. 3.6). We additionally find a strong correlation between the size of the largest phytoplankton mode and the grazing profile width in 1D. There are some minute differences between the bifurcation diagram in 0D and 1D, for example in the exact locations of the bifurcation points in Δl space. We suspect that this may be caused by vertical light- and temperature-limitation terms, and not by any internal ecosystem dynamics.

3.6 Reduced Order Ecosystem Modeling

The SSEM experiments show that that quantization is a robust feature in size structured ecosystem models even in a variable environment, and that the width of the grazing profile determines the location of biomass peaks along the spectrum in both 0D and 1D. This robustness of quantization motivates us to reduce the complexity of the SSEM, approximating each of the biomass peaks as a single size class along the size spectrum. The purpose of this approach is to help inform methods of discretization in models that are not able to resolve a large number of size classes. Often models that fix the size of phytoplankton to general sizes (eg. pico-, nano-, and microplankton) may miss the inherent quantization and thus diversity in the solutions for the ecosystem Henson et al. (2021). We refer to the model we propose as a Reduced-Order Ecosystem Model (ROEM).

3.6.1 Model reduction in size space

The ROEM takes advantage of robust quantization and reduces the entire size spectrum to a few representative points along the biomass spectrum. However, because the correlations between the peak distance and grazing profile width deviate from a linear relationship near bifurcation points, we are unable to find an a priori relationship that accurately predicts the location of the peaks for arbitrary values of the predator-prey selectivity window, $\Delta\ell$. Instead, this process is done numerically from a 0D solution for a specific grazing profile

width. Because the model behavior is approximately the same between 0D and 1D, the location of the biomass peaks in 0D should be sufficient to predict the location of the peaks in 1D, even with some degree of heterogeneity in nutrients, temperature, or light. While the ROEM is derived from a steady state solution of the SSEM in 0D, a reduced order model can increase computational efficiency in higher spatial dimensions, while still providing a representation of ecosystem behavior consistent with the SSEM.

In order to obtain each representative size class, we make the assumption that modes along the biomass spectrum can be represented as a delta function along the size spectra. We select the locations of the phytoplankon and zooplankton size classes in by calculating the concentration-weighted average sizes of each biomass peak (see Equation 3.29a). For all solutions shown in Fig. 3.2, the number of size classes used in the ROEM are equal to the number of biomass peaks. Furthermore, the size classes used are specifically ℓ_k^{peak}. We test the performance of the ROEM in 0D and 1D, see Figs. 3.9 and 3.10.

3.6.2 Model Testing

Fig. 3.9 shows a comparison of the SSEM and the ROEM in 0D. We compare the biomass between a finely discretized SSEM ($n_p = 200$), a coarsely discretized SSEM ($n_p = 5$), and the corresponding representation with the ROEM. Each point corresponds to the integrated biomass in each peak using Equation 3.29b. The ROEM captures the phytoplankton and zooplankton biomass well over various grazing profile widths. However, the coarse representation of the SSEM does not perform well across the full range of grazing profile widths. Overall, we find that as the grazing profile width increases, the RMS error between the SSEM and the ROEM decreases by several orders of magnitude in phytoplankton biomass (figure not shown).

In Fig. 3.10 we perform a similar comparison between the SSEM and ROEM in 1D. We compare the depth structure of the biomass in each size class in the ROEM with that of the total biomass in each peak in the SSEM. Overall the behavior of the SSEM in 1D

is well represented by the ROEM, although some discrepancies remain. Specifically, the large size classes at grazing profile widths of $\Delta\ell = 0.2\log_{10}(\mu\text{m})$ and $0.3\log_{10}(\mu\text{m})$ are less well captured by the ROEM, indicating some limitations with the choice of using a single size class in representing each biomass peak. Furthermore, the SSEM has slightly larger total biomass compared to the ROEM. Despite these discrepancies between the two models in 1D, the ROEM may still be preferable for ecosystem modeling applications due to its greatly reduced computational cost.

3.7 Discussion and Conclusions

In this study, we find that quantization in biomass along the size spectrum as a consequence of top-down control in the form of grazing. Our model suggests an important role for prey-selectivity behavior, which has been identified as a grazing mechanism in laboratory studies of zooplankton and phytoplankton interactions (Hansen et al., 1994). However, comprehensive measurements of selective predation have not been conducted in *in-situ* environments. Perhaps the most compelling studying showing *in-situ* quantization in biomass was Schartau et al. (2010). They found that not only were phytoplankton quantized after a nutrient fertilization event in the IronExII campaign, but the biomass of their predators was also quantized along the size spectra. Observational studies have shown the emergence of dominant size classes reminiscent of quantization in productive regions of the global ocean (i.e. Eastern Boundary Upwelling Systems) that have high nutrient availability and support large plankton cells (Hood et al., 1991; Jonasz and Fournier, 1996; Zubkov et al., 2000; Worden et al., 2004; Schartau et al., 2010; Huete-Ortega et al., 2014). However, understanding environmental controls on quantization in the field can be difficult because of the variety of ecosystem processes involved.

In models, grazing is an important factor in setting the internal ecosystem dynamics (Ingrid et al., 1996; Venrick, 1982; Leibold, 1996; Fuchs and Franks, 2010). The functional

representation of grazing is a determining factor in ecosystem models (Steele and Henderson, 1992; Chenillat et al., 2021), for example affecting population stability (Strom and Loukos, 1998), and driving quantization (Banas, 2011). Often, the choice of zooplankton mortality closure is considered an important discriminant in setting internal ecosystem dynamics (Record et al., 2014). However, the choice of linear versus quadradic mortality in our model does not affect the robustness of quantized biomass. Instead, a linear closure term in both phytoplankton and zooplankton allow for larger sizes classes to emerge following a relationship set by the grazing profile width, but does not influence the location of the peaks (not shown).

We show that the locations (in size space) of the biomass peaks is sensitive to the width of the grazing profile, $\Delta\ell$, which is the first order control on setting the behavior at steady state (see Fig. 3.6 and Banas (2011)). We find an approximately linear relationship between the width of the grazing profile and the distance between biomass peaks in both phytoplankton and zooplankton. This relationship loses explanatory power near bifurcation points in $\Delta\ell$-space. Successive bifurcations suggest that phytoplankton optimize their size based predominantly on grazing pressures, although explicitly showing this behavior is much more challenging. A caveat of our analysis is that the model exhibits non-linear behavior that is difficult to isolate from first principles.

Total nutrient availability and supply are secondary contributors to the distribution of modes along the size spectra. Large and intermediate size classes are responsible for a large fraction of the phytoplankton biomass at high nutrient forcing, while small phytoplankton contribute to most of the biomass at low nutrient forcing. This is consistent with other models and observations (Partensky et al., 1999; Zhou and Huntley, 1997; Sheldon et al., 1972; Hood et al., 1991; Huete-Ortega et al., 2014; Jonasz and Fournier, 1996). While changes in nutrient forcing leave the locations of the biomass peaks in size space approximately unchanged, increased nutrient forcing does result in emergence of larger size classes with spacing predicted by the grazing profile width. Qualitatively, we can describe this behavior

as a mechanism to balance grazing pressures and nutrient uptake limitations. This mechanism in phytoplankton niche-filling has been studied by Leibold (1996), Ingrid et al. (1996), and Fuchs and Franks (2010), which show that large phytoplankton often outpace growth compared to their grazers by their cell size. For our reference solution, we chose a relatively broad grazing profile that is sufficiently far away from bifurcation points. While smaller grazing profile widths are perhaps more plausible (Hansen et al., 1994), they would not alter the model behavior, besides allowing a larger number of size peaks. The small width and high sharpness of the biomass peaks as the model approaches equilibrium are also rather unrealistic compared to broader distributions from *in-situ* studies (Schartau et al., 2010). Natural marine environments with horizontally variable nutrient availability and transport may smooth sharp points in the biomass spectra. Furthermore, we only investigate size as the axis of variability, while many more traits can be identified in natural plankton populations.

In general, quantization appears to be a robust feature of marine ecosystems, and ecosystem models, assuming some degree of competition for resources by the represented ecosystem components (here, size classes). Evolutionary models that focus on niche selection and emergent traits often show biomass peaks along their respective trait spectra (Loeuille and Loreau, 2004, 2005; Brännström et al., 2011; Sauterey et al., 2017; Edwards et al., 2018). In their study, Loeuille and Loreau (2005) note that quantization of biomass can be described as a method of niche selection for a given trait as a consequence of resource competition. In our model, as $\Delta\ell$ increases, zooplankton are able to graze a larger number of phytoplankton size classes, increasing resource competition. This, in effect, gives more zooplankton sizes access to the same resources. As a result of this increased competition, the total number of peaks in phytoplankton and zooplankton biomass decreases, and the preferential sizes are spread further in size space. Another way to induce changes in resource competition is grid resolution. At low resolution, biomass is preferentially aggregated in the smaller size classes, thus reducing competition at larger sizes.

With this set of experiments, we seek to provide insights into the behavior of the ecosys-

tem as it relates to the emergence of peaks in size distribution. The behavior of the model can be summarized in the context of bottom-up and top-down controls. While there is some evidence of size quantization in observational studies Hood et al. (1991); Schartau et al. (2010), there is not global evidence that specific quantization, like the solutions we present in this paper, is consistently present across diverse ocean conditions. An outcome of this study is to enable deeper understanding of the behavior of quantization in regions of the ocean where it occurs. For example, if a region has quantized biomass with a few distinct peaks, and a large average size, one may hypothesize that zooplankton preferentially graze on many size classes. Alternatively, if there are many size classes with a small average size, one may hypothesize that zooplankton prefer to graze a few particular sizes.

A practical application of this study extended to other general marine ecosystem models with robust quantization is to use the same method of model complexity reduction we used to derive the ROEM, *i.e.* to simulate only the subset of organismal classes corresponding to dominant peaks in trait space. The primary assumptions used to define the ROEM are that biomass peaks are infinitesimally narrow and that their locations in size space are insensitive to environmental conditions. We note that biomass quantization collapses to a continuous spectra once we restrict one predator to only graze one prey, i.e., when grazing becomes extremely selective (Poulin and Franks, 2010a). Thus, the representational capacity of the ROEM falls with very selective grazing.

Our solutions show that the total biomass in the SSEM is represented by the ROEM to a good degree of approximation. However, there remain some issues with over-estimation of total biomass for large zooplankton in 0D with highly selective grazing, and issues with the under-estimation of large phytoplankton biomass in 1D. Although the ROEM does not always have high accuracy in representation of the peaks, overall, we find that as the distance between peaks becomes comparable to the width of the grazing profile the reduced model exhibits increased performance and accuracy. However this issue exists in all size structured ecosystem models that are coarsely discretized (see Figure 3.3). These issues

have not be investigated in detail in this study. However, there are implications for the representation of the ecosystem, and specifically the biomass of grazers if large plankton are over or underestimated (Cyr and Pace, 1992; Chenillat et al., 2021).

As a part of the development of the ROEM, we assume that the biomass in each peak can be effectively represented as a delta function in size space; however this is not a realistic assumption for phytoplankton sizes. For example, plankton morphology can change over a cell's lifetime, or across an even limited number of generations, allowing phytoplankton growth as a mechanism of niche adaptation. In order to more accurately resolve the predicted biomass peaks, future studies could allow for more stable solutions by picking a small window, inside of the predicted location of each peak, and resolving a few points within the boundaries of the peak. Additional approaches could also include representing each peaks as a Gaussian function with a fixed width, or including more points near the estimated concentration-weighted size. However, these methods have not been tested.

The most relevant application of the model complexity reduction in the ROEM would be to use in Earth System Models where vertical and horizontal resolution limit the number of biogeochemical tracers due to computational constraints. Ultimately, sharp biomass peaks emerge under constant nutrient forcing over long timescales, but would likely be smoothed out with more dimensions of physical variability and coarser size-grid resolution (e.g., Ward et al. (2012)). This likely would affect the accuracy of the ROEM because of the assumption that each mode can be represented as a relatively narrow peak. We suggest that a possible way to address inaccuracies in the representation of the SSEM by the ROEM is to representing each biomass peak as a resolved interval along the size-grid instead of a single point.

A major benefit of this approach is to resolve an entire high-resolution ecosystem model with a few, emergent modes. The strategy presented in this study to capture ecosystem dynamics in a reduced order model can be extended to a variety of traits that results in robust quantization of biomass. We expect quantization in the SSEM due to size-selectivity

in the grazing profile; however, the functionality and accuracy of ROEM in higher dimensions is yet to be explored. Future work with the ROEM is to test the accuracy of the model in horizontally heterogeneous environments, and compare to quantization in the SSEM. Coupling the ROEM to more comprehensive 2D and 3D models, allows more extensive investigations of the planktonic food-web in a computationally efficient framework.

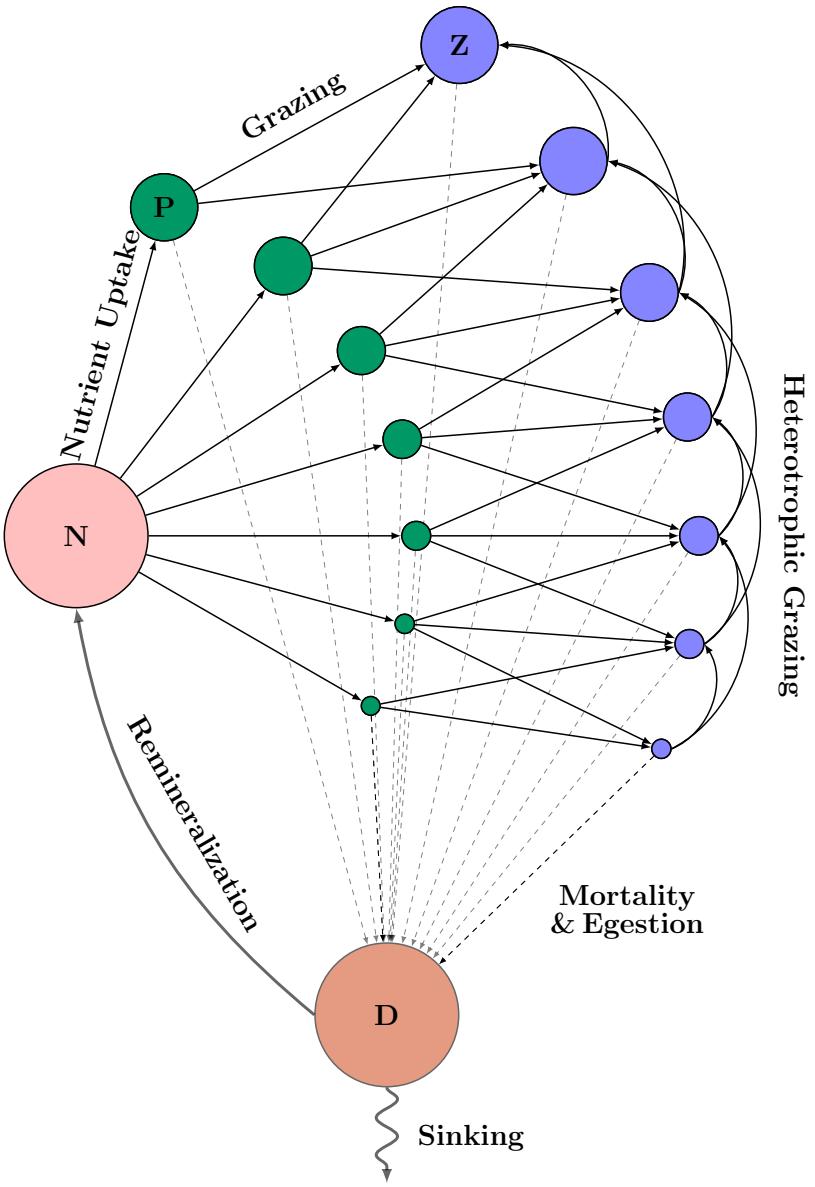

Figure 3.1: Schematic of the size-structured ecosystem model used in this paper. Circles show individual model state variables (nutrient, phytoplankton, zooplankton and detritus biomass). Arrows show the direction of nutrient fluxes and interaction within the ecosystem, from a single nutrient pool to phytoplankton via uptake, from phytoplankton to zooplankton via grazing, and so on. This formulation allows for size-dependent preferential grazing in which zooplankton interact with several phytoplankton size classes, and, potentially, with other zooplankton.

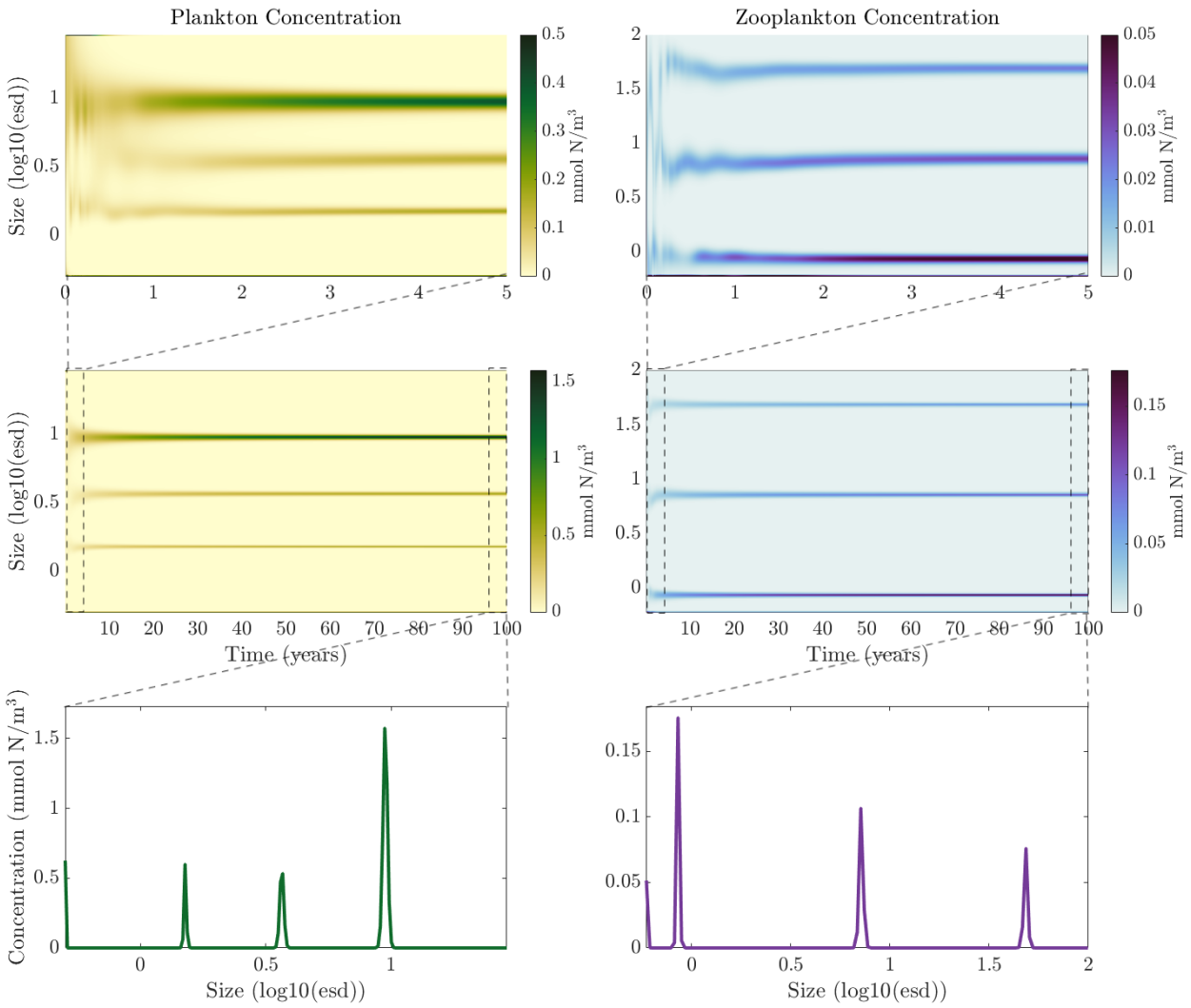

Figure 3.2: Evolution of a reference experiment over one hundred years of integration. The left column shows the phytoplankton concentration, and the right column shows the zooplankton. The top row of this figure shows the plankton concentrations over the first five model years. Note that the colorbar has been shifted to show the internal ecosystem oscillations before becoming stable. The middle row shows the concentrations over the entire model run, and the bottom row shows the plankton concentration as a function of size, averaged over the final five model years.

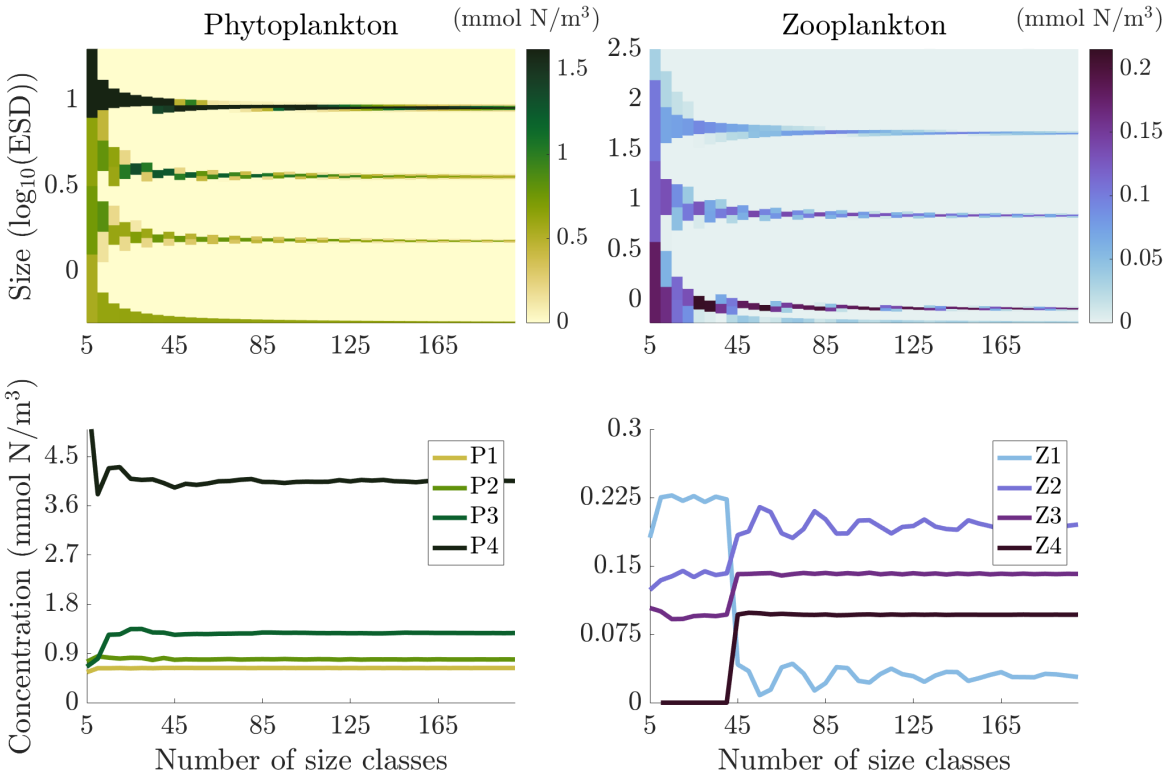

Figure 3.3: Quantization with increasing resolution in size space. The top row shows the parameter sweep diagram, the bottom row shows peak-integrated concentrations. Left column shows phytoplankton biomass, right column shows zooplankton biomass. $P1$ indicates the smallest non-zero biomass peak, $P2$ indicates the second smallest non-zero biomass peak, and so on. The same numbering convention is used for the zooplankton biomass peaks.

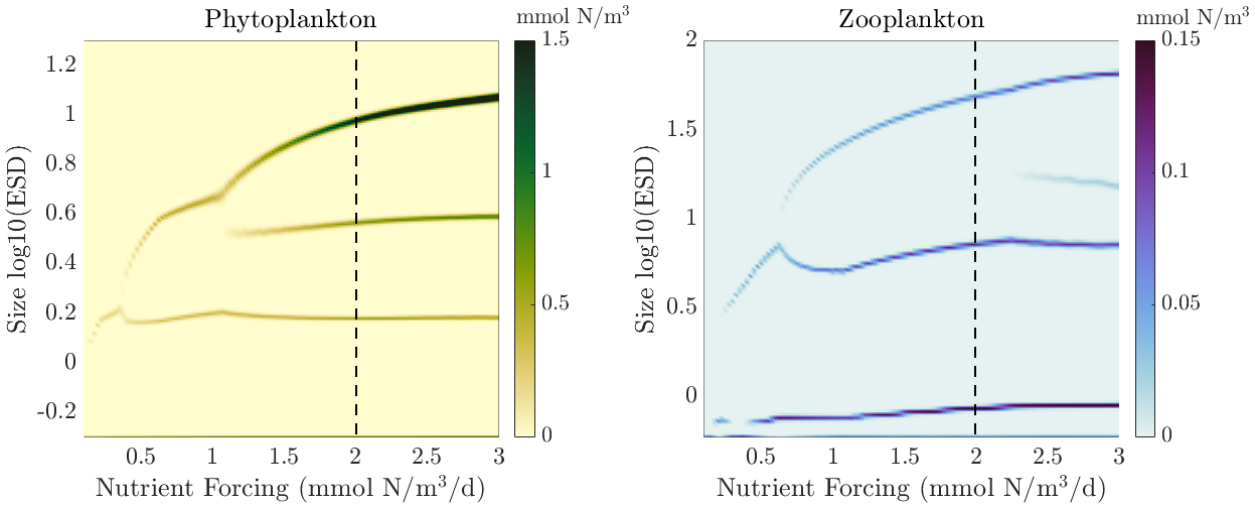

Figure 3.4: Bifurcation diagram for different nutrient forcing. The dashed line shows the location of the value used as a reference nutrient forcing for other experiments.

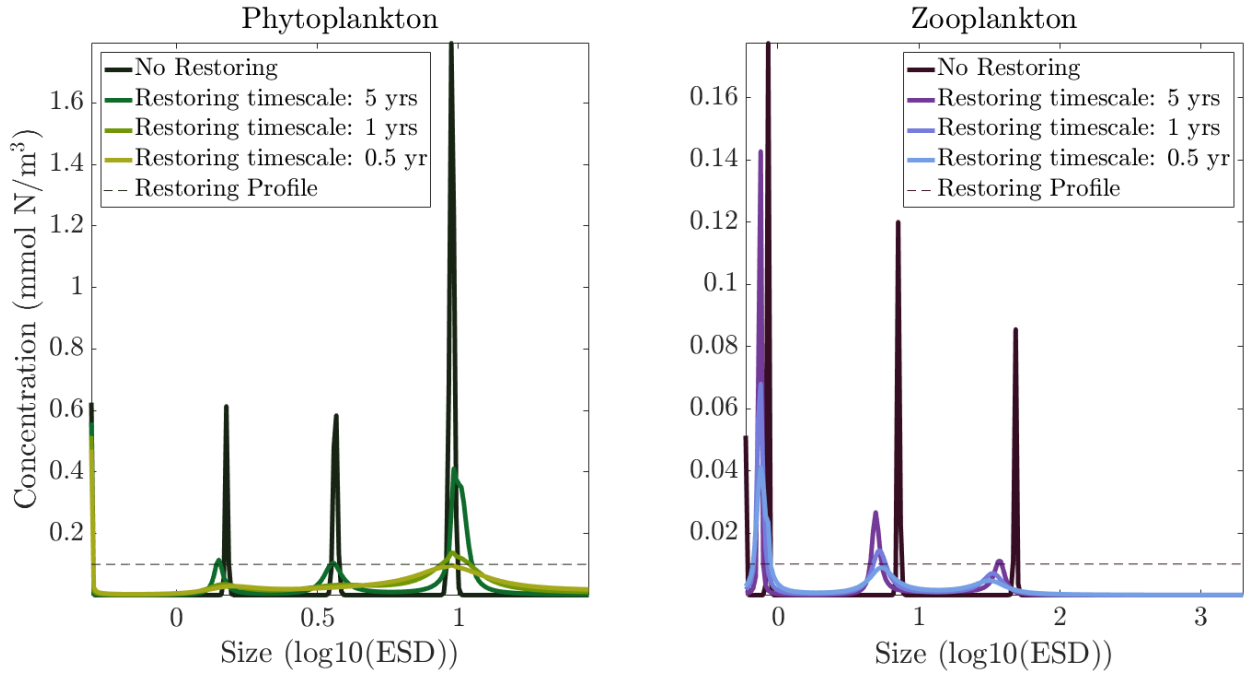

Figure 3.5: Phytoplankton and zooplankton quantization in solutions with restoring to a small constant concentration (black dotted line) over time scales of 5 years, 1 year, and 0.5 years.

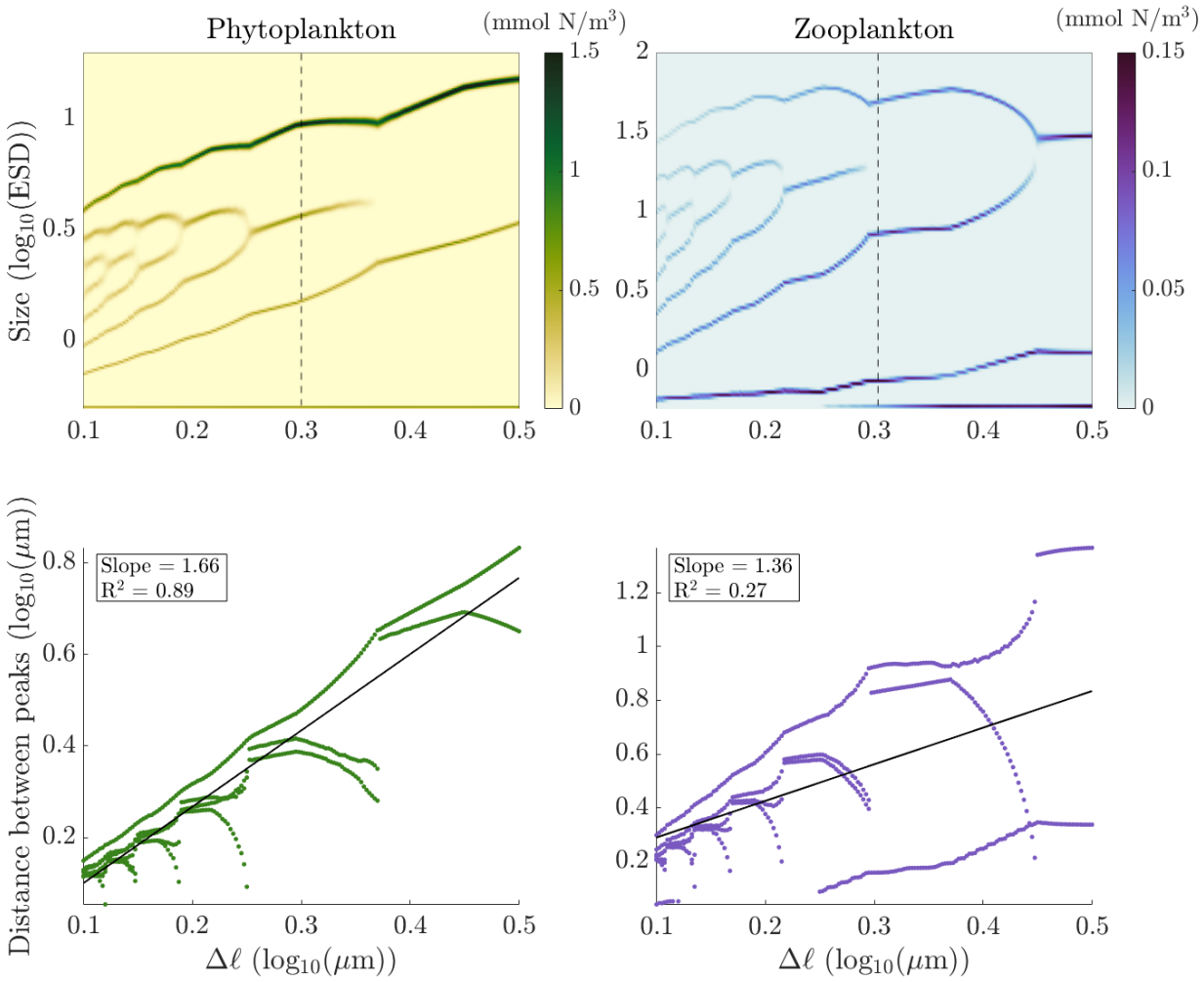

Figure 3.6: This figure shows bifurcation diagrams with respect to the grazing profile width $\Delta\ell$ (top) and distance between the center of mass of each biomass peak (bottom), with respect to phytoplankton biomass (left) and zooplankton biomass (right).

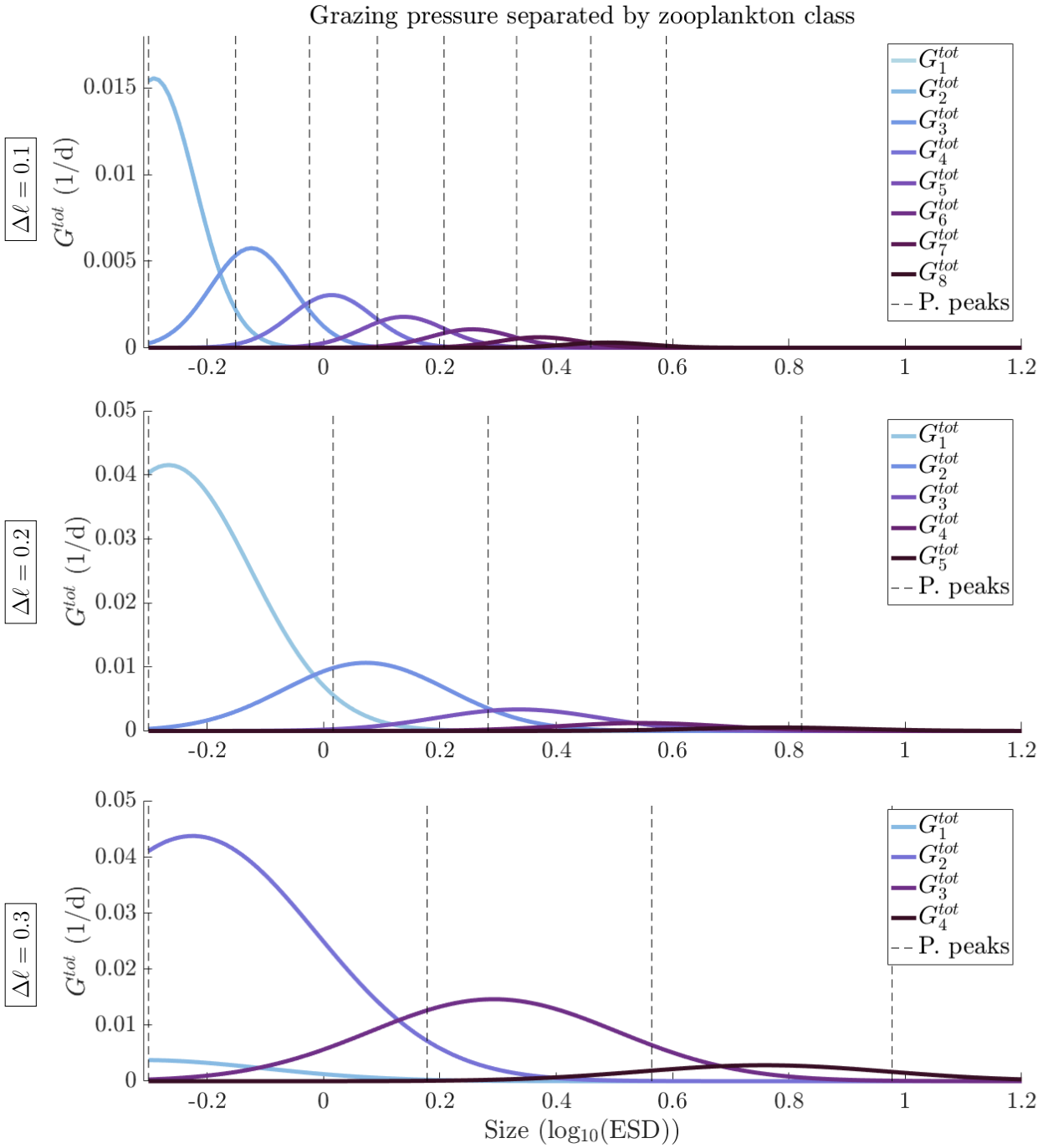

Figure 3.7: Normalized grazing rate of each phytoplankton size class due to each zooplankton biomass peak. The vertical dashed lines indicate the sizes of the phytoplankton biomass peaks.

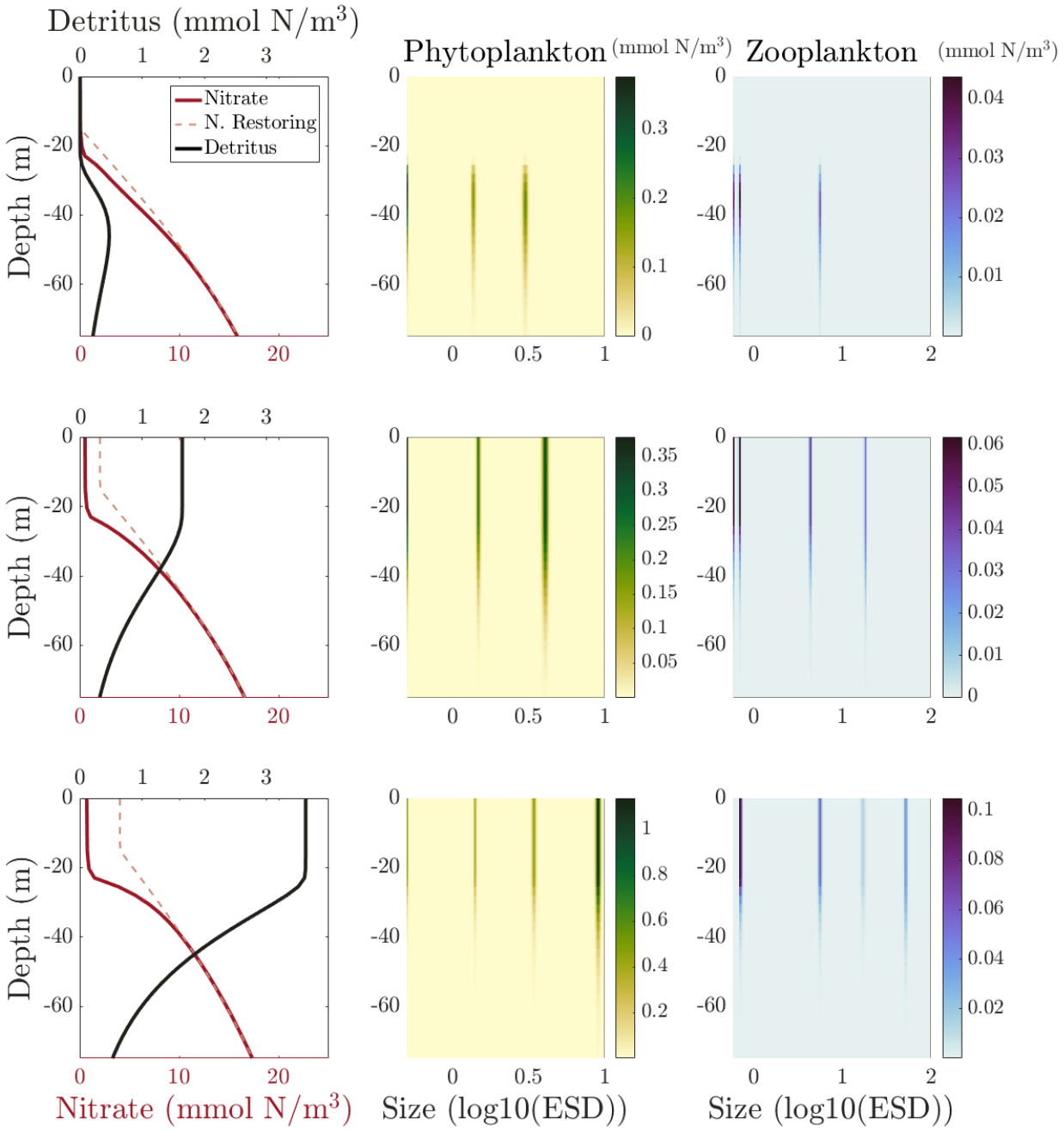

Figure 3.8: The final profiles for nitrate, phytoplankton, zooplankton, and detritus with respect to depth in the 1D model with surface mixed layer estoring rates of 0 mmol N/m^3/d (top), 1 mmol N/m^3/d (center), and 2 mmol N/m^3/d (bottom) to show the response under various surface nutrient forcing. Concentrations of organic and inorganic nitrate (left), phytoplankton (center), and zooplankton (right) are shown.

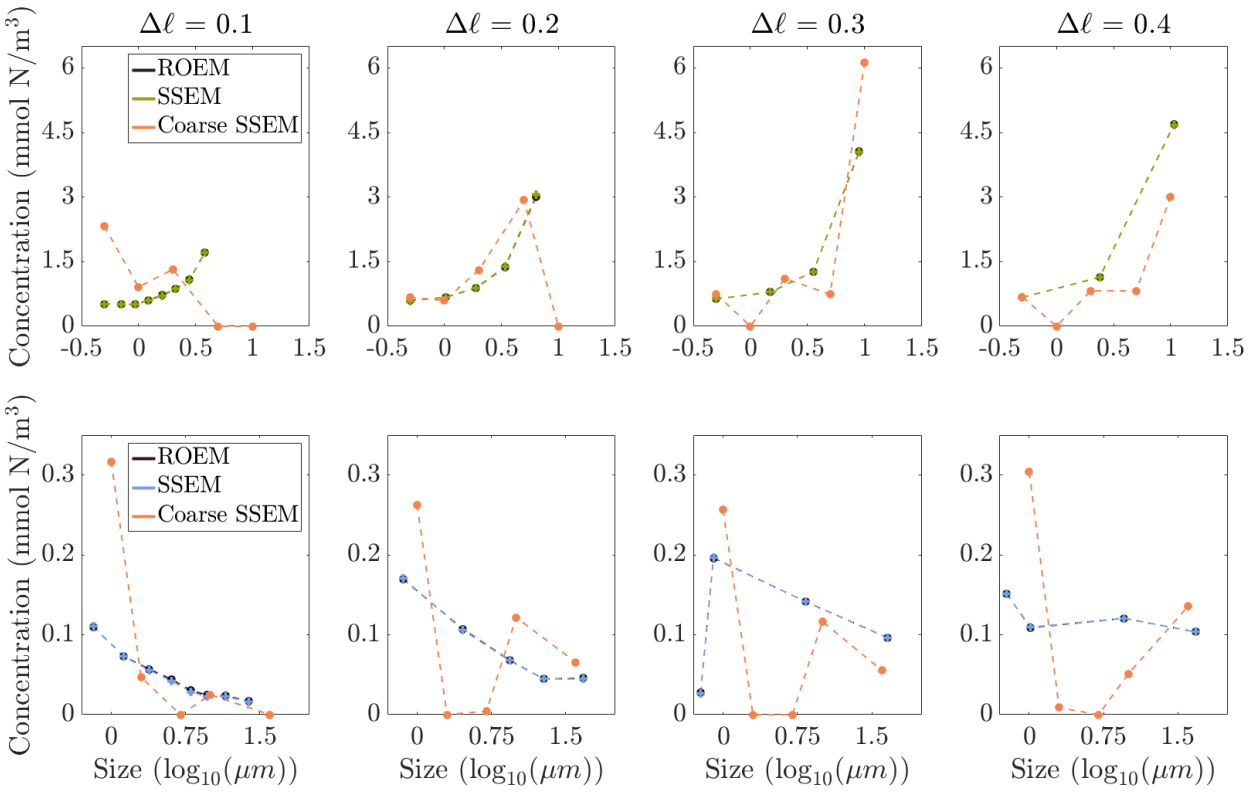

Figure 3.9: Comparison with the biomass in 0D solutions of the reduced order ecosystem model, compared with the total biomass in each corresponding peak from SSEM. The top row shows the phytoplankton solutions from the ROEM (black), high resolution SSEM (green), and coarse SSEM (orange). The bottom row shows zooplankton solutions from the ROEM (black) and SSEM (purple), and coarse SSEM (orange).

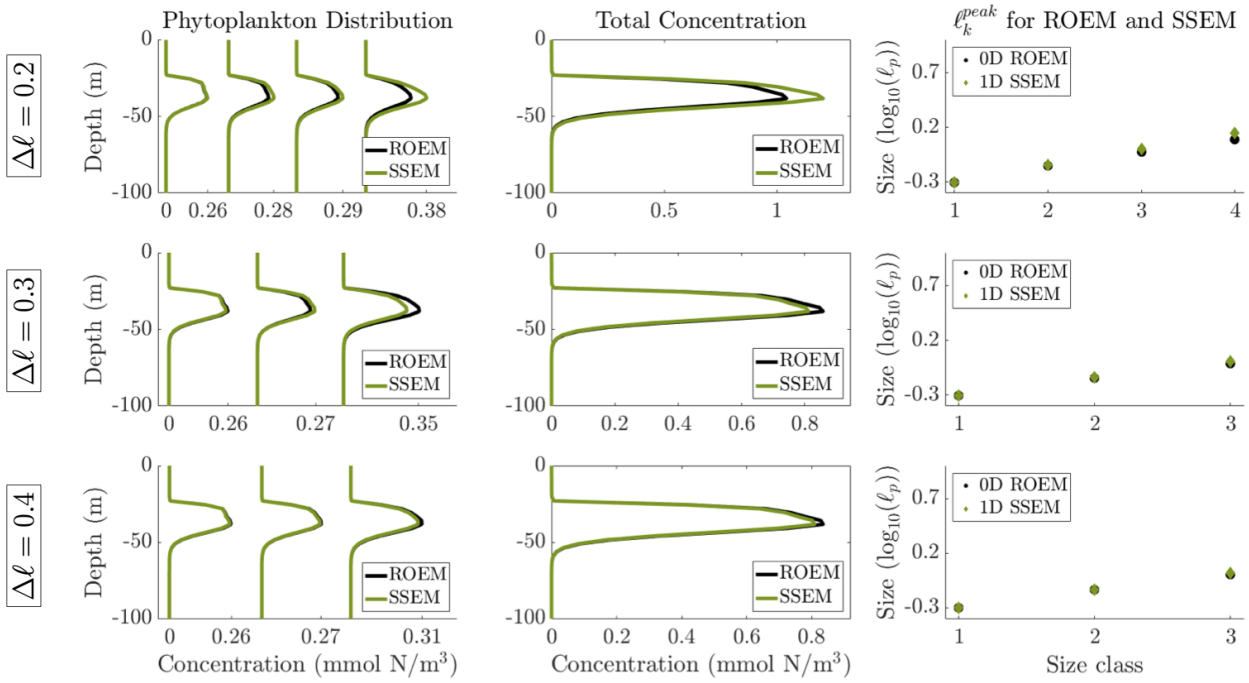

Figure 3.10: A figure showing the solutions for phytoplankton SSEM (green), peaks integrated, and the ROEM (black), integrated for 100 years (left column), the total concentration (center column), and the concentration-weighted average size from the 1D SSEM and 0D-informed ROEM (right column). The restoring nutrient profile is configured to represent an oligotrophic surface ocean.

CHAPTER 4

Modeling the Responses of Planktonic Ecosystem Structure in Eastern Boundary Upwelling Systems

This chapter contains a draft of a manuscript, to be submitted.

4.1 Introduction

Upwelling in Eastern Boundary Upwelling Systems (EBUSs) supports productive and diverse biological communities (Chavez and Messié, 2009; Bakun and Parrish, 1982). The alongshore equatorward winds drive an offshore transport of surface water and resulting Ekman pumping of dense, nutrient-rich water to the surface (Bakun and Nelson, 1991; Jacox and Edwards, 2012, 2011). At the same time, a complex interplay of physical phenomena that arise as a consequence of upwelling often works to redistribute and even subduct nutrients, reducing surface productivity (Colas et al., 2013; Gruber et al., 2011). As a consequence, understanding responses of the local food-web to natural variability in the physical environment is important to the regional socioeconomic stability (Golden et al., 2016; Pozo Buil et al., 2021).

Ecological responses to wind-driven upwelling in EBUSs have long been studied (Messié et al., 2009; Van Oostende et al., 2018; Gruber et al., 2011; Renault et al., 2016), yet uncertainties in the response of ecosystem diversity and the regional structure of the food-web. While the locations of phytoplankton blooms and biomass are predominantly set by the total nutrient supply and availability (Marañón et al., 2014), the controls on the zonal ecosystem

composition in an EBUS are less clear. In regions of high productivity near the coast, large phytoplankton contribute to the plurality of the biomass (Sheldon et al., 1972; Hood et al., 1991; Taylor et al., 2012), whereas offshore in the deep chlorophyll maximum, small phytoplankton dominate the total biomass (Worden et al., 2004; Zubkov et al., 2000).

There are a large number of physical influences that have been shown to be important in determining the structure of the food-web in EBUSs. The strength of the wind, which drives upwelling, controls the total productivity in EBUSs, with stronger upwelling being associated with more surface productivity (Capet et al., 2004; Chavez and Messié, 2009; Rykaczewski and Dunne, 2010; Pozo Buil et al., 2021). Thus an increase in the overall strength of the wind is anticipated to support higher phytoplankton biomass and larger cell sizes (Hood et al., 1991). Additionally, Renault et al. (2016) found that the shape of the wind-stress curl controls the coastal flux of nutrients and net primary productivity in the euphotic zone, with wider wind-stress curl being associated with more net primary productivity in the surface.

While meridional equatorward winds drive bulk coastal upwelling and supports productivity, winds also create a baroclinically unstable jet that sheds mesoscale eddies that restratify the water column, and transports nutrients and other tracers away from the euphotic zone, sequestering productivity (Gruber et al., 2011; Colas et al., 2013; Capet et al., 2008). As as consequence, there is a zonal gradient of productivity that spans several orders of magnitude. These differences in nutrient concentrations drive changes in ecosystem composition (Hood et al., 1991; Worden et al., 2004; Taylor et al., 2012). Both the effect of eddy restratification, eddy stirring, and subduction have been shown to reduce the total productivity at the surface and on the shelf (Renault et al., 2016; Colas et al., 2013). Thus, insofar as productivity and phytoplankton size are positively related (Van Oostende et al., 2018; Moscoso et al., 2022), an increase in eddy activity would work to decrease the size of plankton near the coast (Renault et al., 2016)

The composition of upwelled source waters may also impact the ecosystem structure. While physical controls can modulate the depth of the source water (Jacox and Edwards,

2011), the subsurface distribution of nutrients in the subtropics also impacts the nutrients that are upwelled (Pozo Buil et al., 2021). A shallow, thin nutricline increases the amount of nutrients on the shelf provided that the source depth of water does not change (Jacox and Edwards, 2012), and lead to an increase of productivity and plankton size near the coast.

Previous modeling work has also been successful in capturing zonal patterns of phytoplankton size classes in regional frameworks. Goebel et al. (2010) shows a zonal transition from large plankton onshore to small plankton offshore in the California Current System (CCS) with an intermediate complexity biogeochemical model. Similarly, Van Oostende et al. (2018) showed that a large diatom class was essential in capturing a near-shore surface chlorophyll maximum over an upwelling season in the Southern California Bight. Due to computational limitations in regional modeling, a systematic characterization of the responses of ecosystem diversity as a result to changes in biogeochemical and physical forcing in EBUSs is still lacking. Additionally, the factors that control the distribution of nutrients in EBUS often co-vary. For example, eddies drive both restratification and advection along isopycnal surfaces and correspond to wind changes. These processes are hard to disentangle in complex, 3-D eddy-resolving models. Thus, the use of an idealized model allows us to vary different model parameters independently, thus uncoupling the impact of physical processes that often co-vary in comprehensive regional models.

In this study, we conduct an expansive exploration of the ecological responses to upwelling under a wide physical parameter space. We configure an idealized quasi-2D Meridionally Averaged Model of Eastern Boundary Upwelling Systems (MAMEBUS, Moscoso et al. (2021)) to examine a large number of physical states representative of those found in the California Current System (CCS). The physical model includes a finely-resolved size-structured ecosystem model (Moscoso et al., 2022; Banas, 2011; Ward et al., 2012), which represents the lower-trophic food-web cycling. Size-structured ecological models are often used to represent broad functional diversity in the food-web because size is often used as a proxy for other biological traits (Andersen et al., 2016), and are becoming the de facto state-of-the-art for

global Earth system models (Ward et al., 2012; Henson et al., 2021; Negrete-García et al., 2022). In general, size structured ecosystems with a fine resolution of the size dimension have not been studied in comprehensive regional and global models due to computational constraints. However, using a quasi-2D model, we are able to explore the behavior of a highly resolved planktonic food-web structure in an idealized framework.

The remainder of the paper is organized as follows: In Section 4.2, we describe the physical and biogeochemical model configurations. We present the parameter space in which we vary the model, and provide justification. We additionally define model diagnostics used to identify the responses to perturbations in the model state. In Section 4.3, we present a reference solution focusing on ecosystem size structure and characteristics. We then present the responses to variations across the parameter space in three sub-regions of an idealized EBUS to identify important controls in Section 4.4. Finally, we discuss the results and their implications for ecosystem productivity and diversity in EBUSs in Section 4.5.

4.2 Methods

The simulations presented in this study were conducted using a Meridionally Averaged Model of Eastern Boundary Upwelling Systems (MAMEBUS, Moscoso et al. (2021)), a quasi-2D idealized model coupled to a size-structured nutrient, phytoplankton, zooplankton, detritus (NPZD) model (Moscoso et al., 2022). A schematic of the main components of the model is show in Figure 4.1. The physical setup of the model is similar to that presented in Moscoso et al. (2021); any differences in the model configuration are highlighted below.

4.2.1 Physical Model Configuration

We configure the Meridionally Averaged Model of Eastern Boundary Upwelling Systems to represent an idealized CCS in a quasi-2D framework. While 2D models have been used to investigate upwelling with respect to a wide physical parameter space in other studies of

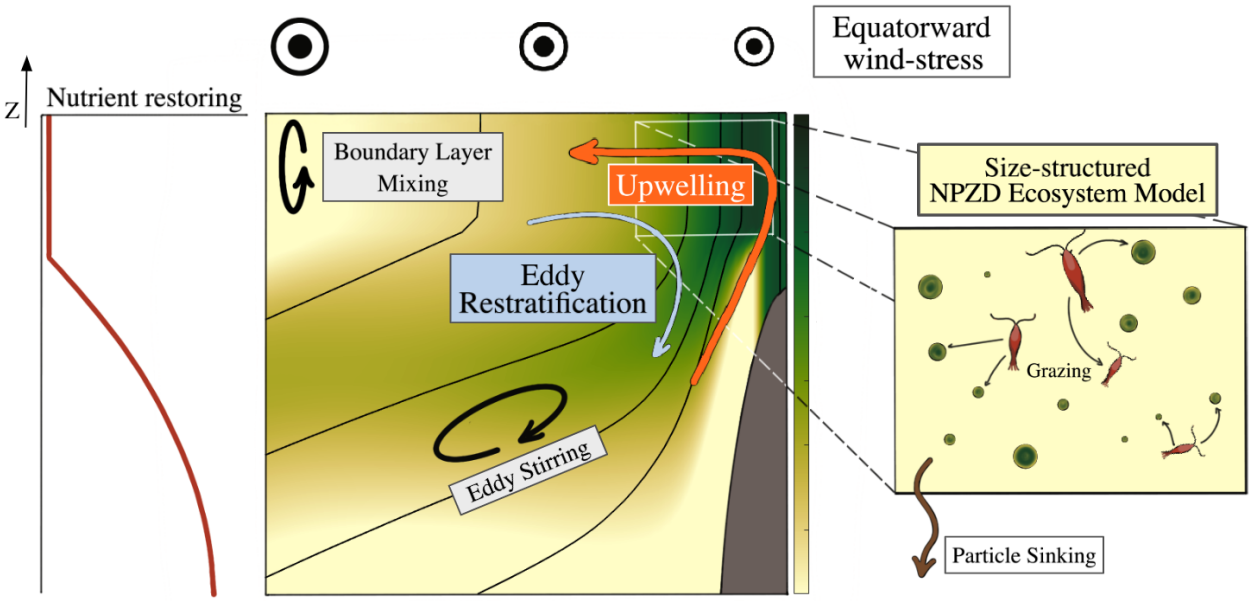

Figure 4.1: Components of our coupled physical-biogeochemical model. The colormap shows total phytoplankton concentration, the black lines indicate isotherms, and the topography is in dark grey. The colormap used in this figure is shown with units and spatial scale in Figure 4.5. The mean circulation is determined by wind-driven upwelling. Eddy restratification, eddy stirring, and boundary layer mixing are parameterized. Temperature and nutrients are restored at the western boundary. The ecosystem model is a size-structured ecosystem model with 50 phytoplanton and 50 zooplankton size classes (Moscoso et al., 2021).

productivity in EBUSs (Jacox and Edwards, 2011, 2012). But, 3D processes that have been shown to be important in controlling biology were not included (Renault et al., 2016; Gruber et al., 2006). The processes and parameterizations we include in MAMEBUS are as follows: The momentum equations are calculated following Dauhajre and McWilliams (2018). The effect of eddy restratification is parameterized following Gent and McWilliams (1990), eddy stirring along isopycnals is parameterized following Redi (1982) and surface and bottom boundary layer mixing is calculated following Ferrari et al. (2008). The explicit formulation of each of these parameterizations is described in Moscoso et al. (2021). With this study, we use consistent functional representation between all parameter sweeps, but change a specific

reference value (e.g. the functional representation of the wind stress forcing is the same, but the maximum offshore value is varied).

The physical design of this model is meant to capture the behavior of upwelling in an idealized EBUS. Here, we configure the model to represent an idealization of the CCS. The model grid is cast in terrain-following coordinates. The model domain is 400 km across-shore, 50m depth on the eastern (i.e., coastal) boundary of the domain, and 4000m depth on the western (i.e., open-ocean) boundary. The boundary conditions for temperature and nitrate at the western boundary are configured using data from The California Cooperative Oceanic Fisheries Investigations (CalCOFI, `https://calcofi.org/`) at Stations 90 and 100 from 1997 – 2018.

The topography is configured using data from ETOPO5 (Amante and Eakins, 2009), and slightly differs from that presented in Moscoso et al. (2021) by adopting a steeper continental shelf. The model resolution is 60 horizontal grid-points and 60 vertical levels. This corresponds to an approximate grid-spacing of 6.7 km in the horizontal. MAMEBUS employs a stretched vertical coordinate, so the approximate vertical grid-spacing varies across the domain, from a minimum of 0.5 m near the coast to a maximum of $\sim$ 215 m at the western boundary.

The wind stress forcing is configured to approximate the median of monthly climatologies of data from ECMWF Reanalysis v5 (ERA5, Hersbach et al. (2020)) and from the Weather Research and Forecasting Model (WRF V4.1, Skamarock et al. (2019)) from 1997 – 2017. The across-slope component of the wind data is calculated as an along-shore average from 34.5^{o}N to 35^{o}N, and shown as a function of distance from the coast over a 400km offshore extent for comparison to *in-situ* data from Line 80 in CalCOFI data. This line is chosen because it falls between the latitudes where the data used for model configuration and forcing is averaged. Other EBUS configurations can be used, however this choice was based on data availability.

The wind stress profile is formulated as,

$$\tau(x) = \tau_{\max} \tanh\left(\frac{L_x - x}{L_x/\tau_x}\right), \tag{4.1}$$

where $\tau_{\max}$ (N/m^2) is the offshore wind stress maximum, L_x is the width of the model domain, and τ_x is a dimensionless tuning parameter that controls the width of the wind stress curl. Higher values of τ_x correspond to a narrower wind stress curl; however, the magnitude of the offshore wind stress does not change. The actual profile of the wind stress curl is given by $\partial_x \tau(x)$ (N/m^3). The reference wind stress profile is shown in Figure 4.2.

To represent the offshore conditions that are set by processes occurring in the Pacific Ocean we define a 50km sponge layer on the western boundary of the domain. In this sponge layer, temperature and nitrate are restored to profiles that are configured to approximate *insitu* observations. The offshore temperature profile is defined as,

$$T_R(z) = T_{\min} + (T_{\max} - T_{\min}) \cdot \left(\frac{\exp\left(\frac{z}{\Delta T_Z} + 1\right) - \exp\left(\frac{-H}{\Delta T_Z} + 1\right)}{\exp(1) - \exp\left(\frac{-H}{\Delta T_Z} + 1\right)}\right), \tag{4.2}$$

where $T_{\min}$ is the minimum temperature in the water column, $T_{\max}$ is the maximum temperature, ΔT_Z is the temperature decay scale, and $-H$ is the maximum depth of the water column. A reference buoyancy restoring profile is shown in Figure 4.3. At the surface, temperature is also restored to an idealized gradient based on observations from CalCOFI, see Moscoso et al. (2021). The eastern boundary and the ocean floor have no flux boundary conditions.

4.2.2 Biogeochemical Model Configuration

MAMEBUS (Moscoso et al., 2021) is augmented with a size structured NPZD model (SSEM, Moscoso et al. (2022)) based on previous work by Banas (2011) and Ward et al. (2012). Size is used as a proxy for ecological diversity, reflecting strong relationships between an organisms size and resource encounter strategies. This choice greatly reduces the dimensionality of the

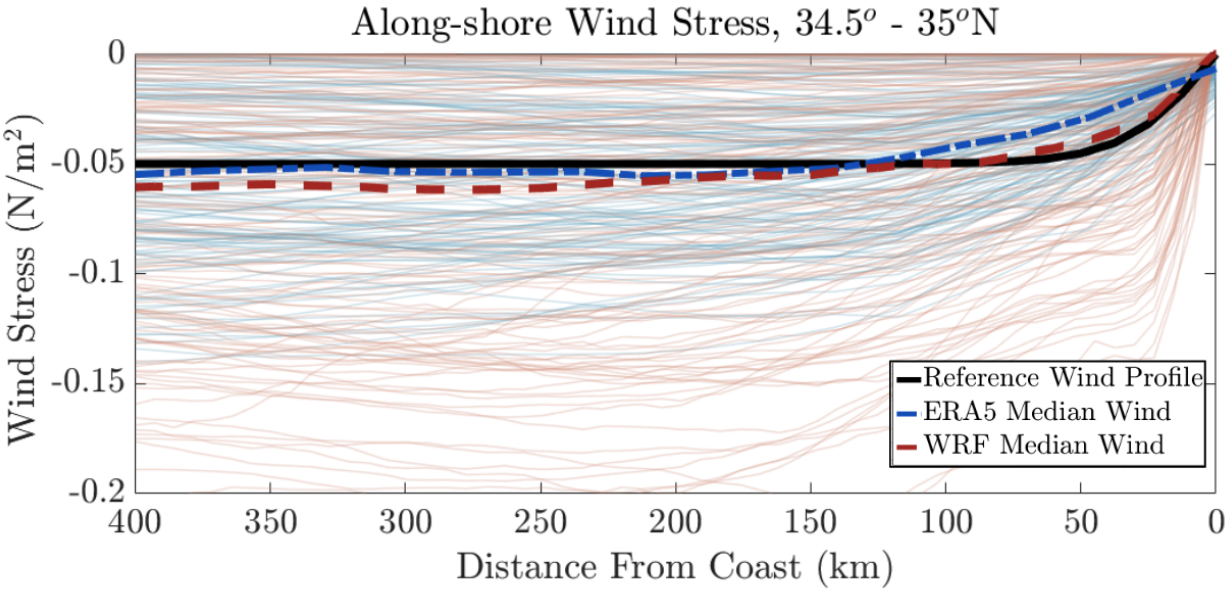

Figure 4.2: Wind profiles derived from ERA5, and WRF, in blue and red, respectively. The thick lines show the median wind profiles for each reanalysis product, and the black line shows the reference wind profile used in MAMEBUS. The thin lines correspond to monthly averaged wind profiles from 1997-2017.

model parameter space (compared to models which simulate functional groups), while capturing important ecological behaviors (Follows and Dutkiewicz, 2011; Sauterey et al., 2017; Loeuille and Loreau, 2005; Banas, 2011). The size-dependent processes in the model include nutrient uptake by phytoplankton, heterotrophic grazing by zooplankton, predator-prey size interactions, plankton mortality, and size diffusion (i.e., mutation). Large phytoplankton have slow uptake rates, tend to be more nutrient limited, and have longer lifespans than their smaller counterparts (Tang, 1995; Eppley et al., 1969). The grazing dynamics are modeled under the assumption that small zooplankton quickly graze phytoplankton of approximately the same size, while large zooplankton prefer proportionally smaller prey, but have slower grazing rates (Hansen et al., 1994). However, this is an approximation that may not be representative of all zooplankton (Kiørboe, 2011). We parameterize phytoplankton

mutations as a weak size diffusion, which allows for plankton to grow or shrink in size over relatively long timescales (Sauterey et al., 2017).

When size structured ecosystem models are highly resolved in trait-space and use size-dependent grazing interactions, the biomass aggregates along preferential modes along the size spectrum – a behavior called quantization (Banas, 2011; Moscoso et al., 2022). In zero dimensions, Moscoso et al. (2022) found that the location of the biomass peaks are approximately explained by a measure of selectivity in zooplankton grazing, called the grazing profile width, $\Delta\ell$. This measures a logarithmic width in size space, indicating that large zooplankton are less selective than smaller zooplankton for the same grazing profile width. Small values of $\Delta\ell$, corresponds to an ecosystem with highly specialized zooplankton grazers. In this configuration, there are more biomass peaks along the size spectrum with more plankton diversity in size space (Vallina et al., 2014). In the limit of $\Delta\ell \to 0$, there is no quantization in biomass. While the formulation of the grazing is responsible for controlling the biomass peaks, the nutrient availability allows for the emergence of large size classes with the approximate spacing between peaks determined by the value of $\Delta\ell$. Quantization occurs on the timescale of approximately one year under both constant (Moscoso et al., 2022) and variable nutrient forcing (Banas, 2011).

The configuration of the model is similar to that presented in Moscoso et al. (2022), with the following changes. In this study, we set $\Delta\ell = 0.2$ as our representative grazing profile width (Hansen et al., 1994). Based on prior simulations, we use 50 phytoplankton and zooplankton size classes, as this is the minimal number of classes to resolve quantization in biomass and converge to a steady state equilibrium over time. The 50 phytoplankton size classes are log-linearly spaced between 0.2 μm and 100 μm, and the 50 zooplankton size classes are log-linearly spaced between 0.5μm and 5000μm. All phytoplankton classes are initialized to a constant value of 0.1 mmol N/m^3, and all zooplankton are initialized to 0.01 mmol N/m^3.

We simulate a single nutrient pool that is configured to represent nitrate. Nitrogen is the

main limiting nutrient in the California Current (Deutsch et al., 2021), and nitrogen fluxes are often used in EBUSs as proxies of productivity (Chavez and Messié, 2009; Messié et al., 2009; Jacox and Edwards, 2012). Note that the model formulation does not explicitly include a distinction between new and regenerated production (Karl, 2002). However, in regions of high productivity, new production often dominates over regenerated production (Sarmiento and Gruber, 2006; Messié et al., 2009). The nitrate profile is initialized to the restoring profile everywhere in the domain, but only restored in the sponge layer after initialization as described in Equation 4.3.

The model includes a single particulate detritus pool, with a constant sinking speed of 10m/day. Thus, we do not include size-dependent sinking or size structure in the detritus component, recognizing that this choice may be important in determining vertical nutrient fluxes to the deep ocean (Kriest, 2002; Polimene et al., 2017). Detritus is initialized to zero everywhere in the domain and at the lower boundary detritus has a no flux condition, and allowed to remineralize in the lowest grid-cell.

At the western boundary, nitrate is restored to an idealized profile defined as,

$$N_R(z) = \begin{cases} 0 & z \leq N_0 \\ N_{\min} - N_{\max} \tanh\left(\frac{z+\zeta_N^0}{\Delta\zeta_N}\right) & z > N_0 \end{cases} \tag{4.3}$$

where $N_{\min}$ is the minimum surface nutrient concentration, $N_{\max}$ is the maximum subsurface nutrient concentration, ζ_N^0 is the nutrient restoring depth, and $\Delta\zeta_N$ is the nutrient decay scale. This functional representation is motivated by an idealized fit to observations, shown in Figure 4.3, with parameters tuned to approximately track the median profile of all observations. Note that both the thermocline and nutricline do not always align in the data (not shown) and are characterized by variable vertical scales. Thus, the profiles of these two variables are varied independently in the parameter sweeps presented in Section 4.2.3.

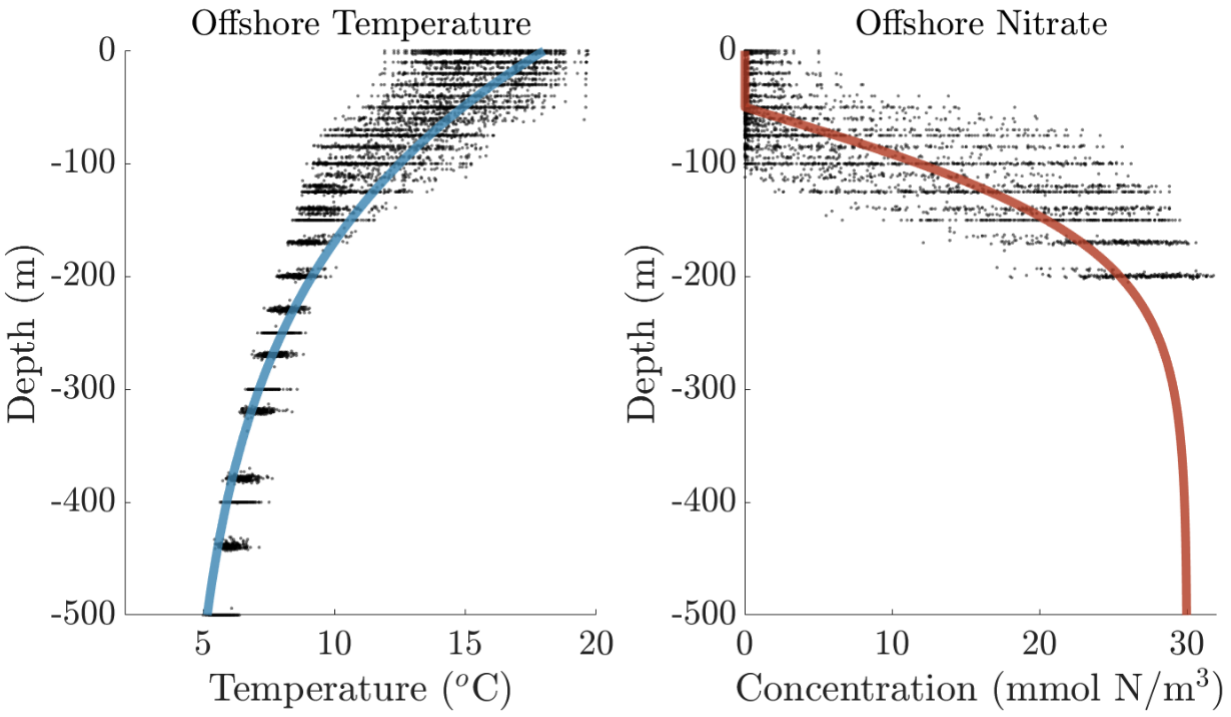

Figure 4.3: Restoring profiles for the temperature (left) and the nitrate (right). The black dots show data taken along Line 80 at stations 90 and 100 from California Cooperative Oceanic Fisheries Investigations (CalCOFI, `https://calcofi.org/`). Each point represents a measured value of nitrate during cruises conducted in January, April, July, and October between 1997 and 2018.

4.2.3 Sensitivity Experiments

The parameter range for the wind profile and nutrient restoring profile are chosen from data and reanalysis products, with perturbations that represents natural variability in the data. The ranges of the eddy diffusivities are informed by previous work by (Colas et al., 2013), (Abernathey and Marshall, 2013) and (Swenson and Niiler, 1996). For each of parameter configuration, the model is spun-up with physics only for 30 model years with constant wind forcing, and buoyancy restoring at the surface and in the western sponge layer. For computational efficiency, the biogeochemical component of the model is activated during

Table 4.1: Parameters varied in this study.

Parameter	Reference Value	Perturbation Range	Data or Reference	Description
$\tau_{\max}$	0.05 N/m^2	[0.01,0.1] N/m^2	ERA5 and WRF Castelao and Luo (2018)	Offshore wind stress maximum
τ_x	12	[4, 18]	ERA5 and WRF Albert et al. (2010)	Width of wind stress curl
ζ_N^0	50 m	[0,100] m	CalCOFI	Nutrient restoring depth
$\Delta\zeta_N$	120 m	[80,160] m	CalCOFI	Nutrient decay scale
κ_{GM}	1200 m^2/s	[600, 1600] m^2/s	Swenson and Niiler (1996)	Maximum surface buoyancy diffusivity
κ_{iso}	2400 m^2/s	[1600, 2400] m^2/s	Abernathey and Marshall (2013)	Maximum surface isopycnal diffusivity

the last 10 model years (corresponding to a total of 40 years of physical integration, and 10 years of biogeochemical model integration). During the biogeochemical spin-up the size-structured ecosystem model, exhibits some internal variability in the location of the biomass peaks, however, the peaks are well established after 1 model year, and sharpen over the remainder of the model run in 0- and 1-D (Moscoso et al., 2022). The biological model is considered spun-up when the L2 norm of the difference in biomass for every size class between time-steps is small ($O(10^{-3}$ mmol N/m^3)), for the reference state, this occurs after approximately five years, but the model is run for twice that length for the full analysis for all parameters.

The range spanned by each parameter is shown in Table 4.1

4.2.3.1 Wind Stress Forcing, $\tau_{\max}$ and τ_x

The magnitude of the wind stress forcing has been shown to control the total upwelling to the surface (Bakun and Nelson, 1991; Capet et al., 2004), while the width of the wind stress curl has been shown to impact the total productivity at the surface combined with eddy compensation (Renault et al., 2016). Therefore, the two parameter sweeps that we choose to control the wind-profile are $\tau_{\max}$, the maximum offshore wind stress, and τ_x, a tuning parameter that allows us to control the width of the wind stress curl. The values of the parameter

sweep, $\tau_{\max}$ and τ_x, are shown in Table 4.1. These values approximately span the range of data from ERA5 and WRF. Jacox and Edwards (2012) find that a nearshore reduction in wind stress reduces inner shelf circulation and bottom boundary layer transport in the region of the wind stress curl. As a result, wind stress profiles with substantial nearshore curl have stronger upwelling and more nutrient injection into the surface mixed layer, while wind stress profiles with less near-shore curl have weaker surface nutrient concentrations (Albert et al., 2010). We suspect this may have an important impact on the total concentration of the near-shore surface chlorophyll maximum, along with the nearshore zonal phytoplankton community structure.

4.2.3.2 Eddies, κ_{GM} and κ_{iso}

As a consequence of upwelling cold, nutrient-rich water to the surface, baroclinic instability and the subsequent generation of eddies occurs in EBUSs with important impacts on zonal transport of nutrients and phytoplankton (Chavez and Messié, 2009; Gruber et al., 2011). Generally, these eddies work to bring heat and buoyancy shoreward and upward, restratifying the ocean and leading to an overall reduction of nutrients at the surface (Gruber et al., 2011). Gruber et al. (2011) also find that eddies work to increase subsurface nutrient concentrations offshore. However there are two components to the eddy parameterization in MAMEBUS that may have distinct impacts on ecosystem diversity: eddy advection (Gent and McWilliams, 1990), and isopycnal mixing (Redi, 1982). In these two parameter sweeps, we vary the strengths of the buoyancy diffusivity κ_{GM}, and the isopycnal diffusivity κ_{iso}. Reference profiles of the buoyancy and isopycnal diffusivity are shown in Moscoso et al. (2021) with surface intensified mixing (Lacasce, 2017). Additionally the reference values and the parameter variations of κ_{GM} and κ_{iso} are given in Table 4.1.

4.2.3.3 Offshore nutrient profile (boundary conditions), ζ_N^0 and $\Delta\zeta_N$

The offshore nutrient profile determines the source waters that are upwelled onto the shelf (Jacox and Edwards, 2012; García-Reyes et al., 2015). In this model, there are two parameters that we vary to determine the effect of changes to the open ocean. First we vary the nutrient restoring depth, ζ_N^0. This parameter allows us to set the level of oligotrophy in the surface ocean. Figure 4.3 shows the variations of the nutrient profile between 1997 – 2018 from Line 80 in CalCOFI. The nutrient restoring depth ζ_N^0, varies from zero nutrients at the surface, to zero nutrients up to 100m depth. Similarly, we vary the nutrient decay scale, $\Delta\zeta_N$, so that our parameter sweep is representative of the variability found in measured nutrient concentrations. The reference values and parameter variations of ζ_N^0 and $\Delta\zeta_N$ are given in Table 4.1.

4.2.4 Model Diagnostics

In this section, we define sub-regions in the model domain that are important to productivity in EBUSs and model diagnostics that will be calculated in each of these regions. The sub-regions we identify are the shelf, the surface chlorophyll maximum (SCM), and the deep chlorophyll maximum (DCM).

4.2.4.1 Continental Shelf

The continental shelf area is defined as the region on the shelf where the mixed layers overlap, shown in orange on Figure 4.4. This region is chosen because upwelling is confined to the bottom boundary layer which directly links the surface to the subsurface. In all of our model simulations, the mixed layers overlap at approximately 25km from the coast. In this study, we do not vary the depth of the mixed layers, however, changes in mixed layer depths may be important in determining the nearshore concentration of plankton. The location of the continental shelf in the reference solution is shown in the orange box in Figure 4.4.

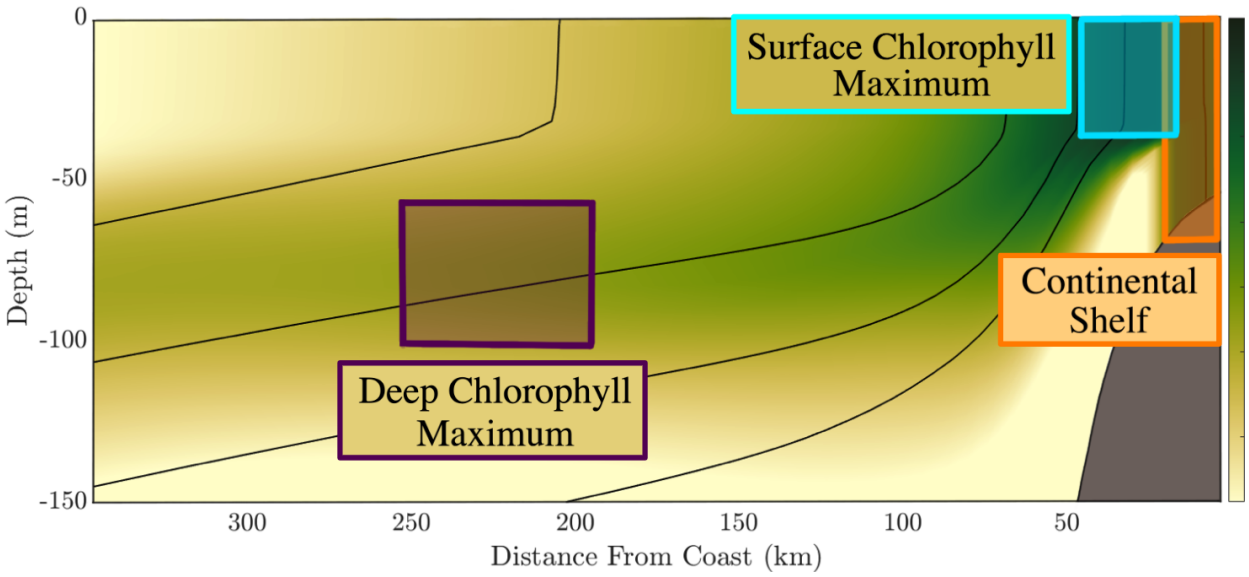

Figure 4.4: A schematic of the locations where ecosystem metrics are calculated. Metrics defined on the 'continental shelf' are area averaged over the region where the mixed layers over-lap. The 'surface chlorophyll maximum' is defined as 25 km around the horizontal center of phytoplankton mass averaged over the mixed layer. The 'deep chlorophyll maximum' is defined as the vertical center of mass of the total phytoplankton concentration averaged over 200-250 km from the coast, and 50 meters vertically.

4.2.4.2 Surface Chlorophyll Maximum (SCM)

We explore the sensitivities of the model diagnostics in the surface chlorophyll maximum. This region is chosen because the surface maximum may not coincide with the region of the model where the mixed layers overlap. This location is additionally important because it gives us a sense of where the subsurface nutrients are ventilated to the surface. We define the location of the SCM as a concentration-weighted distance from the coast, averaged vertically over the surface mixed layer, ζ_{sml}. Mathematically, we define the SCM as,

$$X_{\text{max}}^{\text{surf}} = \frac{1}{P_{\text{tot}}^{A}} \overline{\int (P_{\text{tot}} \cdot x)\, \mathrm{d}x}^{\zeta_{\text{sml}}}, \tag{4.4}$$

Table 4.2: Table showing the area averaged model diagnostics calculated in the surface chlorophyll maximum, on the shelf, and in the deep chlorophyll maximum.

Diagnostic	Description
$X_{\max}^{\text{surf}}$	Surface Chlorophyll Maximum
ζ_{DCM}	Deep Chlorophyll Maximum
P_{tot}	Total phytoplankton concentration
Z_{tot}	Total zooplankton concentration
T	Temperature
U	Total uptake of nutrients by phytoplankton
ℓ_p^*	Concentration-weighted average size
H	Shannon index

where P_{tot}^A is the total phytoplankton concentration in the integrated area, and P_{tot} is the total plankton concentration in the center of each model grid-box. An example of the location of the surface chlorophyll max is shown in the blue box in Figure 4.4.

4.2.4.3 Deep chlorophyll maximum (DCM)

DCMs are a common feature in EBUSs. The depth of the DCM is dependent on the balance between light available in the water column and nutrients available below, in regions where nutrients are not entrained into the surface mixed layer (Cullen, 1982b; Zubkov et al., 2000; Tréguer et al., 2018). Brandini et al. (2014) proposed that a component of the horizontal advection could bring nutrients and productivity into the DCM from regions of strong Ekman forcing, but the magnitude of this contribution is not well constrained.

The DCM is defined as the off-slope region of the domain beneath the surface mixed layer, ζ_{sml} and above $\zeta_e = 200$ m depth, to encompass the depth of the euphotic zone. This location of the DCM in the model domain is chosen to be halfway between the Eastern

and Western boundaries of the domain. This choice was made to include the theoretical maximum depth of the euphotic zone, ~ -115 m in the absence of plankton and detrius, given our formulation of the irradiance profile in the biogeochemical model. The depth of the DCM is calculated as a biomass-weighted average depth,

$$\zeta_{\mathrm{DCM}} = \frac{1}{P_{\mathrm{tot}}} \overline{\int_{\zeta_e}^{\zeta_{\mathrm{sml}}} (P \cdot z)\, \mathrm{d}z}^{\,x} . \tag{4.5}$$

4.2.4.4 Ecosystem metrics

In order to quantify the ecosystem responses to changes in physical forcing, we introduce some metrics to help better capture the responses in the ecological diversity. The first is the concentration-weighted average size,

$$\ell_p^* = \frac{1}{P_{tot}} \sum_i^{n_p} P_i \ell_{p_i} \tag{4.6}$$

where P_i is the concentration of phytoplankton in the i-th size class, $P_{tot} = \sum_i P_i$, is the total phytoplankton concentration, $\ell_{p_i} \log_{10}(\mu\mathrm{m})$ is the size of the phytoplankton in the i-th size class in log-space, and n_p is the number of phytoplankton size classes. If the average size is large, this means that a large portion of the biomass is concentrated in phytoplankton with large sizes. Alternatively small average size means that smaller plankton have most of the biomass along the size spectrum.

An additional metric that we use to determine the responses of ecological diversity in parameter sweeps is the Shannon Index. Following Spellerberg and Fedor (2003), we define the Shannon Index, H as,

$$H = -\sum_{i=1}^{n_p} \frac{P_i}{P_{tot}} \ln\left(\frac{P_i}{P_{tot}}\right). \tag{4.7}$$

The Shannon index is a measure of the evenness in the ecology. At higher values of, H the ecosystem exhibits higher levels of diversity.

We additionally include area averaged diagnostics of total phytoplankton concentration,

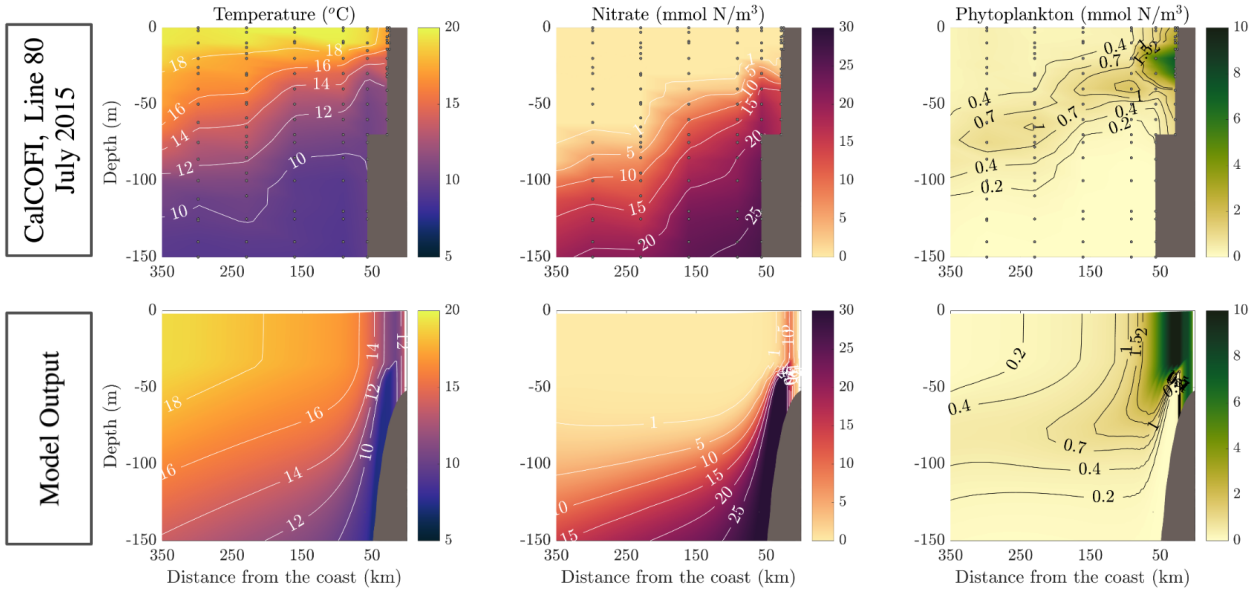

Figure 4.5: Comparison of our model's reference simulation with July 2015 CalCOFI data along Line 80. The black dots are locations where CalCOFI data was collected. The model fields are averaged for the least year of the model run, and the boundary conditions for temperature and nitrate are derived from median offshore properties of stations 90 and 100 along Line 80.

$\overline{P}$, total zooplankton concentration $\overline{Z}$, temperature $\overline{T}$, and the total uptake of nutrients by phytoplankton $\overline{U}$. Here, the overbars denote area averages over the different defined regions of the model domain. The representation of uptake is described in Moscoso et al. (2022).

4.3 Simulated state and ecosystem properties

We compare to data taken from CalCOFI in both the temperature, the nutrients, and the chlorophyll concentration with respect to the reference forcing (see Figure 4.5). As a result, we only expect qualitative agreement between the reference solution and observations because we are comparing a simulation based on average offshore properties.

The simulated and observation phytoplankton biomass are qualitatively similar across

the entire domain. There is a maximum in phytoplankton biomass near the coast, with a transition offshore into a subsurface deep chlorophyll maximum. By using the size structured ecosystem model with large phytoplankton size classes, there is a similar amount of plankton near the eastern boundary of the domain (see Figure 4.5). At the western boundary, the DCM occurs approximately at 80 m depth in the model and 74 m deep in observations. In the center of the domain, the DCM is approximately 67 m deep in the model and 54 m in observations.

The current formulation of MAMEBUS does not include the presence of an along-shore pressure gradient, so there is no idealized along-shore flow, and the model solutions lack an undercurrent (Connolly et al., 2014). We do calculate the meridional component of the momentum equations, which indicate southward transport, but do not include the advection of tracers in and out of the domain. In the presence of the topographically-supported undercurrent, there is local downwelling and incropping of isopycnals near the continental shelf, which would suppress deep upwelling and support local downwelling (Huyer, 1983; Chen et al., 2021). Thus, the model has colder temperatures near the slope and on the shelf.

We now explore the behavior of the ecosystem as a function of size and distance from the coast in the surface mixed layer (see Figure 4.6). We see that plankton biomass aggregates into preferential locations along the size spectrum, which we refer to as quantization (see Chapter 3). Findings presented in Moscoso et al. (2022) conclude that quantization in biomass along the size spectrum is controlled by the formulation of the grazing, with the emergence of large size classes corresponding to high nutrient forcing. The relationship between the grazing profile width, and the spacing between biomass peaks determined in Moscoso et al. (2022) gives a theoretical spacing of $1.66\Delta\ell = 0.33 \log_{10}(\mu\text{m})$ between peaks. The actual width of the spacing between peaks on the shelf is approximately $0.35 \log_{10}(\mu\text{m})$, matching well to the theoretical estimates. This spacing between peaks breaks down at approximately 170 km from the coast, where the width between peaks begins to increase. Offshore, the width between peaks attains a maximum of $1.45 \log_{10}(\mu\text{m})$. We suspect that

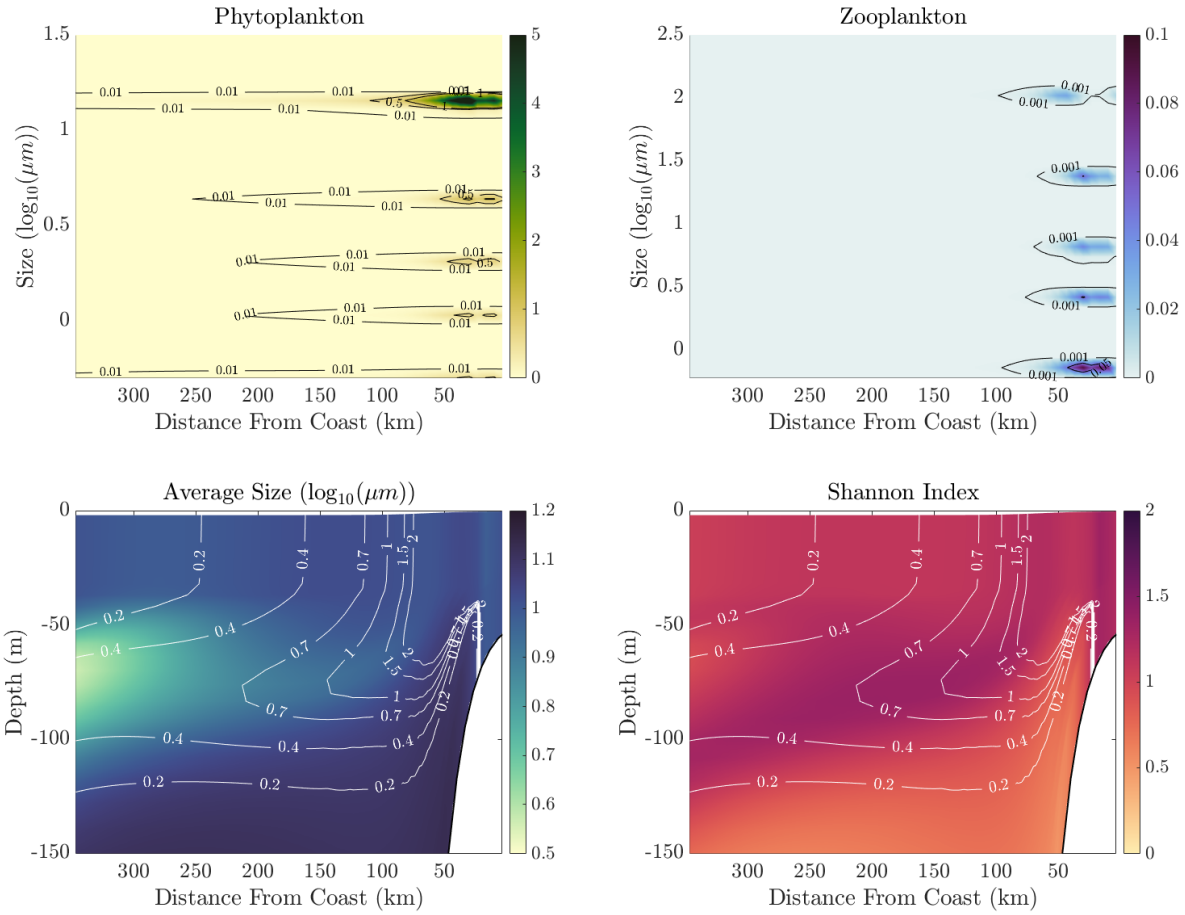

Figure 4.6: Properties of the simulated ecosystem throughout the model domain, outside of the restoring sponge layer. We show the biomass of (a) phytoplankton, and (b) zooplankton, averaged in the surface mixed layer as a function of distance from the coast, and plankton size. The black lines in (a-b) are the biomass contours. The (c) concentration-weighted average size, and (d) Shannon Index are shown with the total concentration of phytoplankton in white contours.

the offshore biomass distribution is controlled by a combination of ecosystem processes and horizontal transport processes.

While the quantization in biomass is the most prominent feature in the plankton distribution, describing the ecosystem as a whole is cumbersome. So, we characterize changes in the ecosystem to parameter perturbations as bulk measure of phytoplankton size and

diversity. Here, we show the ecological diagnostics that we introduced in Section 4.2.4: the concentration-weighted average size and the Shannon Index (Equations 4.6 and 4.7, respectively). We discuss maps of these metrics with the reference model configuration in Figure 4.6.

Figure 4.6 also shows measures of the concentration-weighted average size, ℓ_p, and the Shannon index, H for phytoplankton over the model domain above 150 m depth. Near the coast, in regions with high nutrient concentration and biomass, the average size is the largest. Beneath the surface mixed layer ($Z < -30$ m), the average size decreases and in the deep chlorophyll maximum, the smaller sizes dominate the total biomass. In the SCM, the Shannon index slightly decreases westward from the shelf, as the largest phytoplankton size class dominates in total biomass. Offshore and in the subsurface, the biomass is more evenly distributed, which is reflected in the Shannon Index. Far offshore, between 50 and 100 m depth, where the average size is at a local minimum, the Shannon index slightly decreases, implying that the smallest phytoplankton size classes dominate in this region. Offshore the large size class still persists, however the intermediate size classes are not present above a concentration of 0.01 mmol N/m^3. Below the euphotic zone, the average size of phytoplankton skews high, but the total biomass is small. This size distribution in the deep ocean is likely an artifact of the limiters imposed to prevent phytoplankton and zooplankton concentrations from vanishing and should be disregarded.

4.4 Sensitivity Experiments

To show model sensitivities, we normalize each of the diagnostics described in Section 4.2.4.4 by the value calculated in the corresponding reference solution. In the same vein, the value of each control parameter, p/p_0, is normalized by the corresponding reference value given in Table 4.1. This normalization allows us to compare the relative changes with respect to reference values for all parameters and diagnostics simultaneously. With this normalization,

we conduct linear fits for each of the parameter sweeps and use the slope of the best fit to identify the most important control parameters. Additionally, we calculate the percentage of variance about the best fit line, i.e., the R^2, to determine how well a linear relationship explains the model behavior. Figure 4.7 shows the diagnostics (listed in Table 4.2) and the associated best fit line. The reference values for each of the control parameters in the diagnostic regions is listen in Table 4.3 in Section 4.6. Additionally, a full set of figures for each diagnostic is shown in the Supplementary Information, Section 4.6.

We focus first on the sensitivity of the SCM and DCM positions, and then on the ecosystem response at these location to wind, eddies, and boundary conditions. We also identify significant correlations between various model diagnostics (Figure 4.9).

4.4.1 Regions of model diagnostics

In the reference case, the SCM is located approximately ~ 56 km from the eastern boundary of the model domain. The magnitude of the offshore wind-stress maximum is strongly correlated with location of the SCM, with an increase in wind-stress increasing $\overline{X}^{\text{surf}}_{\text{chl}}$ (Figure 4.7 and 4.9). For brevity in this section, the values of the slopes and corresponding measures of best fit, R^2, are given in Tables 4.4 and 4.5 in Section 4.6. Dynamically, the strength of the wind determines the mean upwelling transport that carries nutrients to the surface (Jacox and Edwards, 2011; Capet et al., 2004; Bakun and Nelson, 1991), so this result agrees with previous findings. The location of the SCM is also sensitive to the nutrient restoring depth, Z^0_N. A shoaling of the nutrient restoring depth pushes the front offshore – i.e., it expands the productive coastal region. Likewise, a deepening moves the location of the SCM shore-ward, although with a weaker sensitivity. This response likely reflects total nutrient concentration in the source waters that are upwelled onto the shelf (Jacox and Edwards, 2011).

The depth of the DCM, with a reference value of ~ -66m depth, is less sensitive to changes in physical drivers. There is some dependence on the nutrient restoring depth, and the offshore wind-stress maximum. An increase in the magnitude of the wind-stress is associ-

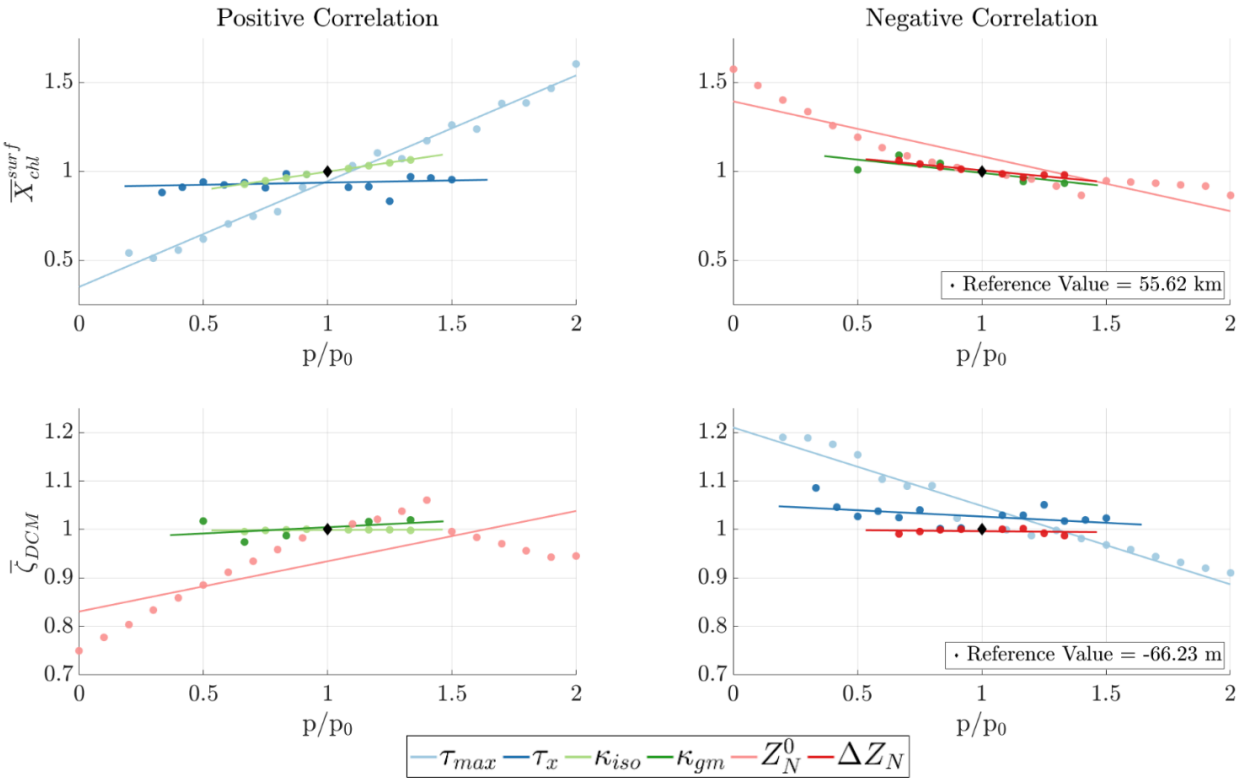

Figure 4.7: Responses of the reference solution-normalized location of the surface chlorophyll maximum (top row) and the normalized depth of the deep chlorophyll maximum (bottom row). The parameter value is shown relative to the reference p_0 for comparison across parameter sweeps.

ated with a shoaling of the DCM, and a strongly linear response (R^2=0.94). With increasing wind-stress, the strength of the upwelling increases, and more nutrients are brought to the surface (Capet et al., 2004; Messié et al., 2009). This shoals the nutricline in the model domain, driving the DCM toward the surface. Like the location of the SCM, the depth of the DCM also exhibits some non-linearity in the response to perturbations in Z_N^0. Previous studies have proposed that the depth of the DCM is determined by a balance between the available light which penetrates from the surface, and the nutrient availability at depth (Cullen, 1982a; Zubkov et al., 2000; Tréguer et al., 2018). In this perturbation experiment, the depth of the DCM deepens with the nutrient restoring depth, although with very deep

resorting depth, this relationship exhibits some nonlinearity. Light penetration from the surface is an important control on the depths of the DCM, at very deep restoring there may be a compensation between the nutrient distribution and light limitation. In fact, we see that the phytoplankton biomass substantially decreases, as nutrient restoring depth deepens.

4.4.2 Wind

Nearly all model diagnostics show a positive sensitivity to the wind stress maximum. Stronger winds increase the concentrations in phytoplankton and zooplankton across the model domain. The uptake on the shelf shows the strongest sensitivity, although the total biomass does not change as dramatically. Diagnostics of ecosystem diversity, ℓ_p and H, show small positive slopes and small R^2 values, indicating weak and more nonlinear sensitivities (Figures 4.12 and 4.13). At very strong wind stress, the average size decreases due to the emergence of a new size class as a consequence of increased nutrients at the surface and in the SCM (see Figures 4.16 and 4.22). Similar nonlinear behavior is further seen in the DCM (see Figure 4.25). This can further be confirmed by a negative correlation in the shelf temperature which implies stronger upwelling near the coast (Capet et al., 2004).

The width of the wind-stress curl has a strong negative impact on the zooplankton biomass in the DCM, while showing a minimal effect on phytoplankton biomass. This impact on zooplankton may reflect a negative impact on phytoplankton uptake. Further, the average size in the DCM increases when the width of the wind-stress curl decreases (Figure 4.15, and 4.25) The response is nearly opposite on the shelf, where a sharper wind-stress curl increases uptake and zooplankton biomass, while uptake slightly decreases at in the SCM. This may indicate some non-linearity in the solutions, for example, see Figure 4.10.

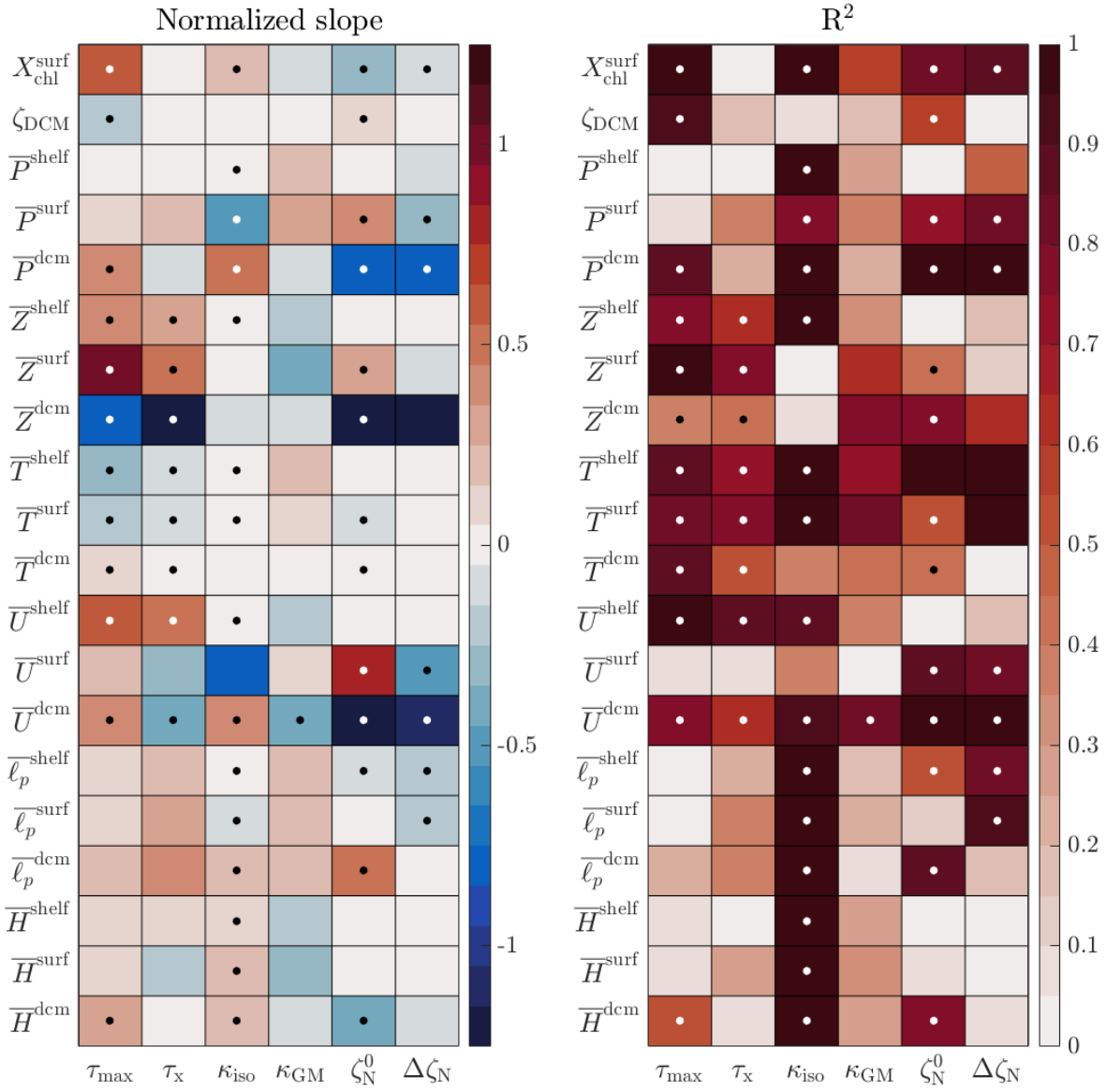

Figure 4.8: Correlation matrix showing the slope of the best fit line for each diagnostic (rows) along with the measure of best fit or R^2 value. The slope of the best fit line for each metric as a function of the control parameters (columns) is shown on the left. Each metric is area-averaged on the shelf, in the surface chlorophyll maximum, and in the deep chlorophyll maximum over one model year. The bullets in the center of the boxes indicate correlations that are statistically significant using the linear Pearson's correlation ($p < 0.01$).

4.4.3 Eddies

The isopycnal diffusivity, κ_{iso} shows statistically significant relationships with plankton biomass in all the diagnostic regions. The total phytoplankton biomass in the SCM and DCM have strong negative and positive slopes, respectively. This suggests that κ_{iso} transfers nutrients and phytoplankton from the SCM to the DCM. Previous work by Gruber et al. (2011) showed that eddies tend to sequester nutrients to depth and decrease surface productivity, a finding consistent with our results. While we find statistically significant relationships between the average phytoplankton sizes and the Shannon Index in the diagnostic regions, these relationships are weak (see Figures 4.18). In the SCM, higher isopycnal diffusion slightly decreases the average size of phytoplankton, while increasing the Shannon Index. Similar patterns are observed on the shelf (Figure 4.23). In both regions, the slight increase in diversity likely corresponds to a reduction of biomass in the larger size classes. Finally, in the DCM, both average size and diversity increase, likely as a result of increased nutrient supply by eddy stirring along isopycnal surfaces (Figure 4.26).

The effect of eddy restratification κ_{GM} on the model diagnostics is small overall. On the shelf and in the SCM, increasing κ_{GM} corresponds to an increase in the total phytoplankton, but a decrease of total zooplankton. The average size of the phytoplankton increases, and the Shannon index decreases, implying that the biomass shifts toward larger sizes. However, the only statistically significant correlation is for the average uptake in the DCM. With increasing κ_{GM}, the the total uptake in the DCM decreases as the surface ocean gets more stratified.Overall, the slopes of most of the relationships are small, with low R^2 values. Section 4.6 shows substantial variability about the best fit line, suggesting nonlinearities in the response to changes in the eddy fluxes (see Figures 4.19, 4.23, and 4.26).

4.4.4 Offshore nutrient profiles

The nutrient restoring depth has strong impacts on the ecosystem behavior in the DCM. The total biomass of plankton in the DCM has strong, statistically significant negative slope, implying that as the nutrient restoring depth deepens, the phytoplankton concentration decreases (see Figures 4.8 and 4.14).Additionally, the average size increases in the DCM, and the Shannon index decreases implying that larger sizes out-compete smaller sizes in this region (see Figure 4.27). This may be a consequence of imposed limits on a minimum concentration of plankton biomass, and thus requires further investigation. The decrease in average uptake also supports this conclusion, as larger sizes have slower uptake rates. On the shelf, the relationship between the nutrient restoring depth and temperature is statistically significant, with positive slopes implying that, as the nutrient restoring depth deepens, more plankton biomass remains at the surface (see Figure 4.24). The average size has a lightly negative correlation, implying that the phytoplankton at the surface are overall smaller as the nutricline deepens as a consequence of reduced nutrient availability (see Figures 4.20 and 4.20).

The nutrient decay scale, which approximates the thickness of the nutricline, reduces total plankton biomass in the DCM. However, the average size and the Shannon index in the DCM are not as sensitive to this parameter (Figure 4.27). In the SCM, the total plankton concentration decreases, likely driven by a decrease in total concentration of nitrate in source waters. This trend is further supported by a decrease in the average uptake (see Figure 4.21). While the total phytoplankton and zooplankton concentration decreases, the size distribution does not change significantly, or slightly decrease. At the SCM, there is a statistically significant decrease in the total phytoplankton concentration and total uptake reflecting lower nutrient concentrations in the source waters. We also observe a statistically significant decrease in the average phytoplankton size on the shelf and at the surface (Figure 4.24). However, the trends in phytoplankton biomass and nutrient uptake are not statistically significant.

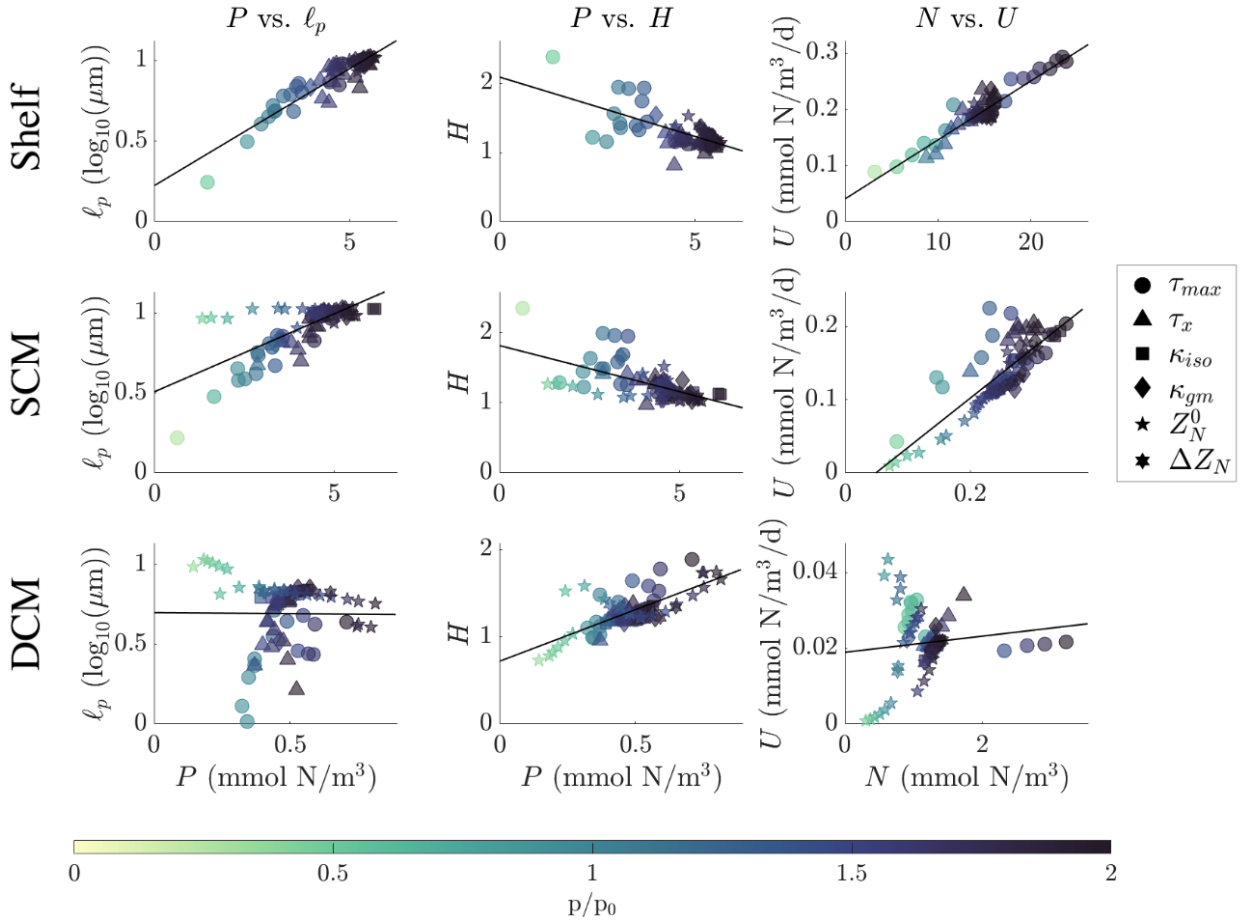

Figure 4.9: Relationships between measured concentrations of phytoplankton and size (left), phytoplankton biomass and Shannon Index (center), and nitrate and uptake by phytoplankton (right). These relationships are calculated on the shelf (top row), the surface chlorophyll maximum (center row), and in the deep chlorophyll maximum (right) across the entire suite of simulations. The color of the marker is associated with the normalized magnitude of the parameter sweep with darker colors indicating the larger values.

4.4.5 Controls on ecosystem composition

Figure 4.9 shows the correlations between model diagnostics in the surface, SCM, and DCM. This comparison allows us to identify likely controls on ecosystem composition with respect to nutrient concentration and phytoplankton biomass.

On the shelf, we observe a linear relationship between the total phytoplankton concentration and the average size across our parameter sweeps. This indicates that as total phytoplankton concentration increases, the average size also increases, in agreement with previous studies (Taylor et al., 2012; Worden et al., 2004; Van Oostende et al., 2018; Moscoso et al., 2022). Similarly, as the total nutrient concentration varies on the shelf, the total uptake shows a linear response, increasing with nutrient concentration across our parameter sweeps. The Shannon Index, however, decreases with increasing phytoplankton concentration. An increase in the average size, but a decrease in the Shannon Index indicate that the largest size class contributes to most of the biomass on the shelf. The behavior is similar in the SCM. A major outlier occurs in the relationship between the total phytoplankton biomass and average size with respect to the nutrient restoring depth (see Figure 4.8). In the SCM, away from the region of strongest upwelling, the total nutrient concentration is much smaller than the shelf concentration; however, the phytoplankton biomass is approximately the same. This may be a consequence of Ekman transport in the surface mixed layer. Additionally, the Shannon Index decreases with increasing phytoplankton biomass, indicating that most of the biomass in the SCM comes from the largest phytoplankton size class.

The total biomass and average size are not well correlated in the DCM. Similarly, the total nutrients and uptake are also not well correlated. A potential explanation for these responses is that the ecosystem composition in the DCM could potentially be impacted by Ekman transport or horizontal advection from the shelf or SCM, which would bring larger plankton and nutrients into the domain. The nutrient restoring depth parameter sweep is a major outlier in the relationship between average size and plankton biomass in the DCM. In this parameter sweep, we see that as the nutrient restoring depth deepens, the average size increases (see Figure 4.15), however the total phytoplankton concentration decreases. This behavior could work to optimize the competition with respect to size.

Additionally, we observe a wide scatter in the relationship between total nutrients and uptake in the DCM. The outliers in this relationship are in model solutions with higher

offshore wind-stress curl. While the total uptake with respect to the wind-stress do not have major outliers (see Figure 4.14), the total nutrient concentration seems to be the reason for the large deviation in the trends. This may be a result of the strong strength of upwelling, which would bring more nutrients to the surface, with nutrient intrusions into the DCM in regions of stronger upwelling.

We observe a strong, positive relationship between the total phytoplankton concentration and the Shannon Index in the DCM, unlike in the SCM and on the shelf. We see that as the total phytoplankton concentration increases, more size classes are able to emerge, increasing the amount of diversity in the ecosystem. Furthermore, the phytoplankton biomass is much lower in the DCM with a small average size (see Figure 4.6), and thus a few small size classes (Moscoso et al., 2022).

4.5 Discussion

Strong productivity in EBUS is driven by the upwelling of dense, nutrient rich water, which supports large phytoplankton blooms, and diverse ecosystems (Bakun and Nelson, 1991; Chavez and Messié, 2009). In regions of high productivity, large phytoplankton contribute to most of the biomass (Hood et al., 1991). In contrast, in regions of low productivity, smaller phytoplankton dominate (Zubkov et al., 2000; Worden et al., 2004). While previous work have identified patterns of ecosystem productivity and size, it is unclear which physical parameters impact plankton diversity and size structure the most, and to what extent. In this study, we conduct a systematic sensitivity analysis to determine the important controls of ecosystem productivity and diversity in an idealized EBUS tuned after the California Current System. We show that the ecosystem responses in three dynamically distinct regions: the continental shelf, the surface chlorophyll maximum, and the deep chlorophyll maximum. The relationships identified in this study are thus ideally suited to allow formulation or mechanistic scaling laws that relate physical drivers to ecosystem characteristics in EBUS.

We find that changes in the wind stress maximum and the nutrient decay scale have the largest impacts on planktonic biomass. Previous work has identified that the magnitude of the offshore wind stress is responsible for setting the total upwelling nutrient fluxes (Bakun and Nelson, 1991; Chavez and Messié, 2009; Messié et al., 2009; Jacox et al., 2014, 2018; Fiechter et al., 2018). Through all three diagnostic regions in our model, we find that the phytoplankton biomass increases with the wind stress maximum as a consequence of increased upwelling (measured by a decrease in temperature on on the shelf and in the SCM). On the shelf and in the SCM, phytoplankton show increasing uptake rates, but the total phytoplankton concentration exhibits saturating behavior, which can be explained by increased grazing by zooplankton (see Figures 4.8, and 4.12).

The offshore depth of the nutricline, ζ_N^0 shows a similar trend as phytoplankton biomass, with an increase in productivity in the SCM and a decrease in the DCM with deepening nutriclines. The diagnostic regions of the model are sensitive to the nutricline depth, with the SCM moving shoreward, and the DCM deepening with increasing nutricline depths. The decrease in plankton biomass in the DCM can be explained by a deepening DCM, which would reduce the total light penetrating from the surface, hence reducing productivity. The surprising response in this perturbation experiment is the increase in plankton biomass in the SCM. This trend may be explained by a shoreward shift in the SCM, which would increase the total phytoplankton biomass as, $\overline{P}^{\text{surf}} < \overline{P}^{\text{shelf}}$, see Figures 4.8, 4.10, and 4.12. Chavez and Messié (2009) note that shoaling of the nutricline in EBUSs increases offshore surface productivity. This response in the model can be seen in the location of the SCM, which has a large offshore extent with very shallow nutricline depths, and in the DCM, which moves toward the surface.

Previous work indicates that a combination of eddy advection and along-isopycnal mixing are responsible for surface nutrient subduction (Gruber et al., 2011; Colas et al., 2013). The studies conducted by Gruber et al. (2011) and Colas et al. (2013) used an eddy resolving regional model of the CCS (Gruber et al., 2006), and the Peru-Chile System (Colas et al.,

2012), with coupled eddy advective and diffusive fluxes. However, in our model, we are able to decouple these effects and study their consequences in isolation. Perhaps surprisingly, ecosystem properties appear very sensitive to perturbations in the isopycnal diffusivity, κ_{iso}. Variations in ecosystem properties with respect κ_{iso} show strongly linear relationships that are highly statistically significant. Previous work has shown that eddies work to remove nutrients and other tracers from the surface, and subduct them beneath the euphotic zone (Gruber et al., 2011; Kessouri et al., 2020). The quantities that more directly reflect this eddy-driven mechanism are the total concentration of phytoplankton, the total concentration of zooplankton, and the uptake of nutrients by phytoplankton. Increased eddy stirring reduces the phytoplankton and zooplankton concentration at the surface, and suppresses uptake of nutrients. In the DCM, on the other hand, there is an increase of phytoplankton and zooplankton, with increased uptake rates, which may reflect the eddy-driven supply of nutrients to the subsurface by subduction. The impact on the average plankton size and ecosystem diversity in the SCM and DCM, however, is minimal, suggesting that ecosystem diversity may be predominantly controlled by the grazing dynamics internal to the ecosystem (Vallina et al., 2014).

The impact of eddy advective fluxes, however, does not align with previous studies (Gruber et al., 2011; Colas et al., 2013). We find that variations in the buoyancy diffusivity, κ_{GM} in many cases have the opposite effect than the isopycnal diffusivity. For example, the correlation between κ_{GM} and plankton biomass on the shelf and in the surface is positive, while the correlation in the DCM is negative (see Figures 4.8, 4.10, 4.12, and 4.14). Thus, we suggest that, at least in the California Current System, eddy quenching is predominantly driven by eddy stirring along isopycnals.

With the exception of the wind stress maximum and the depth of the nutricline offshore, phytoplankton biomass between the SCM and DCM show nearly always opposite correlations. Phytoplankton biomass increases in the SCM and decreases in the DCM with narrower wind stress curl, a stronger eddy buoyancy diffusivity, and deeper nutriclines. The oppo-

site behavior occurs with increasing isopycnal diffusivity. In the DCM, plankton biomass decreases; however, the potential mechanism for controlling this behavior has not been identified. Di Lorenzo (2003) and Rykaczewski and Checkley (2008) found that wider wind stress curl shoals isopycnal surfaces, which may impact the concentration of nutrients transported into the DCM. As a result, we may expect to see a shoaling of the DCM with smaller values of τ_x, however, the physical locations of the diagnostic regions remain largely unchanged. This disagreement with previous work may arise from the lack of momentum advection in the current physical model formulation – an important driver of interior upwelling in the absence of an along-shore pressure gradient (Lentz and Chapman, 2004; Gruber et al., 2011; Jacox and Edwards, 2011; Connolly et al., 2014). These anti-correlated behaviors between the SCM and DCM across many model control parameters may point to connectivity between these two diagnostic regions, but the mechanisms that control this behavior require deeper investigation.

In this study, we focus on a small number of drivers that have been shown or suggested to affect the ecosystem behavior in EBUS. However, additional controls may influence ecosystem diversity in these regions, and call for future studies. For example, we do not include variation in the thickness of the surface and bottom mixed layers. Within the surface layer, phytoplankton are vertically mixed and exposed to a variety of light conditions as a consequence of light attenuation (Sverdrup, 1953; Huisman et al., 1999; Obata et al., 1996; Mahadevan et al., 2012), which may be important in determining the ecosystem composition, specifically nearshore where surface and bottom mixed layer merge. In the absence of along-shore pressure gradients, upwelling is mostly constrained to the bottom boundary layer (Lentz and Chapman, 2004; Jacox and Edwards, 2011). Previous studies have shown that the thickness of the bottom boundary layer increases in the presence of upwelling favorable winds, which likely impacts the nutrient availability on the shelf and in the SCM (Trowbridge and Lentz, 1998; Perlin et al., 2005).

We do not include variations in the topography in this study. The continental slope has

been shown to have important impacts on the strength of upwelling (Jacox and Edwards, 2012; Lentz and Chapman, 2004), and the depth of the shelf may be important in controlling the vertical exchange of nutrients with the bottom boundary layer (Perlin et al., 2005). Finally, MAMEBUS has the ability to explore the effect of idealized along-shore circulation, but we did not explore this component of the model. However, this may be important for the transport of subpolar or subtropical waters with different nutrient contents, and the delivery of nutrients in the subsurface by the poleward undercurrent.

While we focus predominantly on the lower trophic ecosystem, the findings in this study have the potential to inform the larger food-web diversity (Andersen et al., 2016; Stock et al., 2017). In EBUSs and other productive regions of the global oceans, high productivity, dominated by large phytoplantkon sizes generally supports short, productive food-webs (Chavez and Messié, 2009) and rich fisheries (Ryther, 1969). Along with identifying potential controls on plankton diversity in EBUSs, we also show the persistence of biomass quantization in a highly-resolved size-structured ecosystem model with horizontal heterogeneity under a range of physical regimes. Similar to the findings presented in Banas (2011), Vallina et al. (2014), and Moscoso et al. (2022), while plankton productivity appears to be controlled by the nutrient availability, species diversity – here manifest as size quantization – is controlled by the specialization of grazing behavior.

The relationships between ecosystem properties shown in Figure 4.9 provide new insight into the responses of multiple metrics of ecosystem diversity and productivity to more regularly measured quantities (e.g. phytoplankton biomass and nutrient concentration). These findings may be extended and tested in realistic three-dimensional regional modeling efforts, and guide the development of new theoretical scalings.

4.6 Appendix to Moscoso et. al. (in prep): Supplementary Figures

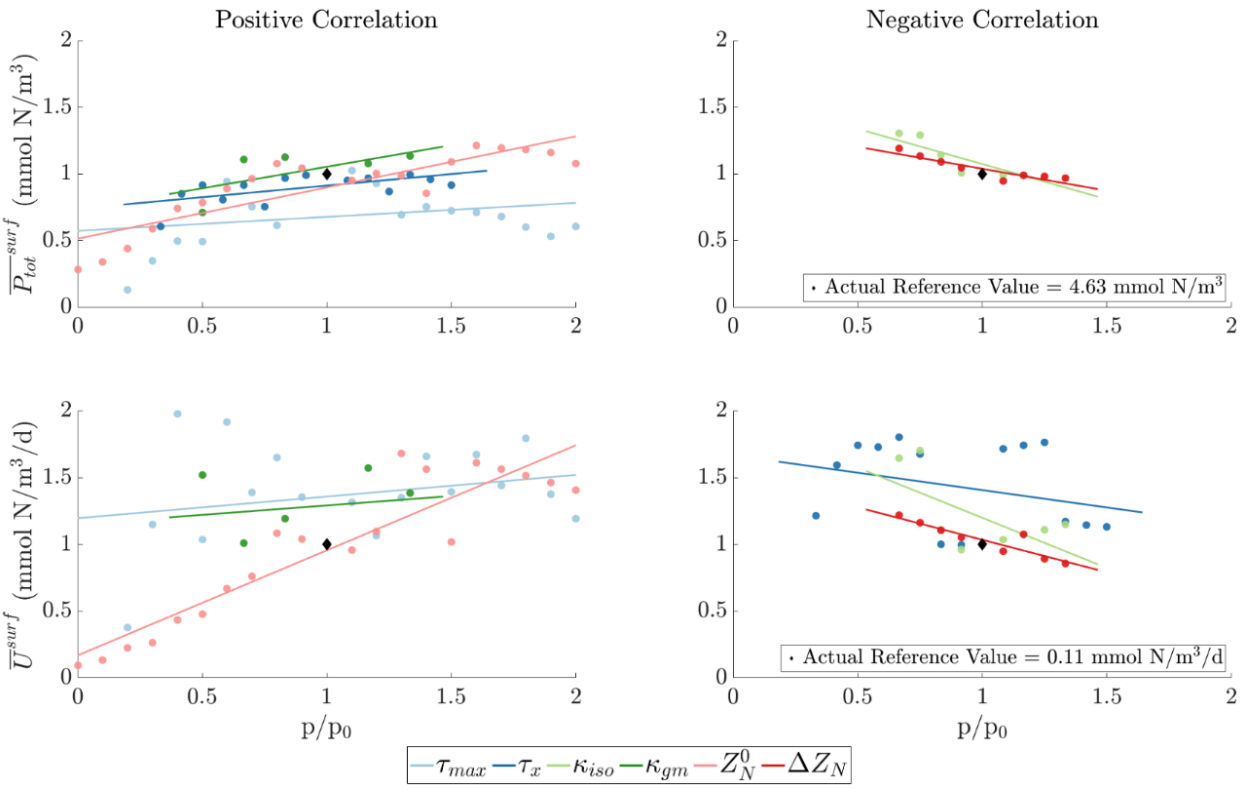

Figure 4.10: Phytoplankton concentration and uptake in the SCM

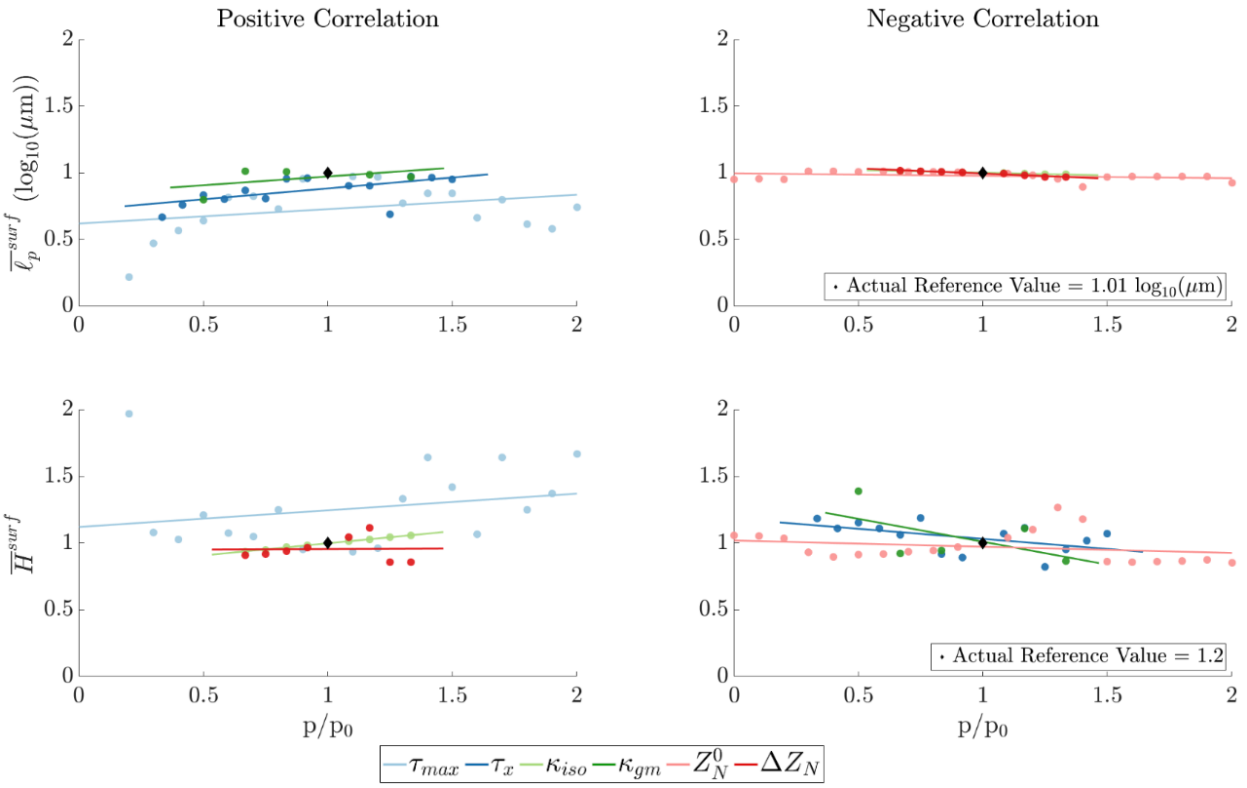

Figure 4.11: Average phytoplankton size and Shannon index in the SCM

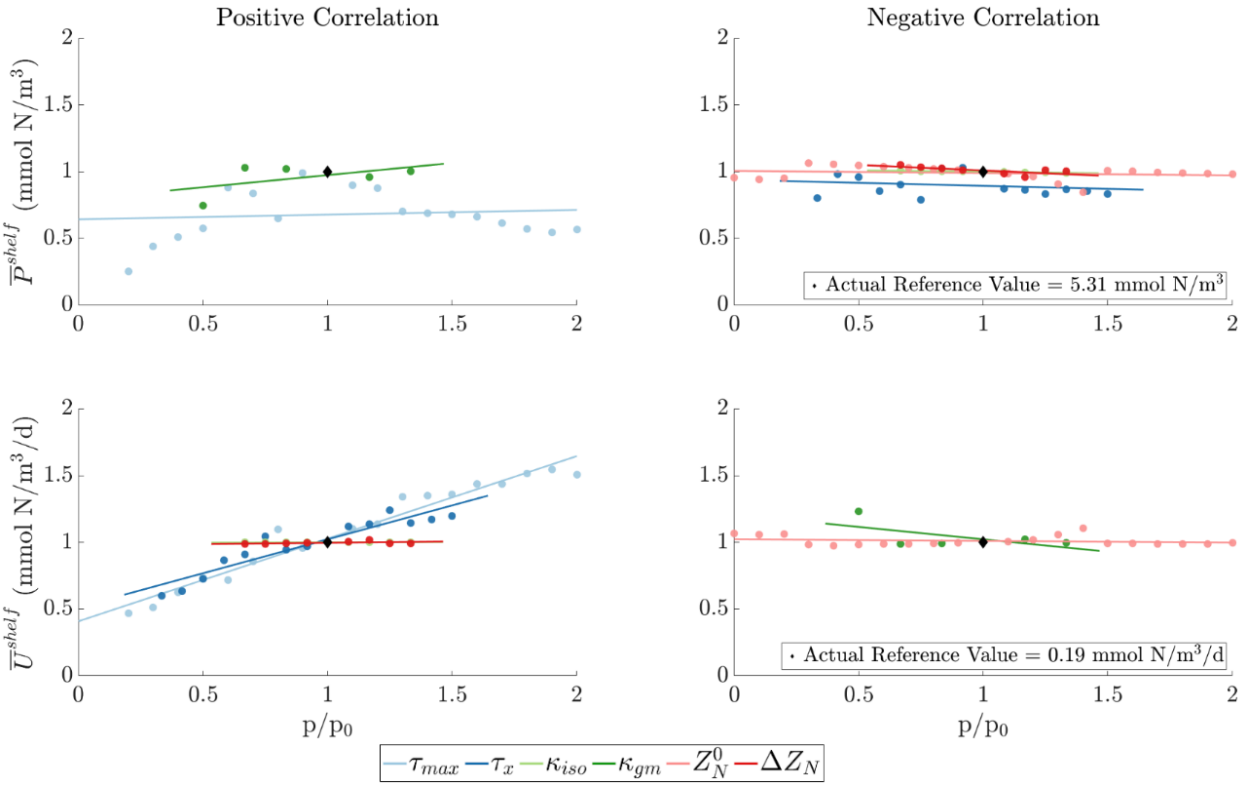

Figure 4.12: Phytoplankton concentration and uptake on the shelf

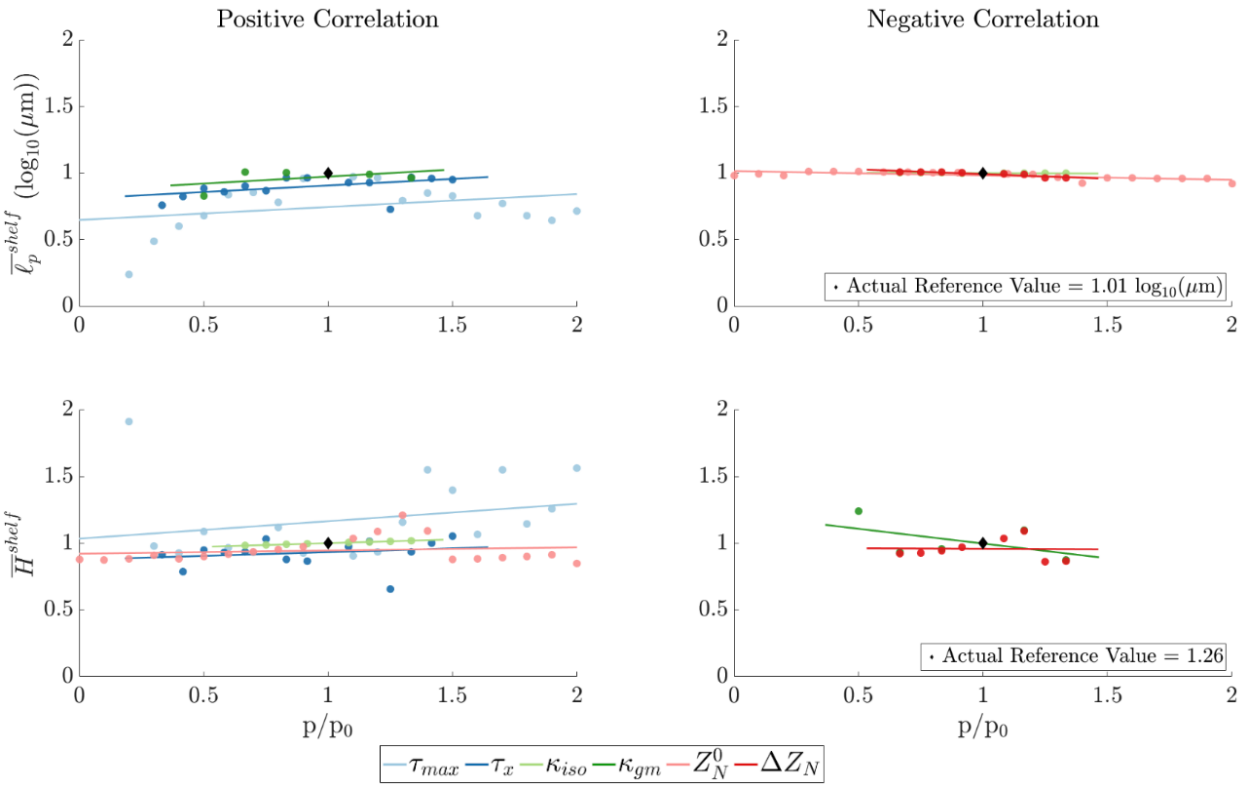

Figure 4.13: Average phytoplankton size and Shannon index on the shelf

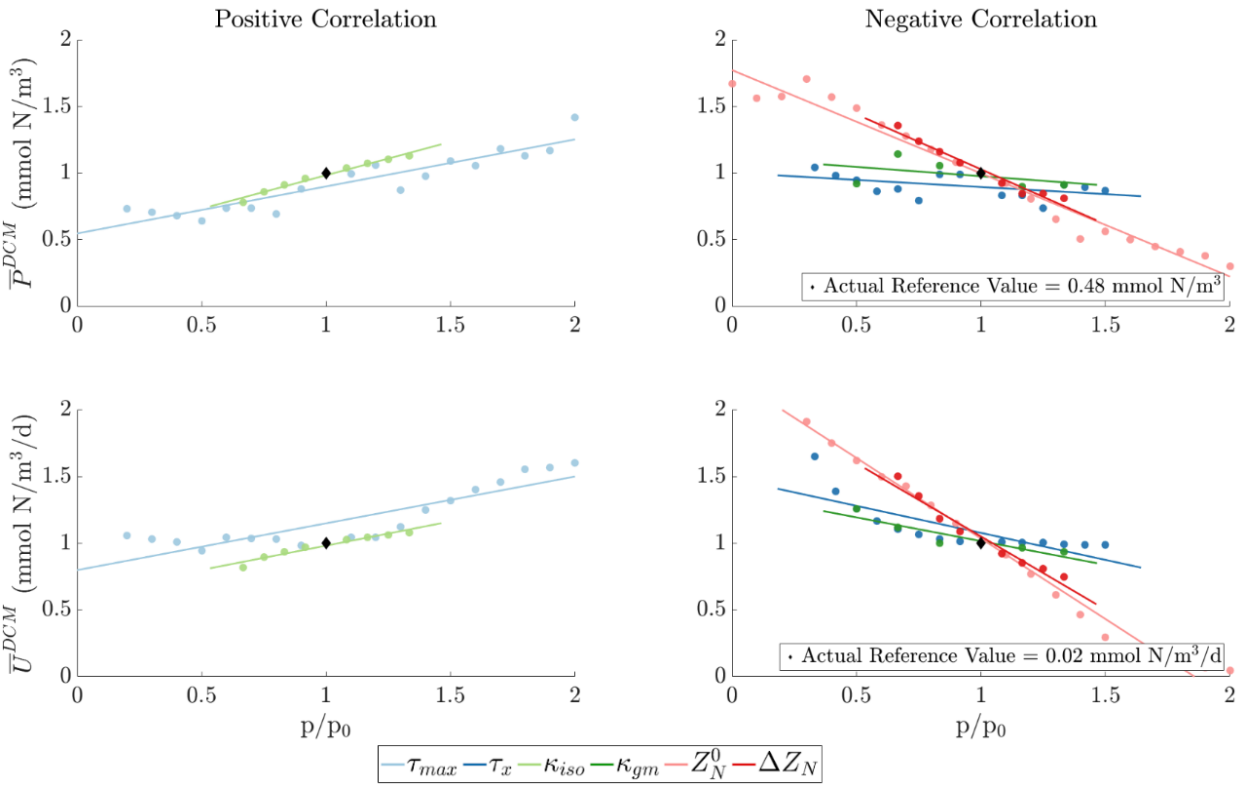

Figure 4.14: Phytoplankton concentration and uptake in the DCM

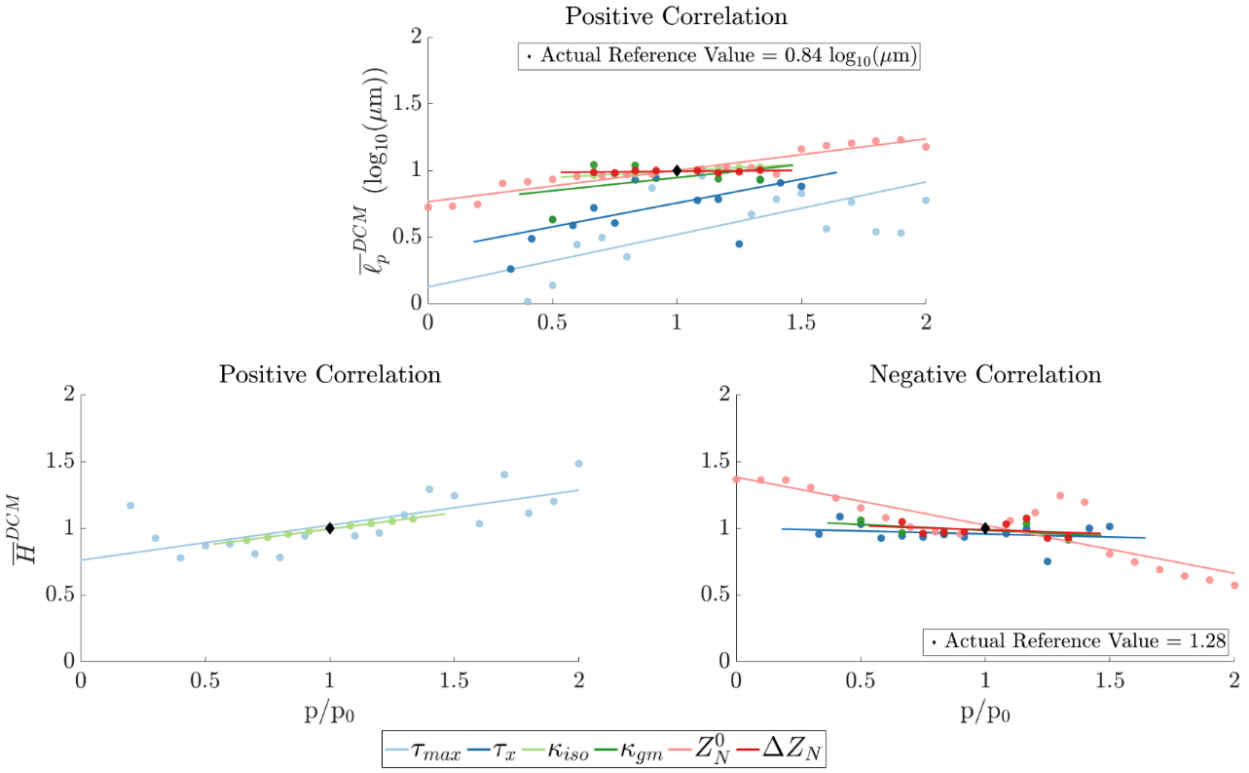

Figure 4.15: Average phytoplankton size and Shannon index in the DCM

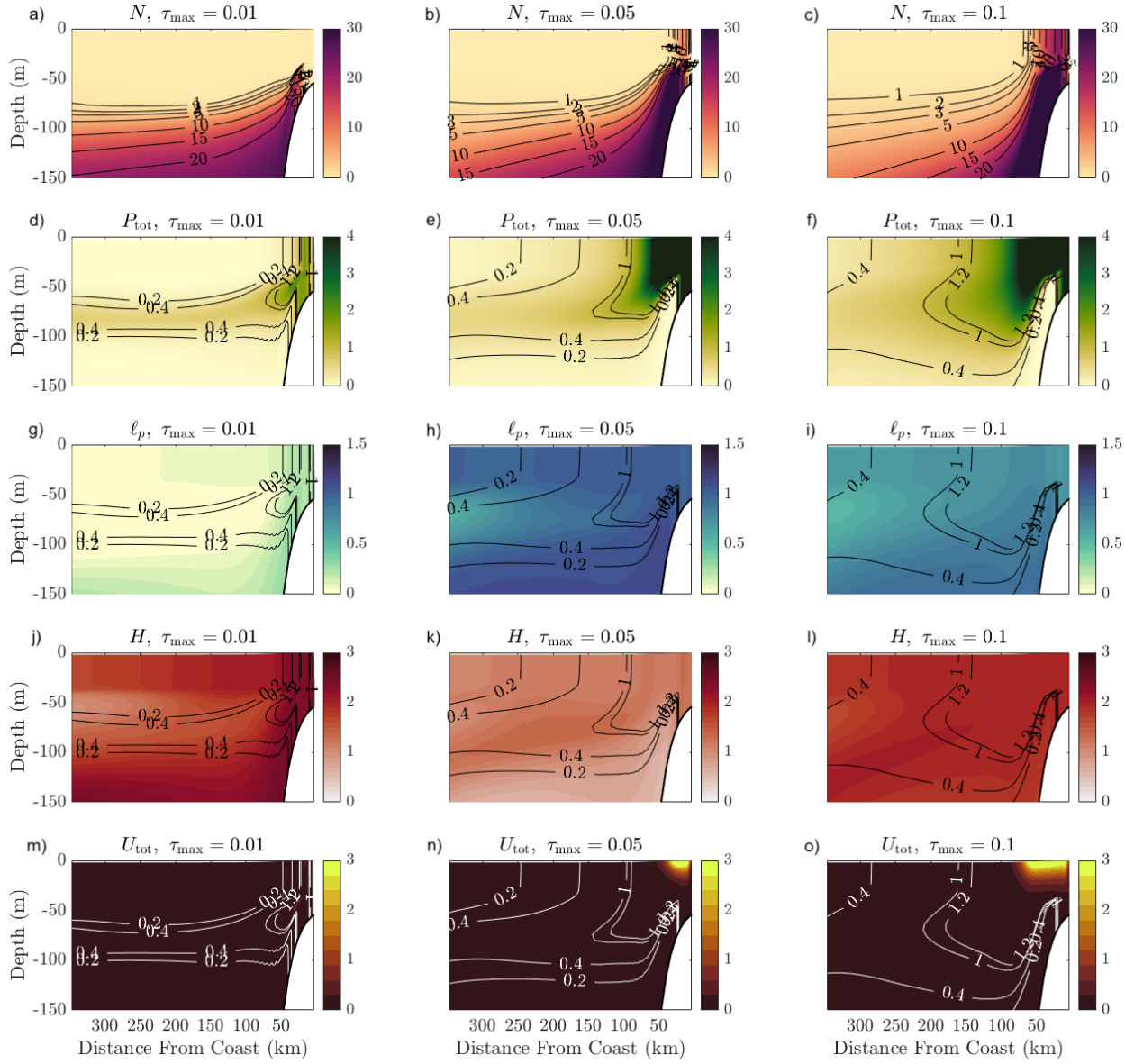

Figure 4.16: Distributions of nutrient (a,b,c), phytoplankton (d,e,f), average size (g,h,i), Shannon index (j,k,l), and uptake (m,n,o) with the minimum (left column), reference (center column), and maximum (right column) values of wind stress maximum, $\tau_{\max}$.

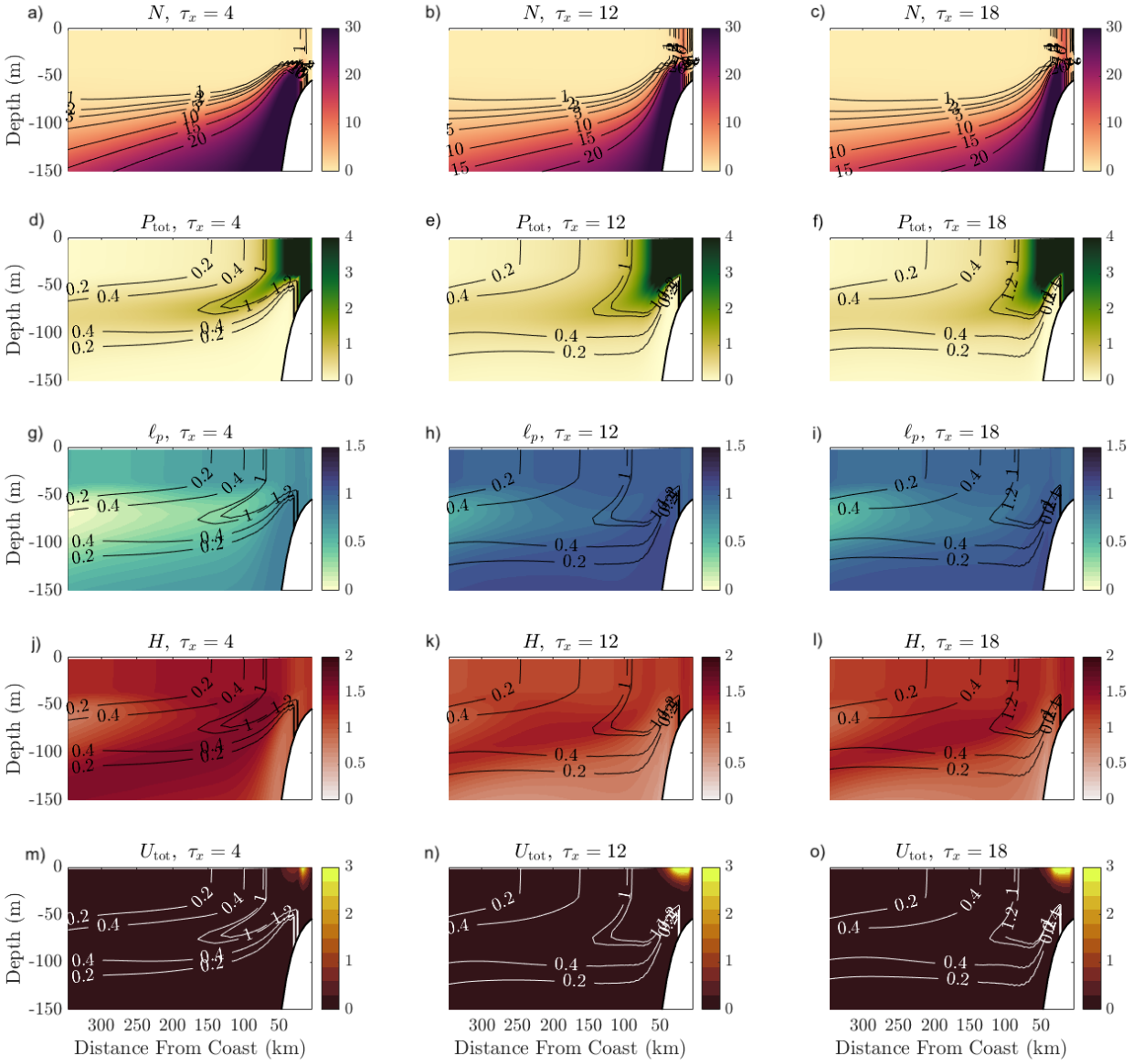

Figure 4.17: Same as 4.16, but for width of wind stress curl, τ_x.

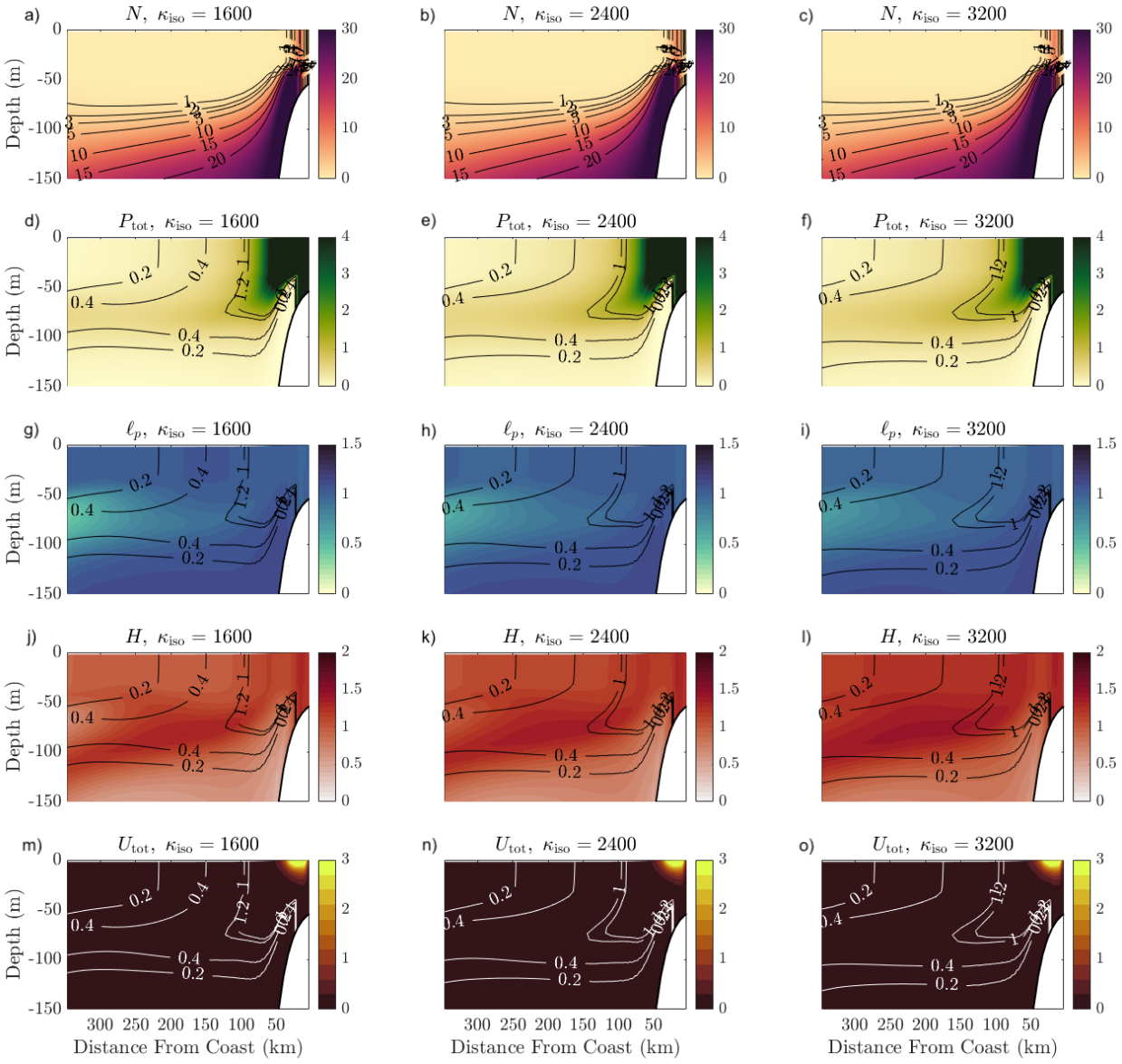

Figure 4.18: Same as 4.16 but for isopyncal diffusivity, $\kappa_{\rm iso}$.

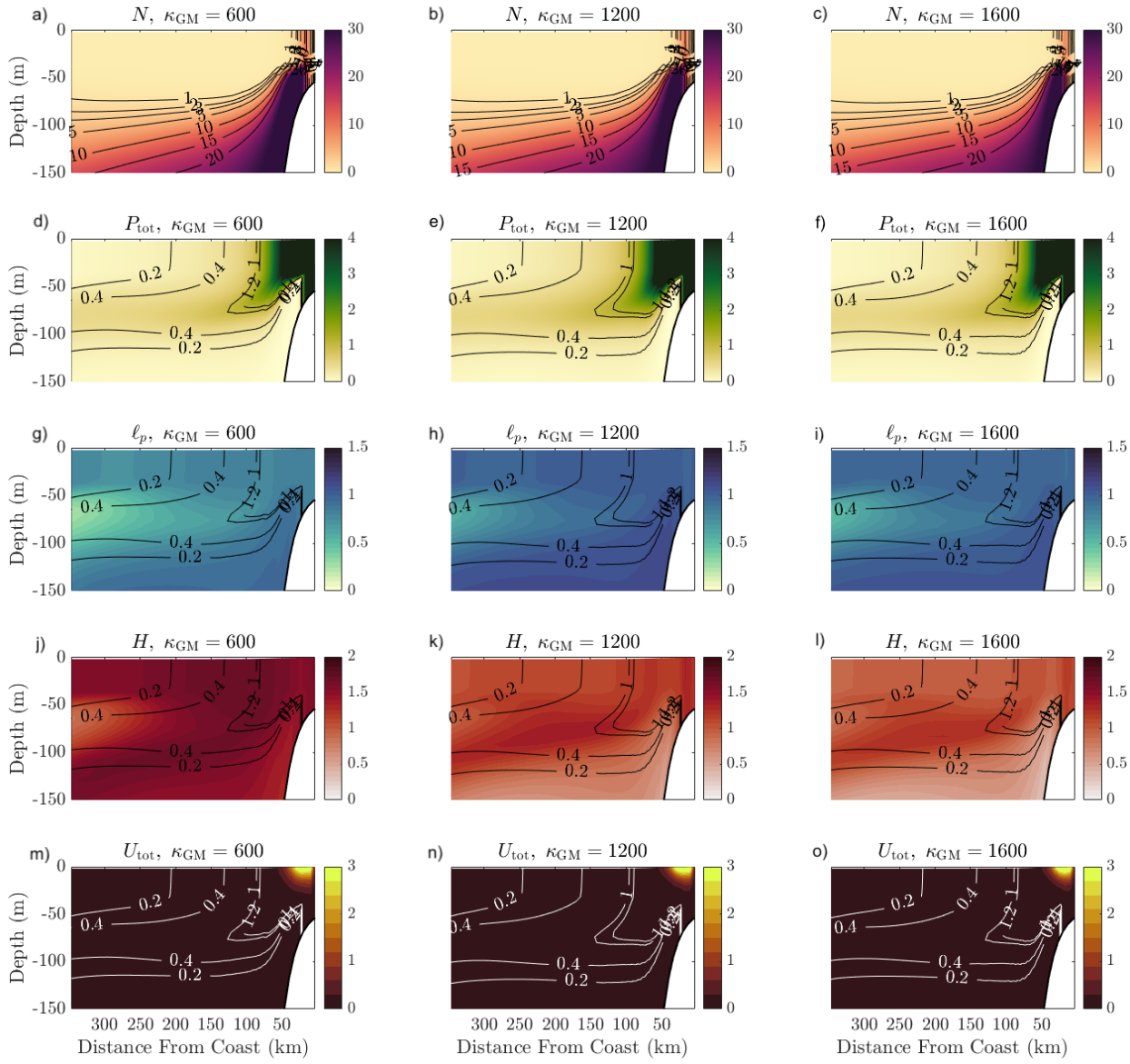

Figure 4.19: Same as 4.16 but for buoyancy diffusivity, κ_{GM}.

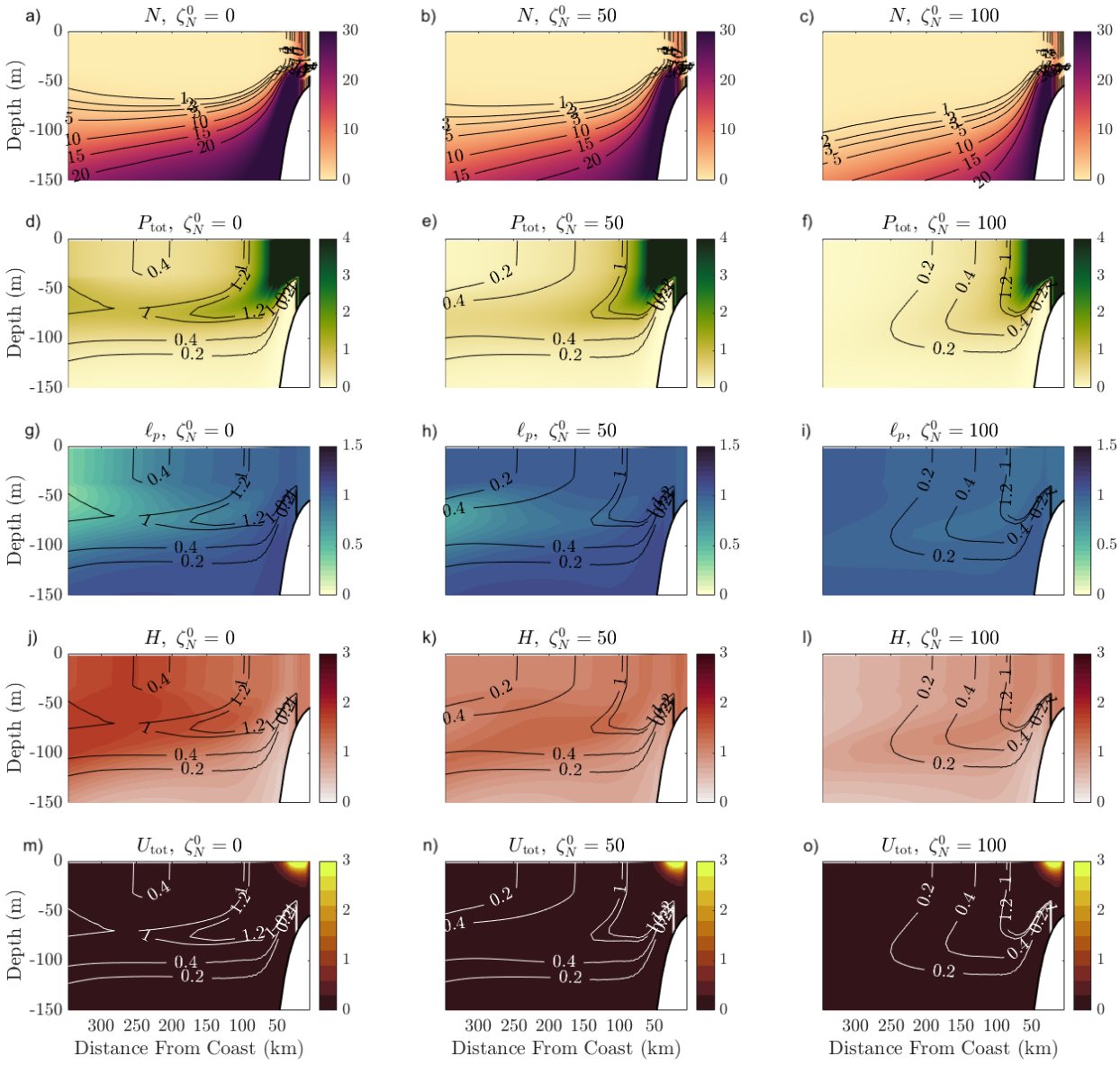

Figure 4.20: Same as 4.16, but for nutrient restoring depth, ζ_N^0.

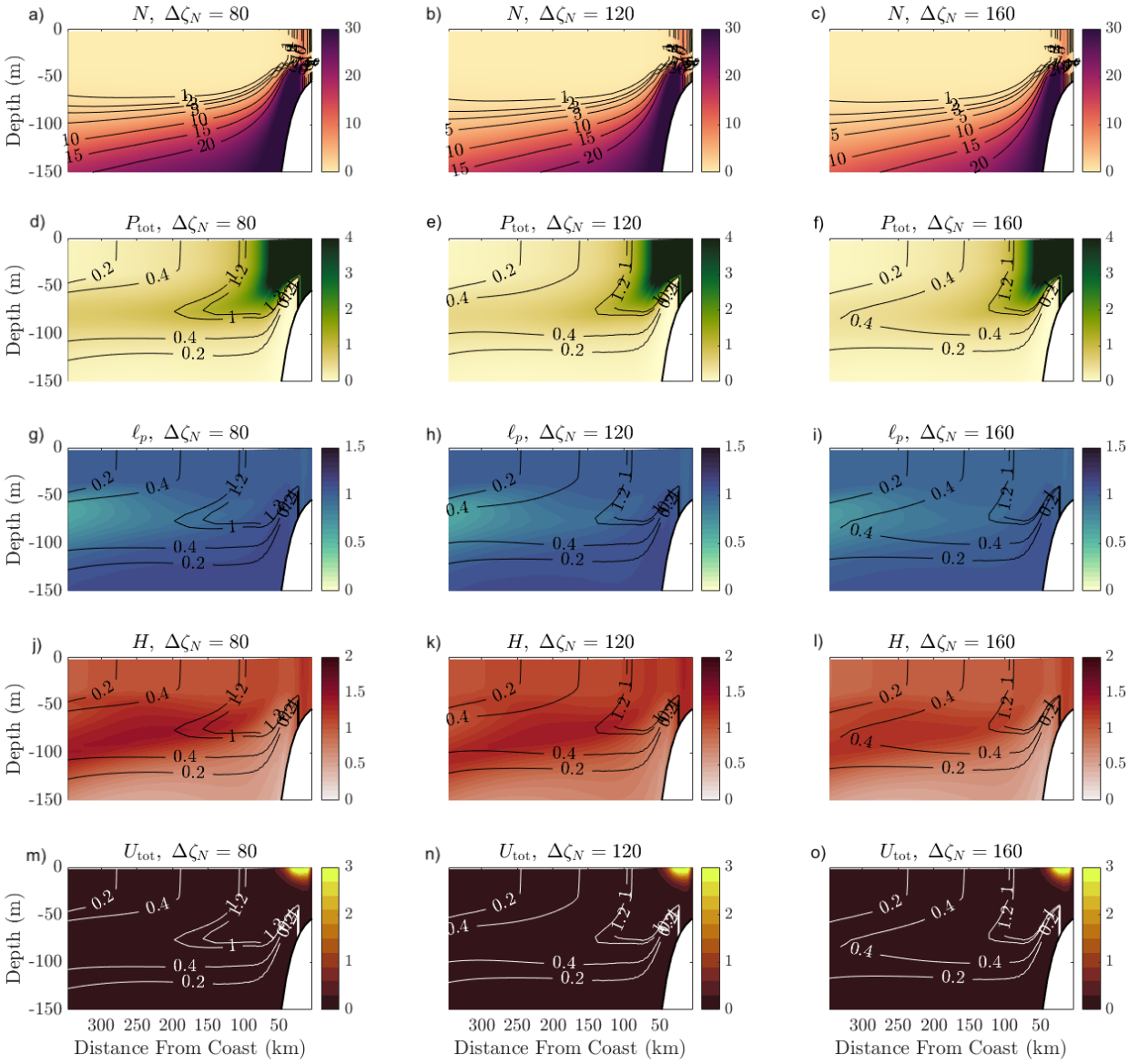

Figure 4.21: Same as 4.16, but for nutricline depth, $\Delta\zeta_N$.

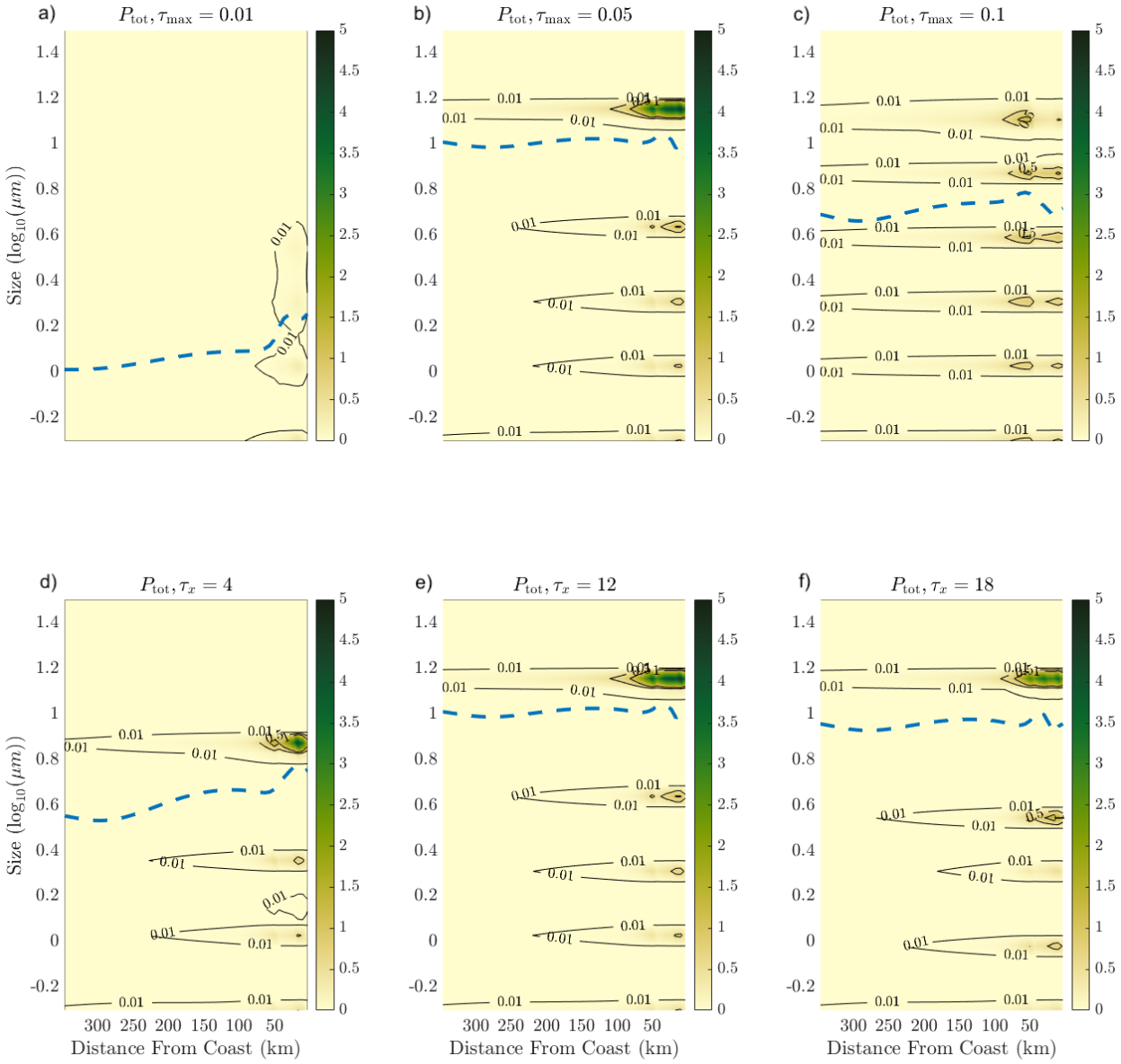

Figure 4.22: Distribution of size in the surface mixed layer in with respect to the minimum (left column), reference (center column), and maximum (right values), with respect to the wind stress maximum τ_{max} (a,b,c), and the width of the wind stress curl τ_x (d,e,f).

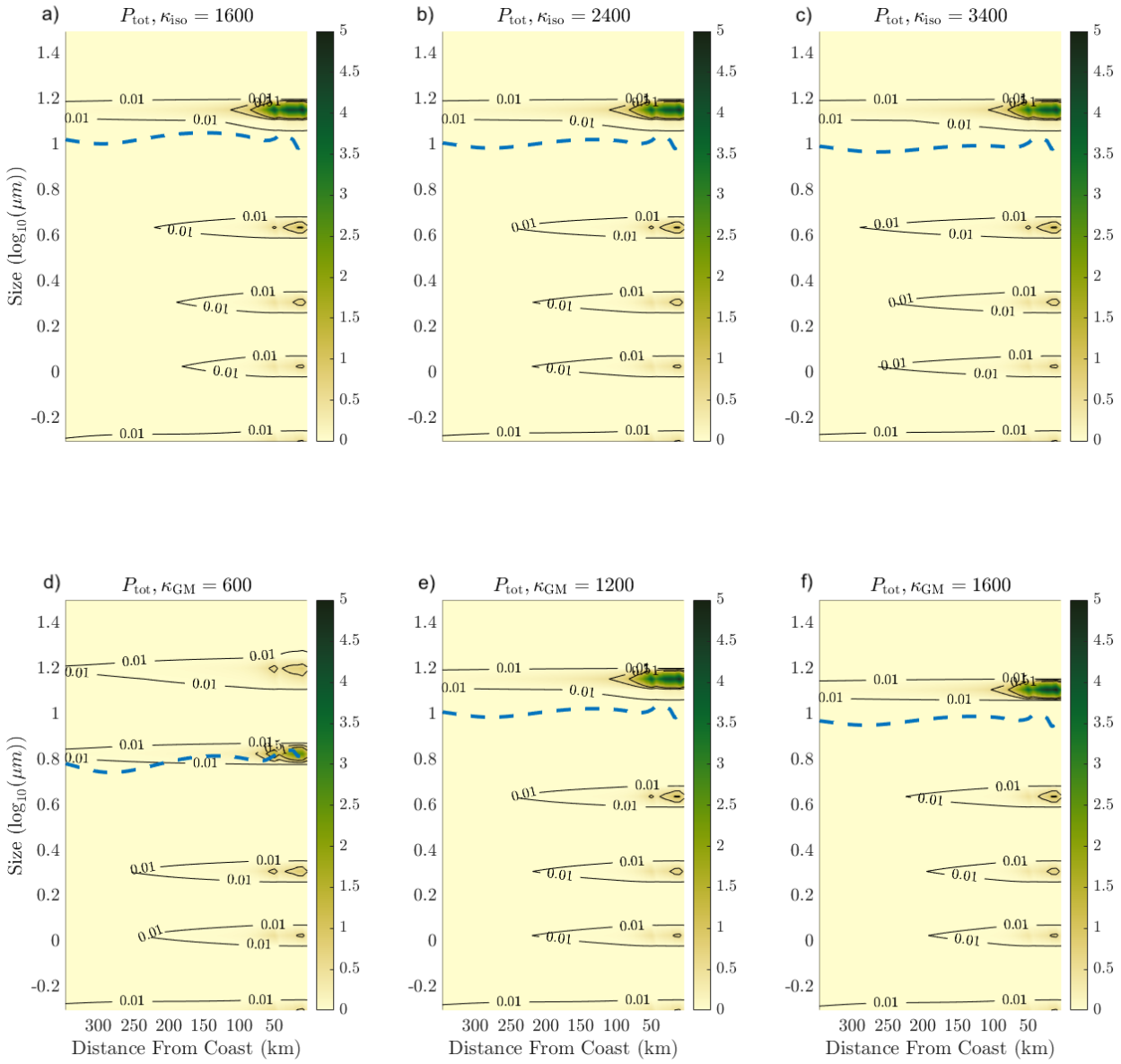

Figure 4.23: Same as 4.22 except for $\kappa_{\rm iso}$ (a,b,c), and $\kappa_{\rm GM}$ (d,e,f).

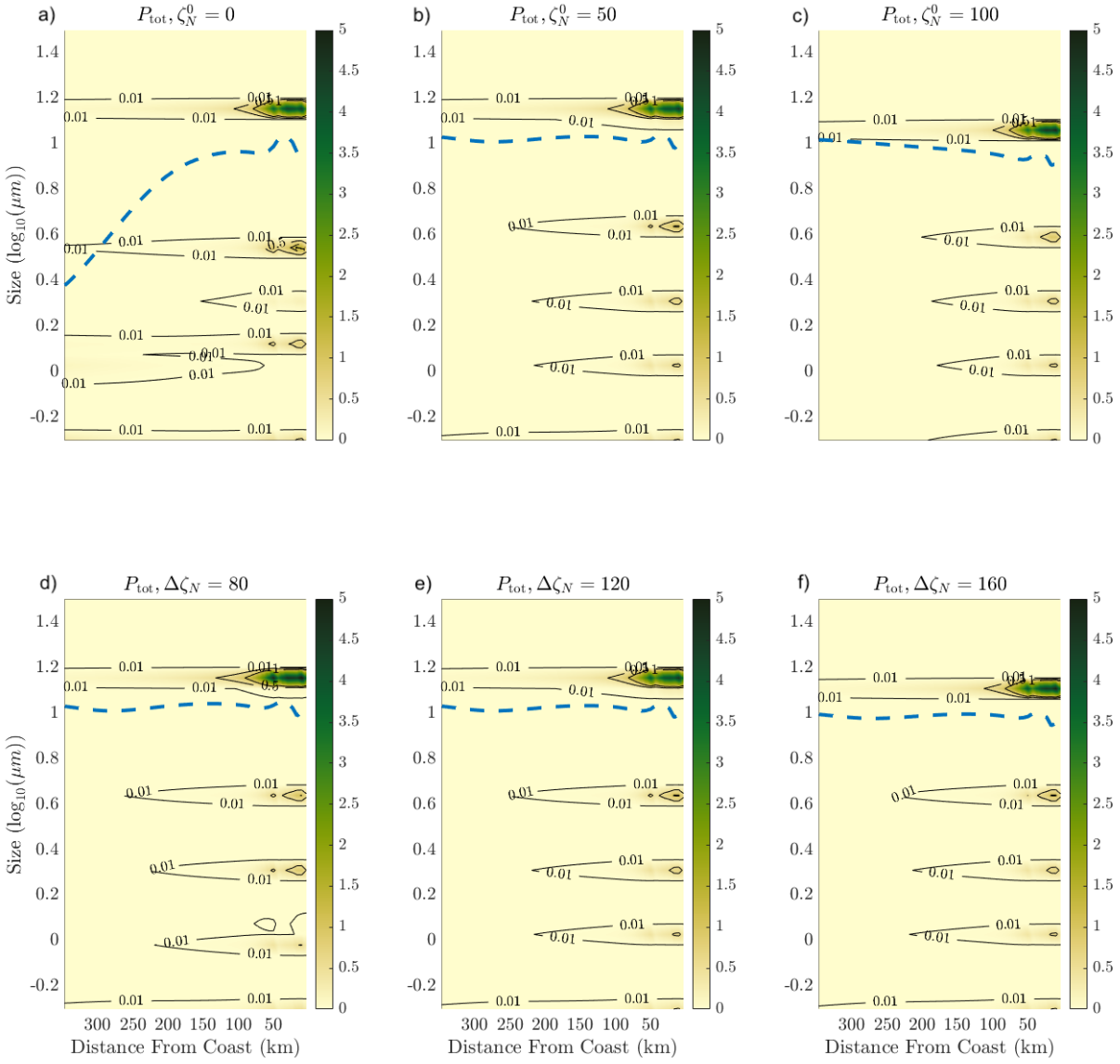

Figure 4.24: Same as 4.22 except for ζ_N^0 (a,b,c), and $\Delta\zeta_N$ (d,e,f).

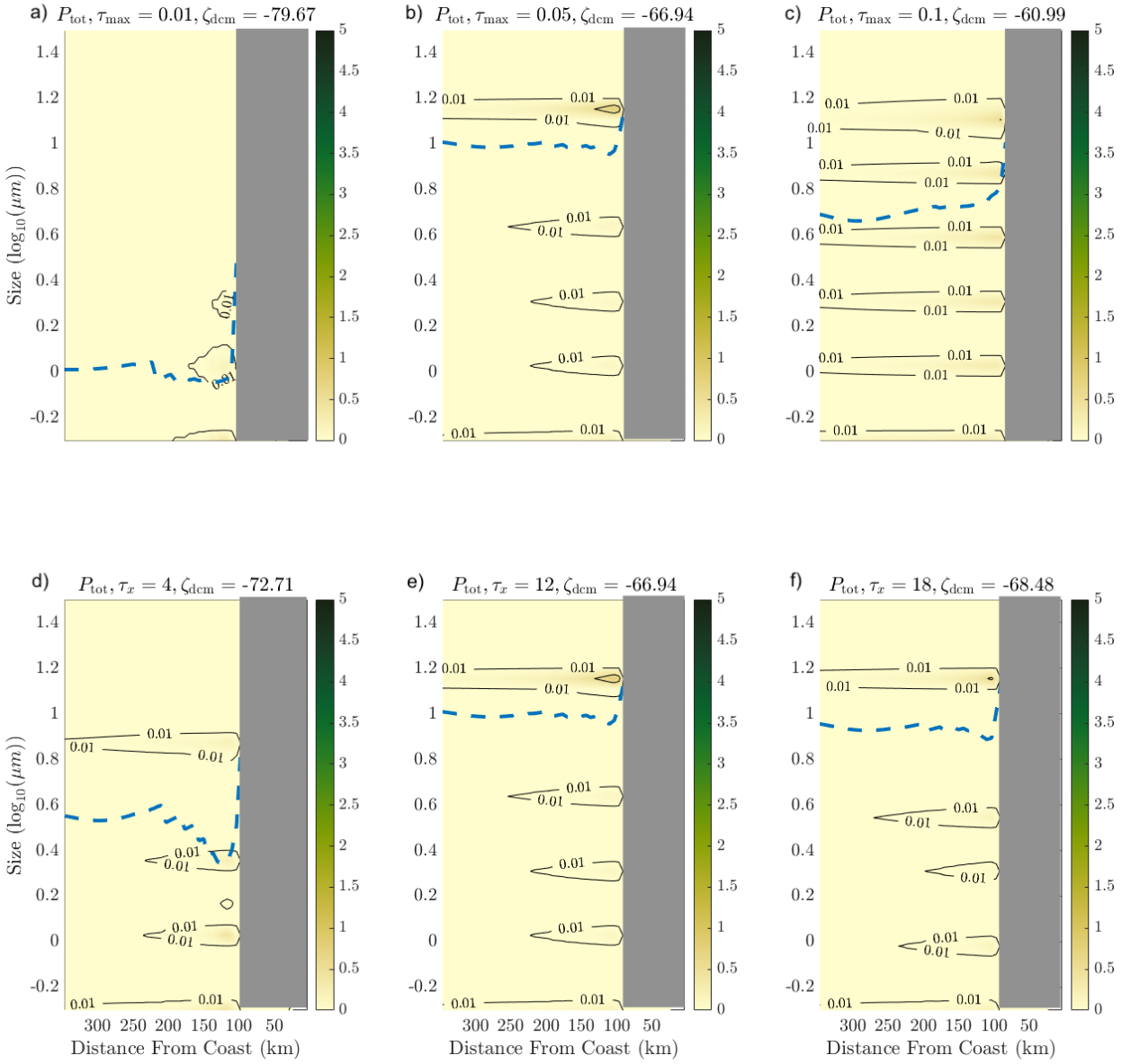

Figure 4.25: Cross section of size across the domain at the depth of the DCM in with respect to the minimum (left column), reference (center column), and maximum (right values), with respect to the wind stress maximum τ_{max} (a,b,c), and τ_x the width of the wind stress curl (d,e,f).

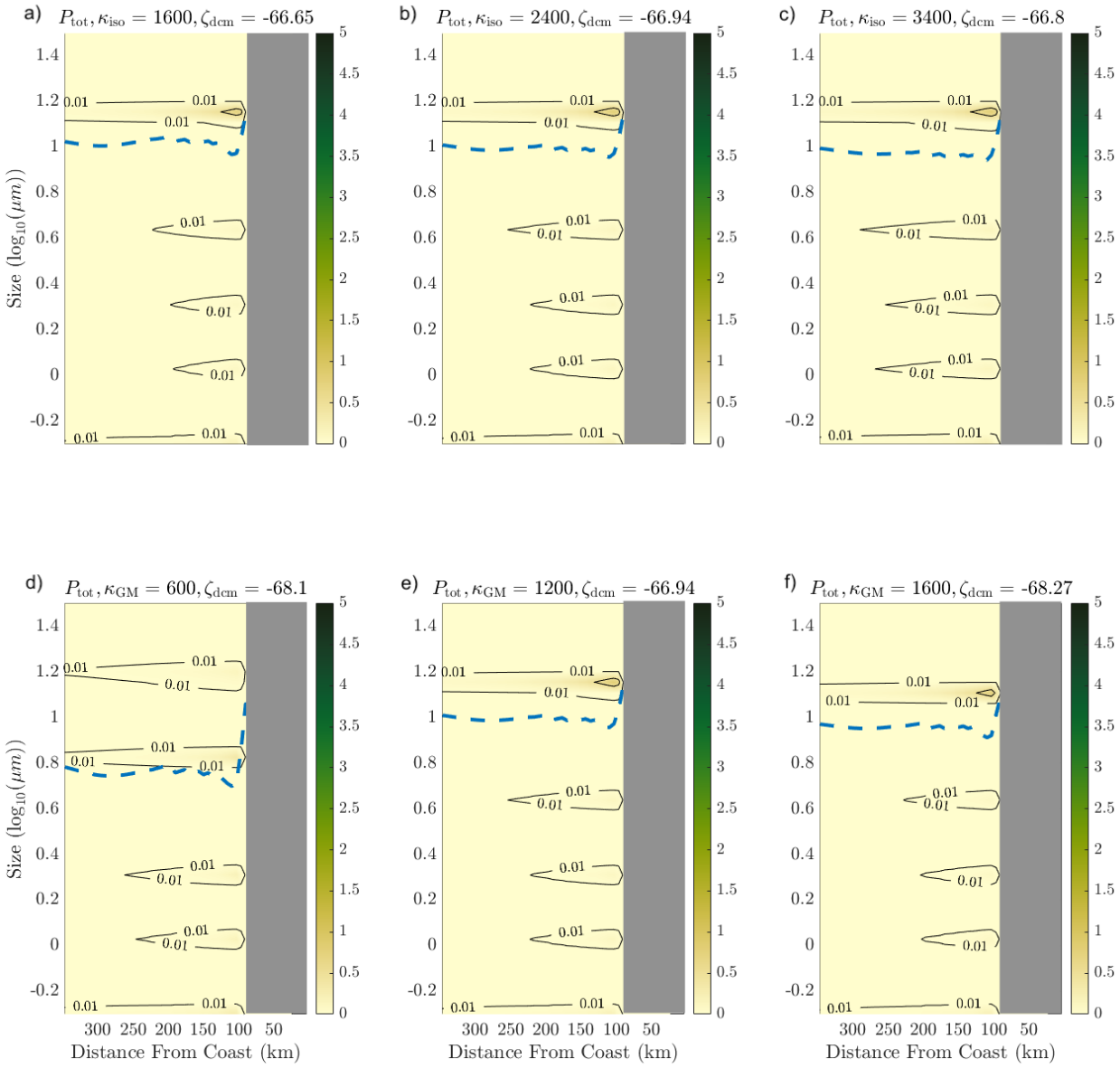

Figure 4.26: Same as 4.25 except for κ_{iso} (a,b,c), and κ_{GM} (d,e,f).

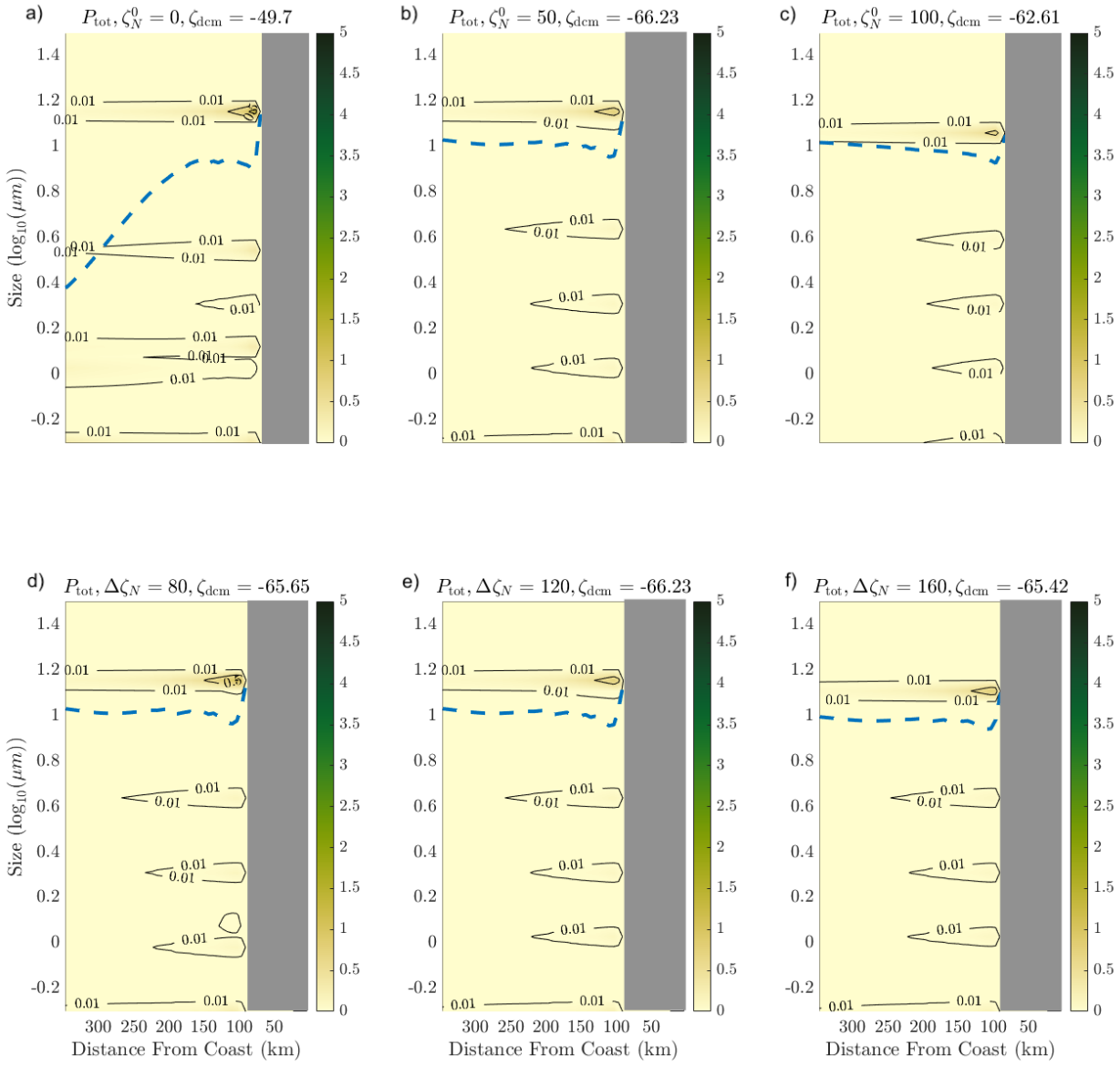

Figure 4.27: Same as 4.25 except for ζ_N^0 (a,b,c), and $\Delta\zeta_N$ (d,e,f).

Control Parameter	Reference Value
$X_{\text{chl}}^{\text{surf}}$	55.62 km
ζ_{DCM}	-66.23 m
$\overline{P}^{\text{shelf}}$	5.31 mmol N/m^3
$\overline{P}^{\text{surf}}$	4.63 mmol N/m^3
$\overline{P}^{\text{dcm}}$	0.48 mmol N/m^3
$\overline{Z}^{\text{shelf}}$	0.12 mmol N/m^3
$\overline{Z}^{\text{surf}}$	0.21 mmol N/m^3
$\overline{Z}^{\text{dcm}}$	4.5 $\times 10^{-5}$ mmol N/m^3
$\overline{T}^{\text{shelf}}$	7.92 ^{o}C
$\overline{T}^{\text{surf}}$	10.1 ^{o}C
$\overline{T}^{\text{dcm}}$	14.75 ^{o}C
$\overline{U}^{\text{shelf}}$	0.19 mmol N/m^3/d
$\overline{U}^{\text{surf}}$	0.11 mmol N/m^3/d
$\overline{U}^{\text{dcm}}$	0.02 mmol N/m^3/d
$\overline{\ell_p}^{\text{shelf}}$	1.01 $\log_{10}(\mu\text{m})$
$\overline{\ell_p}^{\text{surf}}$	1.01 $\log_{10}(\mu\text{m})$
$\overline{\ell_p}^{\text{dcm}}$	0.84 $\log_{10}(\mu\text{m})$
$\overline{H}^{\text{shelf}}$	1.26
$\overline{H}^{\text{surf}}$	1.2
$\overline{H}^{\text{dcm}}$	1.28

Table 4.3: Values of the model diagnostics in each of the diagnostic regions for the reference simulation

Parameter:	$\tau_{\max}$	τ_x	κ_{iso}	κ_{GM}	ζ_N^0	$\Delta\zeta_N$
$X_{\text{chl}}^{\text{surf}}$	0.59	0.02	0.21	-0.15	-0.31	-0.13
ζ_{DCM}	-0.16	-0.03	0	0.03	0.1	0
$\overline{P}^{\text{shelf}}$	0.04	-0.05	-0.02	0.18	-0.02	-0.08
$\overline{P}^{\text{surf}}$	0.1	0.17	-0.53	0.32	0.38	-0.33
$\overline{P}^{\text{dcm}}$	0.35	-0.11	0.5	-0.14	-0.77	-0.82
$\overline{Z}^{\text{shelf}}$	0.4	0.31	0.01	-0.19	-0.02	0.03
$\overline{Z}^{\text{surf}}$	0.98	0.45	0	-0.4	0.26	-0.06
$\overline{Z}^{\text{dcm}}$	-0.83	-1.3	-0.09	-0.1	-4.06	-2.93
$\overline{T}^{\text{shelf}}$	-0.3	-0.11	0.02	0.21	0	0
$\overline{T}^{\text{surf}}$	-0.16	-0.13	0.02	0.13	-0.15	0
$\overline{T}^{\text{dcm}}$	0.11	0.02	0	-0.02	-0.02	0
$\overline{U}^{\text{shelf}}$	0.62	0.51	0	-0.19	-0.01	0.02
$\overline{U}^{\text{surf}}$	0.16	-0.26	-0.75	0.14	0.79	-0.49
$\overline{U}^{\text{dcm}}$	0.35	-0.41	0.36	-0.36	-1.21	-1.1
$\overline{\ell_p}^{\text{shelf}}$	0.07	0.18	-0.02	0.19	-0.07	-0.16
$\overline{\ell_p}^{\text{surf}}$	0.08	0.28	-0.09	0.23	-0.04	-0.18
$\overline{\ell_p}^{\text{dcm}}$	0.24	0.37	0.19	0.22	0.46	0.03
$\overline{H}^{\text{shelf}}$	0.13	0.06	0.06	-0.22	0.02	-0.01
$\overline{H}^{\text{surf}}$	0.13	-0.15	0.18	-0.34	-0.05	0.01
$\overline{H}^{\text{dcm}}$	0.26	-0.05	0.24	-0.09	-0.36	-0.06

Table 4.4: The slope of the best fit line calculated for Figure 4.8

Parameter:	$\tau_{\max}$	τ_x	κ_{iso}	κ_{GM}	ζ_N^0	$\Delta\zeta_N$
$X_{\text{chl}}^{\text{surf}}$	0.99	0.04	1.0	0.59	0.83	0.88
ζ_{DCM}	0.94	0.19	0.09	0.19	0.55	0.03
$\overline{P}^{\text{shelf}}$	0.01	0.04	1.0	0.27	0.04	0.49
$\overline{P}^{\text{surf}}$	0.06	0.36	0.76	0.39	0.74	0.82
$\overline{P}^{\text{dcm}}$	0.85	0.21	0.98	0.2	0.97	0.96
$\overline{Z}^{\text{shelf}}$	0.76	0.61	0.99	0.31	0.05	0.17
$\overline{Z}^{\text{surf}}$	0.95	0.79	0.04	0.62	0.4	0.14
$\overline{Z}^{\text{dcm}}$	0.37	0.41	0.1	0.79	0.77	0.62
$\overline{T}^{\text{shelf}}$	0.9	0.72	0.98	0.74	1.0	1.0
$\overline{T}^{\text{surf}}$	0.81	0.8	1.0	0.83	0.54	1.0
$\overline{T}^{\text{dcm}}$	0.86	0.52	0.4	0.45	0.4	0
$\overline{U}^{\text{shelf}}$	0.96	0.88	0.89	0.36	0.05	0.17
$\overline{U}^{\text{surf}}$	0.06	0.09	0.39	0.03	0.86	0.83
$\overline{U}^{\text{dcm}}$	0.77	0.64	0.94	0.85	0.99	0.96
$\overline{\ell_p}^{\text{shelf}}$	0.03	0.24	1.0	0.2	0.55	0.81
$\overline{\ell_p}^{\text{surf}}$	0.04	0.35	0.99	0.21	0.12	0.94
$\overline{\ell_p}^{\text{dcm}}$	0.23	0.36	0.98	0.1	0.89	0.17
$\overline{H}^{\text{shelf}}$	0.07	0.04	1.0	0.27	0.03	0
$\overline{H}^{\text{surf}}$	0.06	0.26	1.0	0.31	0.06	0
$\overline{H}^{\text{dcm}}$	0.51	0.05	1.0	0.27	0.75	0.07

Table 4.5: Measure of best fit, R^2 value, calculated for Figure 4.8

CHAPTER 5

Conclusion

5.1 Summary

The goal of this thesis is to improve understanding of the factors that control productivity and ecosystem diversity in Eastern Boundary Upwelling Systems. A wide combination of physical forcing have important impacts on the zonal patterns of productivity in EBUSs, and can shape the structure of the upwelling ecosystem (Gruber et al., 2011; Jacox and Edwards, 2011, 2012; Capet et al., 2004, 2008; Renault et al., 2016; Colas et al., 2013). To investigate these impacts, we built a quasi-2D idealized meridionally averaged model (Chapter 2, Moscoso et al. (2021)), and incorporated a size structured planktonic ecosystem model (Chapter 3, Moscoso et al. (2022)), to understand the ecological responses to changes in a variety of physical forcings (Chapter 4). The conclusion of this thesis is meant to provide insight into our current state of understanding toward the overarching science questions that we set out to answer, as discussed in Chapter 1. I summarize these findings below:

What is the minimal configuration for a coupled physical and biogeochemical model to capture the zonal distribution of phytoplankton in an idealized EBUS? (Chapters 2, 3, 4)

Chapter 2 describes a new, idealized quasi-2D model, A Meridionally Averaged Model of Eastern Boundary Upwelling Systems (MAMEBUS), in detail. At a high level, the purpose of creating this model was to provide a new tool to investigate a great variety of physical and biogeochemical states representative of EBUSs, which would otherwise be impossible

with more complex and computationally expensive 3D models. While other 2D models have been used to investigate upwelling with respect to a wide physical parameter space (Jacox and Edwards, 2011, 2012), they did not include 3D processes that have been shown to be important in controlling biology in EBUSs. MAMEBUS includes the effects of eddy restratification, eddy advection (Gent and McWilliams, 1990), eddy stirring along isopycnals (Redi, 1982), surface and bottom boundary layer mixing (Ferrari et al., 2008), and diapycnal mixing. While we do not include explicit parameterizations of diapycnal mixing, the structure of the diapynal mixing in the boundary layers is formulated following Large et al. (1994). The model is cast in terrain-following coordinates, and includes a high-order calculation of the zonal pressure gradient following Shchepetkin and McWilliams (2003). The momentum equations in this model are solved using the time-dependent turbulent thermal wind approximation, following Dauhajre and McWilliams (2018). This formulation allows us to parameterize an idealized along-shore flow. However along shore circulation has not been thoroughly tested at this time. At the western boundary of the domain, we employ a sponge layer to represent forcing from the nearby subtropical gyre. The surface wind-forcing, the restoring, and the shape of the topography are idealized representations meant to represent the California Current System. MAMEBUS can be tuned to any EBUS, but we choose the CCS because of the large amount of data availability. The combination of physical parameterizations and algorithms developed in this work, and used to represent the effect of wind-driven upwelling, is able to capture the main characteristics and zonal gradients of the CCS ecosystem.

In Chapter 2, we evaluate the model using observations from CalCOFI (`https://calcofi.org/`). We find that by including all the parameterized processes described above, the model reproduces the zonal pattern of biomass with a reasonable agreement with observations. The main ecosystem features captured by the model include a surface chlorophyll maximum near the coast, and a subsurface transition into a deep chlorophyll maximum moving offshore (see Figure 2.7). However, the total magnitude of the chlorophyll is not well captured between

the reference solution and observations with a single phytoplankton and zooplankton size class. In Chapter 4, we show that the inclusion of a size-structured ecosystem model allows us to better capture the pattern of chlorophyll across the entire domain (see Figure 4.5).

Thus, to simulate the ecosystem in EBUSs, we use a size structured ecosystem model described in Chapter 3. Size structured ecosystem models are commonly used to represent ecological diversity because of the strong relationship between an organisms size an other biological traits (Armstrong, 1994; Poulin and Franks, 2010b; Follows et al., 2007; Litchman et al., 2007; Tang, 1995; Eppley et al., 1969; Hansen et al., 1994; Klausmeier et al., 2020; Banas, 2011; Ward et al., 2012), and to reduce model complexity and dimensionality (Follows and Dutkiewicz, 2011). Emergent properties of size structured models form the focus of the science question discussed in the following section. The size-dependent parameters used in this model include nutrient uptake by phytoplankton, heterotrophic grazing by zooplankton, predator-prey size interactions, phytoplankton mortality, and diffusion along the size trait – i.e., mutation. Large phytoplankton have slow uptake rates, tend to be more nutrient limited, and have longer lifespans than their smaller counterparts (Tang, 1995; Eppley et al., 1969). Similarly, larger zooplankton have slower grazing rates (Hansen et al., 1994). The grazing dynamics is modeled under the assumption that small zooplankton graze phytoplankton of approximately the same size, while large zooplankton prefer smaller prey (Hansen et al., 1994). This is not the case for all zooplankton. For example, some copepods are able to feed on particles much larger than their own body size (Kiørboe, 2011). The final process that we parameterize is a simple form of random mutation of the diversity trait, which we approximate by a size diffusion that allows for plankton to grow or shrink in size, and thus "mutate" (Sauterey et al., 2017). We include a single nutrient, akin to the limiting nutrient nitrate, and a single sinking detritus pool, to reduce model complexity. In Chapter 3, we additionally determine that in 0- and 1-dimensions, the optimal number of discrete size classes needed to robustly capture the behavior of the ecosystem is approximately 50 phytoplankton and 50 zooplankton size classes. We find that this set of size-dependent

parameterizations and configuration is able to realistically represent the ecosystem behavior in EBUSs (Figure 4.5).

What controls quantization observed in size structured ecosystems? (Chapter 3)

In Chapter 3, we additionally explore the characteristics and controls of quantization with respect to model resolution in size-space, bottom-up nutrient forcing, and top-down grazing (see Section 3.4). Previous work have found that ecological models with coarse resolution do not adequately capture phytoplankton diversity or quantization (Ward et al., 2012; Henson et al., 2021), however models with a finely resolved size dimension are able to capture this behavior in 0- and 1-D configurations (Moscoso et al., 2022; Banas, 2011). We conduct a parameter sweep using a variable number of size classes and find that the minimum number needed to accurately resolve quantizing behavior and total biomass is approximately 50 phytoplankton and 50 zooplankton size classes (see Figure 3.3) in a zero-dimensional setup. This choice in resolution is limited by the behavior of zooplankton and the grazing behavior, which still show small oscillations between varying resolution in the total biomass of each peak, even at very high resolution along the size dimension. We further use these findings to choose the number of size classes implemented in 1D experiments in Section 3.5, and Chapter 4.

We then explore the response of the size structured ecosystem with respect to changes in total nutrient forcing, and spin-up the ecosystem over long timescales to ensure the model reaches steady state. At very low nutrient forcing (i.e. nutrient supply), the smallest size class is the only size class present. As we increase the total nutrient forcing, more size classes emerge with nearly constant spacing between biomass peaks (see Figure 3.4). This behavior occurs in both phytoplankton and zooplankton biomass. Furthermore, as the total nutrient forcing increases, the total biomass becomes more concentrated in the large size classes. Observational studies have shown the emergence of large size classes in productive regions of the global ocean (i.e., EBUSs) with increasing nutrient availability (Hood et al., 1991;

Jonasz and Fournier, 1996; Zubkov et al., 2000; Worden et al., 2004; Schartau et al., 2010; Huete-Ortega et al., 2014).

We find that the dominant control on the behavior of quantization is by the representation of zooplankton grazing. In the model, predator-prey interactions and grazing preference are defined by a Gaussian grazing profile centered around an optimal prey size for each specific zooplankton class. The main parameter that controls the location of the biomass peaks along the size spectrum is the width of the grazing profile which can be thought of as a measure of selectivity in grazing (Ward et al., 2012; Hansen et al., 1994). At smaller grazing profile widths, zooplankton are more selective, grazing fewer size classes. As a result, more peaks along the size spectrum emerge (see Figure 3.6). We find an approximately linear relationship between the width of the grazing profile and the distance between peaks, but this relationship fails to capture the behavior near bifurcations. We additionally show these peaks are found in the "shadow zones" of grazing pressure (see Figure 3.7). A major caveat to this analysis is that the model exhibits significant non-linear behavior, making explicit analytical theories that describe the location of the quanta difficult.

What are the relevant physical drivers that control the total biomass of primary producers and ecosystem diversity in EBUSs (Chapter 4)

By combining MAMEBUS and the size structured ecosystem model, we are able to investigate the controls on ecosystem diversity in EBUSs in an idealized framework. We investigate the responses of several model diagnostics to a wide physical parameter space in three sub-regions of the model: the surface chlorophyll front, the continental shelf, and the deep chlorophyll maximum. In these regions, we explore sensitivities in the total plankton biomass, the uptake of nutrients, the average size of phytoplankton, and the Shannon diversity Index (see Table 4.2)

While there is a large parameter space that can control the ecosystem productivity (Bakun and Nelson, 1991; Capet et al., 2004, 2008; Chavez and Messié, 2009; Jacox and

Edwards, 2011; Gruber et al., 2011; Jacox and Edwards, 2012; Colas et al., 2013; Renault et al., 2016), we choose a subset of parameters that includes the strength of the surface wind-stress, the width of the wind-stress curl, the magnitude of the buoyancy diffusivity, the isopycnal diffusivity, the offshore nutricline depth at the western boundary, and the offshore nutricline thickness at the western boundary. The parameter spaces of interest are informed by observations and previous modeling work (see Table 4.1).

A perhaps surprising response in the model diagnostics is the response of the biology to perturbations in the isopycnal diffusivity. In most models that parameterize or resolve eddies, eddy restratification and stirring are coupled (Griffies, 1998; Gruber et al., 2011). With MAMEBUS, we are able to study the effect of variations in the diffusivities that give rise to eddy restratification κ_{GM}, and eddy stirring κ_{iso} independently. Variations in the ecosystem characteristics with respect to the isopycnal diffusivity, κ_{iso}, has the strongest linear fit, and correlations with the most statistical significance. However, in most of these parameter sweeps, the slope of the best fit line is small in overall magnitude, and thus relatively insensitive to changes in κ_{iso}. Previous work has shown that the effect of eddies work to remove nutrients and other tracers from the surface and subduct them beneath the euphotic zone (Gruber et al., 2011). The three parameters that potentially exhibit this behavior are the total concentration of phytoplankton, the total concentration of zooplankton, and the uptake of nutrients by phytoplankton. At the surface, increased eddy stirring reduces the phytoplankton and zooplankton concentration at the surface, and suppresses uptake of nutrients. In the DCM, on the other hand, there is an increase of phytoplankton and zooplankton, with increased uptake rates (see Figures 4.8, 4.14, and 4.15). This potentially indicates a transfer of nutrients from the surface to the DCM via isopycnal stirring. This finding is consistent with those presented in Gruber et al. (2011) which found a reduction in surface productivity from eddy-induced nutrient burial.

The responses of the model diagnostics with respect to the buoyancy diffusivity, on the other hand, are not as expected. Variations in the buoyancy diffusivity in many cases have

the opposite effect than the isopycnal diffusivity, for example, the slope of the best fit line for plankton biomass on the shelf and in the surface is positive while the slope in the DCM is negative (see Figures 4.8, 4.10, 4.12, and 4.14). This result allows us to preliminary conclude that eddy quenching is predominantly driven by the component of eddy stirring along isopycnals. However, more investigation of this effect is needed at this time, and a clearer ecological response may emerge with a wider parameter sweep.

The impact of variations in the wind-stress forcing aligned with previous understanding of upwelling in EBUSs. With increased wind-stress forcing, more nutrients are upwelled onto the shelf and productivity increases throughout the entire domain (see Figure 4.8, 4.12, 4.10 and 4.14). Additionally, the surface chlorophyll maximum moves offshore, and the depth of the DCM increases. There are slight increases in the Shannon Index across the entire domain, with a statistically significant positive trend in the DCM, likely as a consequence of more size classes. The productivity in the SCM and on the shelf show nonlinear responses to changes in the wind-stress strength (see Figure 4.12 and 4.10), suggesting that more investigation are required to identify the controls of productivity with respect to the wind-stress. For example, there may be increased eddy compensation from the eddy parameterizations as a consequence of stronger upwelling, leading to more eddy-induced transport (Gent and McWilliams, 1990; Redi, 1982).

The offshore nutricline depth, ΔZ_{N} has the strongest impact on the total phytoplankton biomass in the SCM and DCM. In both regions of the model, there is a statistically significant decreases in the total plankton biomass and uptake. With a deeper nutricline, the total nutrients in the upwelling source waters decrease, suppressing productivity (see Figures 4.8, 4.12, and 4.14). Similarly, in the DCM, the total nutrient availability from below decreases, with a similar effect. The location of the surface chlorophyll maximum also shift shore-ward, as less nutrients are upwelled. While there is not much impact on the total biomass, the average size of phytoplankton on the shelf decreases, indicating a redistribution of biomass to smaller sizes (see Figure 4.8 and 4.13).

The profile of nutrient forcing at the western boundary have an important impact on many of the model diagnostics. This profile is important to productivity and diversity across the entire domain as the source waters upwelled onto the shelf and in the surface (Jacox and Edwards, 2011, 2012; Pozo Buil et al., 2021). The nutricline depth, Z_{N}^{0} allows us to investigate the effect of changes to the simulated subtropical gyre. A deepening of the nutricline increases the total productivity in the surfaces, and moves the SCM closer to the coast. Similarly, the depth of the DCM increases, limiting the total light availability from the surface and decreasing productivity (Zubkov et al., 2000; Tréguer et al., 2018). The nutricline depth has a statistically significant impact on the average size and diversity in the DCM, while there is a decrease in total productivity, the average size and Shannon Index increases as the nutricline depth decreases. At this time, the drivers of this behavior requires further investigation.

Figure 4.9 provides new insight into unexpected ecosystem responses that we discovered by investigating the relationship between ecosystem characteristics. For example, we observe a non-linear responses between the total phytoplankton biomass, P_{tot} and the Shannon Index, H. At low biomass in the DCM, H is approximately 1, as total phytoplankton biomass increases to $P_{\mathrm{tot}} = 1$ mmol N/m^3, H increases to 2. In regions of the model with high biomass, we see that increases of productivity correspond to decreases in H. This implies that as P_{tot} increases from low biomass, more size classes are added, but once the size spectrum is saturated in the total number of biomass peaks, the increases in biomass are predominantly in the largest size class (as shown in Moscoso et al. (2022)).

While we focus predominantly on the lower trophic ecosystem, the findings in this study have the potential to inform the larger food-web diversity Andersen et al. (2016); Stock et al. (2017). In EBUSs and other productive regions of the global oceans, strong productivity is able to support short, direct food-webs (Chavez and Messié, 2009). Along with identifying the the controls on species diversity in EBUSs to variations in the physical forcing, an additional new finding is the persistence of biomass quantization in a high resolution size

structured ecosystem model with horizontal heterogeneity. Like the findings presented in Banas (2011), Vallina et al. (2014), and Moscoso et al. (2022), the plankton productivity is controlled by the nutrient availability, and the species diversity – here quantization – is controlled by the grazing behavior.

Our simulations suggest that the sensitivities that control ecosystem biomass are the wind-stress maximum, the effect of eddy stirring, and in the nutrient restoring depth. The impact on the average plankton size and ecosystem diversity, however is minimal, implying that the ecosystem diversity may be predominantly controlled by the internal grazing behavior (Vallina et al., 2014). The relationships between ecosystem properties shown in Figure 4.9 provide insight into the responses of diversity metrics to more regularly measured quantities (e.g. phytoplankton biomass and nutrient concentration). These findings may be extended and tested in regional modeling efforts.

Bibliography

Abernathey, R. P., and J. Marshall, 2013: Global surface eddy diffusivities derived from satellite altimetry. *Journal of Geophysical Research: Oceans*, **118 (2)**, 901–916.

Adjou, M., J. Bendtsen, and K. Richardson, 2012: Modeling the influence from ocean transport, mixing and grazing on phytoplankton diversity. *Ecological modelling*, **225**, 19–27.

Aiki, H., and K. J. Richards, 2008: Energetics of the global ocean: the role of layer-thickness form drag. *J. Phys. Oceanogr.*, **38 (9)**, 1845–1869.

Albert, A., V. Echevin, M. Lévy, and O. Aumont, 2010: Impact of nearshore wind stress curl on coastal circulation and primary productivity in the peru upwelling system. *Journal of Geophysical Research: Oceans*, **115 (C12)**.

Amante, C., and B. W. Eakins, 2009: Etopo1 arc-minute global relief model: procedures, data sources and analysis.

Andersen, K., and Coauthors, 2016: Characteristic sizes of life in the oceans, from bacteria to whales. *Annual Review of Marine Science*, **8 (1)**, 217–241.

Anderson, T. R., 2005: Plankton functional type modelling: running before we can walk? *Journal of Plankton Research*, **27 (11)**, 1073–1081.

Arakawa, A., and M. J. Suarez, 1983: Vertical differencing of the primitive equations in sigma coordinates. *Monthly Weather Review*, **111 (1)**, 34–45.

Armstrong, R. A., 1994: Grazing limitation and nutrient limitation in marine ecosystems: steady state solutions of an ecosystem model with multiple food chains. *Limnology and Oceanography*, **39 (3)**, 597–608.

Armstrong, R. A., and R. McGehee, 1980: Competitive exclusion. *The American Naturalist*, **115 (2)**, 151–170.

Bakun, A., and C. S. Nelson, 1991: The Seasonal Cycle of Wind-Stress Curl in Subtropical Eastern Boundary Current Regions. *J. Phys. Oc.*, **21 (12)**, 1815–1834.

Bakun, A., and R. H. Parrish, 1982: Turbulence, Transport, and Pelagic Fish in the California and Peru Current Systems. *CalCOFI Rep.*, **23**.

Banas, N. S., 2011: Adding complex trophic interactions to a size-spectral plankton model: Emergent diversity patterns and limits on predictability. *Ecol. Modeling*, **222**, 2663–2675.

Banse, K., 1994: Uptake of inorganic carbon and nitrate by marine plankton and the redfield ratio. *Global Biogeochemical Cycles*, **8 (1)**, 81–84.

Barton, A. D., S. Dutkiewicz, G. Flierl, J. Bragg, and M. J. Follows, 2010: Patterns of diversity in marine phytoplankton. *Science*, **327 (5972)**, 1509–1511.

Beckmann, A., and I. Hense, 2007: Beneath the surface: Characteristics of oceanic ecosystems under weak mixing conditions–a theoretical investigation. *Progress in Oceanography*, **75 (4)**, 771–796.

Behrenfeld, M. J., and E. S. Boss, 2014: Resurrecting the ecological underpinnings of ocean plankton blooms.

Boyd, P. W., H. Claustre, M. Levy, D. A. Siegel, and T. Weber, 2019: Multi-faceted particle pumps drive carbon sequestration in the ocean. *Nature*, **568 (7752)**, 327–335.

Brandini, F. P., M. Nogueira Jr, M. Simião, J. C. U. Codina, and M. A. Noernberg, 2014: Deep chlorophyll maximum and plankton community response to oceanic bottom intrusions on the continental shelf in the south brazilian bight. *Continental Shelf Research*, **89**, 61–75.

Brännström, Å., N. Loeuille, M. Loreau, and U. Dieckmann, 2011: Emergence and maintenance of biodiversity in an evolutionary food-web model. *Theoretical Ecology*, **4 (4)**, 467–478.

Bruggeman, J., and S. A. Kooijman, 2007: A biodiversity-inspired approach to aquatic ecosystem modeling. *Limnology and Oceanography*, **52 (4)**, 1533–1544.

Burke, A., A. L. Stewart, J. F. Adkins, R. Ferrari, M. F. Jansen, and A. F. Thompson, 2015: The glacial mid-depth radiocarbon bulge and its implications for the overturning circulation. *Paleoceanography*, **30 (7)**, 1021–1039.

Cabre, A., D. Shields, I. Marinov, and T. S. Kostadinov, 2013: Phenology of Size-Partitioned Phytoplankton Carbon-Biomass from Ocean Color Remote Sensing and CMIP5 Models. *Front. Mar. Sci.*

Cael, B., E. L. Cavan, and G. L. Britten, 2021: Reconciling the size-dependence of marine particle sinking speed. *Geophysical Research Letters*, **48 (5)**, e2020GL091 771.

Capet, X., F. Colas, J. McWilliams, P. Penven, and P. Marchesiello, 2008: Eddies in eastern boundary subtropical upwelling systems. *Ocean Modeling in an Eddying Regime, Geophys. Monogr. Ser*, **177**, 131–147.

Capet, X., P. Marchesiello, and J. McWilliams, 2004: Upwelling response to coastal wind profiles. *Geophysical Research Letters*, **31 (13)**.

Castelao, R. M., and H. Luo, 2018: Upwelling jet separation in the california current system. *Scientific Reports*, **8 (1)**.

Cavender-Bares, K. K., A. Rinaldo, and S. W. Chisholm, 2001: Microbial size spectra from natural and nutrient enriched ecosystems. *Limnology and Oceanography*, **46 (4)**, 778–789.

Chavez, F. P., 1989: Size distribution of phytoplankton in the central and eastern tropical pacific. *Global Biogeochemical Cycles*, **3 (1)**, 27–35.

Chavez, F. P., and M. Messié, 2009: A comparison of eastern boundary upwelling ecosystems. *Prog. in Oceanog.*, **83**, 80–96.

Chelton, D. B., R. A. DeSzoeke, M. G. Schlax, K. El Naggar, and N. Siwertz, 1998: Geographical variability of the first baroclinic Rossby radius of deformation. *J. Phys. Oceanogr.*, **28 (3)**, 433–460.

Chen, R., J. C. McWilliams, and L. Renault, 2021: Momentum governors of california undercurrent transport. *Journal of Physical Oceanography*, **51 (9)**, 2915–2932.

Chenillat, F., P. J. S. Franks, X. Capet, P. Rivière, N. Grima, B. Blanke, and V. Combes, 2018: Eddy properties in the southern california current system. *Ocean Dynamics*, **68 (7)**, 761–777.

Chenillat, F., P. Rivière, X. Capet, P. J. Franks, and B. Blanke, 2013: California coastal upwelling onset variability: cross-shore and bottom-up propagation in the planktonic ecosystem. *PloS one*, **8 (5)**, e62 281.

Chenillat, F., P. Rivière, and M. D. Ohman, 2021: On the sensitivity of plankton ecosystem models to the formulation of zooplankton grazing. *PloS one*, **16 (5)**, e0252 033.

Chisholm, S. W., 1992: Phytoplankton size. *Primary productivity and biogeochemical cycles in the sea*, Springer, 213–237.

Colas, F., X. Capet, J. C. Mcwilliams, and Z. Li, 2013: Mesoscale Eddy Buoyancy Flux and Eddy-Induced Circulation in Eastern Boundary Currents. *J. Phys. Oc.*, **43**.

Colas, F., J. C. McWilliams, X. Capet, and J. Kurian, 2012: Heat balance and eddies in the peru-chile current system. *Climate dynamics*, **39 (1)**, 509–529.

Collier, J. L., and B. Palenik, 2003: Phycoerythrin-containing picoplankton in the southern california bight. *Deep Sea Research Part II: Topical Studies in Oceanography*, **50 (14-16)**, 2405–2422.

Connolly, T. P., B. M. Hickey, I. Shulman, and R. E. Thomson, 2014: Coastal trapped waves, alongshore pressure gradients, and the california undercurrent. *Journal of Physical Oceanography*, **44 (1)**, 319–342.

Croll, D. A., B. Marinovic, S. Benson, F. P. Chavez, N. Black, R. Ternullo, and B. R. Tershy, 2005: From wind to whales: trophic links in a coastal upwelling system. *Marine Ecology Progress Series*, **289**, 117–130.

Cullen, J. J., 1982a: The deep chlorophyll maximum: comparing vertical profiles of chlorophyll a. *Canadian Journal of Fisheries and Aquatic Sciences*, **39 (5)**, 791–803.

Cullen, J. J., 1982b: The deep chlorophyll maximum: comparing vertical profiles of chlorophyll a. *Canadian Journal of Fisheries and Aquatic Sciences*, **39 (5)**, 791–803.

Cyr, H., and M. L. Pace, 1992: Grazing by zooplankton and its relationship to community structure. *Canadian Journal of Fisheries and Aquatic Sciences*, **49 (7)**, 1455–1465.

Dauhajre, D. P., and J. C. McWilliams, 2018: Diurnal evolution of submesoscale front and filament circulations. *Journal of Physical Oceanography*, **48 (10)**, 2343–2361.

Deser, C., and M. S. Timlin, 1997: Atmosphere–ocean interaction on weekly timescales in the north atlantic and pacific. *Journal of climate*, **10 (3)**, 393–408.

Deutsch, C., H. Frenzel, J. C. McWilliams, L. Renault, F. Kessouri, E. Howard, J.-H. Liang, D. Bianchi, and S. Yang, 2021: Biogeochemical variability in the california current system. *Progress in Oceanography*, **196**, 102 565.

Di Lorenzo, E., 2003: Seasonal dynamics of the surface circulation in the southern california current system. *Deep Sea Research Part II: Topical Studies in Oceanography*, **50 (14-16)**, 2371–2388.

Ducklow, H. W., D. K. Steinberg, and K. O. Buesseler, 2001: Upper ocean carbon export and the biological pump. *Oceanography*, **14 (4)**, 50–58.

Dunne, J. P., R. A. Armstrong, A. Gnanadesikan, and J. L. Sarmiento, 2005: Empirical and mechanistic models for the particle export ratio. *Global Biogeochemical Cycles*, **19 (4)**.

Durran, D., 2010: *Numerical Methods for Fluid Dynamics: With Applications to Geophysics*. Texts in Applied Mathematics, Springer New York.

Durran, D. R., 1991: The third-order Adams-Bashforth method: An attractive alternative to leapfrog time differencing. *Mon. Weather Rev.*, **119 (3)**, 702–720.

Dutkiewicz, S., P. Cermeno, O. Jahn, M. J. Follows, A. E. Hickman, D. A. Taniguchi, and B. A. Ward, 2020: Dimensions of marine phytoplankton diversity. *Biogeosciences*, **17 (3)**, 609–634.

Dutkiewicz, S., M. J. Follows, and J. G. Bragg, 2009: Modeling the coupling of ocean ecology and biogeochemistry. *Global Biogeochemical Cycles*, **23 (4)**.

Dutkiewicz, S., B. Ward, F. Monteiro, and M. Follows, 2012: Interconnection of nitrogen fixers and iron in the pacific ocean: Theory and numerical simulations. *Global Biogeochemical Cycles*, **26 (1)**.

Eady, E. T., 1949: Long waves and cyclone waves. *Tellus*, **1 (3)**, 33–52.

Edwards, K. F., C. T. Kremer, E. T. Miller, M. M. Osmond, E. Litchman, and C. A. Klausmeier, 2018: Evolutionarily stable communities: a framework for understanding the role of trait evolution in the maintenance of diversity. *Ecology letters*, **21 (12)**, 1853–1868.

Edwards, K. F., M. K. Thomas, C. A. Klausmeier, and E. Litchman, 2012: Allometric scaling and taxonomic variation in nutrient utilization traits and maximum growth rate of phytoplankton. *Limnology and Oceanography*, **57 (2)**, 554–566.

Edwards, N. R., A. J. Willmott, and P. D. Killworth, 1998: On the role of topography and wind stress on the stability of the thermohaline circulation. *J. Phys. Oceanogr.*, **28 (5)**, 756–778.

Eppley, R., J. Rogers, and J. McCarthy, 1969: Half-saturation constants for uptake of nitrate and ammonium by marine phytoplankton. *Limnology and Oceanography*, **17**, 912—-920.

Ferrari, R., J. C. McWilliams, V. M. Canuto, and M. Dubovikov, 2008: Parameterization of eddy fluxes near oceanic boundaries. *J. Climate*, **21 (12)**, 2770–2789.

Fiechter, J., C. A. Edwards, and A. M. Moore, 2018: Wind, circulation, and topographic effects on alongshore phytoplankton variability in the california current. *Geophysical Research Letters*, **45 (7)**, 3238–3245.

Follows, M. J., and S. Dutkiewicz, 2011: Modeling diverse communities of marine microbes. *Annual review of marine science*, **3**, 427–451.

Follows, M. J., S. Dutkiewicz, S. Grant, and S. W. Chisholm, 2007: Emergent biogeography of microbial communities in a model ocean. *science*, **315 (5820)**, 1843–1846.

Fowler, B. L., M. G. Neubert, K. R. Hunter-Cevera, R. J. Olson, A. Shalapyonok, A. R. Solow, and H. M. Sosik, 2020: Dynamics and functional diversity of the smallest phytoplankton on the northeast us shelf. *Proceedings of the National Academy of Sciences*, **117 (22)**, 12 215–12 221.

Franks, P. J., 2002: Npz models of plankton dynamics: their construction, coupling to physics, and application. *Journal of Oceanography*, **58 (2)**, 379–387.

Franks, P. J., and L. J. Walstad, 1997: Phytoplankton patches at fronts: A model of formation and response to wind events. *Journal of Marine Research*, **55 (1)**, 1–29.

Fuchs, H. L., and P. J. Franks, 2010: Plankton community properties determined by nutrients and size-selective feeding. *Marine Ecology Progress Series*, **413**, 1–15.

Furuya, K., 1990: Subsurface chlorophyll maximum in the tropical and subtropical western pacific ocean: Vertical profiles of phytoplankton biomass and its relationship with chlorophylla and particulate organic carbon. *Marine Biology*, **107**, 529–539.

García-Reyes, M., W. J. Sydeman, D. S. Schoeman, R. R. Rykaczewski, B. A. Black, A. J. Smit, and S. J. Bograd, 2015: Under pressure: Climate change, upwelling, and eastern boundary upwelling ecosystems. *Frontiers in Marine Science*, **2**, 109.

Gent, P. R., 2011: The Gent–McWilliams parameterization: 20/20 hindsight. *Ocean Modell.*, **39 (1-2)**, 2–9.

Gent, P. R., and J. C. McWilliams, 1990: Isopycnal mixing in ocean circulation models. *J. Phys. Oceanogr.*, **20 (1)**, 150–155.

Gentleman, W., A. Leising, B. Frost, S. Strom, and J. Murray, 2003: Functional responses for zooplankton feeding on multiple resources: a review of assumptions and biological dynamics. *Deep Sea Research Part II: Topical Studies in Oceanography*, **50 (22-26)**, 2847–2875.

Giometto, A., F. Altermatt, F. Carrara, A. Maritan, and A. Rinaldo, 2013: Scaling body size fluctuations. *Proceedings of the National Academy of Sciences*, **110 (12)**, 4646–4650.

Goebel, N. L., C. A. Edwards, J. P. Zehr, and M. J. Follows, 2010: An emergent community ecosystem model applied to the california current system. *Journal of Marine Systems*, **83 (3-4)**, 221–241.

Golden, C. D., E. H. Allison, W. W. Cheung, M. M. Dey, B. S. Halpern, D. J. McCauley, M. Smith, B. Vaitla, D. Zeller, and S. S. Myers, 2016: Nutrition: Fall in fish catch threatens human health. *Nature News*, **534 (7607)**, 317.

Gregg, W. W., and N. W. Casey, 2007: Modeling coccolithophores in the global oceans. *Deep Sea Research Part II: Topical Studies in Oceanography*, **54 (5-7)**, 447–477.

Griffies, S., 2018: *Fundamentals of ocean climate models*. Princeton University Press.

Griffies, S. M., 1998: The Gent–McWilliams skew flux. *J. Phys. Oceanogr.*, **28 (5)**, 831–841.

Gruber, N., H. Frenzel, S. C. Doney, P. Marchesiello, J. C. McWilliams, J. R. Moisan, J. J. Oram, G.-K. Plattner, and K. D. Stolzenbach, 2006: Eddy-resolving simulation of plankton ecosystem dynamics in the california current system. *Deep Sea Research Part I: Oceanographic Research Papers*, **53 (9)**, 1483–1516.

Gruber, N., and Coauthors, 2011: Eddy-induced reduction of biological production in eastern boundary upwelling systems. *Nat. Geosciences*, **4**.

Gula, J., M. J. Molemaker, , and J. C. McWilliams, 2014: Submesoscale cold filaments in the Gulf Stream. *Journal of Physical Oceanography*, **44**, 2617–2643.

Hales, B., J. N. Moum, P. Covert, and A. Perlin, 2005: Irreversible nitrate fluxes due to turbulent mixing in a coastal upwelling system. *Journal of Geophysical Research: Oceans*, **110 (C10)**.

Haney, R. L., 1971: Surface thermal boundary condition for ocean circulation models. *J. Phys. Oceanogr.*, **1 (4)**, 241–248.

Haney, R. L., 1991: On the pressure gradient force over steep topography in sigma coordinate ocean models. *Journal of Physical Oceanography*, **21 (4)**, 610–619.

Hansen, B., P. Bjornsen, and P. Hansen, 1994: The size ratio between planktonic predators and their prey. *Limnology and Oceanography*, **39**, 395–403.

Henson, S. A., B. Cael, S. R. Allen, and S. Dutkiewicz, 2021: Future phytoplankton diversity in a changing climate. *Nature communications*, **12 (1)**, 1–8.

Hersbach, H., and Coauthors, 2020: The era5 global reanalysis. *Quarterly Journal of the Royal Meteorological Society*, **146 (730)**, 1999–2049.

Hillebrand, H., and A. I. Azovsky, 2001: Body size determines the strength of the latitudinal diversity gradient. *Ecography*, **24 (3)**, 251–256.

Hood, R. R., M. R. Abbott, and A. Huyer, 1991: Phytoplankton and photosynthetic light response in the coastal transition zone off northern california in june 1987. *Journal of Geophysical Research: Oceans*, **96 (C8)**, 14 769–14 780.

Hood, R. R., and Coauthors, 2006: Pelagic functional group modeling: Progress, challenges and prospects. *Deep Sea Research Part II: Topical Studies in Oceanography*, **53 (5-7)**, 459–512.

Huete-Ortega, M., T. Rodríguez-Ramos, D. López-Sandoval, P. Cermeño, J. M. Blanco, R. L. Palomino, J. Rodríguez, and E. Marañón, 2014: Distinct patterns in the size-scaling of abundance and metabolism in coastal and open-ocean phytoplankton communities. *Marine Ecology Progress Series*, **515**, 61–71.

Huisman, J., P. van Oostveen, and F. J. Weissing, 1999: Critical depth and critical turbulence: two different mechanisms for the development of phytoplankton blooms. *Limnology and oceanography*, **44 (7)**, 1781–1787.

Hutchinson, G. E., 1961: The paradox of the plankton. *The American Naturalist*, **95 (882)**, 137–145.

Huyer, A., 1983: Coastal upwelling in the california current system. *Progress in oceanography*, **12 (3)**, 259–284.

Ingrid, G., T. Andersen, and O. Vadstein, 1996: Pelagic food webs and eutrophication of coastal waters: impact of grazers on algal communities. *Marine Pollution Bulletin*, **33 (1-6)**, 22–35.

Iversen, M. H., and R. S. Lampitt, 2020: Size does not matter after all: No evidence for a size-sinking relationship for marine snow. *Progress in Oceanography*, **189**, 102 445.

Jacox, M., and C. Edwards, 2011: Effects of stratification and shelf slope on nutrient supply in coastal upwelling regions. *Journal of Geophysical Research: Oceans*, **116 (C3)**.

Jacox, M., and C. Edwards, 2012: Upwelling source depth in the presence of nearshore wind stress curl. *J. Phys. Resc.*, **117**.

Jacox, M. G., C. A. Edwards, E. L. Hazen, and S. J. Bograd, 2018: Coastal upwelling revisited: Ekman, bakun, and improved upwelling indices for the us west coast. *Journal of Geophysical Research: Oceans*, **123 (10)**, 7332–7350.

Jacox, M. G., A. M. Moore, C. A. Edwards, and J. Fiechter, 2014: Spatially resolved upwelling in the California Current System and its connections to climate variability. *Geophys. Res. Lett.*, **41**.

Johnson, K. S., S. C. Riser, and D. M. Karl, 2010: Nitrate supply from deep to near-surface waters of the north pacific subtropical gyre. *Nature*, **465 (7301)**, 1062–1065.

Jonasz, M., and G. Fournier, 1996: Approximation of the size distribution of marine particles by a sum of log-normal functions. *Limnology and Oceanography*, **41 (4)**, 744–754.

Kahan, W., 1965: Pracniques: further remarks on reducing truncation errors. *Communications of the ACM*, **8 (1)**, 40.

Karl, D. M., 2002: Nutrient dynamics in the deep blue sea. *TRENDS in Microbiology*, **10 (9)**, 410–418.

Karp-Boss, L., L. Azevedo, and E. Boss, 2007: Lisst-100 measurements of phytoplankton size distribution: Evaluation of the effects of cell shape. *Limnology and Oceanography: Methods*, **5 (11)**, 396–406.

Kays, W. M., 1994: Turbulent Prandtl number. Where are we? *ASME Transactions Journal of Heat Transfer*, **116**, 284–295.

Kessouri, F., D. Bianchi, L. Renault, J. C. McWilliams, H. Frenzel, and C. A. Deutsch, 2020: Submesoscale currents modulate the seasonal cycle of nutrients and productivity in the california current system. *Global Biogeochemical Cycles*, **34 (10)**, e2020GB006 578.

Kiørboe, T., 2011: How zooplankton feed: mechanisms, traits and trade-offs. *Biological reviews*, **86 (2)**, 311–339.

Klausmeier, C. A., C. T. Kremer, and T. Koffel, 2020: Trait-based ecological and eco-evolutionary theory. *Theoretical Ecology*, Oxford University Press, 161–194.

Klausmeier, C. A., and E. Litchman, 2001: Algal games: The vertical distribution of phytoplankton in poorly mixed water columns. *Limnology and Oceanography*, **46 (8)**, 1998–2007.

Kriest, I., 2002: Different parameterizations of marine snow in a 1d-model and their influence on representation of marine snow, nitrogen budget and sedimentation. *Deep Sea Research Part I: Oceanographic Research Papers*, **49 (12)**, 2133–2162.

Kurganov, A., and E. Tadmor, 2000: New high-resolution central schemes for nonlinear conservation laws and convection-diffusion equations. *J. Comput. Phys.*, **160**, 241–282.

Lacasce, J. H., 2017: The prevalence of oceanic surface modes. *Geophysical Research Letters*, **44 (21)**, 11–097.

Lamb, K. G., 2014: Internal wave breaking and dissipation mechanisms on the continental slope/shelf. *Annual Review of Fluid Mechanics*, **46 (1)**, 231–254.

Large, W. G., J. C. McWilliams, and S. C. Doney, 1994: Oceanic vertical mixing: A review and a model with a nonlocal boundary layer parameterization. *Reviews of Geophysics*, **32 (4)**, 363–403.

Lehman, J. T., 1991: Interacting growth and loss rates: The balance of top-down and bottom-up controls in plankton communities. *Limnology and Oceanography*, **36 (8)**, 1546–1554.

Leibold, M. A., 1996: A graphical model of keystone predators in food webs: trophic regulation of abundance, incidence, and diversity patterns in communities. *The American Naturalist*, **147 (5)**, 784–812.

Lentz, S. J., and D. C. Chapman, 2004: The importance of nonlinear cross-shelf momentum flux during wind-driven coastal upwelling. *Journal of Physical Oceanography*, **34 (11)**, 2444–2457.

Lentz, S. J., and M. R. Fewings, 2012: The wind-and wave-driven inner-shelf circulation. *Annual review of marine science*, **4**, 317–343.

Lévy, M., 2003: Mesoscale variability of phytoplankton and of new production: Impact of the large-scale nutrient distribution. *Journal of Geophysical Research: Oceans*, **108 (C11)**.

Lévy, M., O. Jahn, S. Dutkiewicz, and M. J. Follows, 2014: Phytoplankton diversity and community structure affected by oceanic dispersal and mesoscale turbulence. *Limnology and Oceanography: Fluids and Environments*, **4 (1)**, 67–84.

Lévy, M., P. Klein, and A.-M. Treguier, 2001: Impact of sub-mesoscale physics on production and subduction of phytoplankton in an oligotrophic regime. *Journal of marine research*, **59 (4)**, 535–565.

Litchman, E., and C. A. Klausmeier, 2008: Trait-based community ecology of phytoplankton. *Annual review of ecology, evolution, and systematics*, **39**, 615–639.

Litchman, E., C. A. Klausmeier, O. M. Schofield, and P. G. Falkowski, 2007: The role of functional traits and trade-offs in structuring phytoplankton communities: scaling from cellular to ecosystem level. *Ecology letters*, **10 (12)**, 1170–1181.

Loeuille, N., and M. Loreau, 2004: Nutrient enrichment and food chains: can evolution buffer top-down control? *Theoretical population biology*, **65 (3)**, 285–298.

Loeuille, N., and M. Loreau, 2005: Evolutionary emergence of size-structured food webs. *Proceedings of the National Academy of Sciences*, **102 (16)**, 5761–5766.

Mahadevan, A., E. D'asaro, C. Lee, and M. J. Perry, 2012: Eddy-driven stratification initiates north atlantic spring phytoplankton blooms. *Science*, **337 (6090)**, 54–58.

Marañón, E., P. Cermeño, M. Huete-Ortega, D. C. López-Sandoval, B. Mouriño-Carballido, and T. Rodríguez-Ramos, 2014: Resource supply overrides temperature as a controlling factor of marine phytoplankton growth. *PloS one*, **9 (6)**, e99 312.

MATLAB, 2016: *version 9.1.0 (R2016b)*. The MathWorks Inc., Natick, Massachusetts.

McCave, I., 1975: Vertical flux of particles in the ocean. *Deep Sea Research and Oceanographic Abstracts*, Elsevier, Vol. 22, 491–502.

McClatchie, S., 2016: *Regional fisheries oceanography of the California Current System*. Springer.

McDougall, T. J., and R. Ferrari, 2017: Abyssal upwelling and downwelling driven by near-boundary mixing. *Journal of Physical Oceanography*, **47 (2)**, 261–283.

McQueen, D. J., J. R. Post, and E. L. Mills, 1986: Trophic relationships in freshwater pelagic ecosystems. *Canadian Journal of Fisheries and Aquatic Sciences*, **43 (8)**, 1571–1581.

Mellor, G. L., T. Ezer, and L.-Y. Oey, 1994: The pressure gradient conundrum of sigma coordinate ocean models. *Journal of Atmospheric and Oceanic Technology*, **11 (4)**, 1126–1134.

Mellor, G. L., L.-Y. Oey, and T. Ezer, 1998: Sigma coordinate pressure gradient errors and the seamount problem. *Journal of Atmospheric and Oceanic Technology*, **15 (5)**, 1122–1131.

Merico, A., G. Brandt, S. L. Smith, and M. Oliver, 2014: Sustaining diversity in trait-based models of phytoplankton communities. *Frontiers in Ecology and Evolution*, **2**, 59.

Messié, M., J. Ledesma, D. D. Kolber, R. P. Michisaki, D. G. Foley, and F. P. Chavez, 2009: Potential new production estimates in four eastern boundary upwelling ecosystems. *Progress in Oceanography*, **83 (1-4)**, 151–158.

Moore, J., S. C. Doney, J. A. Kleypas, D. M. Glover, and I. Y. Fung, 2001: An intermediate complexity marine ecosystem model for the global domain. *Deep Sea Res.*, **49 (1)**, 403 – 462.

Moscoso, J. E., D. Bianchi, and A. L. Stewart, 2022: Controls and characteristics of biomass quantization in size-structured planktonic ecosystem models. *Ecological Modelling*, **468**, 109 907.

Moscoso, J. E., A. L. Stewart, D. Bianchi, and J. C. McWilliams, 2021: The meridionally averaged model of eastern boundary upwelling systems (mamebusv1. 0). *Geoscientific Model Development*, **14 (2)**, 763–794.

Mousing, E. A., K. Richardson, J. Bendtsen, I. Cetinić, and M. J. Perry, 2016: Evidence of small-scale spatial structuring of phytoplankton alpha-and beta-diversity in the open ocean. *Journal of Ecology*, **104 (6)**, 1682–1695.

Murray, A., and J. Parslow, 1999: The analysis of alternative formulations in a simple model of a coastal ecosystem. *Ecological Modelling*, **119 (2-3)**, 149–166.

Negrete-García, G., J. Y. Luo, M. C. Long, K. Lindsay, M. Levy, and A. D. Barton, 2022: Plankton energy flows using a global size-structured and trait-based model. *bioRxiv*.

NOAA, 1988: Data announcement 88-mgg-02, digital relief of the surface of the earth. NOAA, National Geophysical Data Center, Boulder CO.

Obata, A., J. Ishizaka, and M. Endoh, 1996: Global verification of critical depth theory for phytoplankton bloom with climatological in situ temperature and satellite ocean color data. *Journal of Geophysical Research: Oceans*, **101 (C9)**, 20 657–20 667.

Partensky, F., J. Blanchot, and D. Vaulot, 1999: Differential distribution and ecology of prochlorococcus and synechococcus in oceanic waters: a review. *Bulletin-Institut Oceanographique Monaco-Numero Special-*, 457–476.

Perlin, A., J. Moum, and J. Klymak, 2005: Response of the bottom boundary layer over a sloping shelf to variations in alongshore wind. *Journal of Geophysical Research: Oceans*, **110 (C10)**.

Plumb, R. A., 1979: Eddy fluxes of conserved quantities by small-amplitude waves. *J. Atmos. Sci.*, **36 (9)**, 1699–1704.

Plumb, R. A., and R. Ferrari, 2005a: Transformed eulerian-mean theory. part i: Nonquasi-geostrophic theory for eddies on a zonal-mean flow. *Journal of Physical Oceanography*, **35 (2)**, 165–174.

Plumb, R. A., and R. Ferrari, 2005b: Transformed Eulerian-mean theory. Part I: Nonquasi-geostrophic theory for eddies on a zonal-mean flow. *J. Phys. Oceanogr.*, **35 (2)**, 165–174.

Polimene, L., S. Sailley, D. Clark, A. Mitra, and J. I. Allen, 2017: Biological or microbial carbon pump? the role of phytoplankton stoichiometry in ocean carbon sequestration. *Journal of Plankton Research*, **39 (2)**, 180–186.

Poulin, F. J., and P. J. Franks, 2010a: Size-structured planktonic ecosystems: constraints, controls and assembly instructions. *Journal of plankton research*, **32 (8)**, 1121–1130.

Poulin, F. J., and P. J. S. Franks, 2010b: Size-structured planktonic ecosystems: constraints, controls, and assembly instructions. *Journal of Plankton Research*, **32 (8)**, 1121–1130.

Pozo Buil, M., M. G. Jacox, J. Fiechter, M. A. Alexander, S. J. Bograd, E. N. Curchitser, C. A. Edwards, R. R. Rykaczewski, and C. A. Stock, 2021: A dynamically downscaled ensemble of future projections for the california current system. *Frontiers in Marine Science*, **8**, 324.

Quere, C. L., and Coauthors, 2005: Ecosystem dynamics based on plankton functional types for global ocean biogeochemistry models. *Global Change Biology*, **11 (11)**, 2016–2040.

Raick, C., K. Soetaert, and M. Gregoire, 2006: Model complexity and performance: How far can we simplify? *Progress in Oceanography*, **70 (1)**, 27 – 57.

Record, N. R., A. J. Pershing, and F. Maps, 2014: The paradox of the "paradox of the plankton". *ICES Journal of marine science*, **71 (2)**, 236–240.

Redi, M. H., 1982: Oceanic isopycnal mixing by coordinate rotation. *J. Phys. Oceanogr.*, **12 (10)**, 1154–1158.

Renault, L., C. Deutsch, J. McWilliams, H. Frenzel, J. Liang, and F. Colas, 2016: Partial decoupling of primary productivity from upwelling in the California Current system. *Nat. Geo. Sci.*, **9**, 505–510.

Richardson, T. L., and G. A. Jackson, 2007: Small phytoplankton and carbon export from the surface ocean. *Science*, **315 (5813)**, 838–840.

Righetti, D., M. Vogt, N. Gruber, A. Psomas, and N. E. Zimmermann, 2019: Global pattern of phytoplankton diversity driven by temperature and environmental variability. *Science advances*, **5 (5)**, eaau6253.

Rodriguez, J., J. Tintoré, J. T. Allen, J. M. Blanco, D. Gomis, A. Reul, J. Ruiz, V. Rodríguez, F. Echevarría, and F. Jiménez-Gómez, 2001: Mesoscale vertical motion and the size structure of phytoplankton in the ocean. *Nature*, **410 (6826)**, 360–363.

Ryabov, A. B., L. Rudolf, and B. Blasius, 2010: Vertical distribution and composition of phytoplankton under the influence of an upper mixed layer. *Journal of Theoretical Biology*, **263 (1)**, 120–133.

Rykaczewski, R. R., and D. M. Checkley, 2008: Influence of ocean winds on the pelagic ecosystem in upwelling regions. *Proceedings of the National Academy of Sciences*, **105 (6)**, 1965–1970.

Rykaczewski, R. R., and J. P. Dunne, 2010: Enhanced nutrient supply to the California Current Ecosystem with global warming and increased stratification in an earth system model. *Geo. Res. Lett.*, **37**.

Ryther, J. H., 1969: Photosynthesis and fish production in the sea: The production of organic matter and its conversion to higher forms of life vary throughout the world ocean. *Science*, **166 (3901)**, 72–76.

Sarmiento, J. L., and N. Gruber, 2006: *Ocean Biogeochemical Dynamics*. Princeton University Press.

Sarmiento, J. L., T. M. C. Hughes, R. J. Stouffer, and S. Manabe, 1998: Simulated response of the ocean carbon cycle to anthropogenic climate warming. *Letters to Nature*, **393**.

Sauterey, B., B. Ward, J. Rault, C. Bowler, and D. Claessen, 2017: The implications of eco-evolutionary processes for the emergence of marine plankton community biogeography. *The American Naturalist*, **190 (1)**, 116–130.

Schartau, M., M. R. Landry, and R. A. Armstrong, 2010: Density estimation of plankton size spectra: a reanalysis of ironex ii data. *Journal of plankton research*, **32 (8)**, 1167–1184.

Shchepetkin, A. F., and J. C. McWilliams, 2003: A method for computing horizontal pressure-gradient force in an oceanic model with a nonaligned vertical coordinate. *Journal of Geophysical Research: Oceans*, **108 (C3)**.

Shchepetkin, A. F., and J. C. McWilliams, 2005: The Regional Ocean Modeling System: A split-explicit, free-surface, topography following coordinates ocean model. *Ocean Modell.*, **9**, 347–404.

Sheldon, R., A. Prakash, and W. Sutcliffe Jr, 1972: The size distribution of particles in the ocean 1. *Limnology and oceanography*, **17 (3)**, 327–340.

Sherr, E. B., B. F. Sherr, and P. A. Wheeler, 2005: Distribution of coccoid cyanobacteria and small eukaryotic phytoplankton in the upwelling ecosystem off the oregon coast during 2001 and 2002. *Deep Sea Research Part II: Topical Studies in Oceanography*, **52 (1-2)**, 317–330.

Skamarock, C., and Coauthors, 2019: A description of the advanced research wrf model version 4.

Smith, K. S., and J. Marshall, 2009: Evidence for enhanced eddy mixing at middepth in the southern ocean. *Journal of Physical Oceanography*, **39 (1)**, 50–69.

Sommer, U., 1989: The role of competition for resources in phytoplankton succession. *Plankton ecology*, Springer, 57–106.

Song, Y., and D. Haidvogel, 1994: A semi-implicit ocean circulation model using a generalized topography-following coordinate system. *J. Comput. Phys.*, **115 (1)**, 228–244.

Spellerberg, I. F., and P. J. Fedor, 2003: A tribute to claude shannon (1916–2001) and a plea for more rigorous use of species richness, species diversity and the 'shannon–wiener'index. *Global ecology and biogeography*, **12 (3)**, 177–179.

St. Laurent, L., H. Simmons, and S. Jayne, 2002: Estimating tidally driven mixing in the deep ocean. *Geophysical Research Letters*, **29 (23)**, 21–1.

Steele, J. H., and E. W. Henderson, 1992: The role of predation in plankton models. *Journal of Plankton Research*, **14 (1)**, 157–172.

Stock, C. A., J. G. John, R. R. Rykaczewski, R. G. Asch, W. W. Cheung, J. P. Dunne, K. D. Friedland, V. W. Lam, J. L. Sarmiento, and R. A. Watson, 2017: Reconciling fisheries catch and ocean productivity. *Proceedings of the National Academy of Sciences*, **114 (8)**, E1441–E1449.

Strom, S. L., and H. Loukos, 1998: Selective feeding by protozoa: model and experimental behaviors and their consequences for population stability. *Journal of Plankton Research*, **20 (5)**, 831–846.

Sverdrup, H., 1953: On conditions for the vernal blooming of phytoplankton. *J. Cons. Int. Explor. Mer*, **18 (3)**, 287–295.

Swenson, M. S., and P. P. Niiler, 1996: Statistical analysis of the surface circulation of the california current. *Journal of Geophysical Research: Oceans*, **101 (C10)**, 22 631–22 645.

Tang, E., 1995: The allometry of algal growth rates. *Journal of Plankton Research*, **17**, 1325–1335.

Taylor, A. G., R. Goericke, M. R. Landry, K. E. Selph, D. A. Wick, and M. J. Roadman, 2012: Sharp gradients in phytoplankton community structure across a frontal zone in the california current ecosystem. *Journal of Plankton Research*, **34 (9)**, 778–789.

Terseleer, N., J. Bruggeman, C. Lancelot, and N. Gypens, 2014: Trait-based representation of diatom functional diversity in a plankton functional type model of the eutrophied southern north sea. *Limnology and Oceanography*, **59 (6)**, 1958–1972.

Traganza, E. D., D. G. Redalije, and R. W. Garwood, 1987: Chemical flux, mixed layer entrainment and phytoplankton blooms at upwelling fronts in the california coastal zone. *Continental Shelf Research*, **7 (1)**, 89–105.

Tréguer, P., and Coauthors, 2018: Influence of diatom diversity on the ocean biological carbon pump. *Nature Geoscience*, **11 (1)**, 27–37.

Tréguier, A.-M., I. M. Held, and V. D. Larichev, 1997: Parameterization of quasigeostrophic eddies in primitive equation ocean models. *J. Phys. Oceanogr.*, **27 (4)**, 567–580.

Troen, I. B., and L. Mahrt, 1986: A simple model of the atmospheric boundary layer; sensitivity to surface evaporation. *Boundary-Layer Meteorology*, **37 (1)**, 129–148.

Trowbridge, J., and S. Lentz, 1998: Dynamics of the bottom boundary layer on the northern california shelf. *Journal of Physical Oceanography*, **28 (10)**, 2075–2093.

Vallina, S. M., M. Follows, S. Dutkiewicz, J. M. Montoya, P. Cermeno, and M. Loreau, 2014: Global relationship between phytoplankton diversity and productivity in the ocean. *Nature communications*, **5 (1)**, 1–10.

Vallis, G. K., 2017: *Atmospheric and oceanic fluid dynamics*. Cambridge University Press.

Van Oostende, N., R. Dussin, C. Stock, A. Barton, E. Curchitser, J. Dunne, and B. Ward, 2018: Simulating the ocean's chlorophyll dynamic range from coastal upwelling to oligotrophy. *Progress in Oceanography*, **168**, 232–247.

Van Oostende, N., R. Dussin, C. Stock, A. Barton, E. Curchitser, J. Dunne, and B. Ward, 2018: Simulating the ocean's chlorophyll dynamic range from coastal upwelling to oligotrophy. *Progress in oceanography*, **168**, 232–247.

Venegas, R. M., P. T. Strub, E. Beier, R. Letelier, A. C. Thomas, T. Cowles, C. James, L. Soto-Mardones, and C. Cabrera, 2008: Satellite-derived variability in chlorophyll, wind stress, sea surface height, and temperature in the northern california current system. *Journal of Geophysical Research: Oceans*, **113 (C3)**.

Venrick, E., 1982: Phytoplankton in an oligotrophic ocean: Observations and questions: Ecological archives m052-002. *Ecological Monographs*, **52 (2)**, 129–154.

Venrick, E., 1993: Phytoplankton seasonality in the central north pacific: the endless summer reconsidered. *Limnology and Oceanography*, **38 (6)**, 1135–1149.

Venrick, E., 2002: Floral patterns in the california current system off southern california: 1990-1996. *Journal of Marine Research*, **60 (1)**, 171–189.

Verity, P. G., and V. Smetacek, 1996: Organism life cycles, predation, and the structure of marine pelagic ecosystems. *Marine Ecology Progress Series*, **130**, 277–293.

Wang, Y., and A. L. Stewart, 2018: Eddy dynamics over continental slopes under retrograde winds: Insights from a model inter-comparison. *Ocean Modelling*, **121**, 1–18.

Wang, Y., and A. L. Stewart, 2020: Scalings for eddy buoyancy transfer across continental slopes under retrograde winds. *Ocean Modelling*, **147**, 101 579.

Ward, B. A., S. Dutkiewicz, and M. J. Follows, 2014: Modelling spatial and temporal patterns in size-structured marine plankton communities: top–down and bottom–up controls. *Journal of Plankton Research*, **36 (1)**, 31–47.

Ward, B. A., S. Dutkiewicz, O. Jahn, and M. J. Follows, 2012: A size-structured food-web model for the global ocean. *Luminol. Oceanogr.*, **57 (6)**, 1877–1891.

Whitney, F., C. Wong, and P. Boyd, 1998: Interannual variability in nitrate supply to surface waters of the northeast pacific ocean. *Marine Ecology Progress Series*, **170**, 15–23.

Worden, A. Z., J. K. Nolan, and B. Palenik, 2004: Assessing the dynamics and ecology of marine picophytoplankton: the importance of the eukaryotic component. *Limnology and oceanography*, **49 (1)**, 168–179.

Zhou, M., and M. E. Huntley, 1997: Population dynamics theory of plankton based on biomass spectra. *Marine Ecology Progress Series*, **159**, 61–73.

Zubkov, M. V., M. A. Sleigh, and P. H. Burkill, 2000: Assaying picoplankton distribution by flow cytometry of underway samples collected along a meridional transect across the atlantic ocean. *Aquatic Microbial Ecology*, **21 (1)**, 13–20.